ADVANCED MODELS FOR INFLAMMATION-DEPENDENT DRUG-INDUCED ORGAN TOXICITY.



Linda van den Berk

Stellingen

Behorende bij het proefschrift

Advanced models for inflammation-dependent drug-induced organ toxicity

1. TNF-α-induced NF-κB signalling provides a mechanistically relevant readout for identifying inflammation-associated drug-induced toxicity (this thesis).
2. Mechanism-based approaches integrating high content confocal microscopy and GFP reporters with toxicogenomics are required to improve the interpretation and prediction of drug-induced organ toxicity (this thesis).
3. The integration of inflammatory stress responses into hiPSC-derived models can improve the detection of drug-induced toxicity that is not captured under basal conditions (this thesis).
4. Assessment of drug-induced toxicity across multiple organ-specific hiPSC-derived lineages is essential to identify organ-specific liabilities (this thesis).
5. Improving the prediction of drug-induced liver injury requires moving beyond conventional cell models towards a fit-for-purpose combination of human-relevant *in vitro* systems (based on Weaver et al, 2020, *Nat Rev Drug Discov*.).
6. Without standardized differentiation and validation, hiPSC-derived liver models will remain promising research tools rather than reliable drug discovery platforms (based on Tricot et al, 2022, *Cells*).
7. A toxicity model that excludes inflammatory signalling cannot fully recapitulate the complexity of drug-induced liver injury (based on Woolbright et al, 2018, *Curr Pharmacol Rep*.).
8. The inability to reproduce idiosyncratic drug-induced liver injury *in vitro* reflects its biological complexity rather than the absence of mechanistic pathways (based on Teschke et al, 2020, *Curr Pharmacol Rep*.).
9. Predicting drug-induced liver injury requires moving from detecting cellular damage to understanding its underlying mechanisms (based on Guo et al, 2024, *Cell Biosci*.).
10. Just as PSC differentiation requires sequential steps to achieve cellular maturity, personal growth requires each step to develop into a more mature version of oneself.

Linda van den Berk
Leiden, 11 November 2026

Advanced models for inflammation-dependent drug-induced organ toxicity

Linda van den Berk

Cover design: Stefanie van den Herik | HerikMedia | www.herikmedia.nl
Printing: ProefschriftMaken.nl | www.proefschriftmaken.nl

© Copyright, Linda van den Berk, 2026

ISBN: 978-94-6534-703-5

All rights reserved. No part of this book may be reproduced in any form or by any means without permission of the author.

Advanced models for inflammation-dependent drug-induced organ toxicity

Proefschrift

ter verkrijging van

de graad van doctor aan de Universiteit Leiden,

op gezag van rector magnificus prof.dr. S. de Rijcke,

volgens besluit van het college voor promoties

te verdedigen op woensdag 11 november

klokke 10:00 uur

door

Linda van den Berk

geboren te Rotterdam, Nederland

in 1993

Promotor:
prof.dr. B. van de Water

Copromotor:
dr. S.J. ter Braak

Promotiecommissie:

Prof.dr. M. van Eck	
Prof.dr. E.C.M. de Lange	
Prof.dr. E.H.J. Danen	
Prof.dr. M. Luijten	
dr. L.J.A.C. Hawinkels	Leiden University Medical Centre
dr. A. Wilmes	Vrije Universiteit Amsterdam

The research described in this thesis was performed at the division of Cell Systems and Drug Safety of the Leiden Academic Centre for Drug Research (LACDR), Leiden University (Leiden, The Netherlands). The research was financially supported by the EC Horizon2020 EU-ToxRisk project (grant number 681002); and the EC Horizon2020 RISK-HUNT3R project (grant number 964537).

Voor Tobias

Je hebt zo dapper gestreden tot aan je laatste zucht
Mijn kusjes aan jou gaan nu met liefde in de lucht

Table of contents

Chapter 1 **11**

General introduction, aim & scope of the thesis

Chapter 2 **27**

Squaramide-Based Supramolecular Materials Drive HepG2 Spheroid Differentiation

Chapter 3 **65**

Systemic comparison of in vitro models to assess inflammation-associated drug-induced liver injury

Chapter 4 **97**

Generation of fluorescent reporters in hiPSC to assess inflammation-associated drug-induced organ toxicity

Chapter 5 **133**

A broad kinase inhibitor library live cell imaging screen using liver, kidney and cardiac hiPSC-ICAM1-eGFP reporter lineages identifies liabilities for TNF-α pathway modulation

Chapter 6 **169**

General discussion and future perspectives

Appendix **181**

References
Abbreviations
Nederlandse samenvatting
List of publications
About the author



CHAPTER 1

GENERAL INTRODUCTION, AIM & SCOPE OF THE THESIS

Adverse drug reactions (ADRs) are unwarranted and unintended reactions to medication which can be mild or of a life-threatening nature. They continue to pose significant challenges in drug development, safety evaluation, and clinical practice with rising causes of morbidity and mortality, ultimately leading to a significant public health issue. ADRs are responsible for ~5-10% of hospital admissions and have not significantly improved over the last decade[1]. Advancing mechanistic insights and refining toxicity testing methodologies are imperative for accurately predicting drug-induced organ toxicity risks associated with specific compounds and patient populations. The liver, kidneys, and cardiovascular system are among the most affected organs by ADRs[2]. In this thesis, we especially focused on these target organs of toxicity in relation to compound-induced alterations in inflammatory stress via NF-kB/TNF-α signalling using different human relevant *in vitro* test methods. Below we will first address briefly the cardiovascular system, the kidney and the liver. Since the liver is the major target organ of adverse responses and studied more extensively in this thesis, additionally, mechanisms involved in hepatotoxicity will be discussed.

Commonly affected organs by adverse reactions

The cardiovascular system.

The cardiovascular system encompasses the heart, arteries, veins and capillaries. Its main function is to pump blood carrying oxygen, nutrients, hormones and other substances through the body. The heart is composed of four chambers; the right and left atrium, and the right and left ventricle. Deoxygenated blood arrives in the heart through the right atrium, which is subsequently pumped to the lung via the right ventricle. The left atrium receives oxygen-rich blood from the lungs, and the left ventricle subsequently pumps the blood to the rest of the body[3].

The heart contains several distinct cell types. Cardiomyocytes are the primary cell type of the heart and responsible for cardiac contraction. Cardiac fibroblasts synthesize and remodel the extracellular matrix, interact with immune cells and influence cardiac conductivity and rhythmicity. In addition, they play a key role in myocardial repair processes, such as those occurring post myocardial infarction or during chronic cardiac diseases. Endothelial cells cover the lumen of the cardiac chambers, blood and lymphatic vessels, where they regulate blood flow by modulating vascular relaxation and constriction, and contribute to leukocyte trafficking, haemostasis and angiogenesis[4,5]. The cardiovascular system also includes diverse immune cell populations, including tissue-resident macrophages which are abundant in healthy conditions and contribute to repair following damage[6]. On the other hand, peripheral blood-derived mononuclear cells (PBMCs) can be recruited to the heart following cardiac injury through the CCL2-CCR2 axis, which may promote extensive cardiac damage and adverse remodelling contributing to cardiac dysfunction[7].

Cardiotoxicity is one of the common types of adverse drug reactions. Molecular mechanisms underlying cardiotoxicity are broad and amongst others include disruption of contractility (e.g. by tyrosine kinase inhibitors), impact on electrophysiology (e.g. by antidepressants), mitochondrial malfunctioning (e.g. by antibiotics), and growth factor and immune dysregulation (e.g. by monoclonal antibodies)[8]. Such effects can ultimately result in heart failure and may also manifest as myocardial ischemia, valvular disease, thrombosis, pericarditis, arrhythmias, or conduction disorders[9].

An important mechanism of cardiotoxicity involves the immune response triggered by anti-tumour and anti-viral drugs[10]. Anthracyclines such as doxorubicin induce DNA damage and oxidative stress, , resulting in cardiac cell death. This results in the recruitment of monocytes to the heart and the subsequent initiation of the release of pro-inflammatory cytokines by polarized macrophages, which can result in fibrosis of the heart and ultimately heart failure[11]. In addition, inflammation of the myocardium, called myocarditis, is a rare, but serious condition found in cancer patients treated with immune checkpoint inhibitors, including pembrolizumab, nivolumab atezolizumab, and ipilimumab, which target PD-1, PDL-1 and CTLA-4 respectively, to enhance antitumor immune responses. The precise molecular mechanisms behind drug-induced myocarditis remain unclear but identifying them is of utmost importance to identify at-risk patients and develop target approaches to minimize the development of myocarditis[12].

Another important class of cardiotoxic compounds consists of kinase inhibitors (KIs) which disrupt signalling pathways by inhibition of kinases. While they possess undeniable survival advantages in patients with cancer[13,14], their cardiovascular adverse reactions can be life-threatening[15]. KIs can induce a range of cardiovascular toxicities, including heart failure (e.g. erlotinib), QT interval prolongation (e.g. osimertinib), atrial fibrillation (e.g. gefitinib), myocardial infarction/ischemia (e.g. erlotinib), and myocarditis (e.g. gefitinib)[16,17].

The kidney.

The primary functions of the kidney include filtering blood to remove waste products and excess fluid, electrocyte and blood pressure regulation, maintaining acid-base balance and the production of hormones, including calcitriol (active vitamin D), erythropoietin (red blood cell production), and renin and angiotensin (blood pressure regulation)[18]. The filtration process consists of different processes, starting with glomerular filtration. Here, the glomerulus, a network of capillaries, filters the blood to remove water, small solutes and waste products. Subsequently, the filtrate moves through the renal tubules and nephron to facilitate the reabsorption of water, glucose, electrolytes and amino acids back into the blood stream. To dispose additional waste

products including drugs and metabolites, active secretion takes place to remove those substances from the blood into the tubules to be finally excreted via urine. Finally, urine is produced which is collected from the nephrons and is transported to the bladder for elimination.

The kidneys consist of numerous specialized cell types. Among the most abundant are endothelial cells. Glomerular endothelial cells play a crucial role in filtration within the glomerulus, whereas peritubular capillary endothelial cells are essential for reabsorption processes. Structural support of the glomerulus is provided by mesangial cells, which are primarily responsible for extracellular matrix production, regulation of blood flow, phagocytosis, and maintenance of glomerular homeostasis. Filtration selectivity and the fenestrated structure of the glomerular endothelium are preserved by specialized glomerular epithelial cells known as podocytes. Reabsorption of nutrients, electrolytes, and water is carried out by specialized epithelial cells of the proximal tubule (PT). Proximal tubule cells constitute the majority of renal cells and are particularly susceptible to injury[19]. Similar to the PT, other parts of the nephron tubules are also lined by specialized epithelial cells, including cells of the loop of Henle, which are involved in ion transport; distal tubule cells, which regulate electrolyte balance; and collecting duct cells, which maintain acid–base homeostasis. In addition, the kidney harbours a diverse population of innate and adaptive immune cells, including tissue-resident macrophages, neutrophils, B and T lymphocytes, and natural killer cells. Finally, the renal interstitium contains fibroblasts, myofibroblasts, and perivascular cells, which contribute to kidney function by regulating blood flow and hormone production[20].

Acute kidney injury (AKI) is often induced by drugs, accounting for ~14-26% of cases in hospitalized adults[21]. Drug-induced kidney injury (DIKI) can be induced via various mechanisms, including direct tubular damage and acute interstitial nephritis (AIN). Besides its function in reabsorption, the PT is also a major route where xenobiotics are metabolized and excreted due to the high expression of drug transporters, and phase I and II metabolizing enzymes. Due to the high number of xenobiotics passing through the PT, it is a common site for the development of drug-induced kidney injury[22].

Multiple classes of drugs are implicated in causing PT injury, including antibiotics, analgesics, and chemotherapeutics[23]. Similar to the heart, the immune system contributes to drug-induced kidney injury. During AIN, infiltration of eosinophils in the tubulointerstitium takes place. Various drug classes may induce AIN, including antibiotics, NSAIDs and proton pump inhibitors. In addition, kinase inhibitors can also induce immune-mediated drug reactions in the kidney and include ibrutinib and sunitinib[24,25]. Depending on the drug, additional pathophysiological processes may occur, including acute tubular necrosis, crystal nephropathy, alterations in renal

hemodynamics, and direct cellular toxicity, all of which contribute to impaired kidney function[26].

The liver.

The liver is the largest internal organ of the human body. It is critical for many physiological processes, including macronutrient metabolism, blood volume regulation, endocrine control, lipid and cholesterol homeostasis, support of the immune system, and metabolism of xenobiotics, including drugs. Each of these functions is maintained by a variety of cell types, including hepatocytes, cholangiocytes, stellate cells, tissue-resident macrophages (Kupffer cells), and liver sinusoidal endothelial cells[27]. Hepatocytes are the key epithelial cell type of the liver, followed by cells that line the lumen of the bile duct, called cholangiocytes. Stellate cells constitute a dynamic cell population existing in either a quiescent or activated state. During quiescence, their role is to store vitamin A in lipid droplets. However, during damage, stellate cells become activated, proliferate and transform into extracellular matrix depositing myofibroblasts subsequently contributing to fibrosis. Pathogenic stimuli introduced through the portal vein are recognized by the tissue resident macrophage population of the liver called Kupffer cells. They can acquire both a pro- and anti-inflammatory phenotype depending on various factors. E.g. they become pro-inflammatory when exposed to pathogens or bacterial components including lipopolysaccharide, inducing the secretion of pro-inflammatory cytokines like tumour necrosis factor-α (TNF-α), interleukin (IL) 1β (IL-1β) and IL-6. Subsequently, to halt the inflammatory response after a resolved infection, they predominantly secrete anti-inflammatory factors including IL-10. Macrophage plasticity enables Kupffer cells to regulate hepatic inflammation by dynamically transitioning between pro- and anti-inflammatory phenotypes. Finally, liver sinusoidal endothelial cells (LSECs) represent a specialized endothelial subtype characterized by the formation of fenestrated sieve plates within the sinusoidal lumen, containing transcellular pores ranging from 50 to 180 nm in diameter. These fenestrations facilitate the selective exchange of macromolecules and particles between the blood and hepatocytes while preserving essential barrier functions[28].

The functional units of the liver, called lobules, contain all cell types of the liver. Hepatocytes form chords in a hexagonal shape around the central vein. Portal triads, consisting of the hepatic artery, portal vein and bile duct are located at the vertices of the hexagon. The liver sinusoidal endothelial cells do not form tight junctions, thereby creating a sinusoidal network that minimizes barriers between blood and hepatocytes within the sinusoid. Oxygen-rich blood from the hepatic artery and nutrient-rich blood from the portal vein meet in the sinusoid, transfer through the lobule and eventually drain into the central vein. The composition of the blood varies throughout the liver

lobule. As blood progresses through the liver lobule, oxygen and nutrients are utilized, creating gradients of oxygen, nutrients, metabolites, toxic substances and waste products. This results in partitioning of function and is called metabolic zonation of the liver lobule. Especially the third zone is exposed for a relatively long period to specific molecules, including toxic substances and therefore, especially this zone is sensitive to toxicity[29] (Figure 1).

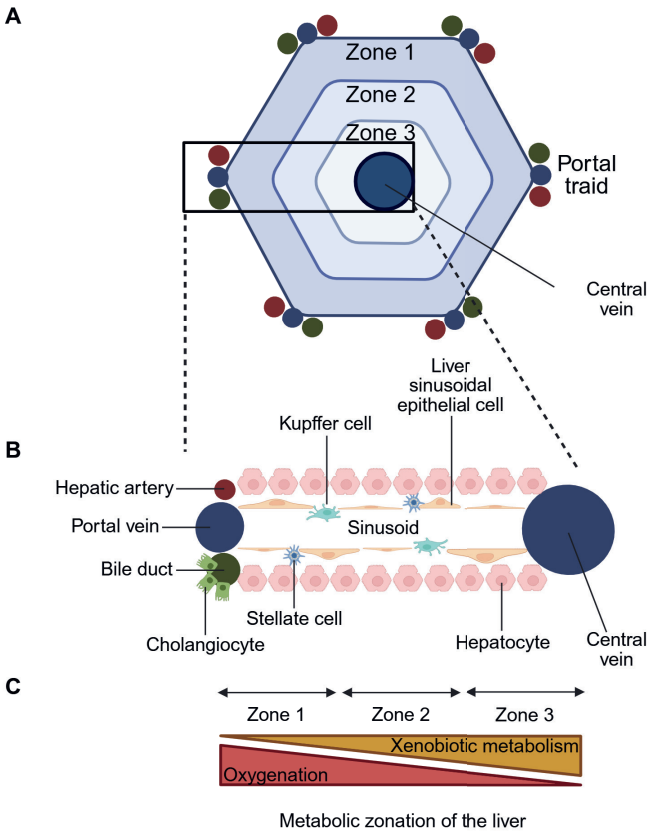


Figure 1. Structure of the liver. A) Schematic representation of a hepatic lobule with the different metabolic zones indicated. The portal triad consists of the bile duct and bile canaliculi (green), the hepatic artery (red), and venal blood flow in the portal vein in blue. **B**) Enlargement of a liver sinusoid with the different cell types indicated. **C)** Corresponding zonation of different processes within the sinusoid. Levels are indicated by the height of the triangles**.**

Drug-induced liver injury (DILI) is a relatively uncommon yet clinically significant adverse reaction to a drug. Although it represents only ~1% of the acute liver injury cases, it remains the leading cause of acute liver injury with a fatality rate of 10-50%[30]. Moreover, liver toxicity is the main cause of safety-related attrition in drug development[31,32]. Gaining a deeper understanding of the molecular mechanisms driving DILI is essential for improving the prediction of hepatotoxic risk associated with specific compounds and susceptible patient populations. DILI can lead to a diversity of pathologies and include acute hepatic necrosis, cholestasis, cirrhosis and hepatitis, depending on which specific function and cell type is affected by the injury.

Drug-induced adverse reactions and the inflammatory stress response

Multiple molecular mechanisms have been shown to contribute to drug-induced organ toxicity, including mitochondrial and lysosomal impairment, oxidative stress, endoplasmic reticulum/unfolded protein stress, and the DNA damage response[33–36]. These pathways enable cells to adapt to harmful conditions by activating protective mechanisms aimed at restoring homeostasis. However, prolonged activation or insufficient cellular adaptation can instead lead to cellular injury and/or cell death. In this thesis, we specifically focus on immune-mediated organ toxicity which is best described in DILI.

The role of the inflammatory stress response in DILI is rare and thought to be a complex multicellular event. It remains challenging to screen for compounds that induce immune-mediated DILI in preclinical models; these drugs are therefore only identified at a late stage during clinical trials or even after market approval, potentially leading to subsequent market withdrawal as has been the case for dilevalol, ximelagatran, and trovafloxacin[37]. Both the adaptive and innate immune system have been implicated to contribute to DILI. Liver biopsies from patients with idiosyncratic DILI have been analysed and showed accumulation of T lymphocytes alongside apoptotic hepatocytes[38]. Furthermore, it was found that drug-specific T cells can be isolated from patients treated with flucloxacillin and co-amoxiclav that developed DILI, but not from tolerant controls[39]. Certain HLA alleles have been associated with susceptibility to specific drugs, e.g. HLA-DRB1*15:01 (amoxicillin/clavulanate), HLA-B*57:01 (flucloxacillin) and HLA-B*35:02 (minocycline) indicating an important role for the adaptive immune system in the development of DILI[40–42]. The innate immune system has mainly been shown to be involved in DILI via the activation of the NF-κB and TNF-α signalling pathways. Co-exposure of bacterial components (e.g. lipopolysaccharide (LPS)) or the pro-inflammatory cytokine tumour necrosis factor-α (TNF-α) with drugs have been demonstrated to contribute to increased synergistic hepatotoxicity. This has been showcased for various drugs, including, sulindac, diclofenac and trovafloxacin[43–46]. The main producer of TNF-α in the liver are Kupffer cells, which start the production

of TNF-α once activated by danger-associated molecular patterns (DAMPs) derived from stressed or apoptotic hepatocytes or during concurrent liver inflammation. Under healthy conditions, hepatocytes are not sensitive to TNF-α induced cell death. However, during excessive or long-term hepatic inflammation, TNF-α can sensitize hepatocytes and induce excessive hepatotoxicity which is associated with several hepatic diseases[47,48].

TNF-α signalling

TNF-α signalling, induced by the pro-inflammatory cytokine TNF-α, is a key regulator of immune responses. It has a dual role in the development and functionality of the immune system by mediating both cell survival as cell death. TNF-α signalling relies on tightly regulated phosphorylation and ubiquitination of various key proteins in the signalling chain[49]. Binding of TNF-α to TNFR1 initiates receptor trimerization and results in the assembly of the TNFR1-associated signalling complex (complex 1). The adaptor proteins receptor interacting protein kinase 1 (RIPK1) and TNF receptor associated death domain (TRADD) are recruited to the TNFR1 via their death domains. Subsequently, the adaptor proteins TRAF2 and TRAF5 are recruited by TRADD and enable the recruitment of the E3 ligases cellular inhibitors of apoptosis 1 and 2 (c-AIP1 and c-IAP2), which leads to self-ubiquitination and ubiquitination of RIPK1. This further enables the recruitment of linear ubiquitin chain assembly complex (LUBAC), consisting of the proteins SHARPIN, HOIL-1L, and HOIP, which promote linear ubiquitin chains on RIPK1, TNFR1, NEMO and itself. These chains allow for the recruitment and retention of the signalling kinase complex consisting of the kinase IKKα, IKKβ and NEMO, and TAK1 and TAB2/3. The phosphorylation of the IKK complex leads to phosphorylation and subsequent proteasomal degradation of IκBα and release of the NF-κB subunits p50 and RelA, which enables nuclear translocation of the subunits. Here, NF-κB acts as a transcription factor leading to the transcription of pro-inflammatory cytokines (e.g. IL-6 and IL-8), adhesion molecules (e.g. ICAM1), pro-survival genes (e.g. c-IAP2 and cFLIP), and its own negative regulator (A20). A20 acts as a ubiquitin ligase, leading to proteasomal degradation of RIPK1, thereby halting the TNF-α pathway. Besides NF-κB activation, also the MAPK pathway can be activated via the TNFR1 signalling complex[50,51].

The TNF-α pathway can also act as a cell death pathway when the NF-κB pathway is inhibited. When the E3 ligases c-IAP1/2 and LUBAC are absent, RIPK1 dissociates from complex 1 and associates with FADD. This results in the recruitment of pro-caspase 8 to form the death platform complex II leading to apoptosis, via caspase 3/7. Alternatively, when caspase-8 is insufficiently activated, RIPK1 can autophosphorylate itself and thereby bind to RIPK3 resulting in necrosome formation via MLKL[52,53] (Figure 2).

Because the TNF-α pathway extensively depends on kinases, it is not surprising that kinase inhibitors can influence this pathway either directly or indirectly. Such interference may disrupt normal downstream signalling, resulting in either sustained or diminished inflammatory responses, which in turn can adversely affect various organs.

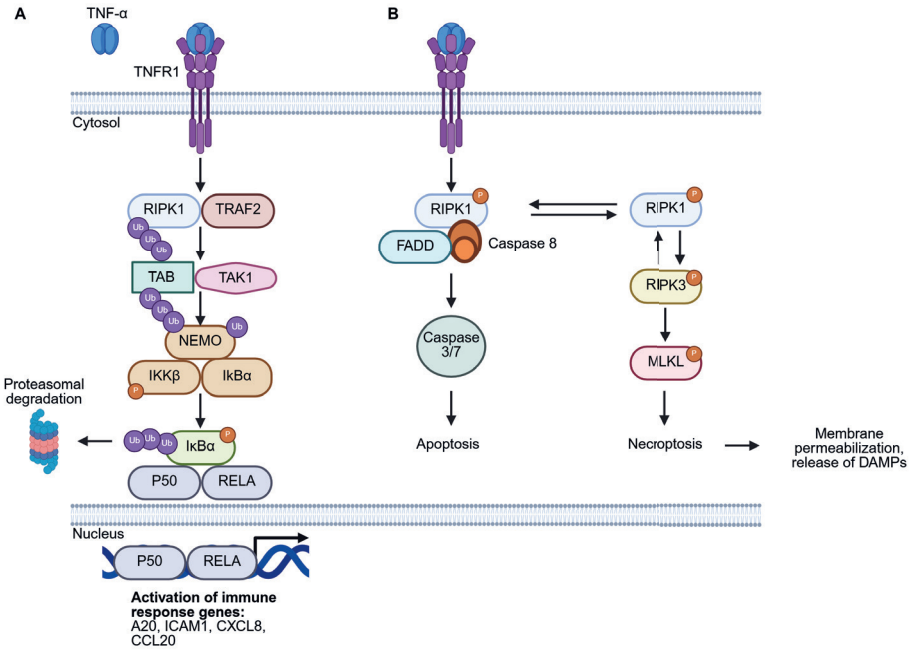


Figure 2. Schematic of the TNF-α signalling pathway. A) Under normal conditions, TNF-α stimulation triggers the recruitment of RIPK1 and TRAF2 and ultimately leads to (self) ubiquitination of RIPK1. This results in recruitment and retention of TAB and TAK1 and subsequent phosphorylation of the IKK complex. This causes proteasomal degradation of IκBα and the release and translocation of the NF-κB subunits p50 and RelA to the nucleus thereby promoting the activation of immune response genes. **B)** When the NF-κB pathway is inhibited, it can divert to a cell death pathway. Apoptosis can be induced in a RIPK1-dependent manner via FADD and caspase 8. Alternatively, when caspase 8 is inhibited or deficient, this can lead to necroptosis via RIPK1, RIPK3 and MLKL. Necroptosis results in membrane permeabilization and the release of DAMPs, which can also activate the NF-κB pathway.

In vitro models for toxicity assessment

Traditionally, preclinical testing was largely conducted using animal models[54]. However, due to several limitations associated with animal testing, including biological differences between animal and humans, preclinical evaluation has been shifted toward high-throughput screens in *in vitro* models. These screens can be integrated with so-called new approach methodologies (NAMs) integrating cell-based assays, computational modelling, and omics technologies to ultimately enhance molecular understanding of underlying mechanisms.

Cardiotoxicity test systems.

In vitro cardiotoxicity testing has traditionally relied on immortalized cell lines, such as H9C2 embryonic rat cardiomyocytes or non-cardiac lines, including HEK or CHO cells transfected with a human ether-à-go-go related gene (hERG) channel since blockage of this channel is a key event in cardiotoxicity[55,56]. Although these models can partly indicate cardiotoxic liabilities, they lack characteristics of cardiomyocytes and human translation. Recently, the use of human induced human pluripotent stem cells (hiPSCs) derived from somatic cells gained increasing popularity for toxicity assessment, including cardiotoxicity. Takahashi and Yamanaka *et al*. were the first to generate hiPSCs from fibroblasts using four pluripotency factors (Oct3/4, Sox2, Klf4, and c-Myc) and showed these cells have the capability to differentiate in cells derived from all three germ lines[57]. Current hiPSC-cardiotoxicity test models include 2D and 3D cultures. 2D models enable high-throughput screening but lack complexity and maturity. 3D models, with or without other cardiac cell types show increase cardiac maturity but are typically medium-throughput[58]. Even more enhanced and mature models for cardiotoxicity assessment include organ-on-a chip models and engineered heart tissues, but they are typically considered low-throughput[59]. A tiered toxicity testing strategy can be used to screen a large panel of compounds in 2D hiPSC-derived models, followed by in-depth testing in more mature 3D models.

Nephrotoxicity test methods.

The expression of drug transporters and metabolizing enzymes is relatively high in the PT and therefore, it is a common site for drug-induced nephrotoxicity[60]. Conventionally, primary PTs have been used because they most closely mimic the physiological state of cells *in vivo*. However, intra-donor variability and limited availability remain a challenge[61]. To overcome this, immortalized PT cell lines, e.g. RPTEC/TERT1, can be utilized for nephrotoxicity assessment. Although differentiated RPTEC/TERT1 cells express many PT markers, the expression of the OAT1 and OAT3

transporters is lacking [62]. PTs can nowadays also be generated from hiPSCs and display a polarized morphology and proper functionality in 2D[63,64]. It is envisioned that the use of these hiPSC-derived PTs will increase rapidly and will also be used more frequently for toxicity screening.

Hepatotoxicity test methods.

In vitro models to assess DILI are centred around hepatocytes, since hepatocytes are the key cell type of the liver and the main site for drug metabolism. Early toxicity screening often utilizes single-cell systems that measure the direct biological effects of a drug on the cell. The gold standard for hepatocyte toxicology assessment are freshly isolated and cryopreserved primary human hepatocytes (PHHs). The metabolic activity of drug metabolizing enzymes is high in these cells and is therefore physiologically relevant. Unfortunately, in 2D, their metabolic activity is quickly lost upon plating due to dedifferentiation, although this is maintained for a longer period when cultured as 3D spheroids[65]. In addition, these cells are difficult to use due to the limited cell viability, interindividual variability and underlying disease status. As an alternative, hepatic cancer cell lines, e.g. HepG2 or HepaRG, are often used, but they do not reach the metabolic maturity of PHH in both 2D and 3D dimensions. On the other hand, they are easy to culture, reproducible and suitable for high-throughput screening[66]. They can contribute to increased mechanistic understanding of hepatotoxicity using fluorescent reporter lines as described by Wink *et al*., where key proteins for various stress response pathways were targeted with green fluorescent protein (GFP) and subsequently imaged upon drug exposure[67]. Relatively novel is the use of human induced pluripotent stem cell (PSC)-derived hepatocyte-like cells (HLCs). hiPSCs are differentiated to HLCs by mimicking embryonic development through endoderm induction, liver specification and further maturation. hiPSC-derived HLCs do not fully reach PHH maturity yet but are more metabolically active compared to liver cell lines[68]. In addition, this hepatocyte model is suitable for high-throughput screening, thereby reducing costs and time to identify drugs with a DILI liability[69]. Besides, patient-derived hiPSC lines can be used to better understand a certain phenotype (e.g. HLA composition or polymorphisms in certain inflammatory-related genes). Studying the immune component in DILI remains difficult. Using PHH, this remains challenging due to the possible contamination with liver immune cells after isolation. Niemeijer *et al*. also showed a variable and minimal response of 50 PHH donors to TNF-α. Possibly, donors with an underlying liver pathology were already at high inflammatory stress levels, leading to a lower response upon TNF-α induction[70]. Despite this drawback, various studies still have showed synergistic cell death of PHH, and HepG2, after co-exposure of drugs (e.g. trovafloxacin) and cytokines (e.g. TNF-α)[71,72].

To subsequently validate a drug candidate, a more complete test system should be introduced. One of those test systems can be 3D microtissues consisting of primary human hepatocyte, stellate cells, and Kupffer cells to better mimic the *in vivo* situation.

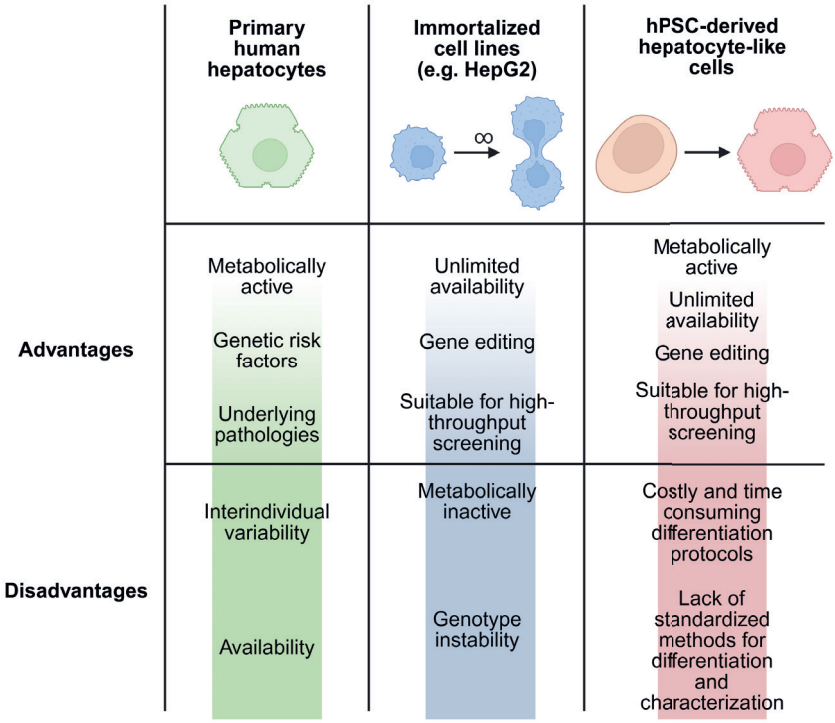


Figure 3. Overview of commonly used *in vitro* test systems to assess drug-induced hepatotoxicity with their (dis-)advantages.

Identification of inflammatory stress: application of fluorescent reporters and high content imaging.

Technological advances over the past two decades have enabled improved methodological approaches for studying a drug's toxicological potency. Fluorescent reporters that target key adaptive stress response pathways involved in drug-induced organ toxicity enhanced the mechanistic understanding of those liabilities. Previously, our research group generated GFP reporters in HepG2 liver carcinoma cells using bacterial artificial chromosome (BAC) engineering, which were used to gain insight in the molecular mechanisms behind DILI[67,73]. However, a major disadvantage was the random integration of the construct in the genome of the cells, which may potentially lead to aberrant reporter activity and changes in cellular cell. More recently, genetic engineering using CRISPR-Cas9 in hiPSC became the standard in the field[74]. This

enables scar-free integration of a fluorescent protein genes at the target of interest. A major advantage of endogenously tagged hiPSC reporters is that they enable high-throughput fluorescent imaging for toxicity assessment in any cell type of interest. The confocal imaging of fluorescent stress pathway activation can be easily combined with other readouts, including cell death imaging using annexin-V and propidium iodide. Thereby, stress pathway activation can be directly related to cytotoxicity. Although these readouts contribute to better mechanistic understanding of drug-induced organ toxicity, the drug candidates must be validated using other readouts, including various omics approaches as it does not directly relate to a clinical outcome. In addition, some compounds will be missed using this methodology as it relies on relatively short compound incubations (<72 hours) and some toxicities have a delayed onset[75,76].

Aim and Scope of this thesis

Previous studies from our laboratory have demonstrated that drug exposure can lead to altered TNF-α signalling in HepG2 cells, in combination with synergistically increased TNF-α-induced apoptosis[77,78]. In addition, we have shown that synergistic drug/TNF-α-induced cell death is dependent on other stress response pathways, including the endoplasmic reticulum/unfolded protein response and Nrf2-mediated oxidative stress signalling pathways[79,80]. This thesis aims to further investigate the role of NF-κB/TNF-α-mediated inflammatory signalling in drug-induced organ toxicity using novel *in vitro* test methods.

In **Chapter 2**, we used a synthetically generated squaramide-based supramolecular hydrogel to enhance HepG2 spheroid differentiation. We show that spheroids within this hydrogel express significantly higher levels of phase I and II metabolic enzymes, drug transporters and other liver markers compared to traditional culturing of HepG2 spheroids in a Matrigel basement membrane.

In **Chapter 3**, we assessed the response of five different *in vitro* hepatocyte models to inflammatory agents, including IL-1β and TNF-α in order to mimic inflammatory stress during drug-induced liver injury. We reveal that the downstream response to IL-1β was similar in all models. However, the response to diclofenac or trovafloxacin in combination with TNF-α was cell model dependent. We finally identified hiPSC-derived hepatocyte-like cells as a suitable model to examine alterations in drug-induced TNF-α signalling.

In **Chapter 4**, we systematically selected six NF-κB signalling biomarkers based on weighted gene co-regulation network analysis (WGCNA) approaches in hepatocytes. Subsequently, we established endogenous fluorescent reporters to assess inflammatory signalling activation in hiPSC-derived hepatocyte-like cells using

CRISPR/Cas9. Furthermore, we show that we can translate the use of these reporters to another cell lineage of interest, namely hiPSC-derived cardiomyocyte-like cells.

In **Chapter 5**, we used the hiPSC-ICAM1-eGFP reporter generated in Chapter 4 to assess the effect of kinase inhibitors on NF-κB target gene expression in hiPSC-derived hepatocyte-, cardiomyocyte- and proximal tubule-like cells. We identified a subset of kinase inhibitors that increased ICAM1-eGFP expression, concurrent with increased chemokine levels that have a function in neutrophil and T-cell recruitment. Using bioinformatic approaches, we propose a potential mechanism for the enhancement of TNF-α-induced target gene expression.

Ultimately, **Chapter 6** serves as a summary of all the findings in this thesis and provides an overview and future perspective on the limitations and implications of these studies.



CHAPTER 2

SQUARAMIDE-BASED SUPRAMOLECULAR MATERIALS DRIVE HEPG2 SPHEROID DIFFERENTIATION

Linda van den Berk[1,‡], Tingxian Liu[2,‡], Joeri A.J. Wondergem[3,4], Ciqing Tong[2], Markus C. Kwakernaak[2], Bas ter Braak[1], Doris Heinrich[3,4], Bob van de Water[1], and Roxanne E. Kieltyka[2]

[1]Division of Drug Discovery and Safety, Leiden Academic Centre for Drug Research (LACDR), Leiden University, Leiden, The Netherlands

[2]Department of Supramolecular and Biomaterials Chemistry, Leiden Institute of Chemistry, Leiden University, Leiden, The Netherlands

[3]Department of Physics, Huygens-Kamerlingh Onnes Laboratory, Leiden University, Leiden, The Netherlands

[4]Fraunhofer Institute for Silicate Research ISC, Würzburg, Germany

[‡]Authors contributed equally

This chapter has been published as:

Liu, T.‡, van den Berk, L.‡, Wondergem, J. A. J., Tong, C., Kwakernaak, M. C., Braak, B. ter, Heinrich, D., van de Water, B., & Kieltyka, R. E. (2021). Squaramide-Based Supramolecular Materials Drive HepG2 Spheroid Differentiation. Advanced Healthcare Materials, 10(11).

Abstract

A major challenge in the use of HepG2 cell culture models for drug toxicity screening is their lack of maturity in 2D culture. 3D culture in Matrigel promotes the formation of spheroids that express liver-relevant markers, yet they still lack various primary hepatocyte functions. Therefore, alternative matrices where chemical composition and materials properties are controlled to steer maturation of HepG2 spheroids remain desired. Herein, a modular approach is taken based on a fully synthetic and minimalistic supramolecular matrix based on squaramide synthons outfitted with a cell-adhesive peptide, RGD for 3D HepG2 spheroid culture. Co-assemblies of RGD-functionalized squaramide-based and native monomers resulted in soft and self-recovering supramolecular hydrogels with a tuneable RGD concentration. HepG2 spheroids are self-assembled and grown (≈150 μm) within the supramolecular hydrogels with high cell viability and differentiation over 21 days of culture. Importantly, significantly higher mRNA and protein expression levels of phase I and II metabolic enzymes, drug transporters, and liver markers are found for the squaramide hydrogels in comparison to Matrigel. Overall, the fully synthetic squaramide hydrogels are proven to be synthetically accessible and effective for HepG2 differentiation showcasing the potential of this supramolecular matrix to rival and replace naturally-derived materials classically used in high-throughput toxicity screening.

Introduction

The liver is a critical organ of the human body that performs the biotransformation of drugs and other xenobiotics. Chemical transformations, such as oxidation, reduction, hydrolysis or other organic reactions, of these foreign agents give rise to active or inactive metabolites that can even be hepatotoxic[81]. Toxic insults to the liver from drug metabolites can eventually result in acute or chronic failure, otherwise known as drug-induced liver injury (DILI). DILI can occur from nearly every class of medication, and when encountered often results in abandonment of the therapy[82]. Thus, a major challenge in the drug discovery pipeline is to more accurately predict DILI early on, as hepatotoxic responses observed in animal models do not fully recapitulate those observed in humans resulting in drug candidates that fail in late-stage clinical trials or even after approval in the clinic[83]. Primary human hepatocytes (PHH) are the current gold standard for in vitro modelling of liver metabolism and toxicity as they represent 70% of total liver cell population. However, these cells are challenged by their limited availability and high donor variability, rapid loss of metabolic activity once harvested for ex vivo culture and costly derivation[84,85]. As an alternative cell source to model liver hepatic processes in vitro, human liver carcinoma cells (HepG2) are used due their wide availability, immortality, facile handling, and stable phenotype in culture. However, these cells often show low expression levels of metabolic enzymes, namely cytochrome P450s that are relevant for xenobiotic metabolism, which has been correlated with the 2D culture methods used to expand them[86]. 3D culture methods have been used to improve the metabolic characteristics of HepG2 cells mainly using Matrigel, a biological matrix derived from murine tumour tissues, consisting of laminin, collagen IV, and entactin[87]. When encapsulated in Matrigel, HepG2 cells self-organize into spheroidal structures and differentiate resulting in increased levels of various metabolic markers and can be dosed repeatedly with increased sensitivity to various hepatotoxic agents in comparison toHepG2 cells cultured in 2D[88,89]. However, Matrigel is costly, lacks definition with lot-to-lot variability,[87] its murine origin is problematic for some applications and chemical modification or decoupling of cues is difficult, leading to the exploration of synthetic polymers for use in 3D hepatocyte culture. Matrices held together by covalent and non-covalent interactions have demonstrated the capacity to form spheroids from liver-derived cells in 3D, including a handful of recent reports examining the effect of cell interactive moieties to facilitate their differentiation and culture with varying degrees of success[90–99]. More recent studies have examined the capacity of the short integrin-binding peptide RGD to guide this process highlighting the importance of peptides derived from extracellular matrix proteins in synthetic materials. While a fully synthetic and covalent PEG hydrogel functionalized with RGD supported the growth of liver organoids, the addition of laminin–entactin complex was necessary for a non-covalent hydrogel based on a polyisocyanopeptide polymer to

stimulate cell proliferative pathways demonstrating the importance of peptide concentration[97,98]. We thus became interested in examining a modular supramolecular polymer matrix based on stacked monomers for HepG2 cell culture to improve their growth and differentiation in 3D. However, such supramolecular systems that have the short peptides derived from matrix proteins is yet to be explored for the preparation of HepG2 spheroids but can more broadly provide a powerful synthetic polymer platform for 3D cell culture where the peptide concentration can be tuned easily and facile cell seeding and release can be achieved. In order to construct supramolecular polymer materials, monomers that contain highly directional, specific, and reversible non-covalent interactions are needed[100–104]. In particular, squaramide synthons because of their ditopic presentation of hydrogen bond donors and acceptors on a minimal scaffold in combination with their synthetic accessibility are of interest for this aim[105–112]. We recently demonstrated their application in a tripodal hydrogelator for the culture of human induced pluripotent stem cells (hiPSCs), using the soft and self-recovering nature of the supramolecular matrix that supports cell self-assembly into spheroids driven by cell–cell contacts[111]. However, cell proliferation within these materials was found to be limited, pointing out the need to further modify this synthetic matrix with bioactive peptides to enable cell–matrix interaction. One short peptide that has been implemented in materials to provide such interactions is the RGD peptide, a short sequence derived from the FN-III repeat in the tenth domain of fibronectin, which binds the $\alpha 5\beta 1$ and $\alpha V\beta 3$ integrins on the cell surface. We therefore sought to introduce this cell-adhesive peptide within squaramide-based supramolecular materials through co-assembly of functional monomers as a facile means to tune peptide concentration for applications in 3D HepG2 culture and differentiation.

Materials & Methods

Materials

All chemicals used in the synthesis of monomers 1 and 2 were purchased from Sigma Aldrich and used without further purification. Fmoc-protected amino acids for peptide synthesis were obtained from Novabiochem. Dulbecco's modified eagle cell culture medium (DMEM), DMEM/F12, fetal calf serum, penicillin, streptomycin, GlutaMAX, pyruvate and trypsin were received from Thermo Fisher Scientific. Angiogenesis slides (15-well) were obtained from Ibidi. Dulbecco's Phosphate Buffered Saline (DPBS), calcein AM (AM = acetoxymethyl), and propidium iodide (PI) were acquired from Sigma-Aldrich. The Click-iT EdU Imaging kit was purchased from Invitrogen. Total RNA Isolation (TRI) Reagent was from Sigma-Aldrich. RevertAid H Minus First Strand cDNA Synthesis Kit and PowerUp™ SYBR™ Green Master Mix were obtained from Thermo Fisher Scientific.

Methods

All synthetic intermediates were characterized by ^{1}H-NMR and ^{13}C-NMR collected on a Bruker DMX-400 operating at 400 MHz and 100 MHz at 298 K, respectively. LC-MS analysis was performed on a TSQ Quantum Access MAX system equipped with a Gemini 3 µm C18 110 Å 50×4.60 mm column (UV detection at 214 nm and 254 nm, mass detection range: 160 to 3000 (Da)). The mobile phase consisted of a gradient of 10-90% of H_2O-CH_3CN with 0.1% trifluoroacetic acid (TFA) over 13.5 minutes. HPLC purification of the monomers was executed on setup equipped with C18 column. A gradient from 10%-90% CH_3CN (0.1% TFA) in H_2O (0.1% TFA) over 15 min at a flow rate of 12 mL/min was used. Matrix-assisted laser desorption ionization-time-of-flight mass spectra (MALDI-TOF-MS) were collected on a Bruker Microflex LRF mass spectrometer on a ground steel target plate. A linear positive-ion mode with an α-cyano-4-hydroxycinnamic acid matrix (5 mg/ml in CH_3CN/ H_2O 1:1 v/v) was used. High resolution mass spectra (HR-MS) were collected on a Thermo Fisher LTQ Orbitrap mass spectrometer equipped with an electrospray ion source in positive mode (resolution R = 60000). The spectra were collected by direct injection of samples (2 µM in H_2O-CH_3CN 50/50 v/v) and recorded with a mass range of 150-2000 and dioctylpthalate (m/z = 391.28428) as a "lock mass". Oscillatory rheology experiments were executed on a Discovery HR-2 hybrid rheometer using a cone-plate geometry (40 mm, 1.995°) at 37 ± 0.2 °C with a peltier-based temperature controller and solvent trap. Cryo-TEM images were acquired on a Tecnai F12 (FEI Company, The Netherlands) equipped with a field emission gun operating at 120 keV using a Gatan UltraScan charge-couple device (CCD) camera (Gatan company, Germany) with a defocus between −6 and −9 µm. UV absorption spectra were recorded on a Cary 300 Bio UV-Vvis spectrometer, scanning from 200 nm to 400 nm with 1 nm intervals with a scan rate of 120 nm/min. Bright field images were taken on an EVOS FL AUTO2 equipped with temperature and a CO_2 gas controller. Confocal fluorescent images were acquired on Leica TCS SP8 confocal laser scanning microscope equipped with a 10× air objective and a 40× oil immersion objective. Images were processed using the Fiji Image J software. Real-time polymerase chain reaction (RT-PCR) measurements were performed on a QuantStudio™ 6 and 7 Flex Real-Time PCR (Applied Biosystems®).

Synthetic procedures

Compound 5. An aqueous NaOH (1.53 g, 38.25 mmol) solution (10 mL) was added to a solution of tetraethylene glycol (45.00 g, 231.68 mmol) dissolved in tetrahydrofuran (THF) (10 mL) at 0°C. *p*-Toluenesulfonyl chloride (4.31 g, 22.61 mmol) dissolved in THF (30 mL) was added dropwise to the reaction mixture over 1h. After stirring at 0 °C for 2h, the reaction mixture was poured onto ice water (150 mL) and extracted 3x with DCM (200 mL). The combined organic layers were then washed with water (2 x 100 mL), dried

with $MgSO_4$, and concentrated on a rotary evaporator. The crude was purified by column chromatography (petroleum ether (PE) /ethyl acetate (EtOAc) 60/40-0/100 v/v). The product was concentrated by rotary evaporation and dried in vacuum oven overnight to obtain a light-yellow oil. Yield: 58%, 4.55 g. ^{1}H-NMR (CDCl3, 400 MHz): 7.81-7.77 (d, 2H), 7.36-7.34 (d, 2H), 4.18-4.14 (m, 2H), 3.71-3.59 (m, 14H), 2.86 (s, 1H), 2.45 (s, 3H). ^{13}C-NMR (CDCl3, 100 MHz): 144.88, 132.94, 129.87, 127.96, 72.51, 70.69, 70.63, 70.44, 70.30, 69.33, 68.66, 61.65, 21.65.

Compound 6. The obtained compound **5** (5.85 g, 16.80 mmol) was dissolved in ethanol (120 mL) and NaN_3 (2.79 g, 42.92 mmol) was added while stirring. The reaction mixture was then refluxed at 70 °C for 18h and water (100 mL) was added prior to concentrating the reaction mixture on a rotary evaporator. The concentrated solution was extracted with EtOAc (3 × 100 mL). The combined organic phases were dried over Na_2SO_4 and evaporated in vacuum to obtain compound **6** as a yellow oil. Yield: 77%, 2.83 g. ^{1}H-NMR ($CDCl_3$, 400 MHz): 3.71-3.58 (m, 14H), 3.40-3.36 (m, 2H), 3.13 (br s, 1H). ^{13}C-NMR ($CDCl_3$, 100 MHz): 72.47, 70.57, 70.54, 70.47, 70.21, 69.95, 61.51, 50.57.

Compound 7.[113] Triphenylmethyl chloride (2.73 g, 9.82 mmol) was dissolved in dichloromethane (DCM) (100 mL), added dropwise over 2h into a cooled (0°C), stirred solution of 1,10-diaminodecane (6.66 g, 38.65 mmol) in DCM (150 mL) and left to stir overnight at room temperature. Subsequently, the reaction mixture was concentrated by rotary evaporation and EtOAc (200 mL) was added before extracting with water (3 x 100 mL). The organic layer was collected, dried with anhydrous Na_2SO_4 and concentrated on a rotary evaporator. The crude was then purified by column chromatography (PE/EtOAC/methanol (MeOH) 50/50/0-50/50/20 v/v/v) and concentrated by rotary evaporation and dried in vacuum oven overnight to obtain a yellow oil. Yield: 79%, 3.20 g. ^{1}H-NMR ($CDCl_3$, 400 MHz): 7.51-7.48 (d, 6H), 7.26-7.22 (t, 6H), 7.19-7.12 (t, 3H), 2.70-2.64 (t, 2H), 2.16-2.10 (t, 2H), 1.51-1.44 (m, 4H), 1.33-1.02 (m, 12H). ^{13}C-NMR ($CDCl_3$, 100 MHz): 146.37, 128.65, 127.71, 126.12, 70.86, 43.56, 41.94, 33.19, 30.90, 29.64, 29.60, 29.58, 29.48, 27.37, 26.89. HR-MS: $[M+H]^+$: calc: 415.3108, found: 415.3103.

Compound 8A. Tetraethyleneglycol monomethyl ether (0.90 g, 4.32 mmol) was activated with 1,1'-carbonyldiimidazole (CDI) (0.78 g, 4.81 mmol) for 1h at room temperature. Subsequently, compound **7** (2.19 g, 5.28 mmol), N,N-Diisopropylethylamine (DIPEA) (2.30 mL, 13.20 mmol) and chloroform (CHCl3) (15 mL) were added to the reaction mixture and refluxed overnight. Then, DCM (30 mL) was added, and the solution was extracted with water (30 mL). The aqueous layer was extracted twice with DCM (30 mL). The organic fractions were combined and dried with Na_2SO_4, filtered and the solvent was removed on a rotary evaporator before purification by column chromatography (PE/EtOAc 100/0-0/100 v/v). The product was

concentrated by rotary evaporation and dried in vacuum to obtain an oil. Yield: 63%, 1.77 g. ^{1}H-NMR ($CDCl_3$, 400 MHz): 7.44-7.41 (d, 6H), 7.21-7.15 (t, 6H), 7.11-7.05 (t, 3H), 5.12 (br s, 1H), 4.15-4.12 (m, 2H), 3.61-3.55 (m, 12H), 3.48-3.45 (m, 2H), 3.29 (s, 3H), 3.10-3.03 (m, 2H), 2.08-2.04 (t, 2H), 1.41-1.37 (m, 4H), 1.25-1.14 (12H, m). ^{13}C-NMR ($CDCl_3$, 100 MHz): 156.23, 146.12, 128.3, 127.46, 125.87, 71.68, 70.60, 70.34, 70.31, 70.24, 69.40, 68.64, 66.78, 63.46, 60.03, 54.41, 43.30, 40.75, 30.61, 29.72, 29.35, 29.28, 29.05, 27.10, 26.51. MALDI-TOF-MS: m/z calc: 648.41; found: 671.74 $[M+Na]^+$.

Compound 8B. Compound **6** (0.78 g, 3.55 mmol) was activated with CDI (0.64 g, 3.95 mmol) for 1h at room temperature. Subsequently, compound **7** (1.61 g, 3.88 mmol), DIPEA (2.00 mL, 5.74 mmol) and $CHCl_3$ (15 mL) were added to the reaction mixture and refluxed overnight. Then, DCM (30 mL) was added, and the solution was extracted with water (30 mL). The aqueous layer was extracted twice with DCM (30 mL). The organic fractions were combined and dried with Na_2SO_4, filtered and the solvent was removed in rotary evaporator before purification by column chromatography (PE/EtOAc 100/0-0/100 v/v). The product was concentrated by rotary evaporation and dried in vacuum to obtain an oil. Yield: 74 %, 1.74 g. ^{1}H-NMR ($CDCl_3$, 400 MHz): 7.52-7.48 (d, 6H), 7.31-7.25 (t, 6H), 7.21-7.17 (t, 3H), 4.87-4.83 (br s, 1H), 4.32-4.20 (t, 2H), 3.72-3.68 (m, 12H), 3.41-3.38 (m, 2H), 3.20-3.13 (m, 2H), 2.15-2.11 (t, 2H), 1.51-1.44 (m, 4H), 1.35-1.26 (m, 12H). ^{13}C-NMR ($CDCl_3$, 100 MHz): 146.46, 128.76, 127.82, 126.23, 70.97, 70.81, 70.78, 70.76, 70.63, 70.16, 69.80, 69.06, 66.93, 63.91, 50.78, 43.67, 41.15, 30.97, 30.05, 29.71, 29.62, 29.38, 27.45, 26.85. MALDI-TOF-MS: m/z calc: 659.40; found: 659.12 $[M+H]^+$.

Compound 9A. Compound **8A** (1.68 g, 2.58 mmol) was dissolved in TFA (1 mL) stirred at room temperature for ~ 20 min. When the reaction was complete (as determined by TLC), the TFA was removed by a gentle stream of air and the solid was redissolved in CHCl3 (15 mL). Subsequently, 3,4-dibutoxy-3-cyclobutene-1,2-dione (0.68 mL, 3.13 mmol) and DIPEA (6.00 mL, 34.44 mmol) were added to the reaction mixture and refluxed overnight. Then, DCM (30 mL) was added, and the solution was extracted with water (30 mL). The aqueous layer was extracted with DCM (2 x 30 mL). The organic fractions were combined and dried with Na_2SO_4, filtered and the solvent was removed in rotary evaporator prior to purification by column chromatography (PE/EtOAc 100/0-0/100 v/v). The product was then concentrated by rotary evaporation and dried in vacuum to obtain an oil. Yield: 87%, 1.26 g. ^{1}H-NMR ($CDCl_3$, 400 MHz): 7.14 (s, 1H), 4.96 (s, 1H), 4.71-4.62 (m, 2H), 4.16-4.13 (t, 2H), 3.63-3.56 (m, 12H), 3.52-3.48 (m, 2H), 3.40-3.32 (m, 5H), 3.12-3.05 (m, 2H), 1.78-1.68 (m, 2H), 1.58-1.51 (m, 2H), 1.44-1.41 (m, 4H), 1.26-1.18 (m, 12H), 0.94-0.89 (t, 3H). ^{13}C-NMR ($CDCl_3$, 100 MHz): 189.75, 182.75, 177.46, 172.51, 156.54, 73.41, 71.96, 70.62, 70.57, 70.55, 70.53, 69.69, 63.85, 60.46, 44.93, 41.06, 32.08, 30.69, 29.96, 29.73, 29.42, 29.23, 29.13, 26.73, 26.40, 18.71, 13.73. MALDI-TOF-MS: m/z calc: 558.35; found: 580.86 $[M+Na]^+$.

Compound 9B. Compound **8B** (1.74 g, 2.64 mmol) was dissolved in TFA (1 mL) stirred at room temperature for ~ 20 min. When the reaction was complete (as determined by TLC), the TFA was removed by a gentle stream of air, and the product was redissolved in $CHCl_3$ (15 mL). Subsequently, 3,4-dibutoxy-3-cyclobutene-1,2-dione (0.68 mL, 3.13 mmol) and DIPEA (5.00 mL, 28.70 mmol) were added to the reaction mixture and refluxed overnight. Then, DCM (30 mL) was added, and the solution was extracted with water (30 mL). The aqueous layer was extracted twice with DCM (30 mL). The organic fractions were combined and dried with Na_2SO_4, filtered and the solvent was removed in a rotary evaporator prior to purification by column chromatography (PE/EtOAc 100/0-0/100 v/v). The product was concentrated by rotary evaporation and dried in vacuum to obtain an oil. Yield: 47%, 0.71 g. ^{1}H-NMR ($CDCl_3$, 400 MHz): 7.00-6.95 (m, 1H), 4.87-4.84 (m, 1H), 4.72-4.64 (m, 2H), 4.20-4.16 (t, 2H), 3.70-3.62 (m, 12H), 3.41-3.34 (m, 4H), 3.14-3.09 (m, 2H), 1.79-1.71 (m, 2H), 1.61-1.56 (m, 2H), 1.46-1.37 (m, 4H), 1.31-1.24 (m, 12H), 0.95-0.92 (t, 3H). ^{13}C-NMR ($CDCl_3$, 100 MHz): 189.79, 182.83, 177.62, 172.99, 172.51, 156.54, 73.49, 70.79, 70.75, 70.72, 70.61, 70.15, 69.76, 68.97, 67.15, 63.93, 50.78, 44.99, 41.11, 32.11, 31.13, 30.73, 29.99, 29.45, 29.26, 29.16, 26.76, 26.43, 18.75, 13.78. MALDI-TOF-MS: m/z calc: 569.34; found: 591.40 $[M+Na]^+$.

Compound 10. Tris(2-aminoethyl)amine (2.99 g, 20.47 mmol) was dissolved in dry DCM (100 mL) and triphenylchloromethane (1.02 g, 3.66 mmol) in dry DCM (100 mL) was added dropwise at room temperature. The mixture was stirred overnight and then washed with 10 wt% NaOH solution (100 mL) and brine (100 mL). The organic phase was dried over Na2SO4 and concentrated in rotary evaporator. The crude was purified by column chromatography (DCM/MeOH/NH_4OH 100/0/0-85/15/0.1 v/v/v). The product was concentrated by rotary evaporation and dried in vacuum to give compound **10** as a yellowish oil. Yield: 62%, 0.88 g. ^{1}H-NMR ($CDCl_3$, 400 MHz): 7.51-7.48 (d, 6H), 7.31-7.26 (t, 6H), 7.21-7.16 (t, 3H), 2.69-2.65 (t, 4H), 2.62-2.58 (t, 2H), 2.36-2.32 (t, 4H), 2.26-2.22 (t, 2H). ^{13}C-NMR ($CDCl_3$, 100 MHz): 146.26, 128.68, 127.91, 126.36, 70.77, 57.51, 55.06. 41.04, 39.83. HR-MS: [M+H]+: calc: 389.2700, found: 389.2696.

Compound 11. Compound **9A** (0.52 g, 0.93 mmol) was dissolved in $CHCl_3$ (10 mL) in a round bottom flask. Compound **10** (0.16 g, 0.41 mmol) and DIPEA (0.50 mL, 2.87 mmol) were added before refluxing the reaction mixture overnight. The crude was concentrated and purified by column chromatography (EtOAc/MeOH 100/0-100/20 v/v). The product was concentrated by rotary evaporation and dried in a vacuum oven to obtain an oil. Yield: 54%, 0.30 g. ^{1}H-NMR ($CDCl_3$, 400 MHz): 8.23 (br s, 2H), 8.05 (br s, 2H), 7.41-7.38 (d, 6H), 7.22-7.17 (t, 6H), 7.13-7.08 (t, 3H), 5.08 (br s, 2H), 4.20-4.17 (t, 4H), 3.66-3.51 (m, 32H), 3.35 (s, 6H), 3.17-3.07 (m, 4H), 2.60-2.55 (m, 8H), 1.61-1.54 (m, 4H), 1.46-1.39 (8H, m), 1.27-1.22 (m, 24H). ^{13}C-NMR ($CDCl_3$, 100 MHz): 182.73, 181.77, 168.95, 167.16, 156.66, 128.75, 127.91, 126.36, 71.96, 70.57, 70.54, 70.50,

69.88, 63.86, 55.87, 54.42, 44.80, 42.67, 41.21, 31.15, 30.07, 29.83, 29.64, 29.61, 29.41, 29.39, 26.91, 26.68. MALDI-TOF-MS: m/z calc: 1356.82; found: 1379.95 $[M+Na]^+$.

Compound 3. Compound **11** (0.15 g, 0.11 mmol) was dissolved in TFA (1 mL) and stirred at room temperature for ~ 20 min. When the reaction was complete (as determined by TLC), the TFA removed by a gentle stream of air and the solid was redissolved in $CHCl_3$ (15 mL). Subsequently, compound **9B** (0.08 g, 0.14 mmol) and DIPEA (3.00 mL, 17.22 mmol) were added to the reaction mixture and refluxed overnight. The crude was concentrated and purified by column chromatography (EtOAc/DCM/MeOH 100/0/0-0/100/0-0/100/10 v/v/v). The product was concentrated by rotary evaporation and dried in vacuum oven to obtain a sticky solid. Yield: 56%, 0.10 g. ^{1}H-NMR ($CDCl_3$, 400 MHz): 7.90-7.80 (m, 6H), 5.12-5.00 (m, 3H), 4.20-4.18 (t, 6H), 3.71-3.53 (m, 52H), 3.39-3.36 (m, 6H), 3.14-3.09 (q, 6H), 2.78 (br s, 6H), 1.61-1.24 (m, 50H). ^{13}C-NMR ($CDCl_3$, 100 MHz): 182.92, 169.48, 167.09, 156.69, 72.03, 70.86, 70.82, 70.80, 70.66, 70.62, 70.59, 70.22, 69.90, 69.86, 63.94, 59.21, 50.78, 44.99, 41.24, 31.27, 30.14, 29.72, 29.50, 26.98, 26.74. LC-MS: t = 6.84 min, m/z: 1610.52. MALDI-TOF-MS: m/z calc: 1609.98; found: 1631.48 $[M+Na]^+$.

Peptide synthesis. RGD Peptides (GGGRGDS, **PEP1**) were synthesized on an automatic CEM peptide synthesizer on a 100 µmol scale. Fmoc-Rink amide AM resin with a loading capacity of 0.74 mmol/g was used. Amino acid coupling was performed with 4 eq. of the amino acid, 4 eq. of the activator HCTU and 8 eq. of DIPEA. Fmoc-deprotection was executed using pyridine: dimethylformamide (DMF) (2:8 v/v). The peptides were cleaved in a TFA solution with 2.5% H_2O and 2.5% Triisopropylsilane (TIPS) for 2h, precipitated in cold diethyl ether, dried and dissolved in water prior to injection into LCMS. **PEP1**: LC-MS: t =0.69 min, m/z calc: 604.26, found: 604.47$[M+H]^+$.

Coupling of the alkyne functionality. Coupling of the alkyne was manually performed on the solid phase. Briefly, the obtained resins (100 µmol) from the peptide synthesizer were suspended in DMF (2 mL) for 15 min. 4-Pentynoic acid (53.3 mg, 0.54 mmol) was coupled to the N-terminus of the peptide by incubation with HCTU (206.8 mg, 0.50 mmol) and DIPEA (175 µL, 1.00 mmol) in DMF (4 mL) at room temperature for 1h. Afterwards, the alkyne-functionalized peptides were cleaved from the resin using a TFA solution with 2.5% H_2O and 2.5% TIPS for 2h and precipitated in cold diethyl ether, dissolved in water, and lyophilized to obtain a pale-yellow solid. The alkyne-functionalized RGD peptides were presented as **PEP2**. The products were confirmed by LC-MS. **PEP2**: LC-MS: t =0.69 min, m/z calc:684.28; found: 684.40 $[M+H]^+$.

Compound 2. Sodium L-ascorbate (38.0 mg, 191.9 µmol) and copper (II) sulfate pentahydrate (6.4 mg, 25.6 µmol) were first dissolved separately in water (100 µL) and then, mixed using a vortex for 30s resulting in a bright yellow solution. Afterwards, tris(3-hydroxypropyltriazolylmethyl) amine (THPTA, 5.5 mg, 12.6 µmol) dissolved in

ethanol (200 µL) and compound **2** (51.6 mg, 32.0 µmol) dissolved in DMF (1.2 mL) were added to the mixture. Lastly, **PEP2** (43.8 mg, 64.0 µmol) dissolved in DMF:H2O (400 µL, v/v 1:1) was added and the reaction mixture was stirred at room temperature for 2h. The crude was first dialyzed against water (mw 500-1000 Da) for 48 h and purified by HPLC. The product was concentrated by evaporation and lyophilized overnight to obtain a white solid. Yield: 35%, 34.9 mg. LC-MS: t = 5.86 min, m/z calc: 2295.27; found: 1148.27 [M+1] /2.

Two-component squaramide-based supramolecular hydrogel preparation method

Compound **1** was synthesized and prepared as a hydrogel as previously reported[114]. However, to prepare the two-component hydrogels with peptide-labelled monomers, a three-step protocol was used. First, stock solutions of compound **1** (25 mM in DMSO) and compound **2** (5 mM in DMSO) were made separately and then pipetted with the appropriate ratios into a new vial and vortexed to obtain a transparent mixture. The mixed solutions in DMSO were left overnight under a gentle flow of nitrogen to yield a dry film. The films were suspended in PBS (pH 7.4) at a final monomer concentration at 3.44 mM in a sterilized flow cabinet, followed by 30 s vortex and sonication in ice-water bath until transparent solutions were obtained (~30 min). Lastly, the transparent solutions were incubated at 37°C for 30 min and left on the bench overnight at room temperature prior to further testing.

Oscillatory rheology

The mechanical properties of the squaramide-based hydrogels were measured on a Discovery HR-2 hybrid rheometer using cone-plate geometry (40 mm, 1.995°) at 37 ± 0.2 °C with a Peltier-based temperature controller and a solvent trap. Hydrogels with various molar percentages of monomer **2** (SQ-2RGD, SQ-5RGD, SQ-10RGD, SQ-15RGD) were prepared according to the protocol above to result in a total final monomer concentration of 3.1 mM. The hydrogels (600 µL) were left to stand overnight and then pipetted onto the lower plate and the geometry was lowered to a gap distance of 54 µm. Time sweep measurements were executed at a frequency of 1.0 Hz and strain of 0.05% and frequency sweeps were conducted from 0.01–2 Hz with 0.05% strain. Subsequently, a step-strain measurement was performed after a plateau in the storage modulus was reached in the time sweep. Then, 100% strain was applied to the squaramide-based hydrogels for 120 s. The hydrogels were left to recover for 20 min while measuring at 0.05% strain (f = 1.0 Hz), during which the storage modulus returned to the original plateau. The measurement was repeated for two cycles. Lastly, an amplitude sweep was performed within the strain range from 0.01% to 100% to determine the linear viscoelastic regime (f = 1.0 Hz).

Cryo-TEM

Cryo-TEM images of the vitrified samples were acquired with a Tecnai F12 (FEI Company, The Netherlands) equipped with a field emission gun operating at 120 keV using a Gatan UltraScan charge-couple device (CCD) camera (Gatan company, Germany) with a defocus between −6 and −9 µm. Cryo-TEM samples were prepared by applying 3 µL of a SQ-10RGD, hydrogel (3.1 mM) and a SQ-40RGD solution (3.1 mM) to a freshly glow-discharged 300 mesh copper grid with a lacey-carbon support film (Supplier-Electron Microscopy Sciences, Pennsylvania, USA). Excess liquid was blotted away for 2 s (95% humidity, 21 °C, Whatman No. 4 filter paper) and plunge-frozen in liquid ethane at −196 °C using a Leica EM GP (Leica Microsystems, Wetzlar, Germany). The samples were stored in liquid nitrogen before imaging.

UV–Vis Spectroscopy

UV-Vis spectra were recorded on a Cary 300 UV-Vis spectrophotometer using a quartz cuvette with a path length of 1 cm. The dry film of monomers mixture was prepared according to gelation protocol above. Then, the films were suspended in PBS (pH 7.4) at a final monomer concentration of 1.0 mM, followed by vortexing for 30 s and sonication (~20 min) in ice-water bath to obtain transparent solutions. The solutions were left to stand overnight and diluted into 30 µM with PBS (pH 7.4) prior to measurement.

NIH 3T3-LifeAct-mCherry cell migration and spreading in 3D

NIH 3T3 fibroblasts with mCherry-LifeAct were cultured in high glucose DMEM supplemented with 10% newborn calf serum (NCS), 1% Glutamax, and 0.2% penicillin-streptomycin in a 37 °C incubator with 5% CO_2. The cells were kindly provided by T. Schmidt (LION, Leiden University) and previously transduced with LifeAct-mCherry through lentiviral infection[115]. In culture, cells were selected for expression of LifeAct-mCherry with 2 µg/ml puromycin. The culture was maintained with a confluency below 70%. Prior to seeding into hydrogel, NIH3T3-LifeAct-mCherry cells cultured in T-75 flask were dissociated and re-suspended in DMEM medium with a final cell concentration at 2.5×10^7 cells/mL. The cell suspension (50 µL) and the prepared hydrogel (450 µL) were mixed by gentle pipetting and transferred to the µ-Slide 8 well (200 µL/well). After gelation at 37 °C for 15 min, the hydrogels were mounted with fresh medium for cell culture. Five positions per well were chosen and time-lapse confocal imaging was performed over 20 hours. Images were captured every 5 minutes under a 40x air objective (Nikon) on a Nikon Eclipse Ti microscope equipped with a confocal spinning disk unit operated at 10,000 rpm (Yokogawa). Images were captured using an exposure time of 300 ms by an Andor iXon Ultra 897 High Speed EM-CCD camera (Andor Technology). During imaging, cells were kept at 37 °C and 5% CO_2 in a humidity-

controlled incubator (Tokai hit). To quantify cell-gel interaction by cell spreading efficiency, cells were cultured under various conditions (SQ, SQ-5RGD, SQ-10RGD, SQ-15RGD) for 24-hours and then imaged. Cell-laden hydrogels were prepared as described above, but with a final cell density at 1×10^6 cell/mL to ensure single cell resolution during edge-detection. After preparation, the cell-gel mixture was pipetted into custom-made mini-well inserts, 20 mm x 30 mm (~20 µL/well), placed in larger 4-well µ-Slides (Ibidi). The well inserts were fabricated as previously described[116]. After gelation, at 37 °C for 15 min, each mini-well was submersed in 1 mL high glucose DMEM medium. After 24-hours, a volume-slice (1.2 mm x 1.2 mm x 0.15 mm, 2.5 µm z-stacks) of each gel was imaged under the same objective, starting at a height of least 50 µm into the gel (above the bottom of the slide). The mCherry fluorescent protein was excited using a 0.2W 561 nm solid-state diode laser (Coherent) supported in an Agilent MLC4 unit (Agilent Technologies), at reduced intensity and controlled by an Acousto-Optic Tunable Filter. Images were captured using an exposure time of 500 ms by an Andor iXon Ultra 897 High Speed EM-CCD camera (Andor Technology). An in-house Matlab (Mathworks) code was used to quantify cell spreading, which allows automated adaption of edge-detection settings for every individual cell recognized. Before edge detection, all images were flattened using FIJI plugin BaSiC[117] and then imported into Matlab. The cell-edge is defined as the perimeter of pixels at the boundary of the cell area in the binary mask. Using the binary mask, the cell area, perimeter, summated skeleton branch length and Feret-diameters were calculated using the scale (0.3449 µm/pix). The skeleton of each cell was found by reducing the area to a line using their corresponding binary image (*bwskel* algorithm, MATLAB 2019a). Circularity and Aspect Ratio were calculated based on following equations.

$$Circularity = \frac{4 * pi * Area}{Perimeter\text{^}2}$$

$$Aspect\ Ratio = \frac{Min\ Feret\ Diameter}{Max\ Feret\ Diameter}$$

HepG2 cell encapsulation and culture in 3D

HepG2 cells cultured in a T-75 flask were first trypsinized, counted and re-suspended in DMEM/F12 supplemented with 10% (v/v) fetal bovine serum (FBS), 25 U/mL penicillin and 25 µg streptomycin and diluted to a final cell concentration of 1×10^6 cells/mL. The cell suspension (20 µL) and the pre-prepared squaramide-based hydrogel (180 µL) according to the gelation protocol were mixed through by gentle pipetting and then, the cell-gel suspension was transferred to an angiogenesis slide (12 µL/well). After being left to stand at 37 °C for 15 min, the hydrogels were mounted with an additional amount of medium (48 µL) for cell culture. For Growth Factor Reduced Matrigel (Corning) encapsulation, Matrigel was diluted to 5 mg/mL and cells were cultured as previously

described[88]. The medium was refreshed twice per week during the three-week culture period in the same volume.

Spheroids diameter determination

HepG2 spheroids were imaged using the EVOS FL AUTO2 equipped with a temperature and CO_2 gas controller at pre-defined time points. Z-stack images were acquired under a 10× objective and an environment of 37°C and 5% CO_2 was maintained during the measurement. The spheroid diameter was measured in Fiji by drawing a straight line horizontally (angle < 3°) with the corresponding scale. Sixty-six spheroids were counted for each group.

LIVE/DEAD staining

At pre-determined time points, the medium on top of the hydrogel was removed by pipetting, rinsed twice with PBS (pH 7.4, 45 µL) and incubated with a prepared staining solution (48 µL) (calcein AM (2 µM) and propidium iodide (1.5 µM)) at 37 °C for 30 min. The staining solution was removed, and the hydrogel was rinsed again with PBS two times (48 µL). The stained cell-laden hydrogel was imaged with Leica TCS SP8 confocal laser scanning microscope equipped with a 10× air objective. Fluorescent images were acquired at a resolution of 1024 × 1024 pixels using an excitation wavelength of 488 nm and an emission filter of 500–545 nm for calcein AM and an excitation wavelength of 532 nm and an emission filter of 594–686 nm for propidium iodide.

EdU staining

At pre-determined time points, cell-laden hydrogels were first diluted with cold medium (4 °C) (100x volume), pipetted and spun down to collect the HepG2 spheroids. Proliferating cells were labelled according to the protocol described in the Click-iT EdU Alexa Fluor 594 Imaging Kit. Briefly, the released HepG2 spheroids were first treated with the EdU solution (10 µM) at 37°C for 4h. Afterwards, the cells were fixed with 5% (w/v) PFA solution for 15 min at room temperature, followed by a 20-min penetration by 0.5% (w/v) Triton X-100 at room temperature. After washing with BSA solution (3%), the cells were incubated with the Click-iT® reaction cocktail for 30 min, followed by another wash and hoechst 33342 (5 µg/mL) incubation for 30 min to stain cell nuclei. The stained cell sample was transferred into another chamber slide that is protected from light and imaged on Leica TCS SP8 confocal laser scanning microscope equipped with a 40× oil immersion objective. Fluorescent Z-stack images were acquired at a resolution of 1024 × 1024 pixels with a step size at 1 µm. The Z-stack images from 3D HepG2 spheroids were projected into 2D by Fiji. Corrected total cell fluorescence (CTCF) for both channels were measured by Fiji and EdU positive ratios were calculated based on according to following equation:

$$CTCF = Integrated\ Density - (area\ of\ selected\ cell\ x\ mean\ fluorescence\ background\ of\ reading)$$

$$EdU\ positive\ ratios = \frac{CTCFEDU}{CTCFHoechst}\ x\ 100\%$$

In each measurement, three random areas around the cell were measured as background. Three spheroids were measured for all the groups.

RT-PCR

The cell-laden hydrogels were cultured at 37°C as previously described. On day 21, the total RNA was extracted using the TRI Reagent. RNA yield and purity were determined using the NANODROP spectrophotometer. 800 ng RNA was used to generate cDNA construct using the RevertAid H Minus First Strand cDNA Synthesis Kit. For RT-qPCR, 5x diluted cDNA was mixed with 1 µM forward and reverse primers (Supplemental Table 2) and X10 POWRUP SYBR MASTER MIX. Parameters used for RT-qPCR were: 50 ºC for 2 minutes, 95 ºC for 10 minutes, followed by 40 cycles at 95 ºC for 15 seconds and 60 ºC for 1 minute, 95 ºC for 15 seconds, 60 ºC for 1 minute, and finally 95 ºC for 15 seconds and run on a QuantStudio™ 6 Flex Real-Time PCR System (Applied Biosystems®). Samples were measured in triplicate, and mRNA expression was quantified using the delta-delta Ct (2–ΔΔCt) method. GAPDH was used as housekeeping gene.

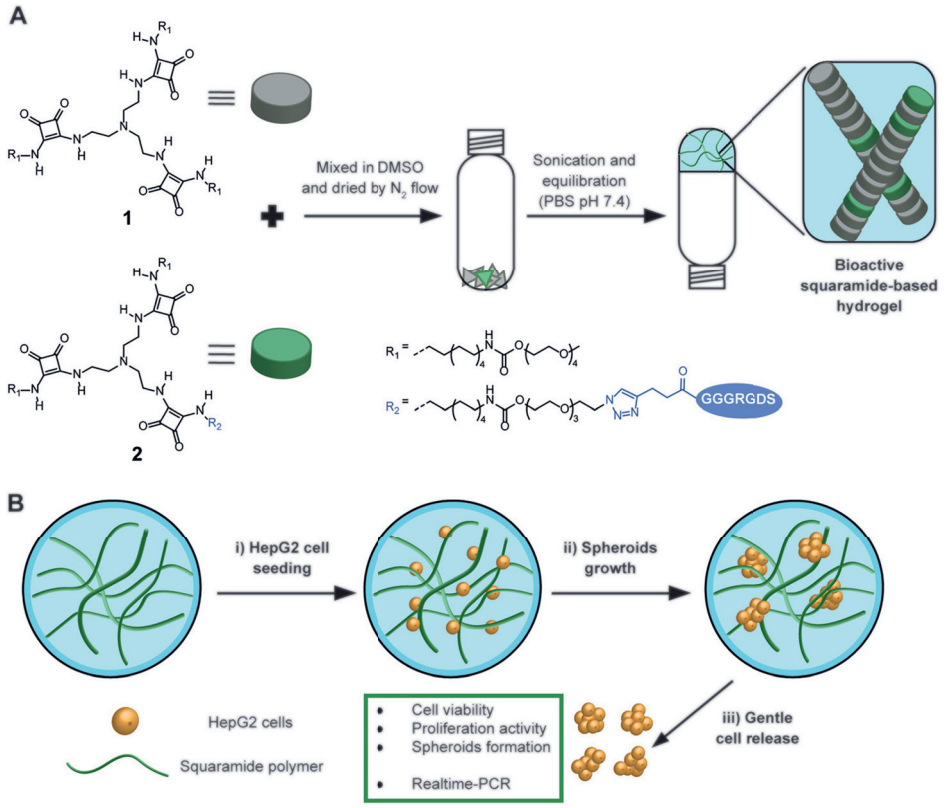
Immunofluorescence Analysis

Cells were cultured at 37°C as previously described. On day 21, the spheroids were fixed with 4% PFA for 30 minutes. Subsequently, the samples were blocked and permeabilized in 0.2% Triton X-100, 0.5% BSA in 1X PBS (TBP) for 1 hour. Spheroids were stained with the primary antibodies against albumin (1:1000, Bethyl laboratories, A80-229F), MRP2 (1:50, Abcam, M2III6) and β-catenin (1:50, Invitrogen, 71-7200) in TBP overnight at 4℃. After washing the samples three times in 1X PBS, spheroids were counter-stained with secondary antibodies (1:1000, Molecular probes, A11001, A11008), Hoechst 33342 (2µg/mL, Sigma) and Rhodamine Phalloidin (1:10.000, Sigma, P1951) in TBP for 1 hour at room temperature and finally washed three times with 1X PBS. Images were acquired with a Nikon TiE2000 confocal microscope with a 20X objective and 2X zoom.

Results

Earlier, we designed a tripodal squaramide-based monomer (1) where three squaramides were embedded within a hydrophobic core consisting of tris(2-aminoethylamine) (TREN), aliphatic, and a peripheral hydrophilic domain with

oligo(ethylene glycol) chains. In this study, we further sought to incorporate the RGD peptide into these squaramide monomers (2) to aid in cell proliferation, but also to provide a cell adhesive contact for cells (Scheme 1). However, the lack of reactive handle, namely the terminal methyl group on the oligo(ethylene glycol) chains of the monomer preclude it from further functionalization with any cargo, such as fluorescent dyes, crosslinkers, peptides, or proteins. Therefore, a desymmetrized tripodal squaramide-based monomer where one of the three arms was end-functionalized with an azide (3) was designed and synthesized starting from a monotrityl-protected TREN core. The azide functionality was first introduced onto tetraethylene glycol by tosylation (Supplemental Scheme 1)[118]. The tetraethylene glycol monomethyl ether and monoazide tetraethylene glycol were then independently activated using 1,1-carbonyldiimidazole and further reacted with monotrityl-protected C10 diamine in presence of N,N-Diisopropylethylamine (DIPEA) resulting in yields of 63% (methyl-terminated) and 74% (azide-terminated), respectively. The trityl protecting group was deprotected by TFA under an inert atmosphere, followed by its subsequent reaction with dibutyl squarate to provide the methyl-terminated and azide-terminated squaramide amphiphiles in yields of 87% and 47%, respectively (Supplemental Scheme 2). Subsequently, the methyl-terminated squaramide amphiphile was reacted onto the desymmetrized TREN core resulting in a yield of 54%. Last, the trityl group on TREN core was deprotected using TFA and further coupled to the azide-terminated squaramide amphiphile giving the final compound 3 in a 56% yield. (Supplemental Scheme 3) The RGD peptides (GGGRGDS, PEP1) were then synthesized by solid-phase peptide synthesis with the introduction of 4-pentyonic acid at the N-terminus to provide a reactive handle for bioconjugation. In a final step, the alkyne-ended RGD peptides (PEP2) were coupled to 3 by copper(I)-catalyzed azide–alkyne cycloaddition (CuAAc) obtaining the peptide-functionalized squaramide monomer 2 (Supplemental Scheme 4). Monomers 1 and 2 were purified by high performance liquid chromatography (HPLC) prior to self-assembly and gel preparation. For subsequent 3D cell culture studies, a supramolecular co-assembly protocol was developed to mix both native monomer 1 and RGD-functionalized squaramide monomer 2 (Supplemental Scheme 1A and Supplemental Figure 1). DMSO stock solutions of monomers 1 and 2 were first prepared at concentrations of 25 and 5 mM, respectively, followed by mixing in a controlled and tunable manner based on concentration and volume calculations. The DMSO mixture was then exposed to nitrogen flow overnight to obtain a dried film. Afterward, hydrogel preparation was performed by rehydration in PBS, vortexing, and sonication in an ice–water bath (4 °C, ≈30 min). Last, the obtained transparent solution was incubated at 37 °C for 30 min and equilibrated overnight prior to further use for subsequent experiments. UV–vis spectroscopy measurements were performed to understand the effect of the mixing protocol on the functional squaramide-based supramolecular monomers and



Scheme 1. A) Preparation of bioactive squaramide-based supramolecular hydrogels: native tripodal squaramide monomer (1) was mixed with an RGD functionalized monomer (2) in DMSO. The dried solid was rehydrated in phosphate buffered saline (PBS, pH 7.4) by sonication, followed by being left to equilibrate overnight to obtain the co-assembled bioactive hydrogels. **B)** HepG2 spheroids cultured in bioactive squaramide-based supramolecular hydrogel for 21 days: i) HepG2 cells were mixed and encapsulated within the hydrogel by pipetting using its self-recovery property; ii) HepG2 cells self-assemble into spheroids, proliferate, and differentiate within the hydrogel; iii) HepG2 spheroids were released by dilution and used for further analysis including cell proliferation and gene expression.

mixtures at the molecular level. UV–vis spectra of both monomer 1 and 2 in DMSO showed a single band at 293 nm that consistent with depolymerization of the squaramide monomers (Supplemental Figure 1)[109]. After rehydration of the films in PBS, samples containing 2, 5, 10, and 15 mol% of monomer 2 (SQ-2RGD, SQ-5RGD, SQ-10RGD, and SQ- 15RGD) displayed two absorption bands at 262 and 322 nm corresponding to the HOMO−LUMO+1 and HOMO−LUMO transitions of squaramide, respectively (Supplemental Figure 5)[109,114]. These bands are identical to the supramolecularly polymerized monomer 1 on its own suggesting that the mixing of monomer 2 up to 15 mol% does not modify its aggregation at the molecular level.

However, further increasing the amount of monomer 2 up to 40 mol%, the HOMO–LUMO+1 and HOMO–LUMO transitions were recorded at 267 and 319 nm, pointing to a slightly lower degree of aggregation compared to the native monomer 1. Together these results suggest DMSO depolymerizes the squaramide monomers, including those with the RGD peptide functionality, and repolymerization is achieved when prepared as co-assemblies in buffered solutions. RGD-functionalized squaramide hydrogels were prepared with various mol% of monomer 2 and their capacity to gelate water was first approximated by a gel inversion test. The total squaramide monomer concentration was maintained at 3.1 mM and the effect of increasing the amount of monomer 2 on co-assembly was examined (0.06–0.45 mM RGD peptides) (Figure 1A). Non-flowing hydrogel materials were observed up to 15 mol% **2**. The mechanical properties of RGD-functionalized squaramide hydrogels were further assessed quantitatively by performing oscillatory rheology. From the time sweep measurements, hydrogel formation was confirmed with storage moduli (*G*') being greater loss moduli (*G*'') for the various samples. Mechanically soft hydrogels were formed for all compositions with a *G*' lower than 100 Pa; a decreasing trend was observed with the increase of monomer **2**. (Figure 1B) An amplitude sweep experiment in a range of strain from 0.1% to 100% was used to determine the linear viscoelastic (LVE) region of the various materials. In the case of hydrogels SQ-2RGD and SQ-5RGD, *G*' and *G*'' remained constant until 4% strain, whereas for hydrogels SQ-10RGD and SQ-15RGD the exit from the linear regime was observed at 6% strain. (Figure 1C) Moreover, frequency sweep measurements showed rheological profiles consistent with viscoelastic materials in a frequency range from 0.01 to 2 Hz for all hydrogels up to 15 mol% monomer **2** with *G*' was greater than *G''* by an order of magnitude (Supplemental Figure 2). Last, step-strain measurements were executed to evaluate the effect of the added monomer **2** on the self-recovery properties of the supramolecular hydrogels. With the addition of monomer **2** up to 15 mol%, the RGD-functionalized squaramide hydrogels showed similar self-recovery behaviour to the previously reported native hydrogel SQ, namely the decrease and inversion of both moduli (*G'* and *G''*) in response to large amplitude strain, and recovery of the material to its initial state after its removal over two cycles[114] (Figure 1D and Supplemental Figure 3). To better understand the effect of increasing peptide monomer concentration, a sample with a greater mol percentage of monomer **2** (SQ-40RGD) was examined. While *G*' > *G*'' in time sweep measurements, *G*' and *G*'' were found to decrease (*G*' = 1.26 Pa, *G*'' = 0.27 Pa) significantly (Supplemental Figure 4) demonstrating a negative effect of the peptide monomer on gelation properties. Further insight into the origin of the measured rheological properties was provided by cryogenic transmission electron microscopy (cryo-TEM). As shown in Supplemental Figure 5, flexible, micron-length nanofibers were observed for SQ-10RGD hydrogels (3.1 mM, PBS) indistinguishable from the SQ hydrogels with a slightly smaller width of

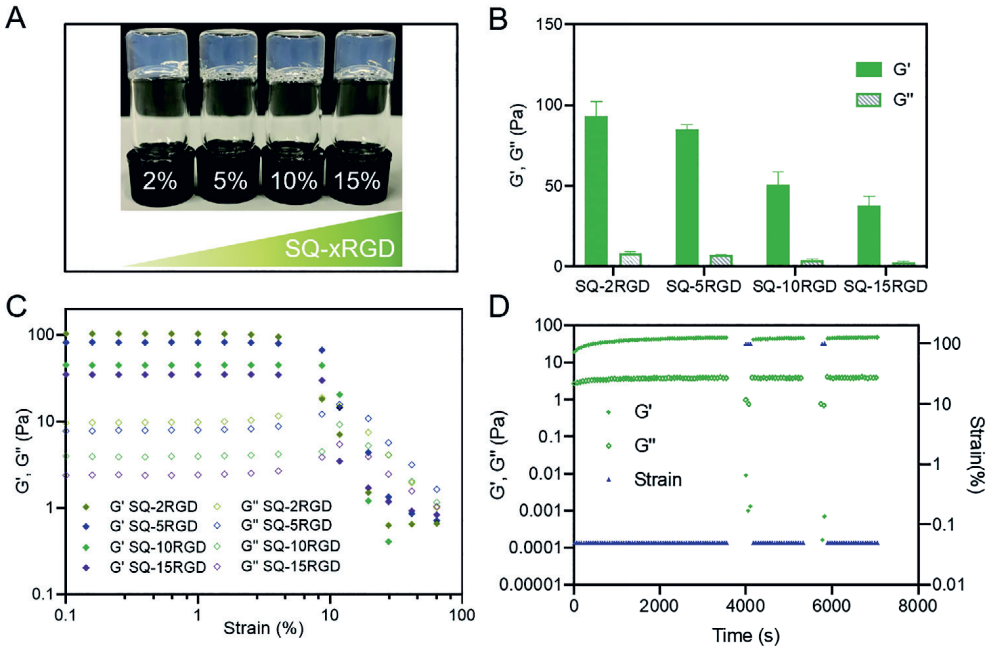


Figure 1. A) Gel inversion test of RGD-functionalized squaramide hydrogels (3.1 mM) prepared in PBS (pH 7.4) SQ-xRGD: hydrogels containing *x* mol% of the monomer **2**. Oscillatory rheology measurements: **B)** Averaged (*N* = 3) storage (*G'*) and loss (*G''*) moduli of hydrogels (3.1 mM, PBS) collected at 37 ± 0.2 °C by a time-sweep measurement with a fixed frequency of 1 Hz and strain of 0.05%. **C)** Amplitude sweep of RGD-functionalized squaramide hydrogels at 37 ± 0.2 °C with a frequency of 1 Hz and strain from 0.1% to 100%. **D)** Step-strain measurements of hydrogel SQ-10RGD (3.1 mM) at 37 ± 0.2 °C with a frequency of 1 Hz. Frequency-sweep measurements (from 0.01 to 2 Hz, γ = 0.05%) were performed between application of low (0.05%) and high strain (100%) (data not shown).

4.8 ± 0.4 nm. Because of the difference in gel rheological properties with increasing peptide concentration, we further examined the effect of increasing monomers **2** on the nanoscale structure of the squaramide-based supramolecular polymer fibres. Similarly, entangled fibres were observed in SQ-40RGD solution, with comparable fibre width of 4.6 ± 0.6 nm, indicating that the co-assembly of monomer **2** was comparable at the nanoscale level (Supplemental Figure 6). RGD peptides bind cell-surface integrins and through these receptors they stimulate actin polymerization upon cell attachment, facilitating cell spreading and contractile movements[119,120]. Therefore, before applying the co-assembled supramolecular polymers for 3D cell culture, we first investigated whether cells can recognize and respond to the RGD peptides presented by the squaramide-based polymers. Consequently, NIH3T3-LifeAct-mCherry cells transduced to express m-Cherry-labelled actin were encapsulated and cultured in squaramide-based hydrogels. Branched, large protrusions (pseudopods) tipped with actin rich filopodia outside of the cell body were observed in the SQ-10RGD

and SQ-15RGD hydrogels, as previously reported in ECM-derived collagen hydrogels[121,122] (Supplemental Videos 1 and 2). Additional to protrusion formation, cell migration was also observed indicating extensive cell-hydrogel interactions in 3D. In contrast, cells in native SQ hydrogels displayed a highly rounded morphology, with minimal spreading and were rarely observed to migrate (Supplemental Video 3). This indicates that the inclusion of RGD peptides is essential for cell spreading and migration in the squaramide-based supramolecular hydrogel. To further quantify cell spreading efficiency as a function of RGD concentration, cells were cultured in squaramide-based hydrogels for 24 h and then subsequently imaged (2.5 µm stepped *z*-stacks). Using image analysis, all cells in each imaged volume slice were recognized and a local 2D z-projection was made around each cell to individually analyse and extract appropriate cell edges. The cell edges were used to calculate morphological parameters such as cell area, perimeter, circularity, summated skeleton branch length, min- and max Feret diameter, and aspect ratio. Cells tended to spread significantly more in RGD-functionalized squaramide hydrogels, as shown in Figure 2A and Supplemental Figure 8, Supporting Information, and quantitatively displayed larger cell areas and longer perimeters in comparison to those in SQ ($P < 0.001$, Figure 2B and Supplemental Figure 8). Consistently, cell circularity was much lower in RGD-functionalized hydrogels, calculated to be 0.726, 0.619, and 0.694 for cells in SQ-5RGD, SQ-10RGD, and SQ-15RGD, respectively, in comparison to that in SQ (0.903). To gather further information of cell protrusion formation, the cell shapes were skeletonized, the Feret diameters were measured, and aspect ratios were calculated. Significantly larger Feret diameters were observed for cells cultured in RGD-functionalized hydrogel in comparison to that in SQ ($P < 0.001$), supporting cell elongation within the RGD-presenting materials. Among them, the lowest aspect ratio was calculated from cells cultured in SQ-10RGD, as shown in Figure 2B. Moreover, the summated skeleton branch lengths for each cell, used as an indicator of protrusion length, was found to be 22.4 ± 3.3 µm in SQ-10RGD, a 4-fold increase over that in SQ (5.2 ± 1.2 µm) (Figure 2B and Supplemental Table 1). Taken together, the cells displayed a more spread and branched morphology with highly dynamic actin polymerization along the cell membrane, especially at the end of branched protrusions as a consequence of interaction with RGD peptides in the bioactive squaramide-based hydrogels as previously reported in literature powering cell migration within the hydrogels[119]. The aggregation of HepG2 cells into spheroidal structures that resemble their presentation in vivo provide a versatile tool to investigate hepatic metabolism, stemness, cancer, and chemical safety assessment[123–125]. Because bioactive squaramide-based hydrogels containing an RGD-ligand support active cell migration and proliferation, we became interested if these materials would further enable the self-assembly of HepG2 cells into spheroids and facilitate their differentiation.

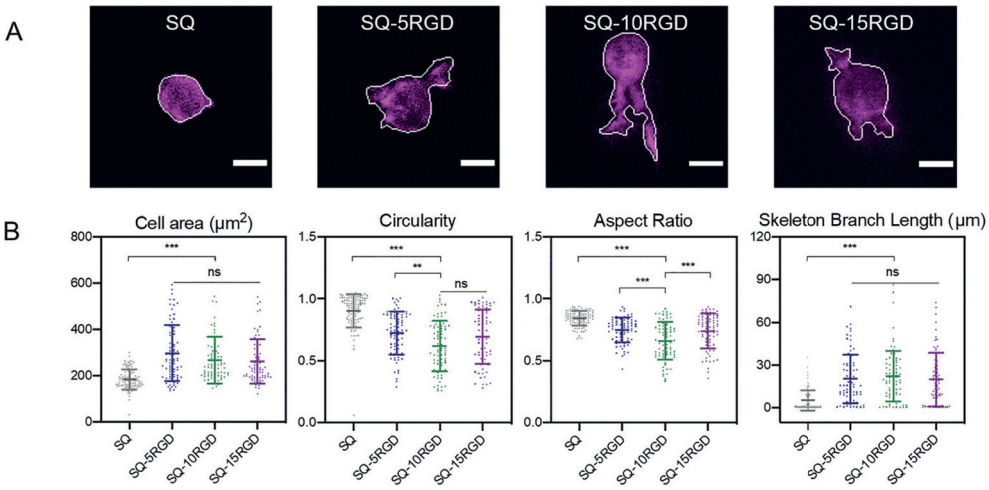


Figure 2. A) Representative images of NIH3T3-LifeAct-mCherry cells cultured within squaramide-based hydrogels after 24 h, scale bar: 10 μm **B)** Quantitative analysis of mean projected cell area, perimeter, circularity, and skeleton branch length from NIH3T3-mCherry-LifeAct cells cultured for 24 h within squaramide-based hydrogel. For each data set, 74–100 cells were analysed. The mean and standard deviation are marked within the graphs (**P* < 0.05, ***P* < 0.01, ****P* < 0.001 one-way Anova).

A recent study demonstrated that low concentrations of RGD peptide (≈0.2 mM) may be not sufficient for human liver organoid proliferation[97], thus bioactive squaramide-based hydrogels were examined at 0.3 and 0.45 mM RGD with hydrogels lacking the RGD monomer **2** and Matrigel being used as controls. As expected, HepG2 cells grew within SQ-10RGD hydrogel by starting from single cells (1×10^5 cells mL) on day 3 to small aggregates on day 7, and finally, rounded spheroids on day 14 that continued to increase slightly in size until day 21 (Figure 3A). HepG2 cells grew similarly in SQ and SQ-15RGD hydrogels forming compact spheroids on day 14. As a control, spheroids cultured in Matrigel, the current gold standard cell culture matrix, displayed a slightly less compacted morphology throughout the culture period. Spheroid diameter was measured to quantitatively compare the performance of the supramolecular matrix against Matrigel in generating these morphological structures. Increase in the spheroidal diameter over the 21-day culture period was confirmed by plotting the measured size distributions in Figure 3B. Cellular aggregates of 58 ± 18, 69 ± 17, and 64 ± 17 μm were obtained on day 7 in SQ, SQ-10RGD and SQ-15RGD hydrogels, and grew into spheroids with diameters of 116 ± 40 μm, 112 ± 32 μm, and 129 ± 49 μm on day 14, respectively. From day 14 to day 21, spheroids in SQ and SQ-10RGD hydrogels were comparable in diameter, 127 ± 30 μm and 119 ± 30 μm, respectively. Conversely, HepG2 cells cultured in Matrigel formed spheroids with average diameter of 102 ± 31 μm on day 7 and increased in size to 128 ± 40 μm on day 14 and 122 ± 22 μm on day 21, respectively. From all hydrogel conditions tested, the HepG2 spheroids in SQ-15RGD

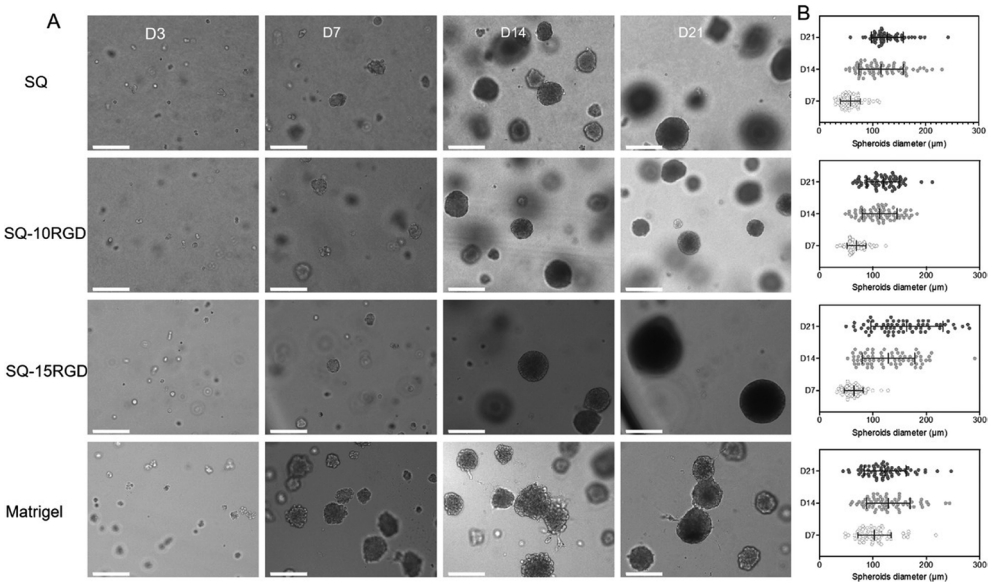


Figure 3. 3D HepG2 cell culture in squaramide-based hydrogels over a 21-day period. **A)** Brightfield images taken on day 3 (D3), 7 (D7), 14 (D14), and21 (D21). Scale bar: 200 µm. **B)** Size distribution of HepG2 spheroids during the 21-day culture period in squaramide-based hydrogels and Matrigel (LOT5215008). For each group, 66 spheroids were measured in Fiji by manually drawing a straight line horizontally (angle < 3°). The means and standard deviations are marked inside the graphs.

hydrogel displayed highest diameters at 163 ± 66 µm on day 21, yet remained below 200 µm providing sufficient oxygen diffusion throughout the spheroid[126,127]. This increase in spheroid diameter in the squaramide-based hydrogels suggests proliferation of HepG2 cells during the culture period. Proliferation of the HepG2 spheroids cultured in the bioactive squaramide-based hydrogels were further assessed by their imaging with 5-ethynyl-2'-deoxyuridine (EdU). In order to facilitate their staining, the HepG2 spheroids were released from the hydrogels by dilution of the supramolecular matrix at predetermined time points, imaged and analysed quantitatively for EdU positive cells. Proliferative cells were observed to be randomly distributed throughout the HepG2 spheroids suggesting that sufficient nutrient diffusion through squaramide-based hydrogels and the spheroids occurs during culture (Figure 4B). In the SQ hydrogel lacking RGD peptides, HepG2 cells displayed comparable proliferative activity based on the EdU-positive percentage over the culture period, namely 18 ± 16.2% on day 7, 8 ± 6.4% on day 14, and 10 ± 6.2% on day 21, respectively. In the RGD-functionalized squaramide-based hydrogel, HepG2 cells were found to proliferate actively at the beginning of the culture period with the measured percentage of EdU-positive cells on day 7 being 25 ± 9.9% and 45 ± 8.4% in

SQ-10RGD and SQ- 15RGD hydrogels, respectively. Notably, HepG2 cells cultured in Matrigel displayed an EdU-positive percentage of 41 ± 12.8% on day 7 that declined to 7 ± 5.0% on day 14 and eventually ended at 6 ± 5.2%. As the culture progressed from day 7 to 14 in both Matrigel and squaramide hydrogels, a dramatic decrease in the percentage of EdU-positive cells was measured pointing to decreased proliferation and suggestive of their differentiation. SQ-15RGD showed the highest proliferation of the HepG2 cells in comparison to Matrigel, SQ and SQ-10RGD hydrogels on day 14, and is consistent with the significantly larger measured diameter of the spheroids. In the case of SQ-10RGD and SQ-15RGD slightly increased proliferation of 13 ± 9.2% and 14 ± 2.8%, respectively, was recorded at the end of culture and is slightly greater than for the SQ monomer (10 ± 6.2%) (Figure 4C and Supplemental Figure 10). Besides the early active cell proliferation, HepG2 spheroids cultured within squaramide-based hydrogels were largely calcein AM positive with few dead cells confirming high cell viability and the absence of a necrotic core during the culture (Figure 4A and Supplemental Figure 9). Collectively, RGD-functionalized squaramide hydrogels support the formation of HepG2 spheroids with a size greater than 150 µm initially showing active cell proliferation that decreases toward the end of the 21-day culture period.

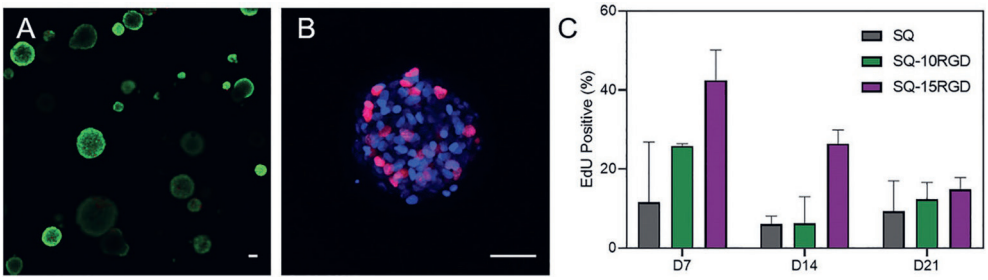


Figure 4. A) Cell viability assay of HepG2 spheroids cultured in SQ-10RGD hydrogel for 21 days stained by a LIVE/DEAD assay with calcein AM (viable cells, green) and propidium iodide (PI) (dead cells, red). **B)** EdU staining of released HepG2 spheroids cultured in SQ-10RGD hydrogels. Proliferating cells were labelled with EdU-Alexa fluor 594 (red) and cell nuclei were stained with Hoechst 33 342 (blue). Scale bar: 50 µm. C) Quantification of EdU percentage in HepG2 spheroids cultured within Matrigel, SQ, SQ-10RGD, and SQ-15RGD hydrogels. *N* = 3.

The initial increased cell proliferation could further affect HepG2 cell differentiation resulting in the induction of metabolic enzymes and expression of hepatic markers. HepG2 cells showed spheroid formation in SQ, SQ-10RGD, and SQ-15RGD hydrogels with high cell viability and increased proliferation in the bioactive gels early on in the culture. However, it was previously demonstrated that the formation of these in vivo mimicking structures in 3D in peptide nanofiber hydrogel-based does not necessarily result in the distinct expression of metabolizing enzymes by RT-PCR[91]. Consequently, to assess the bioactive squaramide-based materials on the maturation of HepG2

spheroids, RT-PCR experiments were performed to evaluate the expression of a panel of metabolic enzymes and hepatic markers. As hypothesized, the HepG2 spheroids showed higher expression of various phase I and II metabolic enzymes and drug transporters in the 3D cultures performed in comparison to 2D (Figure 5A). mRNA expression of CYP1A2 measured from cells cultured in 3D in the Matrigel matrix control was over 40-fold in comparison to the 2D condition. Similarly, both CYP2C19 and CYP3A4 showed an over tenfold enhancement in 3D in comparison to 2D culture and CYP2C9 and CYP2D6 expression was increased 3- and 4.5-fold, respectively. Additionally, mRNA levels of the phase II xenobiotic-metabolizing enzymes UGT1A1 increased by over 45-fold and expression of hepatic markers HNF4a and NCTP were also found to increase over two times during hydrogel-based culture. The overall higher gene expression of metabolic enzymes and hepatic markers are consistent with previous reports that the formation of compact spheroids in 3D is beneficial for hepatocyte maturation[88,92]. When compared against the HepG2 spheroids cultured in Matrigel, cells cultured in the bioactive squaramide-based hydrogel SQ-10RGD in 3D displayed significantly higher mRNA expression in case of CYP2D6 (4.7-fold), CYP2C19 (4.2-fold), CYP2C9 (3.6-fold), and NCTP (4.9-fold) and comparable level in CYP1A2 (1.8-fold), UGT1A1 (1.4-fold), CYP3A5 (1.5-fold), and HNF4a (1.5-fold). These results strongly suggest that the fully synthetic bioactive squaramide-based hydrogel can function well as an alternative matrix of Matrigel for HepG2 culture. More importantly, in comparison to the control SQ hydrogel, cells were cultured within SQ-10RGD hydrogel displayed significant improved mRNA expression of NCTP (**$P < 0.01$) and advantageous expression of CYP2D6, CYP2C19, CYP1A2, HNF4a, and UGT1A1, confirming the importance of incorporating bioactive peptides to further stimulate differentiation. The overall enhancement in gene expression in HepG2 spheroids by introducing RGD peptides is less obvious than that of transferring cells from 2D to 3D culture, implying cell–cell contact plays a critical role in their differentiation rather than cell–matrix interactions, at least under the tested cell seeding condition[128,129]. However, matrix proteins have been earlier demonstrated to play an important role in the assembly of HepG2 spheroids and this can also explain the subtle increases between the RGD and native conditions[130]. To further probe the differentiation of spheroids in 3D in squaramide-based hydrogels, immunostaining of albumin, and bile canaliculi-like structures through MRP2 was performed (Figure 5B and Supplemental Figure 12)[88,89]. Albumin expression was present in both Matrigel and squaramide-based hydrogels culture systems. In contrast, MRP2 expression was localized in actin-rich regions suggesting bile duct formation, with a more intense staining in hepG2 spheroids that were cultured in SQ and SQ-10RGD hydrogels in comparison to those in Matrigel. Conversely, MRP2 staining was hardly observed in spheroids from the SQ-15RGD hydrogel that had the largest aggregates. Moreover, β-catenin expression at the borders of the hepG2 spheroids indicate that independent of the gel used the cells

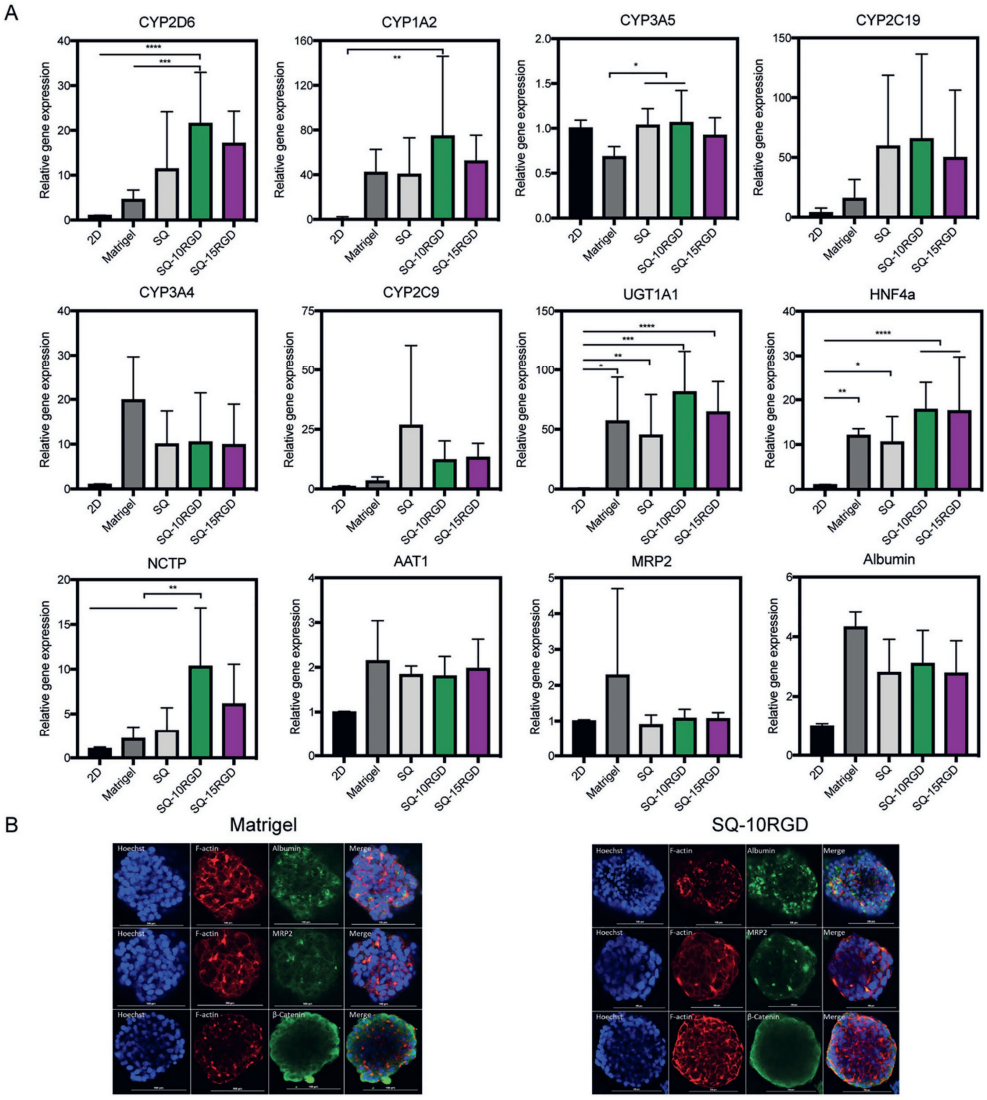


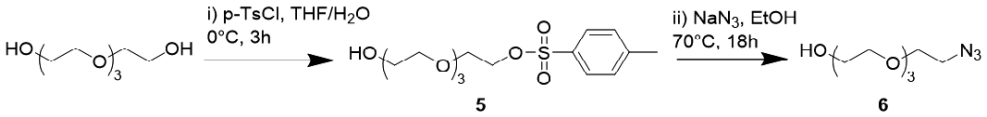
Figure 5. A) Real-time PCR analysis of metabolic enzymes and liver-specific markers in 2D and 3D culture. Fold change gene expression levels of HepG2 spheroids after 3D culture for 21 days compared to 2D culture for 3 days. Data are collected from three biological replicates. (*$P < 0.05$, **$P < 0.01$, ***$P < 0.001$, ****$P < 0.0001$ one-way Anova). **B)** Immunofluorescence staining of the liver markers albumin (upper row), MRP2 (middle row) and β-catenin (lower row) in green, and counter-stained with F-actin rhodamine phalloidin (red) and the nuclear stain Hoechst33342 (blue). Merged channels consist of all three staining's. Scale bar: 100 µm.

establish basal-lateral polarity. To summarize, the quantified mRNA expression of metabolic enzymes and hepatic makers from HepG2 cells cultured in squaramide-based hydrogels confirms our hypothesis that our bioactive and chemical-defined synthetic matrix can be an alternative to Matrigel to support their 3D cell culture, and importantly, incorporation of cell adhesion motifs (RGD) enhanced cell proliferation, and thus improve cell hepatic makers expression in 3D. Still, as observed from real-time PCR analysis in Figure 5A, some variation between biological replicates was observed in the gene expression, which was comparable to that of Matrigel from different lots (Supplemental Figure 11), especially with respect to CYP1A2 and UGT1A1 expression. Likely these variations are due to the non-uniform size of the formed spheroids in 3D within the materials that influence the metabolic activity of the HepG2 cells and further refinement of the overall synthetic matrix composition and/or culture protocol will require methods to control spheroid size prior to cell culture within the materials[131,132]. Gratifyingly, this fully synthetic supramolecular squaramide-based matrix can support HepG2 early proliferation and differentiation with the expression of several key metabolic enzymes and hepatic markers to a greater extent than Matrigel.

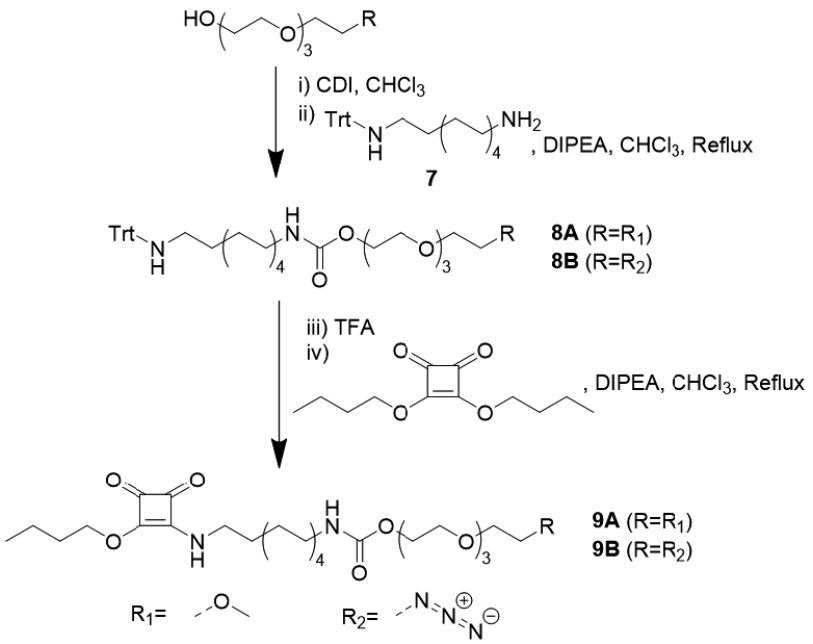
Discussion

A fully synthetic and bioactive squaramide-based supramolecular hydrogel material bearing RGD peptides was prepared for 3D cell culture. The co-assembly approach of the synthesized monomers **1** and **2** to prepare the hydrogel materials enables tuning of the peptide concentration within the materials. The RGD functionalized squaramide-based hydrogels were demonstrated to be optically clear, mechanically soft, and self-recovering. Encapsulated cells recognize the RGD peptides (0.15–0.45 mM) embedded within the network by spreading, initiating actin polymerization, and inducing cell migration in 3D. These RGD functionalized squaramide hydrogels support the growth of HepG2 cells into compact spheroids with high cell viability, active proliferation, and differentiation, resulting in significantly higher gene expression of metabolic enzymes and hepatic markers as well as the formation of liver structures and basal-lateral polarization. This chemically well-defined monomers enable a facile preparation protocol through their co-assembly, cytocompatibility, and capacity to trigger differentiation on par with natural materials challenging Matrigel, the current gold standard for liver spheroid culture, but can be more broadly applied in other areas of tissue culture where cell-matrix interactions are necessary to facilitate various aspects of cell behaviour. Moreover, their self-recovering properties enable gentle spheroid release which can be used for downstream analysis. Finally, the terminal azide on squaramide monomer **3** leaves the door open to further chemically modification and crosslinks for future biomaterials designs, for example, tuning the stiffness of supramolecular network in a straightforward manner to provide a closer in vivo mimicking microenvironment for cells.

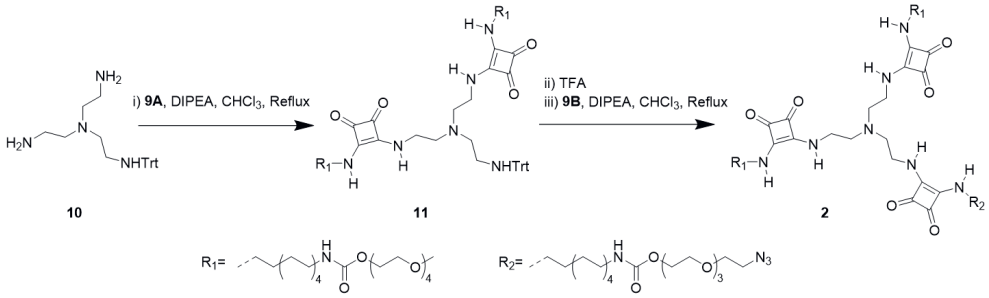
Supplemental Schemes



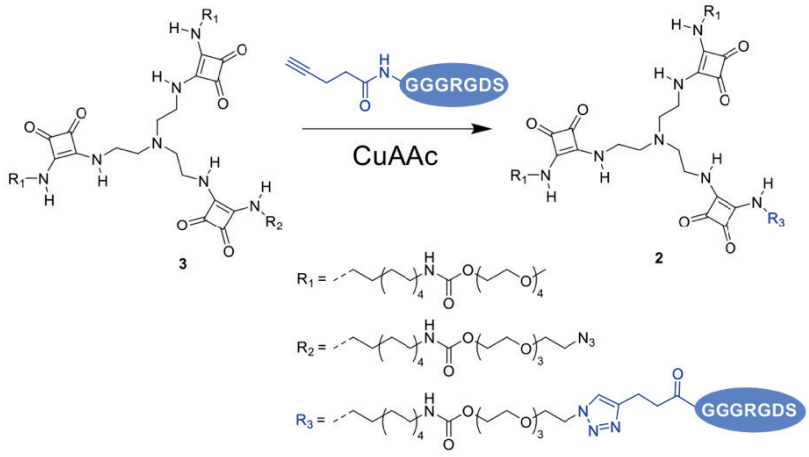
Scheme S1: Synthesis route for compound 6 [133].



Scheme S2: Synthetic route for compound 9A and 9B.

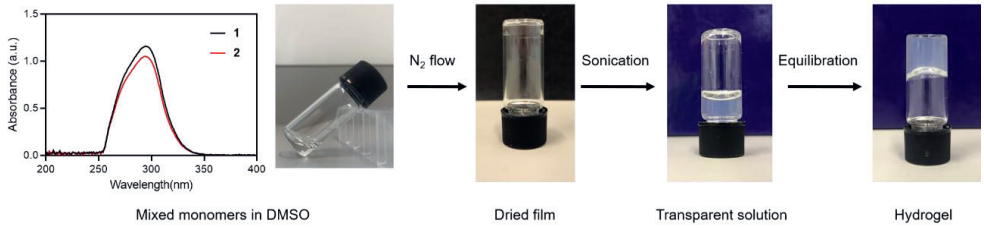


Scheme S3: Synthetic route for compound 3.

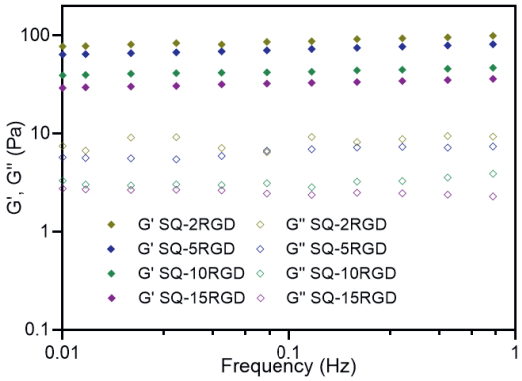


Scheme S4: Synthesis of compound 2.

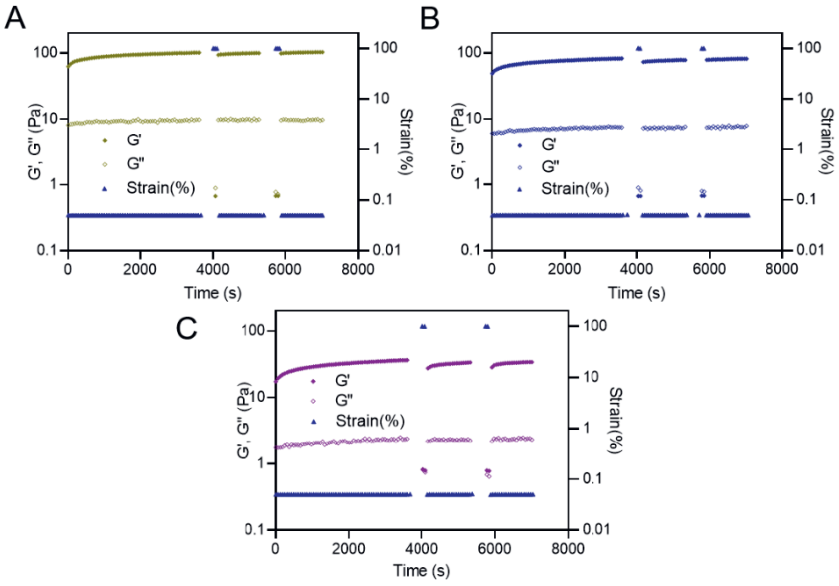
Supplemental Figures



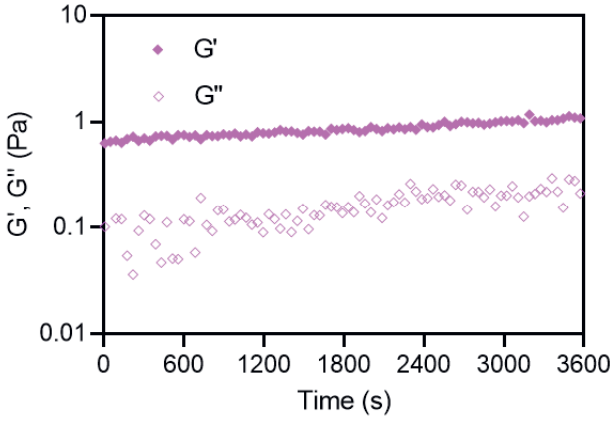
Supplemental Figure 1. Workflow for the preparation of RGD-functionalized squaramide hydrogels. 1) UV spectra show that the squaramide monomers are depolymerized in DMSO due to a broad band centred around 293 nm. **2)** Preparation of a mixture of monomer 1 and 2 starting from their respective DMSO stock solutions. **3)** Representative image of a film obtained after applying a gentle flow of nitrogen gas overnight. **4)** Dried films in PBS (pH 7.4) were sonicated for ~30 min in an ice-water bath (4 °C) until transparent solutions were obtained. **5)** Transparent hydrogels are formed after incubation of the vial at 37°C for 30 min and being left to stand at room temperature overnight.



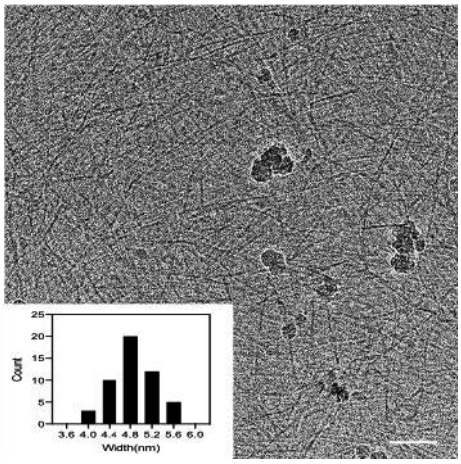
Supplemental Figure 2. Frequency sweep measurements of RGD-functionalized squaramide hydrogels in PBS (pH 7.4) at 37 ± 0.2 °C. Frequency sweep data was collected in a range of 0.01 Hz to 2 Hz with strain of 0.05%. (N = 3).



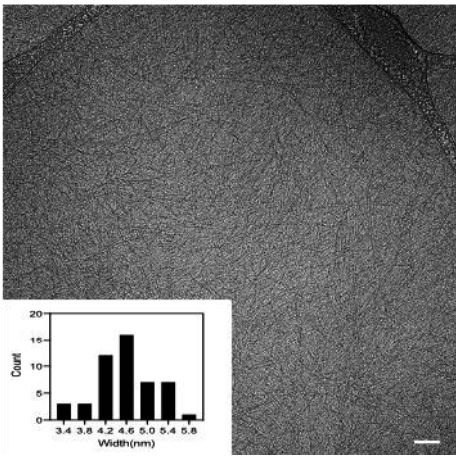
Supplemental Figure 3. Step-strain measurement of RGD-functionalized squaramide hydrogels in PBS (pH 7.4) at 37 ± 0.2 °C. The data were collected at a frequency of 1 Hz. The absence of data between the application of low and high strain is due to the acquisition of a frequency sweep (from 0.01 to 2 Hz, γ= 0.05%) in between these steps. (N = 3).



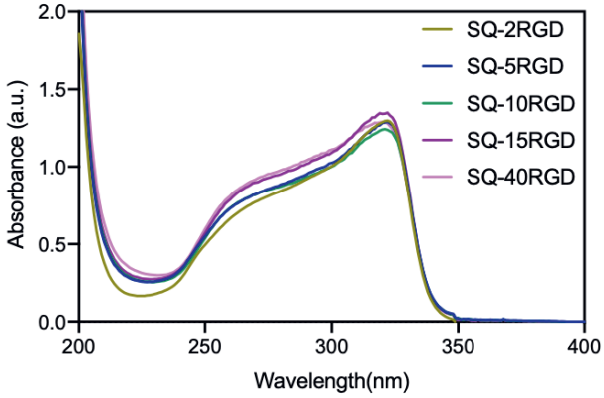
Supplemental Figure 4. Time sweep measurement of SQ-40RGD solution at 37 ± 0.2 °C. Time sweep measurements with strain at 0.05% and frequency of 1 Hz.



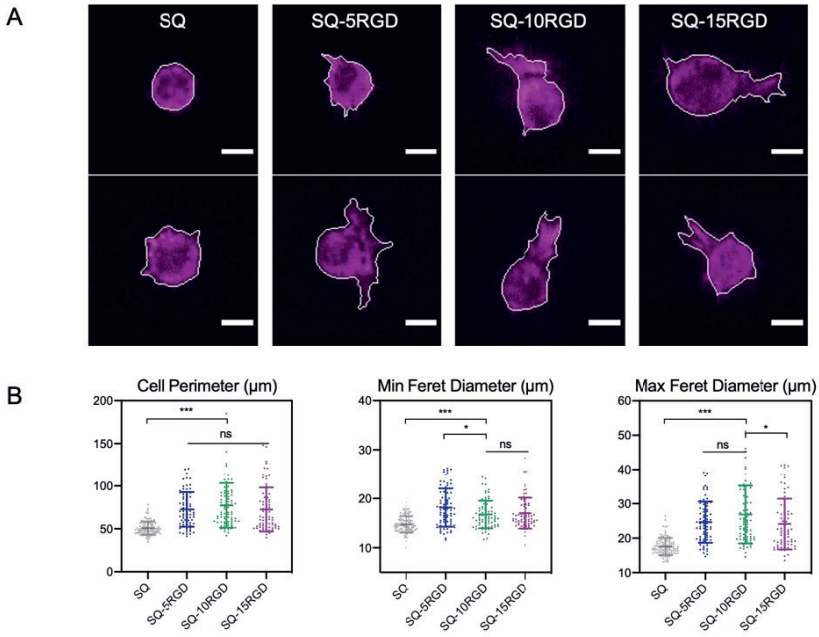
Supplemental Figure 5. Cryo-TEM image of SQ-10RGD hydrogel (3.1 mM, PBS, pH 7.4) as prepared by the gelation protocol. Scale bar: 100 nm. Insert image: histograms of fibre width distribution collected from a sample size N = 50.



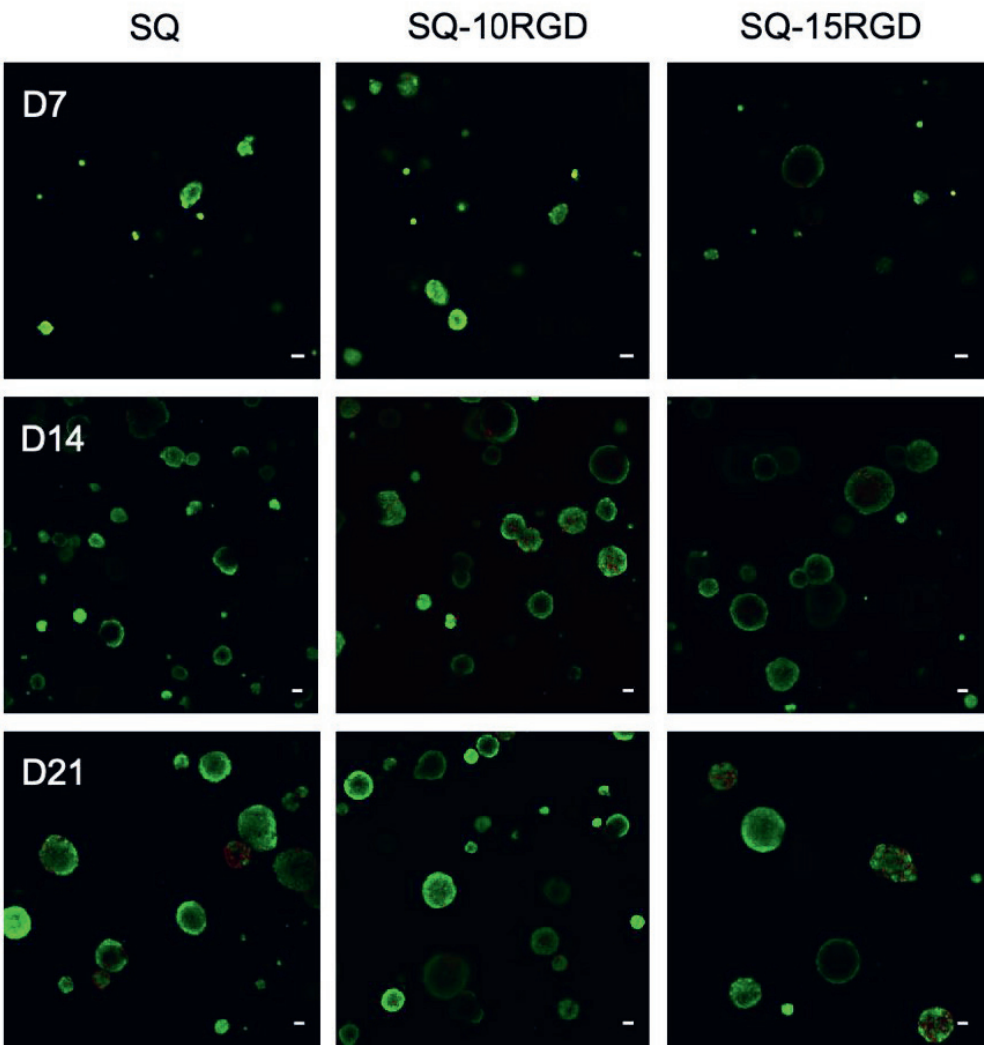
Supplemental Figure 6. Cryo-TEM image of SQ-40RGD solution (3.1 mM, PBS, pH 7.4) as prepared by the gelation protocol. Scale bar: 100 nm. Insert image: histograms of fibre width distribution collected from a sample size N = 50.



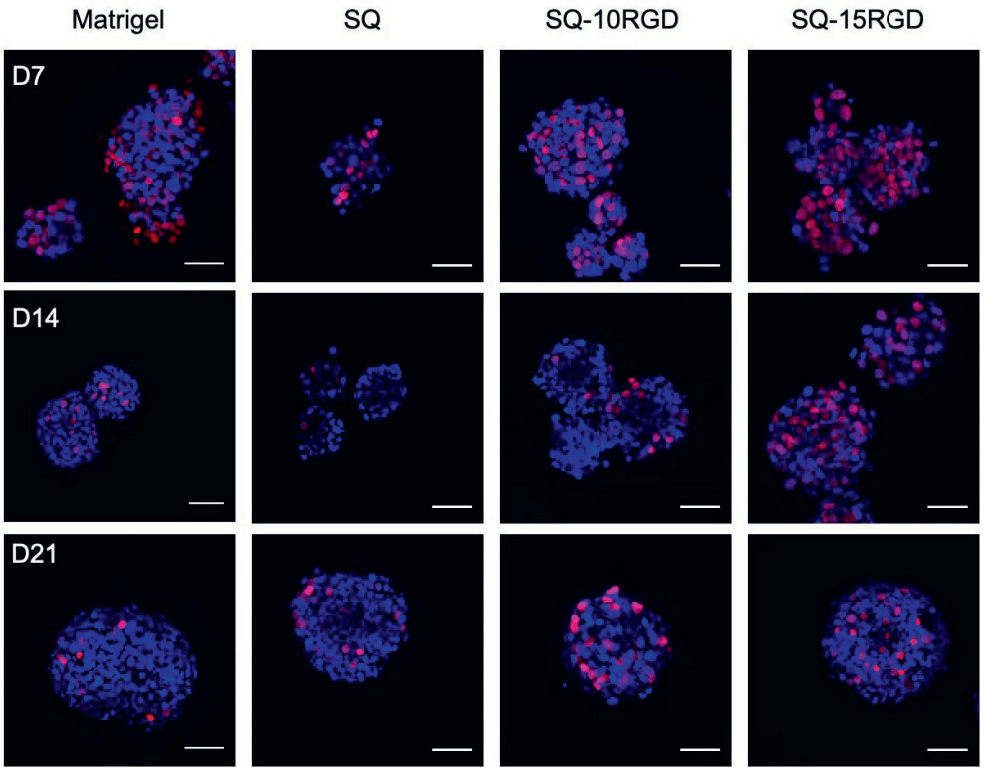
Supplemental Figure 7. UV-Vis spectra of squaramide-based supramolecular polymer solutions (30 µM) containing 2-40 mol% 3 in PBS (pH7.4).



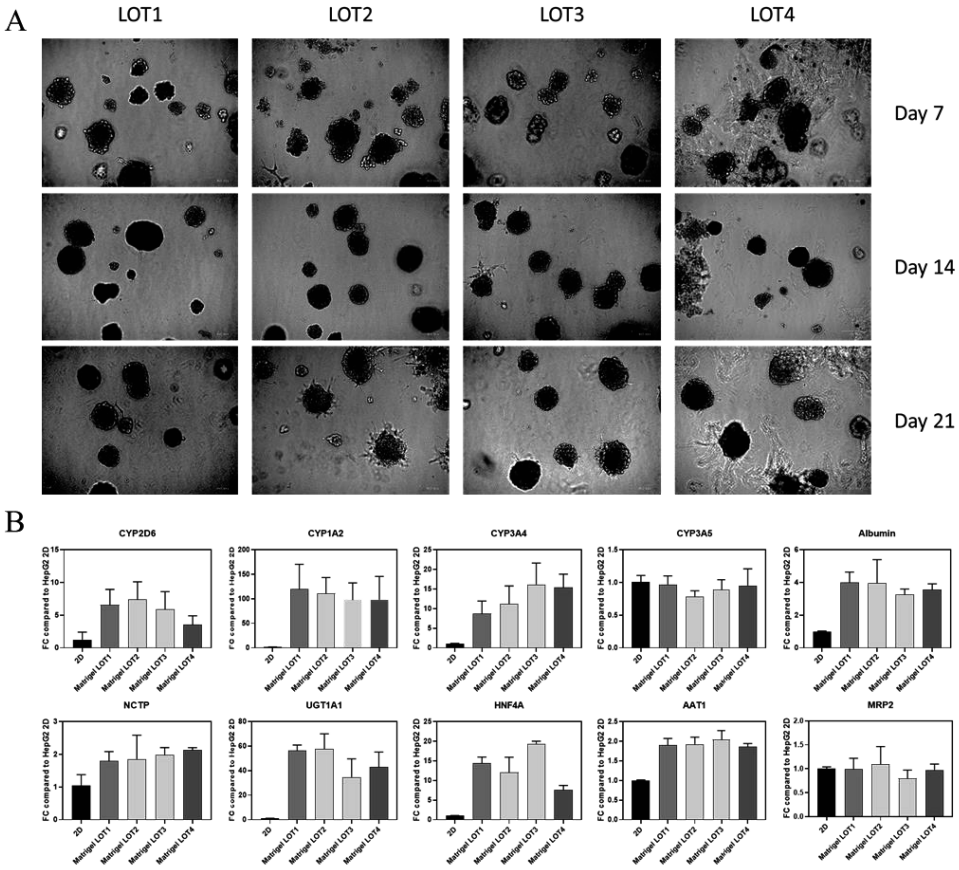
Supplemental Figure 8. A) Representative images of NIH3T3-LifeAct-mCherry cultured within squaramide-based hydrogels, scale bar: 10 µm; **B)** Quantitative analysis of cell perimeter, minimum and maximum Feret diameter of NIH3T3-LifeAct-mCherry cells cultured for 24h within squaramide-based hydrogel in 3D. The means and standard deviations are marked inside the graphs.



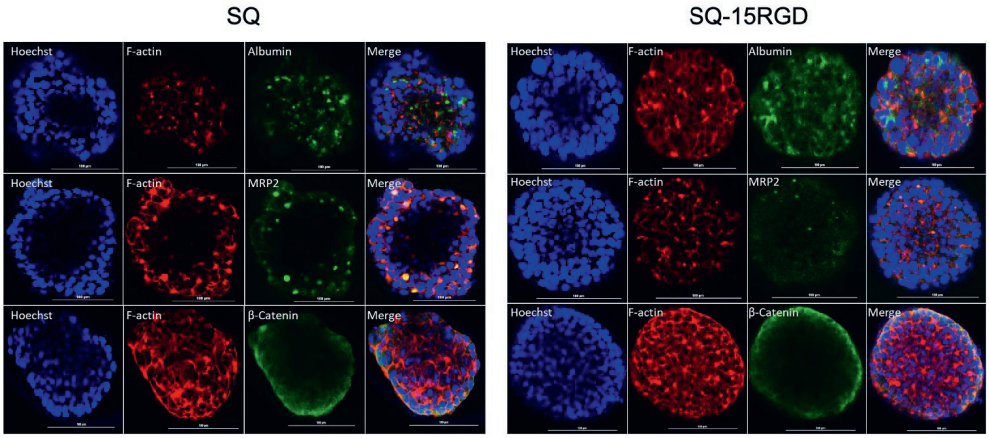
Supplemental Figure 9. Cell viability assay of HepG2 spheroids over a 21-day culture period. LIVE/DEAD staining with calcein AM (viable cells, *green*) and propidium iodide (PI) (dead cells, *red*). Scale bar: 50 µm.



Supplemental Figure 10. Representative images of EdU staining in HepG2 spheroids released during culture in Matrigel and squaramide-based hydrogels. Proliferating cells were labelled with EdU-Alexa fluor 594 (*red*) and cell nuclei were stained with Hoechst 33342 (*blue*). Scale bar: 50 µm.



Supplemental Figure 11. 3D HepG2 cell culture in four different LOTs of Matrigel (LOT5215008, LOT2326787, LOT5061003 and LOT2104930: A) Brightfield images taken on day 7, 14 and 21. **B)** Fold change hepatic gene expression levels of HepG2 spheroids after a 21-day culture in Matrigel in comparison to 2D on tissue culture plates. (N = 3).



Supplemental Figure 12. Immunofluorescence staining of the liver markers albumin (upper row), MRP2 (middle row) and β-catenin (lower row) in green counter-stained with F-actin rhodamine phalloidin (red) and the nuclear staining Hoechst33342 (blue). Merged channels consist of all three stains. Scale bar: 100 µm.

Supplemental Tables

Supplemental Table 1. Summary of quantitative analyses (mean ± 95% confidence intervals).

	SQ	SQ-5RGD	SQ-10RGD	SQ-15RGD
Number of cells	100	76	78	74
Area (μm²)	183.0±7.3	296.3±23.1	266.5±19.0	261.6±18.6
Perimeter (μm)	50.8±1.3	72.7±3.9	77.3±4.9	72.6±5.0
Circularity	0.903±0.022	0.726±0.030	0.619±0.038	0.694±0.042
Skeleton branch length (μm)	5.2±1.2	20.3±3.3	22.4±3.3	20.00±3.6
Min Feret diameter (μm)	14.7±0.2	18.2±0.8	16.7±0.5	17.0±0.6
Max Feret diameter (μm)	17.6±0.4	24.6±1.1	26.9±1.59	24.1±1.4
Aspect ratio	0.844±0.01	0.750±0.02	0.662±0.028	0.741±0.026

Supplemental Table 2. Primer sequences.

Gene	Forward 5'- 3'	Reverse 5'- 3'
CYP3A4	TTCCTCCCTGAAAGATTCAGC	GTTGAAGAAGTCCTCCTAAGCT
CYP1A2	CTTTGACAAGAACAGTGTCCG	AGTGTCCAGCTCCTTCTGGAT
CYP3A5	CTCTCTGTTTCCAAAAGATACC	TGAAGATTATTGACTGGGCTG
CYP2D6	CCTACGCTTCCAAAAGGCTTT	AGAGAACAGGTCAGCCACCACT
CYP2C9	GAACACCAAGAATCGATGGACA	TCAGCAGGAGAAGGAGAGCATA
CYP2C19	CAACAACCCTCGGGACTTTA	GTCTCTGTCCCAGCTCCAAG
AAT1	ACTGGGGTGACCTTGGTTAAT	GACGGCATTGTCGATTCACTG
UGT1A1	CAGCAGAGGGGACATGAAAT	ACGCTGCAGGAAAGAATCAT
HNF4a	ACTACGGTGCCTCGAGCTGT	GGCACTGGTTCCTCTTGTCT
MRP2	GGCAGTGAAGAAGAAGACGATGA	ATTGGACCTAGAACTGCGGCT
NCTP	ATCGTCCTCAAATCCAAACG	CCACATTGATGGCAGAGAGA
Albumin	ATGCTGAGGCAAAGGATGTC	AGCAGCAGCACGACAGAGTA
GAPDH	CTGGTAAAGTGGATATTGTTGCCAT	TGGAATCATATTGGAACATGTAAACC

Supplemental Videos

Supplemental Video 1



Supplemental Video 2



Supplemental Video 3





CHAPTER 3

SYSTEMIC COMPARISON OF IN VITRO MODELS TO ASSESS INFLAMMATION-ASSOCIATED DRUG-INDUCED LIVER INJURY

Linda van den Berk[1,], Matthijs Vlasveld[1], Georgios Galaris[2], Geurt Stokman[2], Peter Bouwman[1], Bob van de Water[1]

[1] Division of Drug Discovery and Safety, Leiden Academic Centre for Drug Research (LACDR), Leiden University, Leiden, The Netherlands

[2] TNO Metabolic Health Research, Sylviusweg 71 2333 BE Leiden, The Netherlands

Keywords: Inflammation, TNF-α signalling, Drug-induced liver injury, Transcriptomics

Abstract

The liver is an immune tolerant organ, but upon exposure to liver toxicants, liver homeostasis can be disrupted, resulting in a pro-inflammatory environment. Subsequent release of pro-inflammatory cytokines, like TNF-α, has been linked to the liver toxicity of various drugs. Due to species differences in immune systems, inflammation-related hepatic drug toxicity is difficult to detect in animal models, stressing a need for test methods that integrate inflammatory signalling relevant for DILI. In this study, we systematically characterized five different human 2D and 3D in vitro liver test systems and their response to six cytokines: TNF-α, interleukin-1β, interleukin-6, interleukin-10, interleukin-12 and interleukin-18. hiPSC-derived hepatocyte-like cells (HLC) responded in a similar, but stronger fashion to TNF-α compared to gold standard primary human hepatocytes. In addition, HLC showed similar adverse stress responses when co-treated with known inflammatory DILI compounds, like diclofenac and trovafloxacin. Using ICAM1-EGFP reporter HLC we could mimic the DILI liability of NSAIDs in combination with TNF-α. Our results show the applicability of HLC in representing human liver hepatocyte inflammatory signalling responses related to DILI.

Introduction

The liver is an essential organ with multiple roles. One of the most important functions is xenobiotic metabolism via phase I, II and III metabolic enzymes. During this process, xenobiotics are chemically transformed from lipophilic molecules to hydrophilic products that can be excreted via urine and bile[134]. Due to the first pass effect and its high metabolic activity, the liver is also sensitive to adverse drug reactions. Drug-induced liver injury (DILI) occurrence is rare with an incidence of 14-19 cases per 100.000 individuals. However, despite the low incidence, DILI is the most common cause of acute liver failure with a fatality rate up to 50%[135–137].

Besides metabolism, the second main role of the liver is maintaining immunological balance. It is continuously exposed to antigens and endotoxins delivered by the portal and arterial vein and, therefore, immunotolerance is an important mechanism to prevent continuous strong immunological responses to harmless dietary and microbial molecules[138]. Resident macrophages in the liver, called Kupffer cells, are the main contributors to hepatic tolerance. These cells express pattern recognition receptors (PRRs) and bind damage and pathogen-associated molecular patterns (DAMPs and PAMPs respectively) which are phagocytosed and under normal conditions induce the production of anti-inflammatory cytokines, like IL-10 and prostaglandins. This leads to downregulation of co-stimulatory molecules on antigen presenting cells (APCs) and prevents activation of CD4+ T cells, thereby preventing an adaptive immune response[139].

In case of an acute infection or sterile inflammation induced by various drugs, Kupffer cells can quickly adopt a pro-inflammatory phenotype and produce pro-inflammatory cytokines and leukocyte attracting chemokines at the site of inflammation[140]. Although it can eliminate infections provoking an adaptive immune response, it can also contribute to the development of immune-mediated DILI. Microbial factors, e.g. lipopolysaccharide (LPS) or pro-inflammatory cytokines, especially TNF-α and IFN-γ, have been demonstrated to induce hepatic injury in several cases in combination with diclofenac, amiodarone, trovafloxacin, and sulindac treatment[141–144]. Investigating the role of inflammation in DILI is challenging due to the complexity in disease pathogenesis, poor understanding of underlying mechanisms and reliable model systems[145]. *In vivo* rodent models are of limited use, because human innate and adaptive immune signalling is not comparable to animal models leading to false negative and false positive hits. Several attempts have been made to perform *in vitro* testing using hepatocytes co-cultured with monocytes or macrophages. It has also been demonstrated that incubation of several drugs, including diclofenac and trovafloxacin, in the presence of TNF-α induces synergistic hepatocyte death. However, this has mainly been performed in hepatic cancer lines that may react

differently compared to benign human cells[146,147]. As primary human hepatocytes (PHH) are the gold standard for *in vitro* liver toxicity assays, it seems preferable to include these cells when testing how inflammation could affect DILI. However, the inter-individual variability in the response of PHH to TNF-α appears to be large[148149]. Especially PHH derived from patients with any type of liver disease lack the induction of TNF-α-induced NF-κB downstream targets and are hence not suitable for studying the role of innate immune reactions in DILI[148].

In this study, we systematically compared five different *in vitro* hepatocyte models including PHH, HepG2 liver cancer cells, differentiated HepG2 cells, hiPSC-derived hepatocyte like cells and liver microtissues consisting of primary human hepatocyte, Kupffer cells and stellate cells for their response to cytokines known to be secreted by Kupffer cells. For this purpose, we selected the Kupffer cell secreted pro-inflammatory cytokines TNF-α, IL-1β, IL-6, IL-12 and IL-18 and the anti-inflammatory cytokine IL-10. In addition, we investigated how the test models respond to trovafloxacin and diclofenac in combination with TNF-α compared to PHH and which molecular mechanisms were affected during these drug-cytokine exposures. Finally, we explored the applicability of an hiPSC ICAM1-EGFP reporter for the prediction of inflammation-associated NSAID-induced DILI in HLC.

Materials & Methods

Cytokines & reagents

Recombinant human tumor necrosis factor alpha (TNF-α) and interleukin-18 (IL-18) were acquired from R&D systems. All other cytokines and growth factors were purchased from Peprotech. NSAIDs were a kind gift from Specs (Delft, the Netherlands).

Cell culture

The hiPSC line iPSC epithelial-1 (IPSC0028, Sigma-Alderich derived from a 24-year-old Caucasian female and reprogrammed using OSKM retrovirus) containing a doxycycline-inducible cassette for the overexpression of the hepatic transcription factors PROX1, HNF1A and FOXA3 was cultured in feeder-free conditions on Matrigel-coated plates[150]. Cells were cultured in mTeSR1 (StemCell Technologies) at 37°C and 5.0% CO_2 and passaged twice a week using ReleSR (StemCell Technologies). The human hepatoma cell line HepG2 (ATCC, clone HB8065) was cultured as described by Wink et al. [151]. In brief, cells were cultured in DMEM high glucose (ThermoFisher) supplemented with 10% (v/v) FBS and 25 U/mL penicillin and 25 µg/mL streptomycin at 37°C and 5.0% CO2 and passaged every 3/4 days.

HepG2 culture in DMEM medium

18.000 cells were plated in 100 µL DMEM high glucose in 96 well SCREENSTAR plates (Greiner Bio-One). Cells were incubated for 48 hours prior to cytokine and/or drug exposure.

HepG2 culture in AAGLY medium

HepG2 cells were plated in a density of 50.000 cells/96well in 100 µL DMEM high glucose medium in SCREENSTAR plates. Cells were allowed to settle for 48 hours. Thereafter, medium was changed to AAGLY medium (DMEM low glucose supplemented with 7.7% (v/v) FBS, 20 U/mL penicillin and 20 µg/mL streptomycin, 160 µL/mL MEM non-essential amino acids (100x), 80 µL/mL MEM essential amino acids (50x) and 2% glycine, pH=7.2). HepG2 cells were matured for 30 days, and medium was refreshed twice a week.

Hepatocyte-like cell differentiation

hiPSCs were differentiated towards hepatocyte-like cells (HLC) as described previously[150]. In short, 9.000 cell/96well were seeded in 100 µL mTeSR1 supplemented with 1:100 RevitaCell (ThermoFisher) in 96 well SCREENSTAR plates. 24 hours post-seeding, mTeSR1 was refreshed. 48 hours after seeding, differentiation was started in liver differentiation medium (LDM) containing 0.6% DMSO until day 10. In addition, LDM was supplemented with Activin A (50 ng/mL), BMP4 (50 ng/mL), Wnt3a (50 ng/mL) or FGF1 (20 ng/mL). On day 10, medium was replaced by LDM supplemented with 160 µL/mL MEM non-essential amino acids (100x), 80 µL/mL MEM essential amino acids (50x) (LDM-AA), 2% DMSO and HGF (20 ng/mL). From day 12 onwards, cells were cultured in LDM-AA supplemented with 2% glycine (LDM-AAGLY) and 20 ng/mL HGF (Figure 1A). In addition, 5 µg/mL doxycycline (Sigma-Aldrich) was added to induce hepatic transcription factors. Medium was refreshed every other day, and cells were used for downstream assays on day 40 of differentiation.

Primary human hepatocyte culture

10-donor mixed gender cryopreserved primary human hepatocytes (PHH) were purchased from BIOIVT (X008001, lot KCB). PHH were thawed and transferred to pre-warmed OptiThaw (Tebu-Bio). Cells were spun down and resuspended in INVITROGRO CP Medium (BIOIVT) supplemented with 1:46 Torpedo antibiotic mix (BIOIVT). Cell viability was assessed and cells were plated at a density of 70.000 cells/96 well (100 µL/well) on BioCoat™ Collagen I Clear Plates (Corning). 6 hours post plating; medium was switched to InVitroGRO HI Medium in addition of 1:46 Torpedo antibiotic mix. Cells were used for functional assays 24 hours after plating.

Liver microtissues

Passage 3 male human stellate cells (BIOIVT, S00354, lot PFP) were thawed in SteCM culture medium (ScienCell) 7 days before seeding microtissues in overnight poly-L-Lysine (2 µg/mL) coated T75 culture flasks. To prepare molds, sterile stamps were placed in 6 well plates filled with sterile 70°C ultra-pure 2% agarose (ThermoFisher) and left to solidify at room temperature for 10 minutes. Solidified stamps were transferred to 24 well plates and incubated overnight with HBM medium (Lonza) until use. Liver microtissues were generated by thawing cryopreserved 10-donor mixed gender primary human hepatocytes (X008001, lot KCB) and male human Kupffer cells (BIOIVT, S00352, lot HGP) and dissociation of the stellate cells using Accutase. Hepatocytes, stellate cells and Kupffer cells were mixed in a ratio of 70:15:15% and 96.000 cells were plated per 24 well (1000 cells/microwell) in HBM supplemented with recombinant human EGF, hydrocortisone, gentamycin/amphotericin (all 1:1000 from HCM aliquots, Lonza), 5.5 µg/mL transferrin (Sigma-Aldrich), 5% FBS, 25 µM L-ascorbic acid, 25 mM HEPES, 4 mg/mL fatty acid free BSA (Sigma-Aldrich) and 1.7 nM insulin (Sigma-Aldrich). Replace medium 48 hours post seeding with Williams E medium (ThermoFisher, A1217601), 1% glutamax, 1% gentamycin/amphotericin, 5.5 µg/mL transferrin, 6.7 ng/mL sodium selenite (Sigma, S5261) 4 mg/mL fatty acid free BSA. On day 5 after seeding, liver microtissues were used for downstream assays.

Cytokine exposures

Cytokines were diluted to 2x the test concentration (200 ng/mL to ensure maximal receptor activation). Medium was removed from the wells, and half the final volume of fresh medium was added. Subsequently, two times concentrated cytokine exposure medium (or vehicle control) was added to each well. Cells were incubated for 24 hours in a humidified incubator (37°C and 5.0% CO2).

CYP3A4 activity assay

CYP3A4 activity was measured using the P450-Glo CYP3A4 assay (Promega) according to the manufacturer's instructions. Activity was thereafter normalized to viable cell number with a CellTiter-Glo® Luminescent Cell Viability Assay (Promega). Luminescence for both assays was measured using the Envision plate reader. CYP3A4 activity and cell viability was measured in three biological replicates for each hepatocyte model.

Diclofenac and trovafloxacin/TNF-α treatment and viability

All in vitro hepatocyte systems were cultured as previously described. Thereafter, cells were exposed to six concentrations diclofenac (Cmax=10.1 µM) or trovafloxacin (Sigma-Aldrich) (Cmax=4.3 µM)[152] at a concentration of 1-100x Cmax. 200 ng/mL TNF-

α or vehicle was added manually to each well 8 hours after compound exposure. Cell viability was assessed 24 hours after compound exposure by LDH release in the supernatant using an LDH cytotoxicity detection kit (Roche). As a positive control, supernatant from cells incubated for 5 minutes with 2% Triton X-100 were taken along. Supernatant was stored for a maximum of 2 days at 4°C. Before the assay, samples were diluted 10x in 1x PBS except for the liver microtissues, these were run undiluted. Samples were assayed in technical duplicate and in three biological replicates. Absorbance was measured using the Perkin Elmer Envision plate reader.

Transcriptomic analysis (TempO-Seq)

Cells were washed twice with 1x PBS and subsequently lysed in 1X TempO-Seq lysis buffer (for 2D cultures) or 1X TempO-Seq Enhanced lysis buffer (liver microtissues). Samples were incubated for 15 minutes at room temperature or 37°C respectively, followed by storage at -80 °C. Samples were shipped to and analysed at BioClavis LTD. Raw counts were normalized using an in-house generated script using DESeq2 and CPM normalization with an input count threshold of 1e6, followed by a log2 fold change normalization[153]. Genes were considered differentially expressed if the false discovery adjusted p-value ≤0.05.

Compound exposure

hiPSC-derived hepatocyte-like cells generated using the Sigma-HC3X-ICAM1-eGFP line were exposed NSAIDs (Supplemental table 1) in a broad concentration range in the presence or absence of TNF-α. In short on day 40, medium was removed manually and half the final volume fresh LDM-AAGLY supplemented with 100 nM propidium iodide (PI) was added to each well followed by 2x the final concentration of each compound dilution. Eight hours post compound exposure, 50 ng/mL TNF-α or vehicle control was added to each well using a Biomek automated workstation for 40 hours. To visualize nuclei, 100 ng/mL $Hoechst_{33342}$ was added during the final 2 hours of the TNF-α challenge. Cells were imaged 48 hours post NSAID exposure on a Nikon Eclipse Ti2 LIPSI microscope equipped with a 408, 488, 561 and 633 nm laser for ICAM1-EGFP expression and cell death induction. All compound stock solutions were generated in DMSO at a 500-fold the highest compound concentration such that the final DMSO concentration would not succeed 0.2%.

Quantitative Image analysis

Confocal imaging analysis was performed using CellProfiler 4.2.1 (Broad Institute, Cambridge, USA). Nuclei segmentation was based on Hoechst and performed in ImageJ using an in-house developed macro based on the watershed masked clustering algorithm as described previously[154]. A LOESS regression analysis was applied on a

TNF-α concentration-response curve to determine thresholds for ICAM1-eGFP up- and down regulation. The threshold was calculated at the level where TNF-$\alpha_{standard}$ + 95%CI ≤ TNF-$\alpha_{concentration}$ – 95%CI.

Statistical analysis

Statistical analyses were performed using GraphPad Prism version 10 software. The Shapiro-Wilk test was used to assess normality of the data. For normally distributed data, statistical significance was analysed using an ordinary one-way analysis of variance (ANOVA) followed by a Tukey's multiple comparison test. P-values <0.05 were considered statistically significant. Levels of significance are indicated as follows: *p<0.05, ** p<0.01, *** p<0.001, ****p<0.0001.

Results

Characterization of liver models

In order to assess liver specific characteristics of in vitro liver models, we assessed their gene expression profiles using targeted RNA sequencing. All five liver models analysed were cultured as previously described. We included a 10-donor pool of primary human hepatocytes (PHH) either as a monolayer or as a liver microtissue spheroid also integrating Kupffer cells and stellate cells. HepG2 hepatoblastoma cells have limited metabolic capacity when cultured in standard DMEM culture medium[155]. Boon et al. described that HepG2 liver metabolism can be enhanced in amino acid rich medium (AAGLY), which led to decreased proliferation and enhanced differentiation capacity[150]. In addition, the morphology of these cells became more comparable to PHH in AAGLY medium. Therefore, we included HepG2 cells cultured in AAGLY medium as differentiated HepG2 in our test panel in comparison with standard HepG2 cultures. Finally, we included hiPSC-derived hepatocyte-like cells (HLC) that were generated through a stepwise protocol following liver embryonic development through the primitive streak and definitive endoderm (Activin A and Wnt3a), hepatic and anterior endoderm (BMP4), liver bud growth (FGF1) and finally HGF for the formation of hepatoblasts and ultimately hepatocyte-like cells. To enhance hepatocyte differentiation, we made use of doxycycline-inducible expression of three hepatocyte transcription factors, namely PROX1, HNF1A and FOXA3 from day 4 of differentiation onwards[150]. (Figure 1A). To gain insight in the shared and unique characteristics of these different liver in vitro test systems, TempO-Seq targeted RNA sequencing was performed. Transcriptomic profiles of the different liver models in basal conditions were assessed by principal component analysis (PCA) (Figure 1B). PHH, HLC, and liver microtissues were relatively similar for PC1, while both HepG2 culture types clustered further apart. PC2 showed mainly differences between PHH, liver microtissues and HLCs, and similarities between PHH and both HepG2 culture types. A spearman correlation plot showed that overall gene expression values correlated fairly well between the different models (Figure 1C). Subsequently, we evaluated liver specific gene expression profiles (Figure 1D). As expected, PHH and liver microtissues showed the highest expression of liver specific genes. HepG2 cells cultured in DMEM medium show lower expression of liver specific genes, especially genes related to phase I and II metabolism. Most of these metabolism genes are expressed at higher levels in HepG2 AAGLY and HLC cells, which showed similar expression of liver specific genes. We further assessed the expression and activity of CYP3A4, a major cytochrome P450 enzyme responsible for metabolizing half of the commonly prescribed drugs. The mRNA expression of CYP3A4 in HepG2 AAGLY and HLC was comparable to PHH levels and significantly higher compared to liver microtissues and DMEM cultured HepG2

cells. However, the actual CYP3A4 activity as measured by the P450 GLO assay was significantly lower in both HepG2 culture types and HLCs compared to liver microtissues and PHH. (Figure 1E).

Response to interleukins is variable across in vitro test systems

Upon LPS challenge, Kupffer cells secrete the anti-inflammatory cytokine IL-10 to regulate the local immune response[156]. Therefore, we tested whether this cytokine directly affects hepatocytes. 24 hours post IL-10 exposure, no differential expressed genes (DEGs) could be observed, likely due to the lack of IL-10 receptor α expression in all hepatocyte models (supplemental Figure 1). In addition, activated Kupffer cells secrete the pro-inflammatory cytokines IL-12 and IL-18 during DILI[157,158]. However, as for IL-10, these cytokines did not have direct effects on hepatocytes as shown by the lack in DEGs, which is in line with the absence of co-expressed IL-12 or IL-18 receptor subunits on hepatocytes (Supplemental Figure 1). Thus, IL-10, IL-12 and IL-18 secreted by Kupffer cells likely do not regulate liver inflammation through hepatocytes, but through different mechanisms and cell types.

Classical IL-6 signalling is associated with the induction of the acute phase response in hepatocytes. In addition, trans signalling is a known mediator of liver regeneration upon injury[159]. Therefore, we also monitored the effect of IL-6 on the five different liver models. Unexpectedly, primary human hepatocytes were the only model responsive to 24 hours IL-6 treatment as shown by the number of DEGs (Supplemental Figure 2A). This distinct behaviour can also be captured by PC analysis: PHH did behave similarly on PC1 compared to HLC and liver microtissues, but differently on PC2. In addition, both HepG2 models behave differently, both on PC1 and PC2 (Supplemental Figure 2B). In contrast, IL-6 downstream targets that are linked to the transcription factor STAT3 and IRF1 according to transcription factor-target interactions using the DoRothEA database[160] (confidence scores A-C) showed a trend in upregulation of those genes upon IL-6 treatment (Supplemental Figure 2C). Unfortunately, the absence in DEGs prevented detailed KEGG pathway analysis in HLCs and liver microtissues (Supplemental Figure 2D). Weighted correlation network analysis (WGCNA) provided more detail in module upregulation that are linked to the transcription factors STAT3 and IRF1. Associated gene modules were partly upregulated in all liver models. Interestingly, modules upregulated in liver microtissues differ substantially from the other four liver test systems (Supplemental Figure 2E). We further investigated the behaviour of individual genes within module 44. We explicitly chose this module as it is being upregulated in PHH and moderately preserved enabling translation of data between biological systems[161].

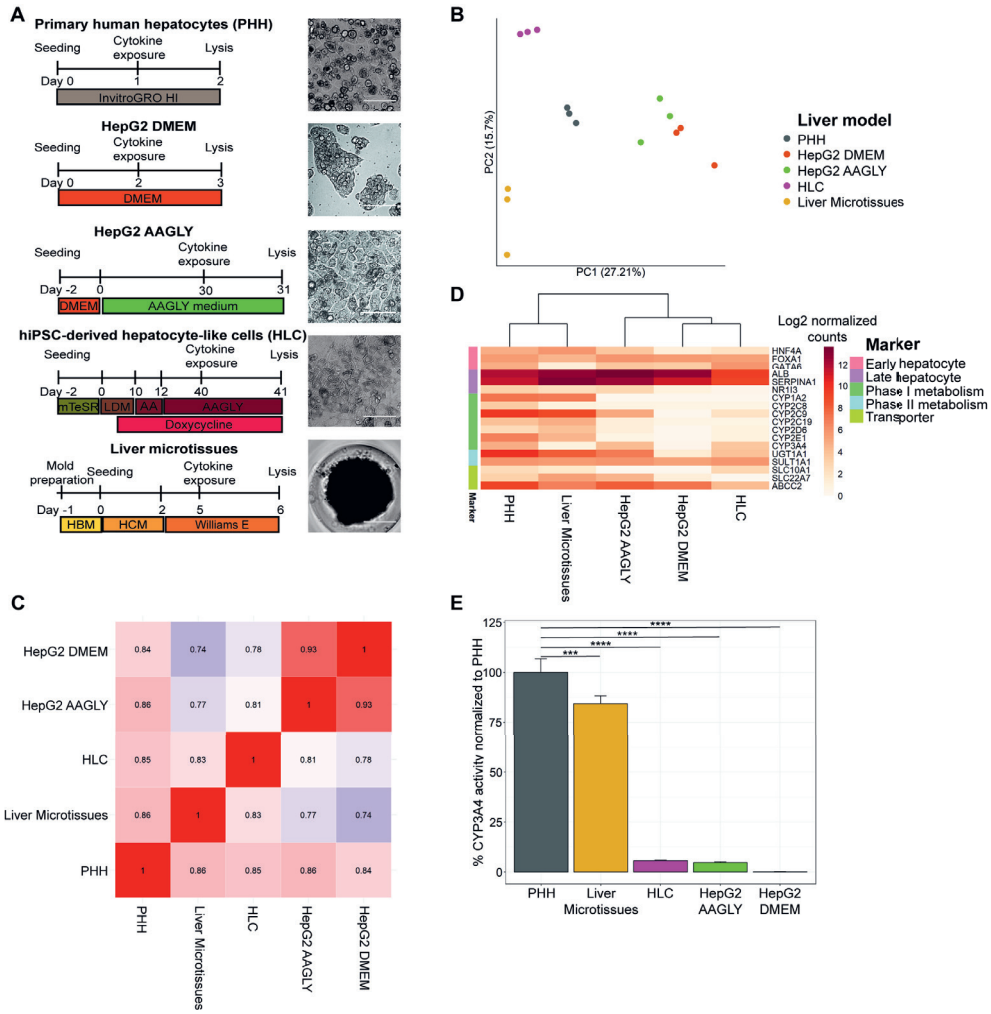
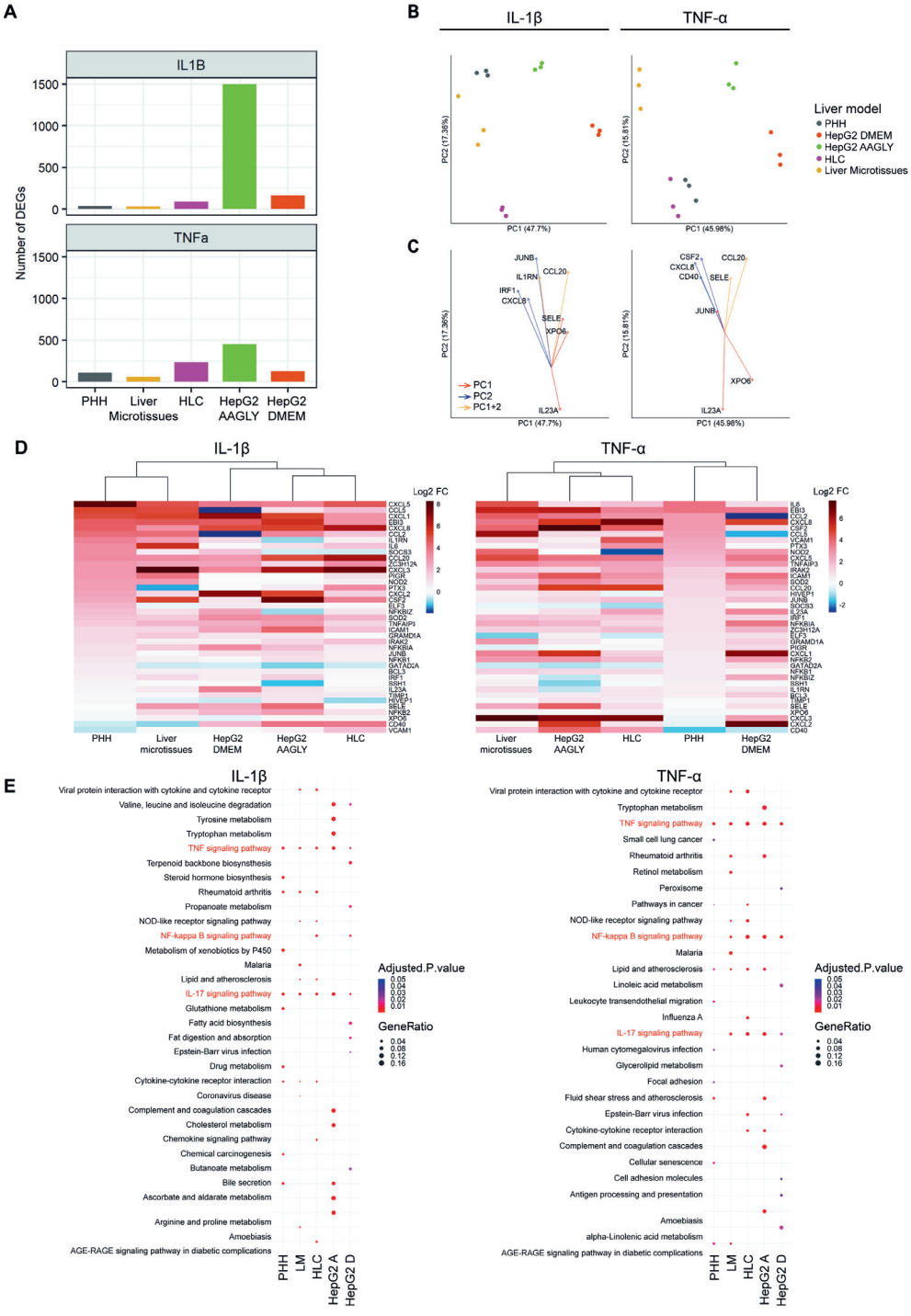


Figure 1. Characterization of liver models. A) Overview of the cell culture protocol of the various liver models with brightfield images at the end of the culture process. **B)** Principal component analysis (PCA) of the various models in basal conditions using Log2 normalized counts. **C)** Spearman correlation matrix on Log2 normalized expression in the different cell models. **D)** Heatmap on Log2 normalized counts of hepatocyte markers. **E)** CYP3A4 activity measured using the P450-Glo kit in the various *in vitro* models. A Shapiro-Wilk test was used to test for normality of the data followed by a one-way ANOVA. ***≤ 0.001, **** ≤0.0001 N=3.

Further investigation of the STAT-associated module 44 showed weak induction of the individual genes within this module for liver microtissues and HLC, while individual genes were being upregulated in both HepG2 system, although less compared to PHH. (Supplemental Figure 2F). To summarize, PHH was the only liver test method that showed a robust transcriptional response to IL-6 treatment.

IL-1β and TNF-α induce downstream signalling in all liver systems

Once Kupffer cells sense damaged cells or pathogens via toll-like receptors (TLRs), the inflammasome will be activated leading to caspase 1-mediated cleavage and maturation of IL-1β. Ultimately, this will result in IL-1β secretion and activation of nearby hepatocytes[162]. Another cytokine released by Kupffer cells under pro-inflammatory conditions is the pleiotropic cytokine TNF-α, which can either have a protective or damaging effect on hepatocytes[163]. We tested the response to those cytokines in all five different liver models (Figure 2). HepG2 cells matured in AAGLY medium were most responsive to IL-1β, followed by DMEM-cultured HepG2 cells. The number of DEGs after TNF-α treatment was limited in PHH, HepG2 cells in DMEM and liver microtissues, but HepG2 cells in AAGLY medium and HLCs were more responsive to TNF-α (Figure 2A). Principle component analysis on DoRothEA identified canonical NF-κB signalling (NFKB1, RELA, and c-REL) downstream targets showed that all test systems responded in a different manner to IL-1β. PHH, liver microtissues and HLC behave similarly on PC1, but HLC were far apart on PC2 (Figure 2B and 2C). A more detailed analysis of Log2 fold change expression of the downstream targets showed that chemokines were upregulated in a similar fashion except for *CCL2* and *CCL5* in HepG2 cells in regular DMEM medium (Figure 2D). PC analysis on NF-κB specific downstream target genes after TNF-α treatment showed clustering of PHH and HLCs on both PC1 and PC2. HepG2 AAGLY cells and liver microtissues displayed a similar shift on PC2 mainly driven by the well-known inflammatory markers *CXCL8*, *CD40* and *CSF2* (Figure 2B and 2C). Although PC analysis showed similarity between PHH and HLC, log2 fold change induction of the NF-κB downstream targets were limited in PHH, while in HLC there was a clear induction upon TNF-α exposure (Figure 2D). This induction was in line with increased expression in liver microtissues and HepG2 AAGLY cells. The limited induction in PHH could be partially explained by the relatively high baseline expression of the NF-κB downstream targets as shown for *CCL2*, *CXCL8*, *TNFAIP3*, and *ICAM1* (Supplemental Figure 3). We subsequently evaluated if upregulated pathways and processes after IL-1β and TNF-α were linked to inflammation. For IL-1β, upregulated pathways were indeed linked to inflammatory pathways and processes, but in the case of HepG2 AAGLY cells also related to amino acid metabolism (Figure 2E). The top ten significantly upregulated KEGG pathways in all the model systems post TNF-α included, as expected, the TNF pathway and various processes related to infections with for instance influenza A, malaria and Eppstein Bar virus. Interestingly, the NF-κB signalling pathway was not one of the ten most upregulated pathways in PHH (Figure 2E).


A
IL1B
TNFa
Number of DEGs
PHH
Liver Microtissues
HLC
HepG2 AAGLY
HepG2 DMEM
B
IL-1β
TNF-α
Liver model
PHH
HepG2 DMEM
HepG2 AAGLY
HLC
Liver Microtissues
C
PC1
PC2
PC1+2
D
IL-1β
TNF-α
Log2 FC
E
IL-1β
TNF-α
Adjusted.P.value
GeneRatio

◀ **Figure 2. Effect of IL-1β and TNF-α on the transcriptomic space and NF-κB signalling in various hepatocyte models. A)** Number of Differential Expressed Genes (DEGs) 24 hours post IL-1β or TNF-α exposure in all test models. **B)** PCA plot on Log2 normalized counts of NF-κB downstream targets identified by Dorothea after IL-1β and TNF-α exposure. **C)** Loading plot representing the top 5 determining genes in PC1 (orange) and PC2 (blue) or both (yellow) upon IL1-β and TNF-α. **D)** Hierarchical clustering of the Log2 fold change of NF-κB target genes in response to IL-1β and TNF-α. **E)** Dot plot showing top 10 KEGG2021 human pathways upregulated upon IL-1β and TNF-α exposure.

WGCNA analysis in the various models post IL-1β and TNF-α

To further investigate gene and process regulation, we used WGCNA-based TXG-MAPr analysis[161] to confirm the activation and repression of various gene network modules related to NF-κB, IL-1β and TNF-α signalling. We first assessed module activation and repression after IL-1β and TNF-α exposure using the complete TXG-MAPr. IL-1β and TNF-α exposure resulted in both an increase and decrease in module expression across the entire TXG-MAPr, which could not be observed for the other models except for HepG2 cultured in AAGLY after IL-1β treatment and to a smaller extend post TNF-α treatment. Module activation after IL-1β and TNF-α treatment appeared more specific to inflammation-related modules in PHH, HLC and HepG2 cells cultured in DMEM (Figure 3A). More in detail, analysis on the EGS behaviour of the inflammatory modules that have been linked to canonical NF-κB transcription factors (Supplemental Table 2) revealed that HLC showed the highest correlation to the gold standard PHH in toxicology research after IL1-β and TNF-α exposure (Figure 3B). More profound analysis of the individual modules itself showed the highest level of changes in inflammation-associated modules for HepG2 cells cultured in AAGLY medium and liver microtissues, while the other systems responded largely in a similar fashion (Figure 3C). This could also be observed by the induction of individual genes within preserved module 242, which is strongly related to immune responses and NF-κB downstream targets (Figure 3C). Taken together, the different models showed a universal response to IL-1β, although IL-1β responses were somewhat higher in HepG2 AAGLY cultured cells and liver microtissues.

In a similar fashion, we assessed the behaviour of those specific modules post TNF-α. Hierarchical clustering revealed that PHH were most similar to HLC, whereas HepG2 cells in DMEM and AAGLY and liver microtissues showed a dissimilar module activation and reduction upon TNF-α treatment. In liver microtissues especially, modules were upregulated more extensively, likely due to their multicellular complexity (Figure 3C). Further investigation of the inflammation-associated module 242 confirmed that PHH least responsive to TNF-α, whereas HepG2 cells in DMEM and AAGLY, HLC and liver microtissues showed an increased downstream target

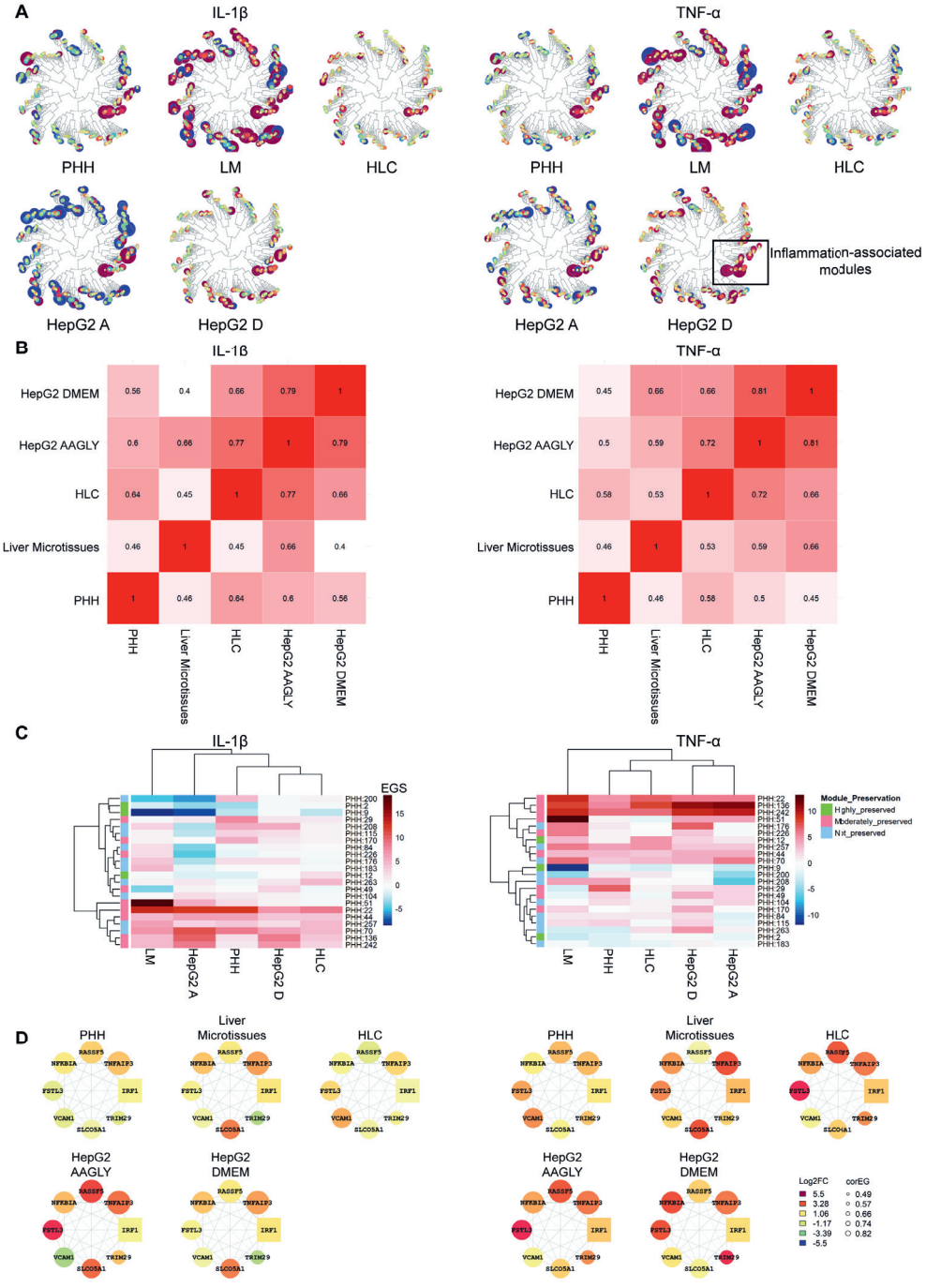
expression post TNF-α exposure (Figure 3D). Collectively, we found model-specific differences in TNF-α response. Therefore, we suggest that a representative model to study the effects of TNF-α signalling on DILI should be selected carefully.

TNF-α enhances diclofenac and trovafloxacin-induced cell death in liver test systems

As TNF-α is known to induce synergistic liver injury response in combination with several DILI drugs[164,165], we assessed how the different test systems respond to a combination treatment of the liver toxicants diclofenac and trovafloxacin with TNF-α. All models were cultured as described in Figure 1B and pre-treated with increasing concentrations of the respective compounds for 8 hours followed by TNF-α/vehicle exposure for an additional 16 hours. 24 hours post compound exposure, LDH release was measured as an indicator for cytotoxicity (Figure 4A). First, we tested the effect of TNF-α on exposure to the non-steroidal anti-inflammatory drug diclofenac. We observed a concentration-dependent increase in LDH release in HepG2 cells cultured in DMEM or AAGLY and HLC. After TNF-α addition, a synergistic and additive effect could be observed for HepG2 cells in DMEM and AAGLY respectively, but not for HLC. On the other hand, PHH and liver microtissues showed limited LDH release upon diclofenac exposure, both with and without TNF-α treatment (Figure 4B). Trovafloxacin alone did induce cytotoxicity in a concentration-dependent manner in both HepG2 models, but not in PHH, HLC and liver microtissues. Similar to diclofenac, TNF-α only induced a synergistic effect in both HepG2 cells cultured in DMEM and AAGLY (Figure 4C).

HLC and HepG2 cultured in AAGLY respond transcriptionally most like PHH upon diclofenac and trovafloxacin treatment in a pro-inflammatory environment

Next, we assessed the effect of an inflammatory environment, mimicked by TNF-α exposure, on the transcriptional response to diclofenac or trovafloxacin treatment. A concentration-dependent increase in DEGs could be observed after diclofenac treatment in all liver models except the liver microtissues (Figure 5A). TNF-α addition increased the number of DEGs in HepG2 cells cultured in DMEM medium compared to the diclofenac treatment alone, but this was not observed in the other liver models. To identify any changes in the transcriptomic profiles upon diclofenac with TNF-α treatment, we performed PC analysis on the various liver models. More specifically, we focused on TXG-MAPr modules related to TNF-α-induced inflammation (see Figure 3C) and intentionally focused on a lower diclofenac concentration (25* Cmax) to prevent taking along cell death effects (Figure 5B).


A
IL-1β
TNF-α
PHH
LM
HLC
PHH
LM
HLC
HepG2 A
HepG2 D
HepG2 A
HepG2 D
Inflammation-associated modules
B
IL-1β
TNF-α
HepG2 DMEM
HepG2 AAGLY
HLC
Liver Microtissues
PHH
C
IL-1β
TNF-α
EGS
Module_Preservation
Highly_preserved
Moderately_preserved
Not_preserved
D
PHH
Liver Microtissues
HLC
HepG2 AAGLY
HepG2 DMEM
Log2FC
corEG

◀ **Figure 3. Induced inflammatory processes and weighted correlation gene network analysis upon IL-1β and TNF-α. A)** TXG-MAPr representing module activity after IL-1β or TNF-α treatment in the different test models **B)** Spearman correlation matrix on inflammatory module activity in the different cell models upon IL-1β or TNF-α treatment. **C)** Hierarchical clustering of Eigengene scores from individual models associated with IL-1β/TNF-α-induced inflammation after weighted correlation gene network analysis (WGCNA). **C)** Gene network of module 22. Colours indicate Log2 fold change compared to vehicle. *IRF1* in the square indicates the hub gene of module 242. The size of the circle or square relates to the correlation of the Eigengene score of that gene with the module Eigengene score.

Especially liver microtissues were responsible for the shift on PC1 (37.75%). HLC and PHH behaved similarly after diclofenac and TNF-α addition on PC2 (33.28%) compared to the other tests systems as could be explained by variation in EGS for the modules 9, 115, and 200. We further assessed the behaviour of four selected inflammatory modules upon diclofenac treatment with and without TNF-α in the various liver models (Figure 5C). Overall, transcriptomic responses were higher in liver microtissues and HepG2 cells cultured in both media compared to PHH and HLC for module 136 and 242. Module EGS in HLC were decreasing when cells were exposed to higher concentrations of diclofenac and could be explained by the higher sensitivity of these as shown by the high LDH release observed previously (Figure 4B). We further assessed gene expression of canonical NF-κB target genes itself and could observe that liver microtissues responded stronger compared to the other test systems Figure 5D). HepG2 cells cultured in AAGLY showed a similar pattern in module activation, whereas the other models responded dissimilar. Interestingly, the chemokines *CXCL1* and *CXCL2* were exclusively induced in HepG2 liver models while its expression was not altered in the other systems. PHH and HLC showed similar fold change inductions upon treatment, but we could observe again that HLCs are more sensitive to diclofenac as can be shown by the decreased FC expression when higher concentrations of diclofenac were used. As diclofenac affects diverse cellular responses including ER stress/UPR pathway and oxidative stress pathway activation, we also assessed activation of these stress responses using the TXG-MAPr module activity analysis (Figure 5C). For ER stress/UPR pathway activation, only HepG2 cells cultured in AAGLY and to a certain extend HLC showed similar responses. However, on single-gene level, we observed a similar trend in upregulation of ER stress between HLC and PHH (*DDIT3*, *HSPA5*, *HERPUD1*). For oxidative stress-related modules and single genes (*SRXN1* and *MAFG*), a similar behaviour could be observed between PHH, HLC and HepG2 AAGLY cells (Figure 5D). In a similar fashion, we investigated the effect of TNF-α on trovafloxacin treatment. The number of DEGs post treatment varied per liver model, but the number of DEGs appeared to be similar at 25* and 50* Cmax for all models except for liver microtissues (Supplemental figure 4A).



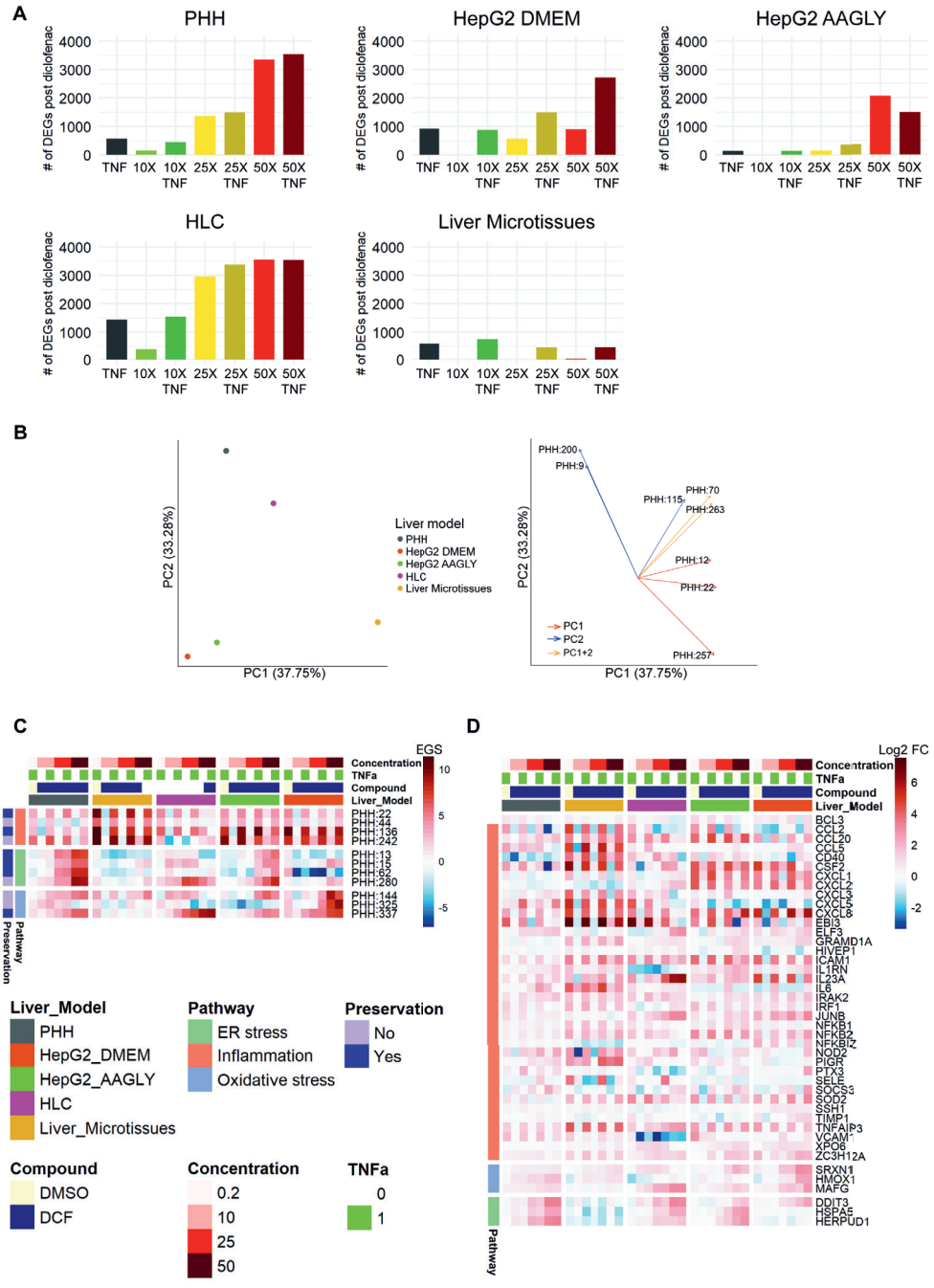
Figure 4. TNF-α enhances diclofenac and trovafloxacin-mediated cell death in HepG2, but not in other liver models. A) Overview of the cell culture and exposure setup. **B)** Bar plot showing LDH release as a measure for cell death after diclofenac or **C)** trovafloxacin with or without TNF-α in all liver models 24 hours post compound exposure.

After 25* Cmax trovafloxacin + TNF-α exposure, most of the liver models were not clustering together. HLC and HepG2 showed similar responses on PC1 (41.64%), but HLC and HepG2 AAGLY were separated from HepG2 cells cultured in DMEM on PC2 (34.25%). Both models behaved similarly however to PHH and liver microtissues on PC2 (Supplemental figure 4B). Again, we assessed module activity upon exposure to trovafloxacin +/- TNF-α. Similar responses could be observed, however a stronger induction in inflammatory modules were found again for liver microtissues. In addition, HLC treated with the highest concentration trovafloxacin induced slight activity of module 22 and 242 (Supplemental figure 4C). Single gene analysis again showed a higher response to TNF-α in liver microtissues and chemokine upregulation in both HepG2 models. Interestingly, NFKB2 was downregulated by trovafloxacin in all test systems while this was not observed after diclofenac + TNF-α incubation. Log2 FC induction of NF-κB downstream targets appeared to be similar between HLC and PHH, except for *ICAM1* and *SELE* (Supplemental figure 4D). As trovafloxacin enhances mitochondrial stress and induces the DNA damage response, modules and single

genes associated with those types of stress were analysed in more detail[166,167]. All liver systems showed a similar pattern upon trovafloxacin treatment except for the mitochondrial response in liver microtissues. In addition, HepG2 cells in DMEM showed a stronger response to trovafloxacin as shown for DNA damage-associated module 243, and the genes *BTG2* and *GADD45A* and might be explained by the proliferative nature of this hepatocyte model (Supplemental figure 4C and D).

The NSAIDs diclofenac and sulindac alter ICAM1-eGFP expression in HLC post compounds/TNF-α exposure

Non-steroidal inflammatory drugs (NSAIDs) prescribed to treat pain, fever and other inflammatory processes are among the most frequent causes of DILI [168]. Especially naproxen, nimesulide, diclofenac and sulindac are well known to contribute to hepatotoxicity[168,169]. The TNF-α signalling pathway is one of the stress response pathways thought to be disturbed by NSAIDs, either directly or indirectly, which leads to altered expression of downstream NF-κB downstream target genes, such as TNFAIP3 and ICAM1. As HLC are benign cells that behave fairly similar to PHH upon diclofenac and trovafloxacin exposure, but have a stronger response to TNF-α, we used an iPSC ICAM1-eGFP reporter line to analyse NSAID-induced alterations in ICAM1 expression in HLC in the presence or absence of TNF-α. Upon 8 hours NSAID pre-treatment to enable generation of metabolites, ICAM1-eGFP HLC were incubated with 50 ng/mL TNF-α or vehicle and used live cell microscopy to monitor ICAM1-eGFP expression for 40 hours (Figure 6A, Supplemental table 1). To analyse alterations in ICAM1-eGFP expression upon NSAID exposure, we used a LOESS curve on normalized ICAM1-eGFP intensity across a TNF-α concentration range. Intensities above the green line indicate significant increased ICAM1-eGFP expression, within the blue and orange line a decrease in ICAM1-eGFP expression and a block in ICAM1-eGFP expression below the orange line (Figure 6B). Ketorolac and methimazole, which are both not associated with causing DILI, did not induce alterations in ICAM1-eGFP in HLC upon treatment in combination with TNF-α. Naproxen and sulindac increased ICAM1-eGFP expression. On the other hand, diclofenac did inhibit ICAM1-eGFP expression (Figure 6C and D). These data suggest that ICAM1-eGFP reporter HLC can be used to uncover the DILI liability of candidate drugs.


A
PHH
HepG2 DMEM
HepG2 AAGLY
HLC
Liver Microtissues
of DEGs post diclofenac
TNF 10X TNF 10X TNF 25X TNF 25X TNF 50X TNF 50X TNF
B
PC2 (33.28%)
PC1 (37.75%)
Liver model
PHH
HepG2 DMEM
HepG2 AAGLY
HLC
Liver Microtissues
PHH:200
PHH:9
PHH:115
PHH:70
PHH:263
PHH:12
PHH:22
PHH:257
PC1
PC2
PC1+2
C
EGS
Concentration
TNFa
Compound
Liver_Model
Pathway
Preservation
Liver_Model
PHH
HepG2_DMEM
HepG2_AAGLY
HLC
Liver_Microtissues
Pathway
ER stress
Inflammation
Oxidative stress
Preservation
No
Yes
Compound
DMSO
DCF
Concentration
0.2
10
25
50
TNFa
0
1
D
Log2 FC
Concentration
TNFa
Compound
Liver_Model
Pathway
BCL3
CCL2
CCL20
CCL5
CD40
CSF2
CXCL1
CXCL2
CXCL3
CXCL5
CXCL8
EBI3
ELF3
GRAMD1A
HIVEP1
ICAM1
IL1RN
IL23A
IL6
IRAK2
IRF1
JUNB
NFKB1
NFKB2
NFKBIZ
NOD2
PIGR
PTX3
SELE
SOCS3
SOD2
SSH1
TIMP1
TNFAIP3
VCAM1
XPO6
ZC3H12A
SRXN1
HMOX1
MAFG
DDIT3
HSPA5
HERPUD1

◀ **Figure 5. Effect of diclofenac +/- TNF-α on transcriptomic space in all liver models. A)** Number of DEGs after vehicle/diclofenac exposure in presence or absence of TNF-α. **B)** PC analysis on WGCNA-derived module EGS related to inflammation after exposure to 25* Cmax diclofenac with TNF-α in all five liver models. **C)** Hierarchical clustering of Eigengene scores from individual modules associated with inflammation, ER-stress and oxidative stress after diclofenac treatment with or without TNF-α challenge. **D)** Heatmap of selected targets of NF-κB-mediated inflammation, ER stress and oxidative stress upon exposure to diclofenac +/- TNF-α.

Discussion

In this study, we systematically compared five different human in vitro liver test systems with respect to their response to cytokines that are secreted by Kupffer cells upon inflammation[170]. We identified that responses to TNF-α, a pleiotropic cytokine associated with DILI, is liver test system dependent. HLC showed a similar, but stronger response to TNF-α compared to PHH. We found that HLC transcriptomic responses to diclofenac and trovafloxacin in combination with TNF-α are comparable to PHH. Therefore, we performed a proof-of-concept study in HLC to test the effect of various NSAIDs co-treated with TNF-α on TNF-α signalling modulation using an ICAM1-eGFP fluorescent reporter. We found that ICAM1-eGFP HLC can differentiate the effects of NSAIDs with respect to inflammatory signalling modulation. We envision that HLC are a good representative model to pre-clinically test the effect of novel drug candidates on TNF-α signalling which may contribute to adverse drug reactions.

To assess immune-related DILI, it is essential to use an immune responsive liver model. Previous research has shown that PHH are variable in their immune responsiveness due to underlying diseases of the donors, like non-alcoholic fatty liver disease and steatohepatitis, and liver cancer and/or the hepatocyte isolation process itself[171–173]. Therefore, we analysed five different in vitro hepatocyte models, including PHH, HLC, liver microtissues, HepG2 cells in original medium and in an optimized medium, for their responses to stimulation with the cytokines TNF-α, IL-1β, IL-6, IL-12, IL-18, and IL-10. The cytokines have particularly been chosen due to their abundant release upon Kupffer cell stimulation[174]. We identified that IL-6, IL-10, IL12 and IL-18 do not exhibit strong direct effects on inflammatory signalling in our hepatocyte systems. However, all our liver models were responsive to IL-1β and TNF-α. Based on in depth transcriptomic analysis post IL-1β treatment, we identified that HepG2 cells, PHH or HLC are proper in vitro models to study IL-1β signalling. As TNF-α has been shown to be required for liver injury to develop in combination with various drugs, our most in depth analysis focused on this cytokine[144,164,165]. In this paper, we show that responses to TNF-α are largely similar in PHH and HLC based on downstream target and TNF-α module activation.

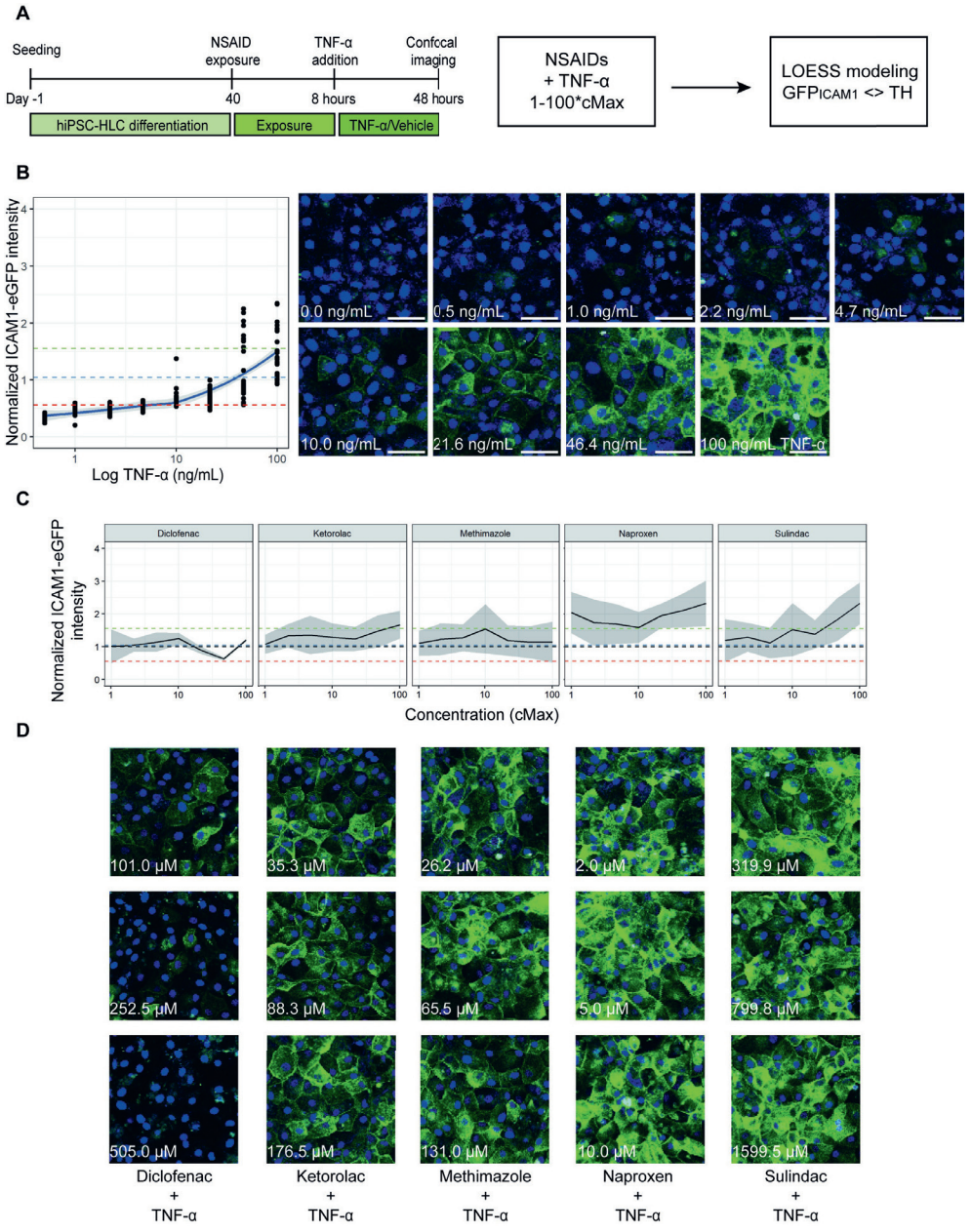

A
Seeding
NSAID exposure
TNF-α addition
Confocal imaging
Day -1
40
8 hours
48 hours
hiPSC-HLC differentiation
Exposure
TNF-α/Vehicle
NSAIDs + TNF-α 1-100*cMax
LOESS modeling GFPICAM1 <> TH
B
Normalized ICAM1-eGFP intensity
Log TNF-α (ng/mL)
0.0 ng/mL
0.5 ng/mL
1.0 ng/mL
2.2 ng/mL
4.7 ng/mL
10.0 ng/mL
21.6 ng/mL
46.4 ng/mL
100 ng/mL TNF-α
C
Diclofenac
Ketorolac
Methimazole
Naproxen
Sulindac
Normalized ICAM1-eGFP intensity
Concentration (cMax)
D
101.0 µM
35.3 µM
26.2 µM
2.0 µM
319.9 µM
252.5 µM
88.3 µM
65.5 µM
5.0 µM
799.8 µM
505.0 µM
176.5 µM
131.0 µM
10.0 µM
1599.5 µM
Diclofenac + TNF-α
Ketorolac + TNF-α
Methimazole + TNF-α
Naproxen + TNF-α
Sulindac + TNF-α

Figure 6. The role of NSAIDs on ICAM1-GFP expression in HLC A) Experimental setup of cell culture process and subsequent NSAID exposure in the presence or absence of 50 ng/mL TNF-α. **B)** Point-of-departure (PoD) calculations for ICAM1-eGFP expression. Cells were treated with a concentration-response TNF-α. Thereafter, a LOESS curve-fit was performed with estimated standard errors between the lowest and highest TNF-α concentration. The thresholds for ICAM1-eGFP increase (above green line), decrease (between blue and red line) or blockage (below red line) were set at the point where the predicted ICAM1-eGFP expression + standard error was larger or smaller compared to the ICAM1-eGFP expression + standard error predicted using the concentration response TNF-α curve. **C)** ICAM1-eGFP intensity plot with standard error in grey of five NSAIDs. Ketorolac and methimazole are not associated with DILI, while diclofenac, naproxen and sulindac are known DILI-inducing compounds. The black dotted line indicates ICAM1-eGFP expression after 50 ng/mL TNF-α incubation. **D)** Representative images of ICAM1-eGFP HLC 48 hours post NSAID/TNF-α exposure at 10, 25 and 50* Cmax and 50 ng/mL TNF-α.

However, the response is more robust in HLC. This is in line with a previous study from our lab where we compared different hepatocyte models and their response to TNF-α[175]. To further assess the relevance of HLC to study the role of inflammation in DILI, we also performed treatments with diclofenac and trovafloxacin in combination with TNF-α. Besides inflammatory signalling, diclofenac also upregulates the ER stress pathway, unfolded protein response and oxidative stress[176] and trovafloxacin induces mitochondrial stress and the DNA damage response[167,177]. We confirmed that both HLC and PHH also induce downstream targets related to these stress-response pathways, including *SRXN1* (oxidative stress), DDIT3 (ER stress) and GADD45A (DNA damage response). This is similar to the findings of Ghosh et al. where hiPSC-derived HLC generated through the same differentiation protocol are also sensitive to diclofenac treatment and also induce oxidative stress and the unfolded protein response[178].

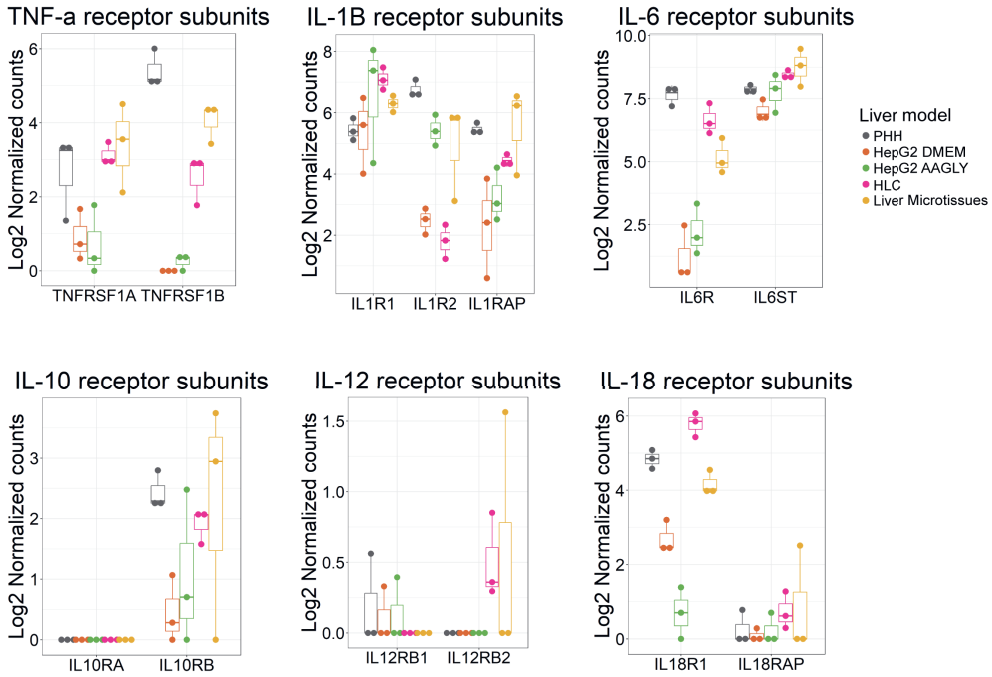
We performed a proof-of-concept study in HLC using an ICAM1-eGFP reporter to assess NF-κB downstream signalling alterations upon NSAID exposure using live cell imaging. Use of ICAM1-eGFP reporters in HepG2 cells has supported the evaluation of DILI liabilities[179]. We specifically focused on NSAIDs given their established DILI risk[172]. We identified that ketorolac and methimazole, two compounds not associated with DILI, did not induce any changes in ICAM1-eGFP expression. On the other hand, the DILI-inducing drugs diclofenac, naproxen and sulindac did alter ICAM1-eGFP expression and in all cases, they have been linked to inflammatory stress involved in the progression of DILI[143,144,165,180,181]. As the inflammatory response could be both direct and indirect due to crosstalk with other stress response pathways, like mitochondrial stress, ER stress/UPR, or oxidative stress[182–184], other mechanisms should be investigated too to obtain better mechanistic under-standing of the processes behind NSAID-induced hepatotoxicity.

Limitations in this study can be found in the cytokine concentrations that we used in our study. To mimic full receptor activation in each of the liver test systems, we used cytokines at relatively high concentrations. Although we are aware that this may impact

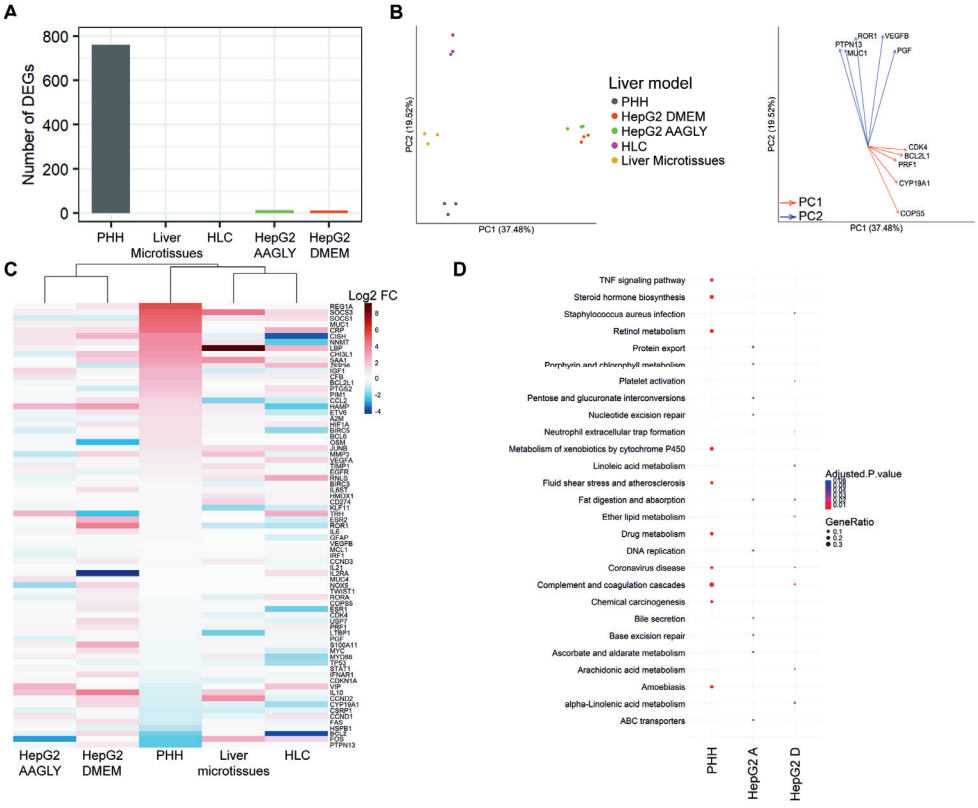
the physiological relevance of our findings. In addition, we used a TXG-MAPr that was generated from a publicly available transcriptomic dataset generated in PHH from the TG-GATES database[185]. As gene modules are partially not preserved between liver modules, this could lead to dissimilarities in their co-expression and module response. Therefore, we also assessed the induction of certain stress response pathways by verifying single gene expression levels.

Despite limited hepatocyte maturation in HLC based on transcriptomics and CYP3A4 activity, activation of adaptive stress response pathways, like inflammation, ER stress, oxidative stress and the DNA damage response were comparable or stronger compared to PHH. Given the fact that HLC are benign cells with unlimited supply, we conclude that they might be a suitable alternative to PHH or hepatocellular carcinoma cell lines, like HepG2, to study inflammatory responses in relation to DILI.

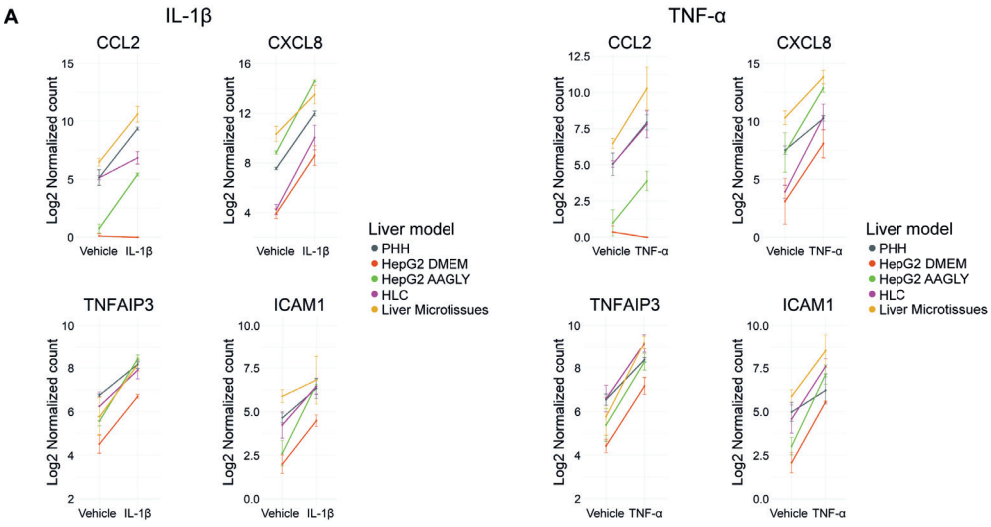
Supplemental Figures



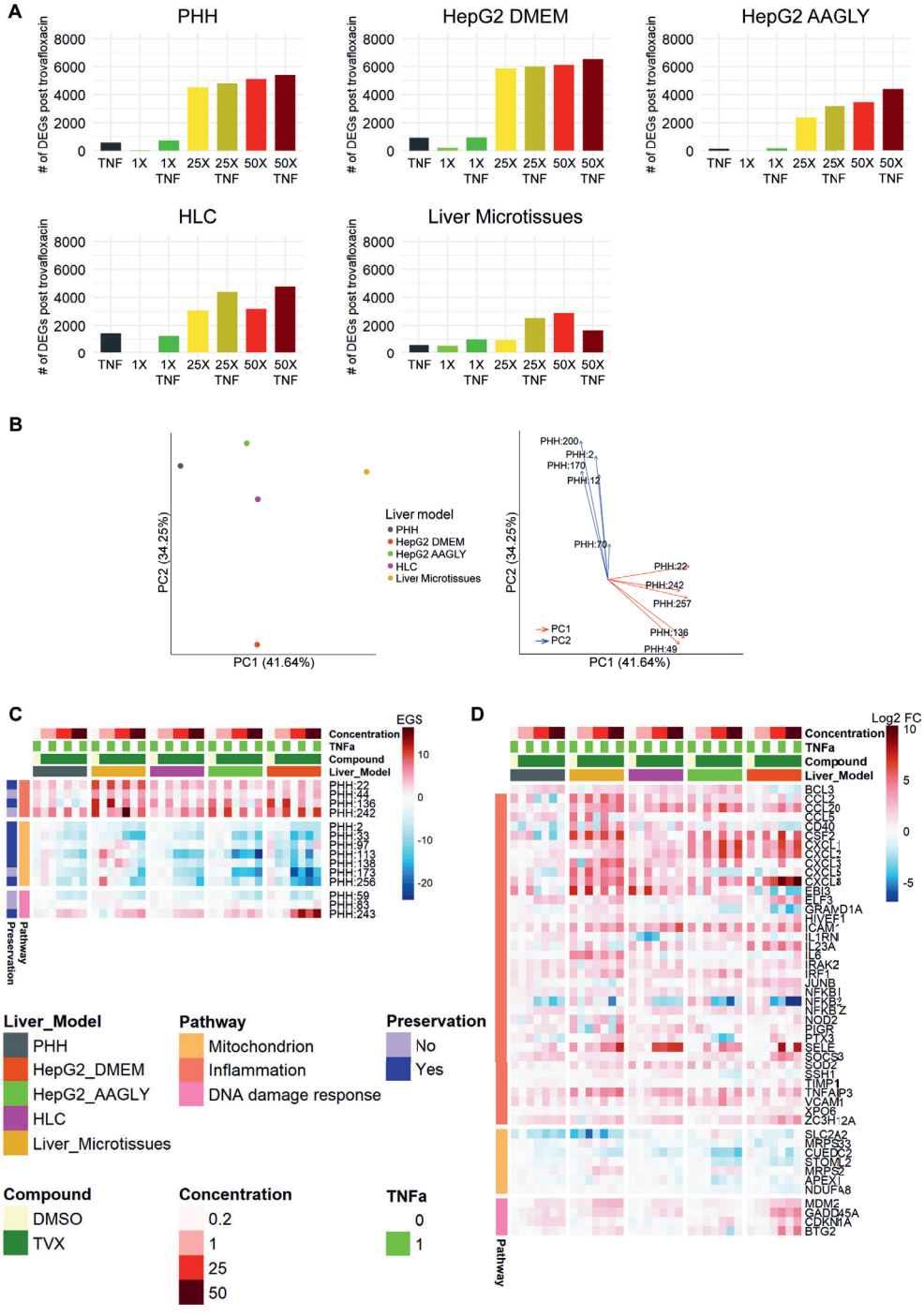
Supplemental Figure 1. Expression of cytokine receptor subunits in the various liver models.


A
Number of DEGs
800
600
400
200
0
PHH
Liver Microtissues
HLC
HepG2 AAGLY
HepG2 DMEM
B
Liver model
PHH
HepG2 DMEM
HepG2 AAGLY
HLC
Liver Microtissues
PC2 (19.52%)
PC1 (37.48%)
ROR1
VEGFB
PTPN13
MUC1
PGF
CDK4
BCL2L1
PRF1
CYP19A1
COPS5
PC1
PC2
C
Log2 FC
HepG2 AAGLY
HepG2 DMEM
PHH
Liver microtissues
HLC
D
TNF signaling pathway
Steroid hormone biosynthesis
Staphylococcus aureus infection
Retinol metabolism
Protein export
Porphyrin and chlorophyll metabolism
Platelet activation
Pentose and glucuronate interconversions
Nucleotide excision repair
Neutrophil extracellular trap formation
Metabolism of xenobiotics by cytochrome P450
Linoleic acid metabolism
Fluid shear stress and atherosclerosis
Fat digestion and absorption
Ether lipid metabolism
Drug metabolism
DNA replication
Coronavirus disease
Complement and coagulation cascades
Chemical carcinogenesis
Bile secretion
Base excision repair
Ascorbate and aldarate metabolism
Arachidonic acid metabolism
Amoebiasis
alpha-Linolenic acid metabolism
ABC transporters
Adjusted.P.value
GeneRatio
PHH
HepG2 A
HepG2 D
E
Module_Preservation
Highly_preserved
Moderately_preserved
Not_preserved
LM
PHH
HepG2 A
HepG2 D
HLC
F
PHH
Liver Microtissues
HLC
HepG2 AAGLY
HepG2 DMEM
Log2FC
corEG

◀ Supplemental Figure 2. Effect of IL-6 on the transcriptomic space and JAK-STAT signalling in various hepatocyte models. A) Number of Differential Expressed Genes (DEGs) 24 hours post IL-6 exposure in all test models. **B)** Left panel: PCA plot on Log2 normalized counts of STAT3/IRF1 downstream targets identified by Dorothea. Right panel: loading plot representing the top 5 determining genes in PC1 (orange) or PC2 (blue). **C)** Hierarchical clustering of the Log2 fold change of STAT3/IRF1 downstream targets in the top panel **D)** Dot plot showing top 10 KEGG2021 human pathways upregulated upon IL-6 exposure. **E)** Hierarchical clustering of Eigengene scores from individual models associated with IL-6-induced inflammation after weighted correlation gene network analysis (WGCNA). **F)** Gene network of module 44. Colours indicate Log2 fold change compared to vehicle. *CXCL1* in the square indicates the hub gene of module 44. The size of the circle or square relates to the correlation of the Eigengene score of that gene for module 44.



Supplemental Figure 3. Log2 normalized counts of various downstream targets in the vehicle and post IL-1β or TNF-α treatment.


A
PHH
HepG2 DMEM
HepG2 AAGLY
HLC
Liver Microtissues
of DEGs post trovafloxacin
TNF 1X 1X TNF 25X 25X TNF 50X 50X TNF
B
PC2 (34.25%)
PC1 (41.64%)
Liver model
PHH
HepG2 DMEM
HepG2 AAGLY
HLC
Liver Microtissues
PHH:200
PHH:2
PHH:170
PHH:12
PHH:70
PHH:22
PHH:242
PHH:257
PHH:136
PHH:49
PC1
PC2
C
EGS
Concentration
TNFa
Compound
Liver_Model
Pathway
Preservation
Liver_Model
PHH
HepG2_DMEM
HepG2_AAGLY
HLC
Liver_Microtissues
Pathway
Mitochondrion
Inflammation
DNA damage response
Preservation
No
Yes
Compound
DMSO
TVX
Concentration
0.2
1
25
50
TNFa
0
1
D
Log2 FC
Concentration
TNFa
Compound
Liver_Model
Pathway

◀ **Supplemental Figure 4. Effect of trovafloxacin +/- TNF-α on transcriptomic space in all liver models. A)** Number of DEGs after vehicle/diclofenac exposure in presence or absence of TNF-α. **B)** PC analysis on WGCNA-derived inflammatory module EGS after exposure to 25* Cmax trovafloxacin with or without TNF-α in all tested liver systems. **C)** Hierarchical clustering of Eigengene scores from individual modules associated with inflammation, the DNA damage response of mitochondrial stress after trovafloxacin treatment with or without TNF-α challenge. **D)** Heatmap of selected targets of NF-κB-mediated inflammation, the DNA damage response pathway or mitochondrial stress upon trovafloxacin +/- TNF-α.

Supplemental Table 1: Predicted maximum blood-plasma concentrations (Cmax) for the selected NSAIDs).

Molecule name	Cas NO.	PubChem_CID	InChi Key	Canonical SMILES	cMax (µM)	Reference
Ketorolac	74103-07-4	84003	BWHLPLXXIDYSNW-UHFFFAOYSA-N	C1CN2C(=CC=C2C(=O)C3=CC=CC=C3)C1C(=O)O.C(C(CO)(CO)N)O	3.53	Wink/FDA
Methimazole	60-56-0	1349907	PMRYVIKBURPHAH-UHFFFAOYSA-N	CN1C=CNC1=S	2.62	Wink/FDA
Acetaminophen	103-90-2	1983	RZVAJINKPMORJF-UHFFFAOYSA-N	CC(=O)NC1=CC=C(C=C1)O	139	Wink/Xu/O'Brien
Diclofenac	15307-79-6	5018304	KPHWPUGNDIVLNH-UHFFFAOYSA-M	C1=CC=C(C(=C1)CC(=O)[O-])NC2=C(C=CC=C2Cl)Cl.[Na+]	10.1	Regenthal
Naproxen	23981-80-8	1302	CMWTZPSULFXXJA-UHFFFAOYSA-N	CC(C1=CC2=C(C=C1)C=C(C=C2)OC)C(=O)O	0.2	Wink/Regenthal
Sulindac	38194-50-2 (32004-68-5)	5352	MLKXDPUZXIRXEP-UHFFFAOYSA-N	CC1=C(C2=C(C1=CC3=CC=C(C=C3)S(=O)C)C=CC(=C2)F)CC(=O)O	31.99	Wink/FDA

Supplemental Table 2. Genes within NF-κB or IL-6 signalling modules selected by RELA, REL, NFKB1 (IL-1B/TNF-α) or STAT3 and IRF1 (IL-6) transcription factor activity





CHAPTER 4

GENERATION OF FLUORESCENT REPORTERS IN HIPSC TO ASSESS INFLAMMATION-ASSOCIATED DRUG-INDUCED ORGAN TOXICITY

Linda van den Berk[1], Kirsten E. Snijders[1], Tamara Danilyuk[1], Rob van Rossom[2], Bela Z. Schmidt[2], Catherine Verfaillie[2], Bas ter Braak[1], Peter Bouwman[1], Bob van de Water[1]

[1]Division of Drug Discovery and Safety, Leiden Academic Centre for Drug Research (LACDR), Leiden University, Leiden, The Netherlands

[2] Stem Cell Institute, Department of Stem Cell and Developmental Biology, KU Leuven, 3000 Leuven, Belgium

Keywords: TNF signalling pathway, NF-κB, drug-induced liver injury, hiPSC, fluorescent reporter, CRISPR-Cas9

Abstract

Adverse drug reactions are harmful, unintended responses to a drug that can result in life threatening risks, and the liver is one of the most affected organs due to its role in drug metabolism. The liver is a critical target organ of toxicity. Inflammatory responses are central in liver toxicity and screening for immune modulatory responses may facilitate the identification of drug candidates with hazards for liver adversity. Here we established a panel of endogenously tagged fluorescent reporter lines in hiPSCs to assess the dynamics of inflammatory induction in various differentiated cell types including hepatocyte-like cells (HLCs) using confocal imaging. Candidate biomarkers including RND1, LCN2, IRF1, A20, and VCAM1, were systematically selected based on gene network analysis mRNA expression data from primary human hepatocytes and rat livers exposed to inflammatory cytokines. All selected biomarkers were tagged c-terminally with eGFP in hiPSCs using CRISPR/Cas9-assisted homologous recombination. We validated the upregulation of the A20, ICAM1 and IRF1 reporters upon cytokine exposure in hiPSC-derived HLCs using western blot and confocal imaging. In addition, we show that the use of the ICAM1 and IRF1 reporters can also be exploited to assess inflammatory-stress induction in hiPSC-derived cardiomyocyte-like cells. To conclude, we have generated hiPSC reporters that can be used to assess the role of inflammation in adverse drug reactions in hepatocytes and cardiomyocytes and can add to the overall identification of drug-induced adversity liabilities.

Introduction

Adverse drug reactions (ADRs) are unwanted responses to drugs that can result in mild to severe life-threatening target organ effects. The liver is the most critical target organ for drug-induced liver injury (DILI). Despite many efforts to understand and prevent DILI, incidence remains high with rates ranging from 1.3 to 19.1 per 100.000 individuals worldwide[186]. DILI can be classified in 3 general mechanisms. The first is direct DILI which is dose-dependent, intrinsic and therefore predictable. Molecular mechanisms responsible for direct DILI involve mitochondrial dysfunction, oxidative stress, endoplasmic reticulum stress, and bile duct injury, potentially resulting in increased cell death via apoptosis and necrosis mechanisms[187]. The second type of DILI is idiosyncratic DILI. As this type of DILI is largely dose-independent, it is difficult to predict. Underlying mechanisms remain largely unknown, but it is believed that the immune system plays an important role. Antigen-presenting cells activated by released danger-associated molecular patterns (DAMPs), or drug-protein complexes can activate CD4+ and CD8+ T- and B-cell responses, ultimately resulting in liver damage[188]. The third type of DILI, indirect DILI, is in fact similar to idiosyncratic DILI as it is characterized by dose-independency and the involvement of the immune system. In this case, the intended biological action of the drug affects the host immune system and may lead to drug-induced autoimmune hepatitis[189]. Checkpoint inhibitors targeting cytotoxic T lymphocyte-associated antigen-4 (CTLA4) and programmed cell death-ligand-1 (PDL1) are inducing indirect DILI and with their emergence in the clinic, the incidence is increasing[190].

As the development of DILI is a major cause of late drug development failure during clinical testing and drug withdrawal from the market post-approval, novel preclinical models are necessary to predict DILI in early stages of development. Various *in vitro* models are available to predict the induction of DILI in early development, but each have their limitations. The hepatocellular carcinoma cell line HepG2 is easy to use and readily available, however drug metabolism is limited and therefore it remains challenging to link drug (dose) and adverse outcomes. Primary human hepatocytes (PHHs) are still considered the gold standard in DILI research as they best resemble the human *in vivo* liver condition in terms of drug metabolism, morphology and function. However, drug metabolizing enzymes drop within two days after plating, resulting in hampered functionality. In addition, the availability of PHH is limited and therefore performing high-throughput drug screens with identical PHH material is not feasible[186]. Human-induced pluripotent stem cell (hiPSC)-derived hepatocyte-like cells (HLCs) are an alternative to the traditional *in vitro* models. The use of hiPSCs has several advantages. Many different hiPSC lines are available with various genetic backgrounds. They provide an unlimited source of cells that can be used for subsequent differentiation in any cell type of interest. Therefore, they are a suitable

model to assess organ-specific drug toxicity, including the liver and heart[191,192]. Additionally, hiPSCs can be genetically modified to generate mutations that can influence toxicity or to generate fluorescent reporters to visualize stress pathway activation during drug toxicity[193]. Pluripotent hiPSCs can be differentiated towards hepatocyte-like cells through a stepwise process following embryonic developmental stages. Using an hiPSC line with doxycycline-induced overexpression of the hepatic transcription factors HNF1A, PROX1 and FOXA3, hiPSCs can be differentiated towards HLCs with biotransformation capacities comparable to PHH[194].

As inflammation is involved in both idiosyncratic and indirect DILI, it is important to establish an *in vitro* test system that reflects inflammatory signalling responses. TNF-α plays a central role in DILI by activating the nuclear translocation of the transcription factor nuclear factor κB (NF-κB), thereby inducing the expression of various pro-inflammatory molecules, such as cytokines, chemokines, and adhesion molecules, (e.g., ICAM1). This role of TNF-α has been shown for various DILI-associated drugs, including amiodarone[195], trovafloxacin[196] and diclofenac[197,198]. Previously, we have shown that dynamic imaging of an TNF-α-induced ICAM1-eGFP reporter in HepG2 cell provides useful information on alterations in the TNF-α signalling pathway upon drug exposure and that this platform could be used for high-throughput screening of compounds[199]. Currently, relevant fluorescent protein reporters in hiPSC that reflect inflammatory signalling are lacking.

Here we systematically identified six specific NF-κB downstream targets that are upregulated upon TNF-α, interleukin 1β and lipopolysaccharide (LPS) exposure in human hepatocytes or in the rat liver. VCAM1, TNFAIP3, IRF1, RND1, and LCN2 were selected as specific targets and were chosen to build endogenous fluorescent reporters in hiPSCs using CRISPR/Cas9 to assess the effect of xenobiotics on inflammatory signalling in hiPSC-derived HLC using automated imaging.

Materials & Methods

Reagents & cytokines

Recombinant human TNF-α was acquired from R&D systems (Abingdon, UK). IL-1β and IFN-γ were purchased from Peprotech. Recombinant human Activin A, Wnt3a, BMP-4, FGF1 and HGF were acquired from Peprotech. CHIR99021 was purchased at Axon Medchem and XAV939 was acquired from Tocris. RevitaCell was from Thermo Fisher. All used restriction enzymes were purchased at NEB.

Reporter candidate selection

Selection of potential NF-κB-mediated inflammatory reporter genes was performed using the TXG-MAPr (https://txg-mapr.eu/)[200], which displays weighted gene co-expression network analysis (WGCNA) on publicly available transcriptomic data from the TG-GATEs database[201]. Specifically, data from rats exposed to 3 µg/kg TNF-α or 300 µg/kg LPS *(*also called *in vivo* rat) and *in vitro* human hepatocytes exposed to 10 ng/mL TNF-α, 10 ng/mL IL-1β or 60 ng/mL LPS were used. Time points that were included in the analysis were 2, 8, and 24 hours post exposure for i*n vitro* hepatocytes and 3, 6, 9, and 24 hours for *in vivo* rat to enable capturing both early and late NF-κB target genes. For each NF-κB inducer and time point, the top 20 modules with the highest Eigengene Score, both positive as negative, were selected. Subsequently from these top 20 modules, the top 100 most up-regulated genes were selected based on the fold change. Thereafter, we selected the 16 genes that were overlapping between the *in vivo* rat and the *in vitro* hepatocyte dataset. Finally, we excluded 6 potential candidates since these proteins are secreted from the cell and therefore not the ideal candidate for a reporter gene.

Cell culture

The hiPSC cell line iPSC-EPITHELIAL-1 (Sigma-Alderich, iPSC0028), in this chapter referred to as 'Sigma-HC3X' (https://hpscreg.eu/cell-line/SIGi001-A-23), was derived from epithelial cells from a 24-year-old Caucasian female and was reprogrammed using OSKM virus and contains a doxycycline-inducible cassette to overexpress the hepatic transcription factors *PROX1*, *HNF1A*, and *FOXA3* [194]. Cells were maintained on growth factor reduced (GFR) Matrigel (Corning)-coated plates in mTeSR1 at 37°C and 5.0% CO_2 and passaged twice a week using ReleSR (StemCell Technologies).

Differentiation of hiPSCs toward hepatocyte-like cells

hiPSCs were differentiated to HLCs as described by Boon et al. [194]. hiPSCs were seeded on day -1 at a density of 28.000 cells/cm^2 on GFR Matrigel-coated plates in mTeSR1 +1:100 RevitaCell[194]. Differentiation was started 48 hours post seeding in liver

differentiation medium (LDM) containing 0.6% DMSO until day 10. From day 4 until the end of differentiation, 5 µg/mL doxycycline was used to activate the doxycycline-inducible hepatic transcription factors. To generate definitive endoderm, hepatoblasts and immature hepatocytes, LDM was supplemented with 50 ng/mL Activin A (50 ng/mL), 50 ng/mL BMP4 (50 ng/mL), 50 ng/mL Wnt3a (50 ng/mL) or 20 ng/mL FGF1. From day 10 to 12, LDM was supplemented with 160 µL/mL MEM non-essential amino acids (100x), 80 µL/mL MEM essential amino acids (50x) (LDM-AA), 2% DMSO and 20 ng/mL HGF. Hepatocyte-like cell maturation from day 12-40 was induced using LDM-AA supplemented with 2% glycine (LDM-AAGLY) and 20 ng/mL HGF.

Differentiation of hiPSCs toward cardiomyocyte-like cells

hiPSCs were differentiated to CMLCs as described by van den Berg et al.[202]. In brief, on day -1 cells were seeded in a density of 52.000 cells/cm^2 in mTeSR1 supplemented with 1:100 RevitaCell on GFR Matrigel-coated plates. On day 0, cardiac mesoderm was induced using 20 ng/mL Activin A, 20 ng/mL BMP-4 and 1.5 µM CHIR99021. On day 3, 5 µM XAV939 was supplemented to the differentiation medium to induce cardiac progenitors. From day 6 onwards, the medium was refreshed every 2-3 days using differentiation medium. On day 15, cells were reseeded in a density of 450.000 cells/cm^2 in black Greiner SCREENSTAR plates at refreshed every 2-3 days until day 21.

Transcriptomic analysis (TempO-Seq)

TNF-α or IL1-β treated hiPSC-derived HLC were washed twice with 1× PBS and lysed in 1× TempO-Seq lysis buffer. Samples were incubated for 15 minutes at room temperature before being stored at −80°C. The samples were subsequently shipped to BioClavis Ltd. for TempO-Seq analysis. Raw count data were normalized using an in-house script implementing DESeq2 and counts-per-million (CPM) normalization with an input count threshold of 1×10^6, followed by $\log_2$ fold-change transformation. Differentially expressed genes were identified using a false discovery rate (FDR)-adjusted p-value threshold of ≤ 0.05.

Western blot

To isolate cellular proteins, cells were washed with ice-cold PBS and harvested in lysis buffer containing 50 mM Tris pH 7.5, 150 mM NaCl, 0.1% (v/v) SDS, 2 mM EDTA, 1% (v/v) Nonidet P-40 and 0.5% sodium deoxycholate and was supplemented with 1:100 protease inhibitor cocktail (Sigma-Alderich, p8340). Thereafter, protein concentration was determined using a standard BCA assay (Thermofisher, 23225). 20 µg protein per sample was loaded on polyacrylamide gels for SDS-PAGE. After electrophoresis, proteins were transferred to polyvinyldine (PVDF) membranes and blocked and stained with antibodies according to the antibody manufacturer's protocol. Antibodies are

listed in supplemental table 1. After staining, blots were visualized using the Amersham Imager 600 (GE Healthcare). A-tubulin and GAPDH were used as loading control.

Donor plasmids, gRNAs and Cas9 protein

Donor plasmids were designed uniquely for each target locus of interest. Homology arms (HAs) 5' and 3' the insertion site were ~1000 bp in length using the GRCh38 reference genome. All genes of interest were targeted C-terminally and the linker between the GOI and eGFP was universal (GGCGGAGGCGGTGGG). Firstly, we performed an overhang PCR with restriction enzyme sites (Supplemental table 2). For the left HA, SphI and SalI were used and for the right HA, either XmaI and EcoRI (*IRF1*, *LCN2* and *RND1*) or BamHI and SacI (*TNFAIP3* and *VCAM1*) were used. For the right HA we had to make use of 2 different combinations of restriction enzymes due to the presence of restriction sites in the homology arm itself. Subsequently, the pUC19 eGFP plasmid and left and right HA overhang PCR products were digested with the aforementioned restriction enzymes and the pUC19 eGFP plasmid was dephosphorylated using Antartic Phosphatase (NEB) to prevent self-ligation. The right HA was ligated in the pUC19 eGFP plasmid using T7 DNA ligase (NEB) and transformed in NEB® 5-alpha Competent E. coli competent cells and plated on LB-Ampicillin plates. Correct integration of the HA in the pUC19 plasmid was confirmed using colony PCR. Plasmids from 3 positive colonies were isolated using the NucleoSpin Plasmid prep kit (Macherrey-Nagel) and subsequently analysed using sanger sequencing. Subsequently, the left HA was integrated in a similar manner.

gRNAs for each target specifically were generated using CHOPCHOP (https://chopchop.cbu.uib.no/)[203]. A region of 20 bp around the stop codon was checked for potential gRNAs. gRNAs were ordered as oligos (Sigma-Alderich) (Supplemental table 3) and were annealed using T4 Polynucleotide Kinase (NEB). The annealed oligo duplex was inserted in the Cas9 plasmid pSpCas9(BB)-2A-Blast plasmid (Addgene, 118055) by means of a digestion-ligation reaction with FastDigest BbsI and T7 DNA ligase (both NEB) followed by an exonuclease step (Biosearch technologies). The final product was transformed in NEB® 5-alpha Competent *E. coli* competent cells and plated on LB-Ampicillin plates. Plasmids were isolated from bacterial colonies using the NucleoSpin Plasmid prep kit and correct integration of the gRNA in the Cas9 plasmid pSpCas9(BB)-2A-Blast plasmid was verified using Sanger sequencing using this primer: 5'-GACTATCATATGCTTACCGT-3'.

Nucleofection for the generation of IRF1, LCN2, RND1, TNFAIP3, and VCAM1-eGFP reporters

Sigma-HC3X cells were incubated with penicillin/streptomycin-free mTeSR1 supplemented with 1:100 RevitaCell 24 hours before transfection. On the day of

nucleofection, confluency of the wells was <50% to enable homology-directed repair in proliferating cells. Cells were washed with 1x PBS and dissociated using 1x TryplE for 5 minutes at 37°C and collected in DMEM/F12. 1.5x10^6 cells were nucleofected with 2 µg of the target specific homology arm containing pUC19-eGFP plasmid and the pSpCas9(BB)_2A_Blast gRNA plasmid using the Amaxa Nucleofector II, program A023. Post nucleofection, cells were plated on 2x 100 mm dishes containing penicillin/streptomycin-free mTeSR1 supplemented with 1:100 RevitaCell. 2 µg/mL blasticidin selection was started 24 hours post nucleofection and lasted for 72 hours. Once hiPSC colonies appeared, colonies were picked on 96 well plates. Once confluent, cells were split and samples were taken for junction PCRs using QuickExtract (Biosearch technologies).

Nucleofection for the generation the ICAM1-eGFP reporter

Sigma-HC3X hiPSCs were cultured in penicillin/streptomycin-free mTeSR1 medium supplemented with 1:100 RevitaCell for 24 hours. Cells were washed with 1x PBS and dissociated with 1x TryplE for 5 minutes at 37°C and collected in DMEM/F12. 1.5x10^6 cells were nucleofected with 2 µg of the target specific homology arm containing pUC19-eGFP donor plasmid and the Cas9 plasmid using the Amaxa Nucleofector II, program A023. Post nucleofection, cells were plated on 2x 100 mm dishes containing penicillin/streptomycin-free mTeSR1 supplemented with 1:100 RevitaCell. 24 hours post nucleofection, 100 µg/mL hygromycin selection was started for 72 hours. Clonal hiPSC colonies were picked at grown on 96-well plates. Once confluent, colonies were split and samples were taken for junction PCR using QuickExtract. Following the selection of clones with integration of eGFP and the selection cassette, positive clones were nucleofected with 8 µg PiggyBac Transposase Expression Vector as previously described to remove the selection cassette. Cells were selected with 0.5M FIAU (Sigma-Alderich) to select for clones that removed the selection cassette and clones were further expanded and checked for correct eGFP integration using junction PCR.

Genetic screening by junction PCR

PCR was used to verify correct eGFP integration using primers spanning the left and right HA, linker sequence and eGFP, including parts of the genetic regions left and right of the HAs (figure 3C) using gene specific primers (Supplemental table 4). All PCRs were performed using NEBQ5 (New England Biolabs), 1 µM of forward and reverse primer and 3 µL of the QuickExtract gDNA mixture. Clones with correct eGFP insertion based on size were further analysed bidirectionally with PCR primers using Sanger Sequencing (LUMC).

Copy Number Variation (CNV) Analysis

Reporter hiPSCs between passage 56 and 59 were cultured as described above. gDNA was isolated using the GenElute Mammalian Genomic DNA Miniprep Kit (Sigma-Alderich, G1N350). 500 µg gDNA in 10 µL dH_2O was sent to Stem Genomics for copy number variation analysis using the 24-probe iCS-digital PSC assay service.

Immunofluorescence

hiPSCs were cultured in SCREENSTAR 96 well black imaging plates (Greiner Bio one). Cells were washed once with 1x PBS, followed by fixation using buffered formaldehyde 4% for 15 minutes. Cells were blocked and permeabilized for 1 hour with 5% donkey serum in 0.2% PBS-T at room temperature. Staining for Oct4 (1:1000 in Dako REAL antibody diluent, Abcam, 19857) was performed overnight at 4°C. Thereafter, samples were incubated with a goat anti-rabbit Alexa 647 antibody (1:1000 in Dako REAL antibody diluent, Jackson, 111-605-003) and 1:10000 Hoechst $_{33342}$ for 1 hour at room temperature. Finally, samples were washed twice with 1X PBS and stored at 4°C until confocal imaging using a Nikon TE-2000-E eclipse microscope equipped with 408, 488, 561 and 633 nm lasers and using a 20× Plan Apo objective,

Live cell imaging

CMLCs were pre-stained with 100 ng/mL Hoechst $_{33342}$ for one hour. Thereafter, medium was removed and cells were exposed to a concentration range of TNF-α, IL-1β or IFN-γ. GFP levels were measured in hiPSC-derived hepatocyte-like cells and cardiomyocyte-like cells after 24 hours post exposure using a Nikon Eclipse Ti2 LIPSI microscope, equipped with a 408, 488, 561 and 633 nm laser, using four images per well. Due to Hoechst efflux from HLC nuclei, 10x concentrated Hoechst was added to cytokine exposed cells one hour before imaging to enable proper nuclei segmentation.

Image analysis

Image analysis was performed using CellProfiler 4.2.1. First, nuclei were segmented using watershed-masked clustering using an in-house developed module[204]. The integrated eGFP intensity in the nucleus (IRF1) or cytoplasm/membrane (A20, VCAM1, ICAM1) was calculated and normalized to the vehicle control.

Statistical analysis

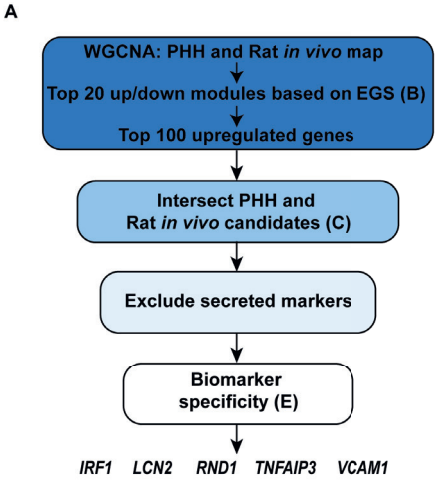
Statistical analyses were performed using GraphPad Prism version 10 software. The Shapiro-Wilk test was used to assess normality of the data. All datasets met the assumption of normality and group differences were analysed using an ordinary one-way analysis of variance (ANOVA) followed by a Tukey's multiple comparison test. P-

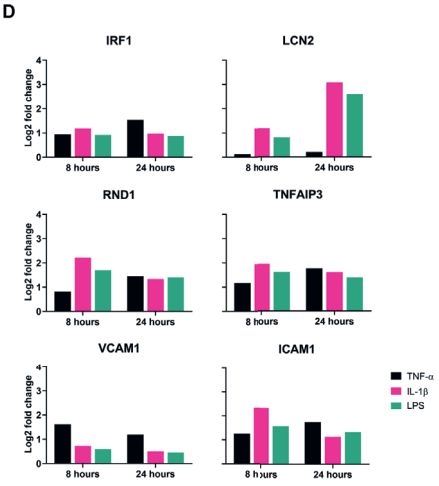
values <0.05 were considered statistically significant. Levels of significance are indicated as follows: *p<0.05, ** p<0.01, *** p<0.001, ****p<0.0001.

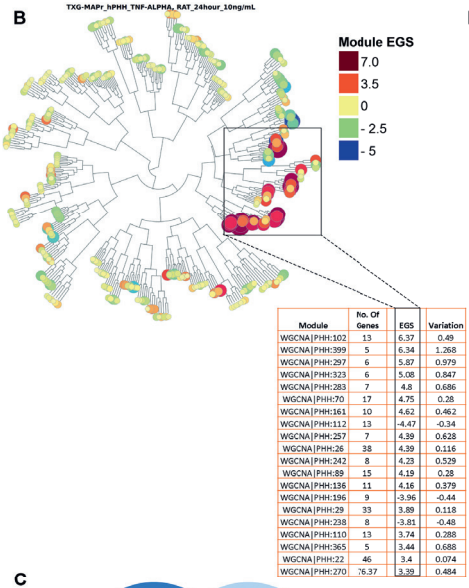
Results

Systematic selection of biomarkers for inflammatory stress induction

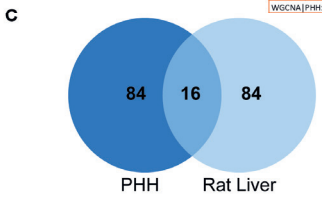
In order to identify, biomarkers for inflammatory stress response activation in drug-induced liver injury, we used the TXG-MAPr tool where weighted gene co-expression network analysis was performed on the TG-GATEs datasets (Figure 1A). For this dataset, primary human hepatocytes (PHH) and rat *in vivo* liver were exposed to 158 compounds at various concentrations and time points. First, we assessed the top 20 induced and repressed modules based on the module's eigengene score (EG) after treatment with known inflammatory inducers (PHH; TNF-α, IL-1β and Lipopolysaccharide (LPS), Rat liver; TNF-α and LPS). These EGs are representative for the behaviour of the genes in the entire module [200] (Figure 1B). Subsequently, the top 100 most upregulated genes in both model systems were identified based on the Log2 fold change (FC). Thereafter, we selected the 16 candidates that were identified in PHH as well as rat liver (Figure 1C), as upregulation in both model systems suggests that they are robust biomarkers of inflammatory stress. Next, we filtered on subcellular location of each potential target as secreted biomarkers, including cytokines and chemokines, are not suitable as fluorescent reporters for intracellular confocal imaging. This approach resulted in 10 potential biomarkers (Table 1). We thereafter followed up with the five biomarkers that were upregulated in response to multiple cytokines and LPS identified from the WGCNA analysis, RND1, LCN2, IRF1, TNFAIP3 and VCAM1 (Supplementary figure 1A), and assessed their log 2 FC induction in both model systems (Figure 1D and Supplemental figure 1B). In addition, we added ICAM1 as a biomarker although it was not identified as a hit based on our approach, since ICAM1 has been proven to be a promising biomarker for the inflammatory stress response[199,205]. To confirm the specificity of all chosen biomarkers, we assessed the induction of the biomarkers upon exposure to compounds inducing the DNA damage response, ER/UPR stress and oxidative stress using the same TXG-MAPr in both PHH and the rat liver (Figure 1E and Supplemental figure 1C). All biomarkers of inflammation appeared to be mainly upregulated by inflammatory cytokines. Of note, some inflammatory biomarkers also responded to other types of stress inducers, e.g. the DNA damaging hepatocarcinogen Aflatoxin B1 induced *ICAM1* and *RND1* mRNA levels. However, it has been shown that aflatoxin B1 can also activate inflammation[206].

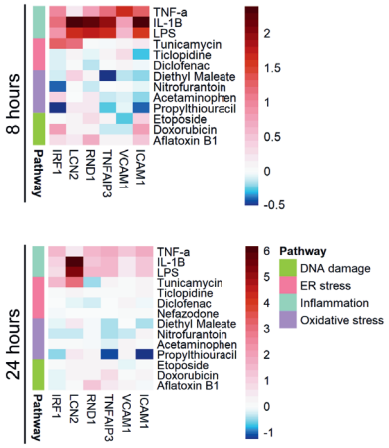






Module	No. Of Genes	EGS	Variation
WGCNA|PHH:102	13	6.37	0.49
WGCNA|PHH:399	5	6.34	1.268
WGCNA|PHH:297	6	5.87	0.979
WGCNA|PHH:323	6	5.08	0.847
WGCNA|PHH:283	7	4.8	0.686
WGCNA|PHH:70	17	4.75	0.28
WGCNA|PHH:161	10	4.62	0.462
WGCNA|PHH:112	13	-4.47	-0.34
WGCNA|PHH:257	7	4.39	0.628
WGCNA|PHH:26	38	4.39	0.116
WGCNA|PHH:242	8	4.23	0.529
WGCNA|PHH:89	15	4.19	0.28
WGCNA|PHH:136	11	4.16	0.379
WGCNA|PHH:196	9	-3.96	-0.44
WGCNA|PHH:29	33	3.89	0.118
WGCNA|PHH:238	8	-3.85	-0.48
WGCNA|PHH:110	13	3.74	0.288
WGCNA|PHH:365	5	3.44	0.688
WGCNA|PHH:22	46	3.4	0.074
WGCNA|PHH:270	76.37	3.39	0.484





◀ **Figure 1. Identification of inflammatory biomarkers in the liver. A)** Schematic overview of the biomarker selection process. **B)** Example of a TXG-MAPr map 24 hours after 10 ng/mL TNF-α exposure in PHH. **C)** Visualization of unique and overlapping biomarkers in PHH and the Rat liver. **D)** Log2 fold change induction of the selected biomarkers after treatment with TNF-α, IL-1β or LPS in PHH. **E)** Log2 fold change mRNA induction of the selected biomarkers upon inflammatory, DNA damage, ER stress and oxidative stress inducers eight- and 24-hours post treatment.

Table 1. Overview of the 16 overlapping biomarkers between PHH and rat in vivo liver.

Gene	Module PHH	Module Rat In Vivo	Subcellular location	Suitable as reporter? Y/N
CCL2	44	6	Extracellular	N
CCL20	22	6	Extracellular	N
CEBPD	170	6	Nucleus	Y
CXCL2	44	6	Extracellular	N
IL6	22	6	Plasma membrane, extracellular	N
IRF1	242	6	Nucleus, cytosol	Y
LAMC2	89	129	extracellular	N
LCN2	22	120	ER, Extracellular	Y
MAP3K8	22	6	Cytosol	Y
NCOA7	170	6	Nucleus	Y
RND1	22	6	Vesicles, Plasma membrane, actin filaments	Y
SELE	22	6	Plasma membrane, extracellular, cytoskeleton	Y
TLR2	26	6	Plasma membrane, Golgi	Y
TNFAIP3	242	6	Nucleus, cytosol, Lysosome	Y
TNFAIP6	22	6	Extracellular	N
VCAM1	242	6	Plasma membrane, extracellular, ER, endosome, golgi	Y

Confirmation of biomarkers upregulation in hiPSC-derived hepatocyte-like cells

To confirm biomarker upregulation in our model system hiPSC-derived hepatocyte-like cells, we treated the cells upon differentiation with TNF-α or IL-1β for 24 hours and assessed RNA and protein expression (Figure 2A). mRNA levels post TNF-α or IL-1β exposed were increased for all biomarkers except for RND1 (Figure 2B). Although RND1 mRNA levels were not increased, a dose-dependent increase could be observed on protein level. In addition, protein levels of the other biomarkers were upregulated upon TNF-α exposure (Figure 2C). Therefore, all biomarkers were selected to establish endogenous fluorescent reporters from in hiPSCs.

Fluorescent reporter generation

CRISPR/Cas9 was used as a gene-editing tool to enable homology directed repair-mediated incorporation of the enhanced green fluorescent protein (eGFP) sequence c-terminally of each gene of interest (GOI) (Figure 3A). For all reporters except ICAM1, two plasmids were used to promote insertion of the eGFP sequence in the GOI. The first plasmid consisted of the specific gRNA for each GOI, Cas9 and blasticidin resistance gene to enable transient blasticidin selection. The second plasmid contained the homology arms flanking the stop codon, the linker sequences, eGFP sequence and stop codon (Figure 3A). Both plasmids were electroporated in wild-type Sigma-HC3X hiPSCs. 24 hours post nucleofection, a 48-hour blasticidin selection procedure was performed to enrich for the cells that had taken up the gRNA plasmid. Subsequently, single clones were expanded, and each clone was extensively screened for correct integration of eGFP c-terminally of the GOI (Figure 3B). For this, junctional PCRs were performed of the tagged allele to determine precise on-target eGFP insertion (Figure 3C). To target the ICAM1 gene, another targeting strategy was performed (Supplemental figure 2). In this case, along with the linker and eGFP sequence, a selection cassette flanked by PiggyBac transposon inverted terminal repeats was introduced to enable antibiotic selection and visualization of targeted hiPSC clones using mScarlet fluorescence (Supplemental figure 2A). Again, both plasmids were introduced in the cell using nucleofection. Instead of blasticidin, hygromycin was used for antibiotic selection of targeted hiPSC clones. Expanded single clones were screened for correct c-terminal integration of eGFP. Verified clones were then nucleofected with a PiggyBac Transposase Expression Vector to remove the selection cassette to end up with a scar-free eGFP integration 3'of the ICAM1 gene. Cells were subjected to FIAU selection to specially enrich for clones without the PiggyBac-excised selection cassette, making use of the incorporated HSV-tk negative selection marker, which phosphorylates FIAU into toxic intermediates that disrupt cellular DNA replication, resulting in cell death[207]. Finally, we again performed clonal enrichment and subsequent PCR genotyping for correct removal of the selection cassette.

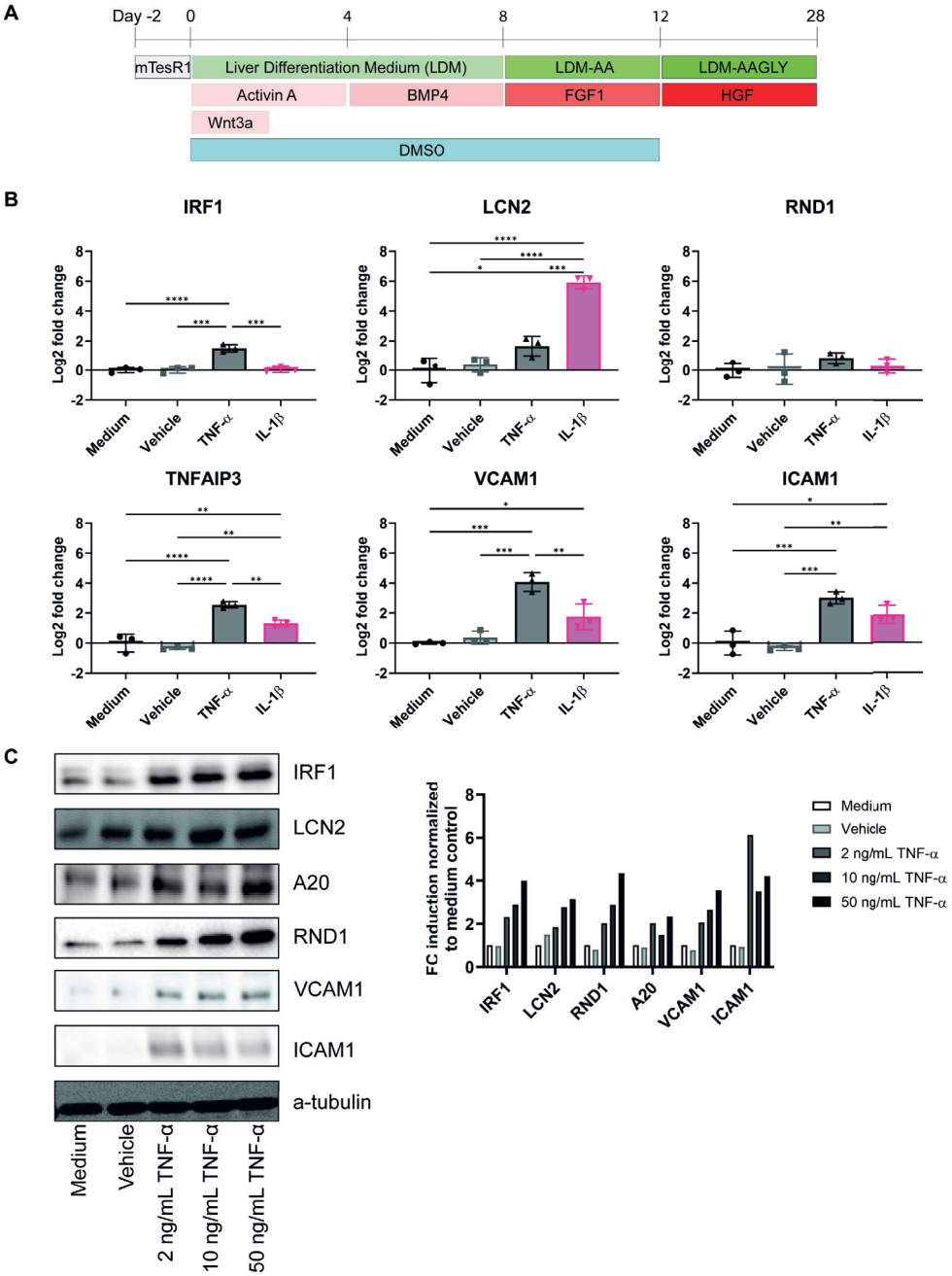


Figure 2. Biomarker validation in hiPSC derived HLC. A) Overview of the differentiation process to hiPSC-derived HLC **B)** Log2 fold change mRNA expression of selected biomarkers 24 hours post 100 ng/mL TNF-α or IL-1β exposure. Data are presented as mean ± SEM (N=3) **C)** Protein induction of the selected biomarkers upon 24-hour TNF-α exposure. N=1.

Thereafter, correct clones were cryopreserved (Supplemental figure 2B). For each target, one clone with correct eGFP insertion was selected as final clone. Each of them retained typical stem-cell like morphology (Supplemental figure 3A). In addition, all fluorescent hiPSC reporter lines remained positive for the pluripotency marker OCT4 (Supplemental figure 3B). Copy number variation analysis further showed the absence of 24 of the most frequent genetic abnormalities found in hiPSCs in our IRF1, A20, VCAM1 and ICAM1 reporter hiPSCs (Supplemental figure 3C).

Functional characterization of reporters in hiPSC-derived hepatocyte-like cells

To assess reporter functionality, hiPSC reporter lines were differentiated towards hepatocyte-like cells in 40 days. At this stage, HLCs were exposed to TNF-α, IL-1β and IFN-γ to induce the endogenous GFP-tagged proteins of interest (Figure 4A). Western blot analysis was performed against the protein of interest to validate upregulation of the tagged protein after inflammatory induction. Untagged and tagged IRF1 was exclusively induced post exposure to IFN-γ. For A20, an increase could be observed with TNF-α and IFN-γ, but this was less prominent with IL-1β. Untagged and tagged VCAM1 appeared to be induced only mildly with all three cytokines. For ICAM1, untagged and tagged protein was upregulated upon TNF-α and IL-1β induction but was lacking post IFN-γ exposure (Figure 4B). We also assessed eGFP upregulation after cytokine induction using live confocal imaging. A mild, concentration-dependent increase in A20-eGFP could be observed upon cytokine treatment. In line with the western blot data, ICAM1-eGFP was exclusively upregulated upon TNF-α and IL-1β treatment. Similarly, minimal IRF1-eGFP upregulation could be observed using IFN-γ. Similar to western blot, no VCAM1-eGFP induction could be observed after 24 hours of treatment (Figure 4C).

Fluorescent imaging of inflammatory reporters in cardiomyocyte-like cells

Next, we evaluated if the generated reporters for inflammatory stress could also be used in other lineages compared to HLCs. Therefore, we differentiated the hiPSC reporters to cardiomyocyte-like cells (CMLCs) in 21 days. Thereafter, the cells were challenged with a concentration range of TNF-α, IL-1β or IFN-γ and imaged through confocal imaging 24 hours post exposure (Figure 5A). While A20-eGFP showed a concentration-dependent increase in HLCs, this increased could not be observed in CMLCs. Already with the lowest concentration of 2 ng/mL TNF-α and IL-1β a minimal increase in A20-eGFP could be observed. In a similar fashion, ICAM1-eGFP was induced with low cytokine concentrations. In this cell lineage, IFN-γ is also an ICAM1-eGFP inducer. The IRF1-eGFP reporter was exclusively induced with IFN-γ. The VCAM1-eGFP reporter was already expressed in vehicle conditions, in line with the fact that VCAM1 is also a well-known marker of CMLC differentiation[202]. No further induction in the eGFP signal could be observed upon cytokine treatment (Figure 5B).

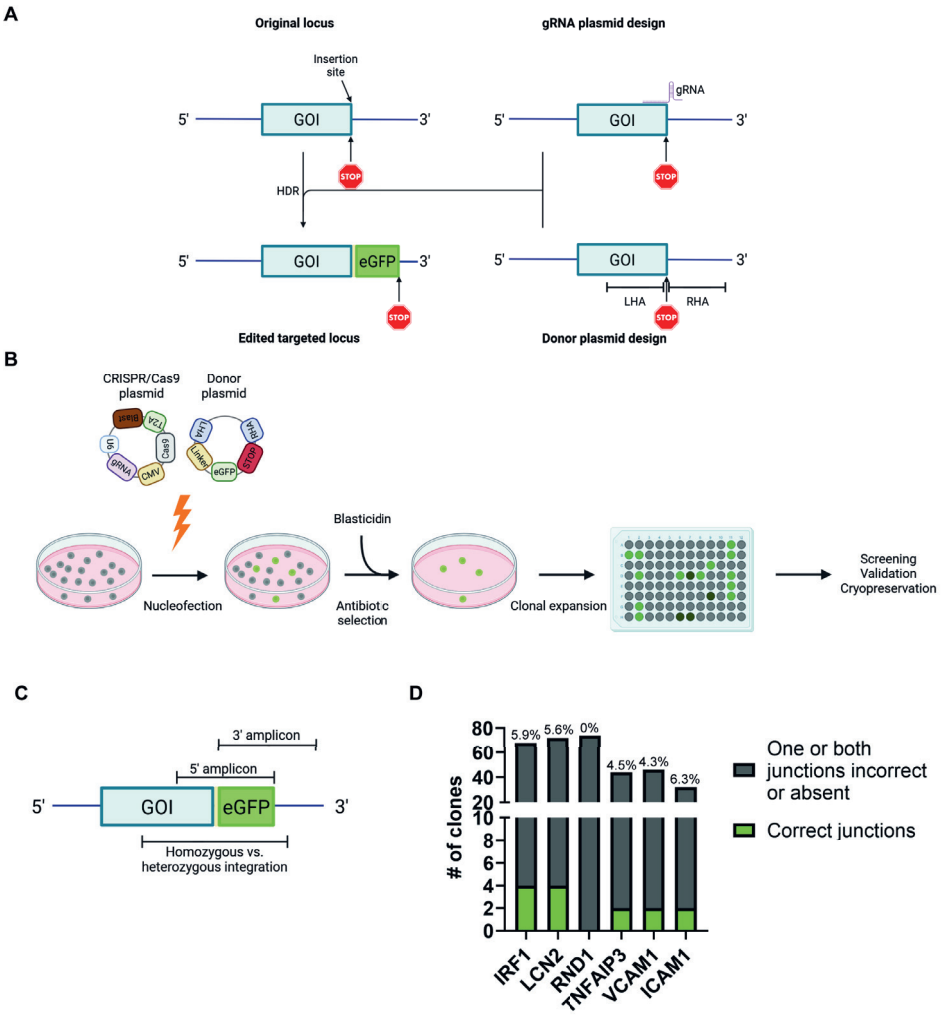
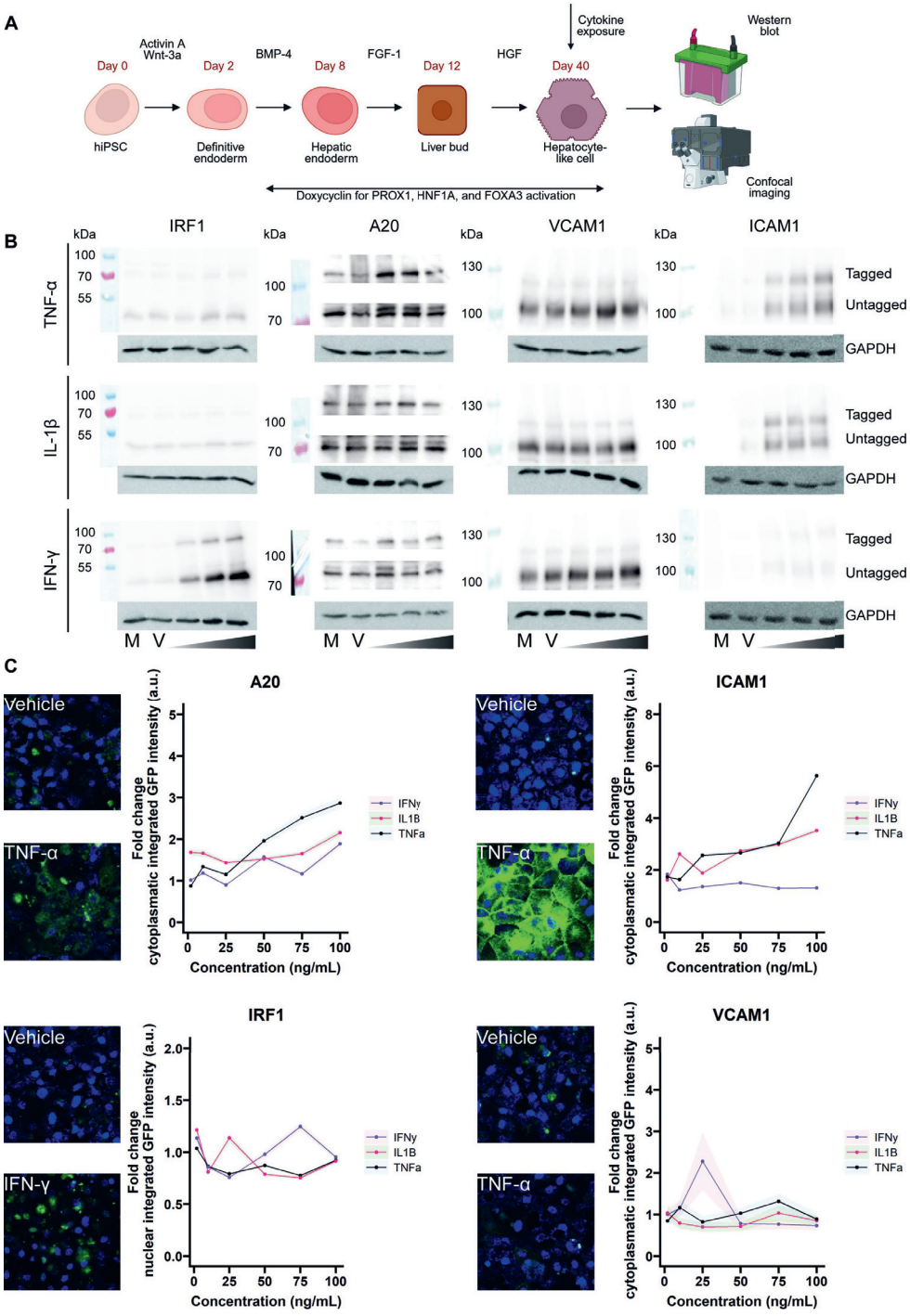


Figure 3. Overview of gene editing strategy for the LCN2, RND1, VCAM1, TNFAIP3 and IRF1 reporters. A) Schematic overview of gene-editing strategy demonstrating important design features. All reporters were targeted C-terminally. The gRNA binding sequences are indicated 3' from the stop codon. The protospacer-adjacent motif (PAM) sequence is located right before the stop codon leading to anticipated double-stranded breaks via HDR 5' of the stop codon. The donor plasmid contained a 1-kb left and right HA with a linker sequence and eGFP. The example shows a successful eGFP integration just before the stop codon. **B)** Schematic visualization of the genome-editing process. Both donor plasmids were presented to the hiPSCs using nucleofection. Cells were selected using blasticidin and single clones were further expanded, screened and validated for proper eGFP integration. In the meantime, potential clones were cryopreserved. **C)** Schematic overview of the junction PCR amplification of the targeted allele to determine exact on-target eGFP insertion. **D)** Overview of the number of clones screened for each reporter and the percentage of clones with correct eGFP insertion based on junction PCRs.


A
Day 0
Activin A
Wnt-3a
Day 2
BMP-4
Day 8
FGF-1
Day 12
HGF
Day 40
Cytokine exposure
Western blot
hiPSC
Definitive endoderm
Hepatic endoderm
Liver bud
Hepatocyte-like cell
Confocal imaging
Doxycyclin for PROX1, HNF1A, and FOXA3 activation
B
IRF1
A20
VCAM1
ICAM1
kDa
TNF-α
IL-1β
IFN-γ
Tagged
Untagged
GAPDH
M V
C
Vehicle
TNF-α
IFN-γ
A20
ICAM1
IRF1
VCAM1
Fold change cytoplasmatic integrated GFP intensity (a.u.)
Fold change nuclear integrated GFP intensity (a.u.)
Concentration (ng/mL)
IFNγ
IL1B
TNFa

◀ **Figure 4. Reporter validation in hiPSC-derived HLC using western blot and confocal imaging. A)** Schematic representation of the differentiation process to HLCs and subsequent exposure and validation strategy. **B)** Protein levels of the biomarker and eGFP in non-treated and 24-hour treated conditions. **C)** Confocal imaging of the reporters 24-hours post exposure to a concentration range of TNF-α, IL-1β or IFN -γ. Data are presented as mean ± SEM (N=3). Scale bar = 50 µm.

Discussion

Inflammatory stress is often observed in drug-induced organ toxicity, and thought to contribute to tissue damage and organ dysfunction[208–210]. Especially the liver is often prone to adverse drug reactions due to its main function in drug metabolism. In this chapter we describe the generation of hiPSC-based fluorescent reporters to study the activation of inflammatory stress signalling in different cell types including HLCs. We systematically identified six (*VCAM1*, *TNFAIP3*, *IRF1*, *LCN2*, *RND1,* and *ICAM1*) NF-κB downstream targets that are upregulated upon TNF-α, IL-1β or LPS exposure in PHH and the rat liver using WGCNA. We generated endogenous fluorescent eGFP reporters for those biomarkers in hiPSC using CRISPR/Cas9 and validated the functionality of the reporters using confocal imaging with the ultimate goal to perform compound screen to assess the role of inflammation in DILI.

CRISPR/Cas9 technology enables scar-free endogenous tagging at the locus of interest with high specificity and has been proven effective in hiPSC[211]. The targeting efficiency is relatively low with CRISPR/Cas9 compared to for instance BAC recombineering and this was also observed in our study (0% for RND1 to 6.3% for ICAM1)[212]. This is likely dependent on the targeting locus, primarily due to differences in chromatin accessibility and active gene expression[213].

Unfortunately, for most of the reporters we were unable to test their functionality in undifferentiated hiPSC due to the lack of biomarker expression in pluripotent cells. In addition, hiPSCs appeared to be unresponsive to TNF-α and IL-1β, which was also described by Chen et al who found no increase in ICAM1 expression upon exposure to both cytokines in hiPSCs[214]. Therefore, differentiation of our hiPSC reporter lines was required to allow functional testing. All reporters, except for LCN2-eGFP were functional in hiPSC-derived HLCs, but signal-to-noise ratio was low except for ICAM1-eGFP. A possible explanation for this is the high presence of naturally fluorescent molecules in hepatocytes, including NADH and FAD that are partially overlapping with the eGFP excitation and emission spectra[215]. Possibly, brighter fluorescent proteins within the same excitation and emission window, like mNeonGreen and StayGold, would give better results[216,217]. Alternatively, red fluorescent reporters can be generated with the bright fluorescent protein mScarlet to minimize the chance of

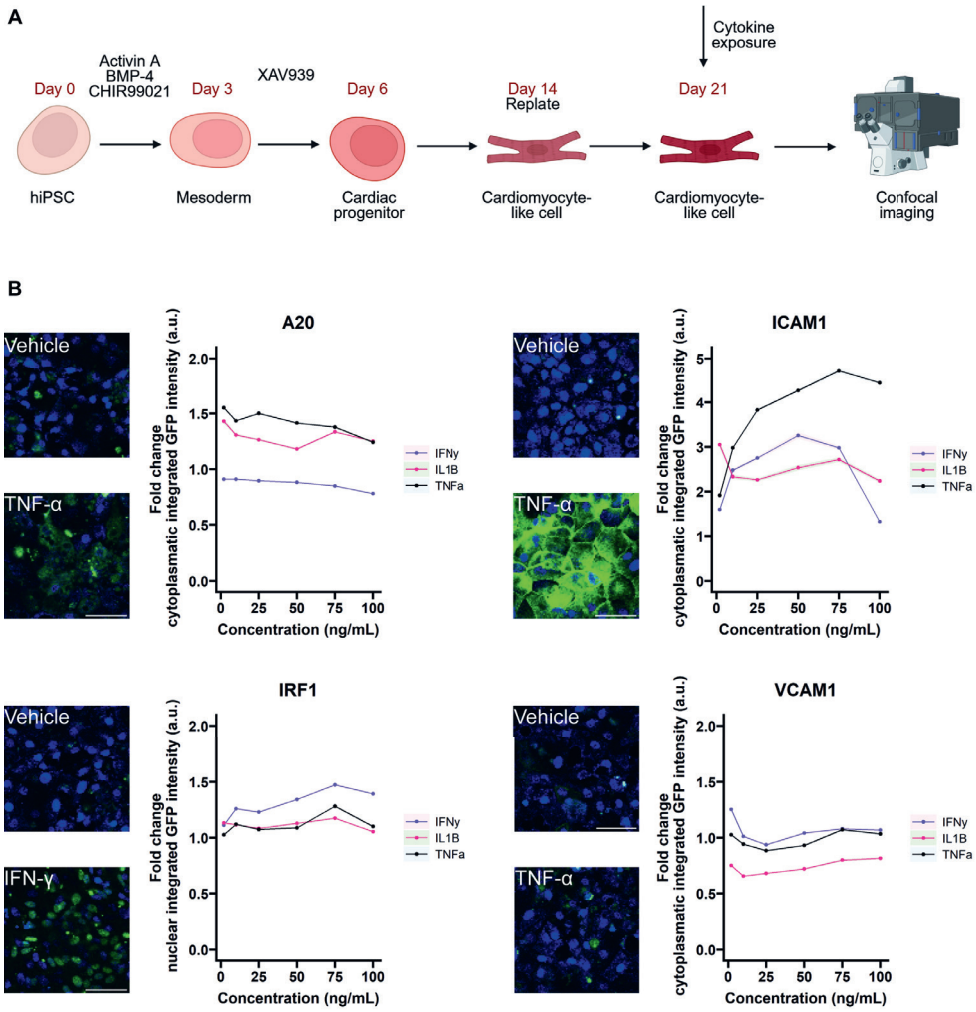


Figure 5. Validation of the generated reporters in hiPSC-derived CMLC using confocal imaging. A) Schematic overview of the CMLC differentiation protocol, exposure and imaging strategy. **B)** Confocal imaging of the reporters 24-hours post exposure to a concentration range of TNF-α, IL-1β or IFN -γ. Data are presented as mean ± SEM (N=3). Scale bar = 50 µm.

compound autofluorescence and already have been proven to be functional in other hiPSC models[218,219]. Another possible way to improve signal-to-noise ratio is the use of phenol-red free medium as phenol red is excited at similar ranges compared to eGFP. All selected hiPSC reporter were tagged heterozygously. To increase eGFP levels during imaging, another clone could be selected that was homozygously tagged. However, homozygously tagged clones where not identified for every target due to its low targeting efficiency and therefore, additional screening on the bulk population should be applied. Furthermore, homozygous tagging could also perturb endogenous protein

functionality via altered stability, degradation and localization and should therefore be taken into consideration for each target individually[220].

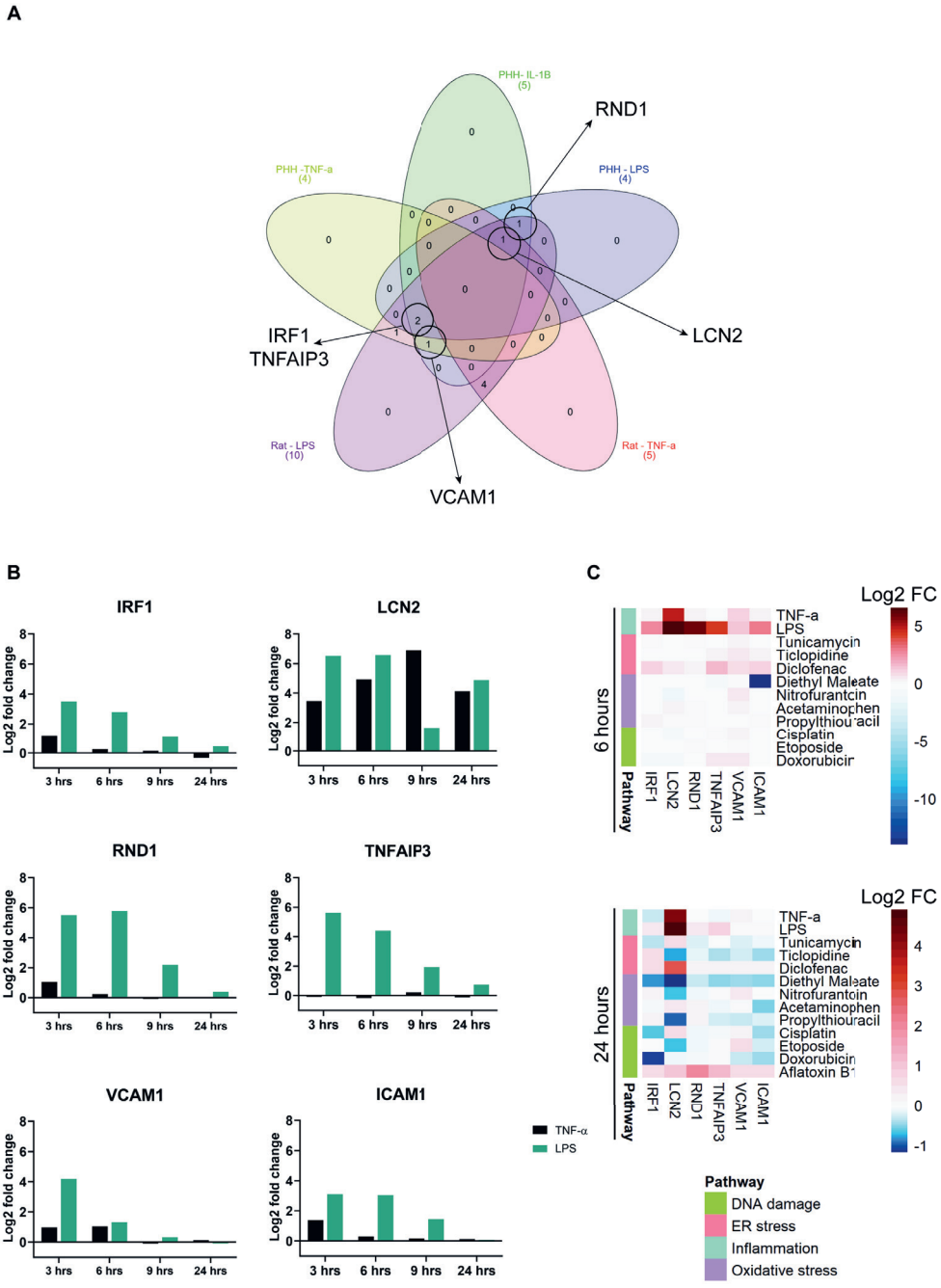
Confocal imaging and subsequent analysis were compromised by the efflux of Hoechst from mainly the nuclei of hiPSC-HLCs possibly via the ABCG2 transporter that is normally crucial for the detoxification of the liver from drugs and other xenobiotics[221]. To overcome this, for future experiments we suggest to further clone a fluorescent protein, like BFP, in the histone H2B type 1-J gene in the existing fluorescent reporters for inflammatory stress. H2B is a protein that is functioning in DNA organization together with other histone proteins and in this way, it enables constitutive visualization of the nuclei in hiPSC and its derived lineages.

We specifically selected the proposed inflammatory biomarkers based on hepatocyte model systems to investigate the (de)activation of inflammation in DILI. However, multiple organs are prone to undergo drug-induced adverse effects. For instance, the cardiovascular system is prone to adverse drug reactions[222]. More particularly it has been shown that inflammation plays a role in the development anticancer-drug induced toxicity, including traditional agents, like doxorubicin, but also novel immune checkpoint inhibitors, like ipilimumab and nivolumab[223,224]. To validate whether the generated inflammatory reporters were also functional in hiPSC-derived cardiomyocyte-like cells, we exposed them to cytokines and measured eGFP induction. We identified that some biomarkers were expressed more in cardiomyocytes (IRF1) compared to hepatocytes (A20) and vice versa. The variation in expression of these targets can be explained by cell-type specific differences in NF-κB/TNF-α signalling. An example of this is the specific NF-κB dimers that are active, like RelA, RelB, c-Rel, p50 and p52[225]. Another example is the chromatin epigenome of the cell type. This controls the expression of downstream NF-κB targets and leads to cell-type specific responses to NF-κB[226]. Before using one of the fluorescent reporters to assess the effect of drugs on inflammatory signalling, the reporter should first be tested using known inflammatory agents, including TNF-α, IL-1β and IFN-γ. Alternatively, we suggest to perform a similar systematic approach to identify the most promising cell-type specific inflammatory markers for each cell type that will be assessed.

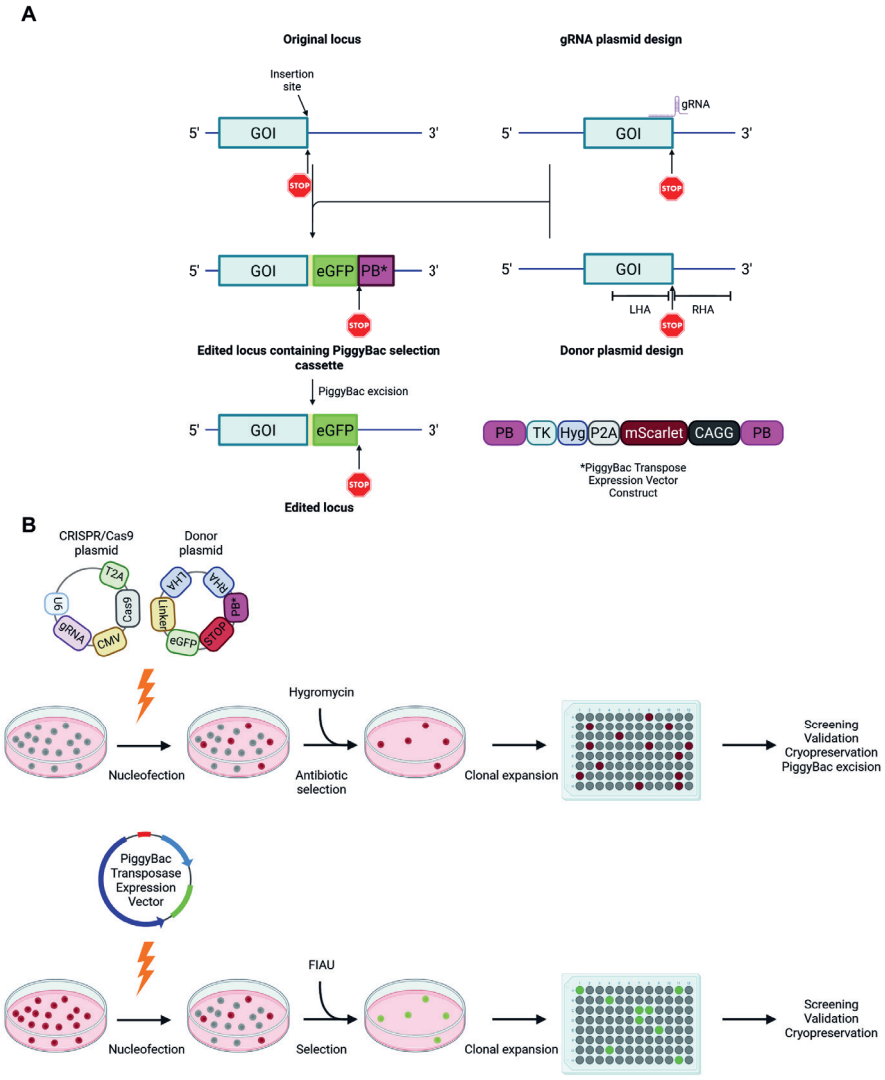
In conclusion, we systematically selected key biomarkers for the inflammatory stress pathway in hepatocytes and generated endogenous fluorescent reporters for these targets in hiPSC using CRISPR/Cas9. The ICAM1, IRF1 and A20 reporter appeared to be the most induced upon cytokine treatment in hiPSC-derived HLCs. We anticipate that these reporters can be used to assess the effect of xenobiotics on the inflammatory signalling pathway in HLCs in the future. Furthermore, the generated reporters for ICAM1 and IRF1 have also been shown to be activated in CMLCs and therefore our

generated reporters can also be used in other hiPSC lineages as well to detect drug liabilities.

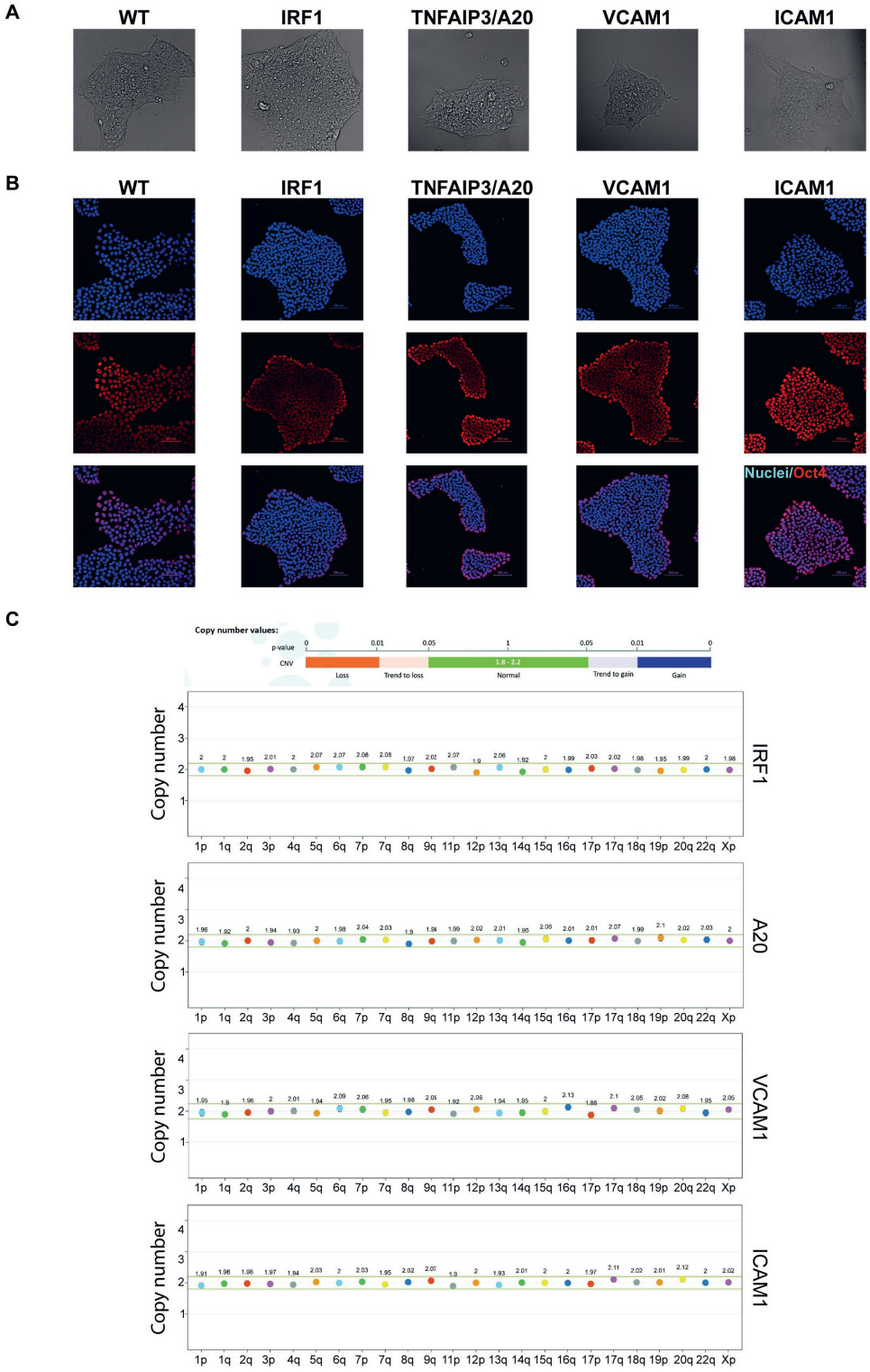
Supplemental Figures



◀ **Supplemental Figure 1. Identification of inflammatory biomarkers in the liver. A)** Venn diagram showing the conditions the selected biomarkers were identified upregulated. The biomarkers upregulated in the most conditions were selected. **B)** Log2 fold change induction of the selected biomarkers after treatment with TNF-α or LPS in rats. **C)** Log2 fold change induction of the selected biomarkers upon inflammatory, DNA damage, ER stress and oxidative stress inducers six- and 24-hours post treatment.



◀ **Supplemental Figure 2. Overview of gene editing strategy for the ICAM1 reporter. A)** Schematic overview of gene-editing strategy demonstrating important design features. The ICAM1 reporter was targeted C-terminally. The gRNA binding sequence is indicated 3' from the stop codon. The protospacer-adjacent motif (PAM) sequence is located right before the stop codon leading to an anticipated double-stranded break via HDR 5' of the stop codon. The donor plasmid contained a 1-kb left and right HA with a linker sequence, eGFP and selection cassette. The example shows a successful eGFP integration before and after selection cassette removal using the PiggyBAC Transposase Expression Vector just before the stop codon. **B)** Schematic visualization of the genome-editing process. Both donor plasmids were presented to the hiPSCs using nucleofection. Cells were selected using hygromycin and single clones were further expanded, screened and validated for proper eGFP and selection cassette integration. In the meantime, potential clones were cryopreserved. Subsequently, the selection cassette was removed using a PiggyBac Transposase Expression Vector and subsequent FIAU selection to enrich for cells where selection cassette removal was successful. Those clones were also further expanded, screen and validated for correct eGFP integration and selection cassette removal.


A
WT
IRF1
TNFAIP3/A20
VCAM1
ICAM1
B
WT
IRF1
TNFAIP3/A20
VCAM1
ICAM1
Nuclei/Oct4
C
Copy number values:
p-value
CNV
Loss
Trend to loss
Normal
Trend to gain
Gain
Copy number
IRF1
A20
VCAM1
ICAM1
1p 1q 2q 3p 4q 5q 6q 7p 7q 8q 9q 11p 12p 13q 14q 15q 16q 17p 17q 18q 19p 20q 22q Xp

◀ **Supplemental Figure 3. Assessment of pluripotent quality of generated hiPSC reporters after genome editing. A)** Representative phase-contrast images depicting morphology in unedited (WT) and eGFP tagged reporters. **B)** Expression of Oct4 in WT and edited lines by immunofluorescence. Scale bar = 100 µm. **C)** Copy number variation (CNV) analysis of the 24 most common abnormalities in hiPSC for the generated hiPSC reporters.

Supplemental tables

Supplemental Table 1. Overview of used antibodies

Target	Source	Catalog #	RRID	Blocking solution	Dilution
A20	Cell Signaling	4625	AB_2204524	5% BSA	1:1000
ICAM1	Cell Signaling	4915S	AB_2280018	5% BSA	1:1000
IRF1	Cell Signaling	8478	AB_10949108	5% BSA	1:1000
LCN2	Cell Signaling	44058	AB_2799257	5% BSA	1:1000
RND1	Abcam	ab118299	AB_10901881	5% non-fat dry milk	1:500 (1 µg/mL)
VCAM1	Cell Signaling	13662	AB_2798286	5% BSA	1:1000
GAPDH	Santa Cruz	sc-32233	AB_627679	5% BSA	1:1000
B-actin	Santa Cruz	sc-47778	AB_626632	5% BSA	1:1000
A-Tubulin	Sigma-Alderich	T-9026	AB_477593	5% BSA	1:1000

Supplemental Table 2. Overview of primer sequences for HA insertion in the donor plasmid.

Target	Homology arm placement	Cloning strategy	HA design strategy	Fw/rvs	Restriction enzymes	Filler + Enzyme sequence	Annealing Sequence	Full primer sequence
A20/TNFAIP3	**Left HA**	RHA first	x	fw	SphI + SalI	GTAGCATGC	TTCTACCGACAGTGACAAGC	GTAGCATGCTTCTACCGACAGTGACAAGC
				rvs		GTTGTCGAC	GCCATACATCTGCTTGAACTG	GTTGTCGACGCCATACATCTGCTTGAACTG
	Right HA		smaller than 965 bp	fw	BamHI + SacI	GATGGATCC	CCGGAAACAGGTGGGTCAC	GATGGATCCCCGGAAACAGGTGGGTCAC
				rvs		GTAGAGCTC	CCTATTGTACTTCTAGGGCAGC	GTAGAGCTCCCTATTGTACTTCTAGGGCAGC
IRF1	**Left HA**	RHA first	smaller than 1108bp	fw	SphI + SalI	GTAGCATGC	TACACAGTTGAGAGGGAAGTCGTGG	GTAGCATGCTACACAGTTGAGAGGGAAGTCGTGG

VCAM1							GTTGTCGACC GGTGCACAGG GAATGGCCTG
	Right HA		rvs		GTTGTCGAC	CGGTGCACAGGGAA TGGCCTG	
		x	fw	XmaI + EcoRI	GTACCCGGG	CAGGGCCCCTGGG CCCCTCTTATTC	GTACCCGGGC AGGGCCCCTG GGCCCCTCTT ATTC
			rvs		GTCAGAATTC	TACCAAGGCGCTCA CACTTCCCTCC	GTCAGAATTCT ACCAAGGCGC TCACACTTCCC TCC
	Left HA	x	fw	SphI + SalI	GTAGCATGC	TGGCTGTTCAGTGAT GGAC	GTAGCATGCT GGCTGTTCAGT GATGGAC
			rvs		GTTGTCGAC	CACTTTTGACTTCTGT GCTTCTAC	GTTGTCGACCA CTTTTGACTTCT GTGCTTCTAC
	Right HA	x	fw	BamHI + SacI	GATGGATCCCTG	ATGCTTGATATGTTCA ACTGGAGAC	GATGGATCCCT GATGCTTGATA TGTTCAACTG AGAC

				rvs		GTAGAGCTC	AGTCTGGCACCAAGAAATCTAC	GTAGAGCTCAGTCTGGCACCAAGAAATCTAC
RND1	**Left HA**	LHA first	smaller than 1056	fw	SphI + SalI	GTAGCATGC	TCACTACAGTGCAGAACTC	GTAGCATGCTCACTACAGTGCAGAACTC
				rvs		GTTGTCGAC	CATAATGGAACAGCTTTTGG	GTTGTCGACCATAATGGAACAGCTTTTGG
	Right HA		x	fw	XmaI + EcoRI	GTACCCGGG	AGTGGAAATTGGAGGGGGGAG	GTACCCGGGAGTGGAAATTGGAGGGGGGAG
				rvs		GTCAGAATTC	CCCACACTCTGCAAGAGAAG	GTCAGAATTCCCCACACTCTGCAAGAGAAG
LCN2	**Left HA**		Both smaller than 681 and 599bp	fw	SphI + SalI	GTAGCATGC	TCTGCCCAGACAAGGATTTC	GTAGCATGCTCTGCCCAGACAAGGATTTC
				rvs		GTTGTCGAC	GCCGTCGATACACTGGTCTG	GTTGTCGACGCCGTCGATACACTGGTCTG

	Right HA			fw	Xmal + EcoRI	GTACCCGGG TGCACAGTGA GTGTGGCTG
				rvs		GTCAGAATTC AATGTGAGAAC TGCCGCTG
				fw		GTGCACAGTGAGTGT GGCTG
				rvs		GAATGTGAGAACTGC CGCTG

Restriction Enzyme	
RE sequence	**RE specific extra bp/ filler**
GCATGC	SphI 3bp before RE
GTCGAC	SalI 3bp before RE
GGATCC	BamHI 3bp before RE
GAGCTC	SacI 3bp before RE
CCCGGG	XmaI 3bp before RE
GAATTC	EcoRI 4bp before RE

Legend:
Extra bp/ filler
Restriction Enzyme
silent mutation PAM
Annealing Region

Supplemental Table 3. Overview of gRNAs used to target specific loci.

Gene	gRNA sequence	PAM	Gene strand	bp between insertion site and PAM site
VCAM1	TAATGCTTGATATGTTCAAC	TGG	+	21
TNFAIP3	TATGGCTAACCGGAAACAGG	TGG	+	11
RND1	AGCTGTTCCATTATGTGAAG	TGG	+	2
LCN2	GCACTCAGCCGTCGATACAC	TGG	-	13
IRF1	ATTCCCTGTGCACCGTAGCA	GGG	+	2
ICAM1	CCCTGAACCTATCCCGGGAC	AGG	+	14

Supplemental Table 4. Overview of junction PCR primers.

Chromo-some	Gene after	Gene	Fw/ Rvs	Primer sequence	Amplicon Size	Region	Genotype
6	LINC02528	TNFAIP3/XM_011536095.1/ XP_011534397.1	Fw	GCAACTGGTGAGACACTTG	WT: 2019	HA upstream	wt/ integration
			Rvs	GCTGGTTGAGTTTATGCAAG	2760	HA downstream	
			Fw	GCAACTGGTGAGACACTTG	1794	HA upstream	Upstream eGFP integration
			Rvs	GTCCATGCCGAGAGTGATC		eGFP	
			Fw	CGACGTAAACGGCCACAAG	1609	eGFP	Down-stream eGFP integration
			Rvs	GCTGGTTGAGTTTATGCAAG		HA downstream	
5	SLC22A5	IRF1/NM_001354924.1/NP_001341853.1	Fw	GGATGTCGTTCCTTATCTCTAG	WT: 1868	HA upstream	wt/ integration
			Rvs	ATGCCAATAATAAGTCCATCAGTG	2609	HA downstream	
			Fw	GGATGTCGTTCCTTATCTCTAG	1637	HA upstream	Upstream eGFP integration
			Rvs	GTCCATGCCGAGAGTGATC		eGFP	
			Fw	CGACGTAAACGGCCACAAG	1615	eGFP	Down-stream eGFP integration
			Rvs	ATGCCAATAATAAGTCCATCAGTG		HA downstream	
1	EXTCL2	VCAM1/NM_080682.2/NP_542413.1	Fw	TAAACAGGAGTGAGTCTTCAG	WT: 2485	HA upstream	wt/ integration
			Rvs	TTATGGGTTACTGCTCAGTG	3226	HA downstream	
			Fw	TAAACAGGAGTGAGTCTTCAG	2018	HA upstream	Upstream eGFP integration
			Rvs	GTCCATGCCGAGAGTGATC		eGFP	

			Fw	CGACGTAAACGGCCACAAG	1851	eGFP	Down-stream eGFP integration
			Rvs	TTATGGGTTACTGCTCAGTG		HA downstream	
9	c9orf16	LCN2/NM_005564.5/NP_005555.2	Fw	CCGCTTCTCCAAATCTCTG	WT: 1685	HA upstream	wt/ integration
			Rvs	GGGTTAGCATGGACATGG	2426	HA downstream	
			Fw	CCGCTTCTCCAAATCTCTG	1614	HA upstream	Upstream eGFP integration
			Rvs	GTCCATGCCGAGAGTGATC		eGFP	
			Fw	CGACGTAAACGGCCACAAG	1455	eGFP	Down-stream eGFP integration
			Rvs	GGGTTAGCATGGACATGG		HA downstream	
12	DDX23	RND1/NM_014470.4	Fw	TTTCCAGAGACAGGGTCTTAC	WT: 1645	HA upstream	wt/ integration
			Rvs	CCCAATTCCAAAGACAAGAG	2386	HA downstream	
			Fw	TTTCCAGAGACAGGGTCTTAC	1604	HA upstream	Upstream eGFP integration
			Rvs	GTCCATGCCGAGAGTGATC		eGFP	
			Fw	CGACGTAAACGGCCACAAG	1425	eGFP	Down-stream eGFP integration
			Rvs	CCCAATTCCAAAGACAAGAG		HA downstream	
NA	NA	NA	Fw	CGACGTAAACGGCCACAAG	643	eGFP	eGFP
			Rvs	GTCCATGCCGAGAGTGATC		eGFP	



CHAPTER 5

A BROAD KINASE INHIBITOR LIBRARY LIVE CELL IMAGING SCREEN USING LIVER, KIDNEY AND CARDIAC HIPSC-ICAM1-EGFP REPORTER LINEAGES IDENTIFIES LIABILITIES FOR TNF-α PATHWAY MODULATION

Linda van den Berk[1,†], Matthijs Vlasveld[1,†], Janet Piñero[2], Palle S. Helmke[3], Gerhard F. Ecker[3], Rob van Rossom[4], Bela Z. Schmidt[4], Catherine Verfaillie[4], Konstantinos Tassis[1], Giulia Callegaro[1], Peter Bouwman[1], Bob van de Water[1]

[1]Division of Cell Systems and Drug Safety, Leiden Academic Centre for Drug Research (LACDR), Leiden University, Leiden, The Netherlands

[2]MedBioinformatics Solutions, Barcelona, Spain

[3]Department of Pharmaceutical Sciences, University of Vienna, Vienna, Austria

[4] Stem Cell Institute, Department of Stem Cell and Developmental Biology, KU Leuven, 3000 Leuven, Belgium

[†]Authors contributed equally

This chapter has been published as:

Vlasveld, M.[‡], **van den Berk, L.[‡]**, Piñero, J., Helmke, P. S., Ecker, G. F., van Rossom, R., Schmidt, B. Z., Verfaillie, C., Tassis, K., Callegaro, G., Bouwman, P., & van de Water, B. (2025). A broad kinase inhibitor library live cell imaging screen using liver, kidney and cardiac hiPSC-ICAM1-eGFP reporter lineages identifies liabilities for TNF-α pathway modulation. *Archives of Toxicology*.

[‡] *Authors contributed equally*

Abstract

Kinase inhibitors (KIs) are an increasing class of drugs targeting protein kinase activity in various pathologies, but predominantly in cancer and autoimmune diseases. Despite successful clinical applications, one of the challenges that remains is their safety, since many KIs lack selectivity and inhibit multi kinases or block pathways that are also important for homeostasis of healthy cells. This may lead to adverse reactions in several critical target organs of toxicity, including heart, liver and kidney. Inflammatory cytokine-mediated intracellular signalling is critical for the control of cell survival and adverse outcome and are modulated by diverse kinases. Likewise, inhibition of kinase activities by on- or off-target effects of KIs may contribute to adverse effects. In this study we systematically screened 760 different KIs targeting the majority of the kinome for their ability to affect TNF-α-mediated expression of ICAM1 in hiPSC-derived renal proximal tubule-like cells (PTLCs), cardiomyocytes-like cells (CMLC) and hepatocyte-like cells (HLC). Palbociclib (CDK4/6), miltefosine (PI3K/AKT/mTOR), gilteritinib (FLT3/AXL), and erdafitinib (FGFR) led to increased expression of the ICAM1-eGFP reporter and the release of chemokines. Kinase inhibitor activity data from the ChEMBL database indicated off-target kinase inhibitor activity associated with enhanced ICAM1-eGFP expression. Finally, clinically relevant KIs that enhanced ICAM1-eGFP expression in PTLCs were found to be associated with renal adverse events in patients. Our overall findings support the application of imaging-based hiPSC-derived ICAM1-eGFP reporter covering different differentiated cell lineages to identify liabilities of novel kinase inhibitors to modulate TNF-α pathways.

Introduction

Dysregulation of protein kinase activity is associated with many diseases and contributes to the development of cancer and neurological, cardiovascular and autoimmune disorders. Therefore, targeting the kinome via kinase inhibitors (KIs) has become a critical therapeutic strategy[227]. About 30% of the drug development efforts are focusing on kinase inhibitors and a total of 72 KIs were approved in 2022[228]. Despite the great potential of these small molecule KIs, it remains challenging to develop selective candidates that are effective and safe[229]. A significant number of KIs exhibit multi kinase inhibition, leading to increased liability to adverse reactions that can be of mild to life threatening nature and can affect numerous target organs[230]. The heart, liver and kidney are most frequently affected by on- or off-target adverse[231–233]. Immune responses that are controlled by inflammatory cytokine signalling are critical in various target organ toxicities[234–236]. Given the critical importance of various kinases in controlling cytokine signalling, inflammatory signalling is at risk for modulation by KIs, in particular for those KIs that are less specific[230]. So far, a systematic evaluation of the effect of KIs on cytokine signalling in different target organs is missing.

TNF-α signalling regulates a broad range of biological activities, including cell proliferation, inflammation and cell death. TNF-α interacts with the cell surface receptors TNFR1 and TNFR2 and triggers receptor trimerization leading to an associated signalling complex consisting of TRADD, TRAF2, c-IAPs and RIPK1[237]. Subsequent engagement of the LUBAC complex, consisting of SHARPIN, HOIL-1L and HOIP, leads to linear ubiquitination of LUBAC, RIPK1, TNFR1 and NF-κB essential modulator (NEMO). Thereafter, a signalling kinase complex is formed consisting of the kinases IKKα, IKKβ and adaptor protein NEMO, and the ubiquitin binding proteins TAK1 and TAB2/3, leading to phosphorylation and degradation of the inhibitor of the κB (IκB) kinase (IKK) complex[237].This enables translocation of the transcription factor Nuclear factor kappa-light-chain-enhancer of activated B cells (NF-κB) to the nucleus. In addition, TAK1 phosphorylates mitogen-activated protein kinase kinases (MAPKKs) leading to activation of the JUN N-terminal kinase (JNK) and the p38 pathway[238]. All these pathways contribute to the induction of downstream targets involved in inflammation, and pro-survival signalling[237]. Expression of cytokines, chemokines and cell adhesion molecules, including intracellular adhesion molecule 1 (ICAM1), enhances the recruitment of pro-inflammatory immune cells[239,240]. Sustained inflammatory signalling can also lead to the induction of cell death via apoptosis, necrosis and necroptosis and thus contribute to tissue injury[241,242]. TNF-α signalling, and in a broader sense inflammation, plays a pivotal role in drug-induced organ toxicity[165,243–245] and liver regeneration upon injury[246]. In addition, inflammation has been shown to play a role in doxorubicin-induced cardiotoxicity and cisplatin-induced renal proximal-tubule toxicity[247,248]. In the context of KI toxicity, involvement of

inflammatory signalling in the mechanism of toxicity of the tyrosine KIs afatinib, ponatinib and sorafenib have been described [249]. Furthermore, VEGF inhibitors and other KIs (e.g. ibrutinib and belvarafenib) have been linked to acute interstitial nephritis[250–252]. Lastly, the TNF-α signalling pathway is dependent on the activity of various kinases, including RIPKs[253], IKKs[254], MAPKs[255] and could therefore be impacted by KIs via on- or off-target pharmacology. Therefore, KIs may have a liability for modulating the TNF-α signalling pathways in normal cells representing different critical organs.

Here we performed a systematic screening of 760 pre-clinical and clinically relevant KIs that are covering a majority of the kinome on the modulation of the TNF-α signalling pathway. We used human-induced pluripotent stem cells (hiPSC) that expressed an endogenously tagged ICAM1-eGFP reporter and were differentiated in hepatocyte-like cells (HLC)[256], cardiomyocyte-like cells (CMLC)[257] and proximal tubule-like cells (PTLC)[258]. Sixteen KIs were identified as enhancers of ICAM1 expression particular in PTLCs, but not HLC and CMLC. Importantly, we were able to associate twelve of these KIs with observed (inflammatory) renal adverse events in clinical trials. Furthermore, we found that eight of these KIs also enhanced pro-inflammatory CXCL8 and CCL20 expression in PTLC. We therefore suggest that our hiPSC screening model is a relevant pre-clinical tool to identify TNF-α pathway modulating agents that might indicate potential adverse events.

Materials & Methods

Reagents

All growth factors for hiPSC differentiations were obtained from Peprotech. CHIR99021 (S1263) and and TTNPB (S4627) were purchased at SelleckChem. XAV-939 (3748) was obtained from Tocris.

Cell culture & Differentiations

The hiPSC Sigma HC3x wildtype (https://hpscreg.eu/cell-line/SIGi001-A-23) and ICAM1-eGFP (https://hpscreg.eu/cell-line/SIGi001-A-24) lines were cultured on Matrigel (Corning) coated plates in mTesR1 medium (Stem Cell Technologies, Vancouver, Canada) and medium was refreshed daily. Cells were split twice a week using ReleSR (Stem Cell Technologies). The hiPSC line with doxycycline-inducible hepatic transcription factors *HNF1A, PROX1 and FOXA3* was a kind gift from the Verfaillie laboratory, Leuven, Belgium[256]. hiPSC differentiation towards hepatocyte-like cells (HLCs), cardiomyocyte-like cells (CMLCs) and proximal tubule-like cells (PTLCs) was performed as previously described[257,258] (Figure 1A). For HLC differentiation, 9,000 cells were directly plated on SCREENSTAR 96 well black imaging plates (655866, Greiner Bio one). To generate CMLCs, hiPSC were initially plated at a density of 200,000 cells/12 well and subsequently, 150.000 cells/96well were reseeded on day 14. $3.0 \cdot 10^6$ cells per T75 were seeded for PTLC differentiation and were replated on day 16 at a density of 52,000 cells per 96-well of a SCREENSTAR plate to enable confocal imaging.

TempO-Seq analysis

After complete differentiation, cells were treated with 0.1% PBS or indicated TNF-α concentrations for a period of 24 hours. Thereafter, cells were lysed using 1x TempO-Seq buffer for 15 minutes at room temperature, followed by storage at -80°C. Whole transcriptome gene expression data was acquired using targeted RNA sequencing technology (BioSpyder Technologies, Inc., Carlsbad, CA, USA). Raw counts were normalized in R using the DEeSeq2 package, followed by log2 fold change normalization[259]. Genes were considered differentially expressed if the false discovery adjusted p-value ≤ 0.05.

High-throughput screening of kinase inhibitor library

CMLCs and PTLCs were pre-stained with 100 ng/mL $Hoechst_{33342}$ for a period of 1 hour. Next, medium was removed and samples were exposed up to 10 µM of the kinase inhibitor library (L1200, SelleckChem, version June 2019). 100 nM propidium iodide (P1304MP, ThermoFisher) was added to the exposure medium, to visualize cell death

induction. After 8 hours of incubation, cells were challenged with TNF-α at the indicated concentrations for a period of 16 hours. For the last two hours of the TNF-α challenge, nuclei of HLCs were stained with 100 ng/mL $Hoechst_{33342}$. Then, cells were imaged on a Nikon Eclipse Ti2 LIPSI microscope, equipped with a 408, 488, 561 and 633 nm laser, using four images per well with an average of 1,034±278, 1,014±198, 765±149 cells/image for PTLCs, CMLCs and HLCs, respectively. After 48 hours, were imaged again to follow-up on further increase of the ICAM1-eGFP signal and cell death induction. The primary screen consisted of one replicate per hiPSC lineage. The secondary screen in PTLCs was performed using three independent biological replicates.

Image analysis & Hit selection

Nuclei were segmented using watershed-masked clustering, as described previously[260]. Segmented nuclei and the other images were then quantified using CellProfiler 4.2.1. The integrated intensity eGFP and area per object of the nuclei and PI positive staining were calculated. To calculate the fraction PI positive cells, the PI positive area was divided by the nuclear area on a cell-by-cell basis. A cell was considered PI positive if 10 % of the nuclear area was covered by PI staining.

For the eGFP intensity hit selection, first the samples where excessive (>35%) cell death was observed were removed from the primary analysis. Compounds exceeding this threshold were included in the secondary screen. Then, a LOESS regression was applied on the TNF-α dose-response curve to determine the threshold for ICAM1 upregulation, compared to standard TNF-α conditions. The threshold was calculated per cell type and set at the level where $TNF\text{-}\alpha_{standard}$ + 95 % CI ≤ $TNF\text{-}\alpha_{dose}$ – 95 % CI, where standard indicates the used concentration for the TNF-α challenge in all samples. All compounds exceeding the threshold were considered an enhanced hit. For downregulating compounds, a similar threshold was set at $TNF\text{-}\alpha_{dose}$ – 95 % CI ≤ $TNF\text{-}\alpha_{standard}$ + 95 % CI. For the validation screen, a similar approach was chosen. Here, all hit compounds were screened in a dose-response between 0.1 nM and 10 µM. Hit candidates were considered validated if the threshold was exceeded at any concentration, independent of their potency.

LegendPlex assay

Upon hiPSC differentiation, cells were exposed to 10 µM of the selected kinase inhibitors. Eight hours post treatment, cells were challenged with TNF-α at indicated concentrations. After sixteen hours, supernatant was collected and spun down to remove cell debris and stored at -80℃ until further usage. Chemokine secretion was determined using the LEGENDplex™ HU Proinflam. Chemokine Panel 1 (740985, Biolegend) according to manufacturer's instructions. Samples were diluted twice and

chemokine concentrations were measured on an Aurora spectral flow cytometer equipped with three lasers and a plate loader (Cytek). Statistics were performed using a student's t-test. P-values were adjusted (p-adj) using the false discovery rate. Chemokine secretion was considered significantly changed if p-adj ≤ 0.05.

Adverse event data

We used ChEMBL data, version 33, to normalize the kinase inhibitors and to generate a compound dictionary. We downloaded the data from Clinical Trials from the Clinical Trials Transformation Initiative (CTTI, https://aact.ctti-clinicaltrials.org/download) on August 2, 2023. We parsed the fields "*name*" and "*description*" from the "interventions.txt" file, and the *brief_title*, and *official_title* from the file studies.txt to keep clinical trials in which there were mentions of the drugs or their synonyms. Reported events (reported_events.txt) were extracted from clinical trials mentioning the kinase inhibitors and kept the clinical trials in which at least one subject was affected. We used the category organ_system to filter ADRs belonging to "Renal and urinary disorders". The data was downloaded from the FDA Adverse Event Reporting System (FAERS, https://open.fda.gov/data/downloads/) on August 2, 2023. We kept reports where the drug was reported as Primary Suspect Drug and matched the names of the drugs to the dictionary generated using ChEMBL. We normalized the names of the adverse events to MedDRA codes using the Unified Medical Language System Metathesaurus. We used the semantic relationships to extract also the codes corresponding to the category "Renal".

Results

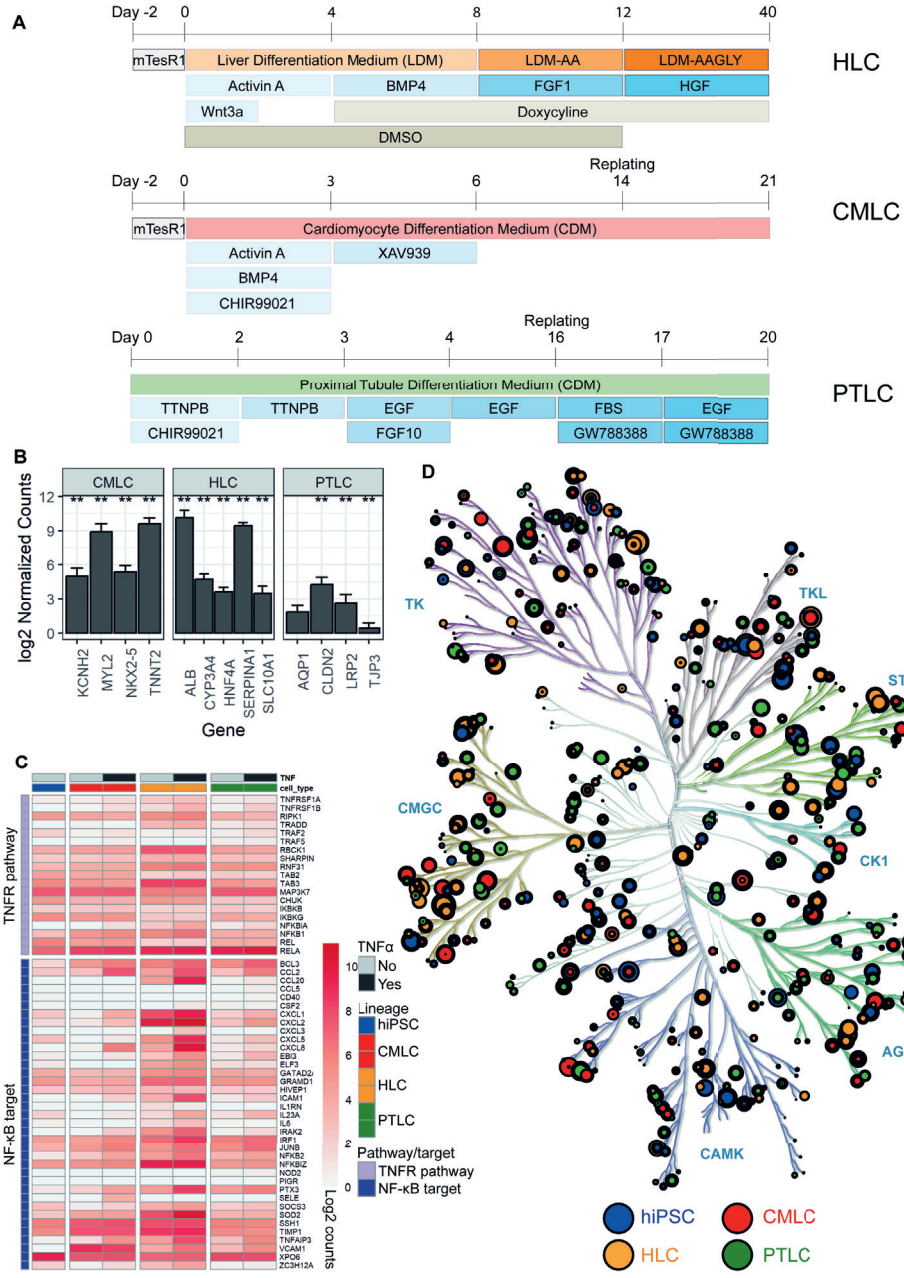
Human iPSC-derived PTLCs, CMLCs and HLCs show differences in the expression levels of protein kinases

To gain insight in the applicability of an hiPSC-based screening system for kinase inhibitor safety assessment, we first characterized the different hiPSC-derived cell lineages. Induced pluripotent stem cells were differentiated to PTLCs, CMLCs and HLCs following previously established[256–258] protocols (Figure 1A) and RNA expression was analysed by targeted whole transcriptome sequencing. First, we analysed cell type specific markers compared to undifferentiated hiPSCs and determined that most markers were significantly (fdr p-adj ≤ 0.01) expressed in their specific cell lineage, except for AQP1 in PTLCs (fdr p-adj = 0.096; Figure 1B). Next, we compared the gene expression of signalling molecules that are downstream of TNFR1, with a focus on genes enriched for the canonical NF-κB pathway according to the DoRoThea[261] database (Figure 1C). The relative expression of genes involved in the TNF-α signalling pathway (Figure 1C, upper panel) was similar between all cell types, independent of

TNF-α stimulation. The expression of TNF-α pathway NF-κB target genes was generally higher in HLCs compared to CMLCs and PTLCs (Figure 1C, lower panel). The latter two lineages showed similar expression levels for most of the target genes. Given our focus on kinase inhibitors, we also examined the expression of the kinome in the three different lineages. We extracted the expression data of 536 human kinases (Supp. table 1) and projected the expression of these kinases on a kinome map[262,263]. Although the expression levels of various kinases are different between cell types, in general, similar kinases were expressed (Figure 1C).

ICAM1 reporter can be used as read-out for TNF target gene expression in all cell types

To monitor any enhancement of TNF-α target gene expression that can be linked to adversity upon KI exposure and TNF-α challenge, we used fluorescent reporters for TNF-α-induced activation of the NF-κB pathway. The NF-κB target genes *ICAM1* and *VCAM1* encode surface glycoproteins expressed under inflammatory conditions and act as a major regulator of leukocyte attractions[264]. For both targets, an eGFP reporter was generated (Supplemental Figure 1 and Supplemental Table 2) in hiPSCs using CRISPR-Cas9 assisted tagging of the endogenous proteins and both reporters were differentiated in PTLCs, CMLCs and HLCs, followed by 24 hours exposure to TNF-α and subsequent confocal imaging. In all three cell types, the ICAM1-eGFP reporter was expressed at higher levels than the VCAM1-eGFP reporter (Figure 2A-C) and the VCAM1-eGFP reporter did not show a dose-response in CMLCs and HLCs (Figure 2B, 2C). Importantly, most inhibitors that target the IKK complex upstream of NF-κB activation were able to block ICAM1-eGFP induction by TNF-α in all three cell lineages (Supplemental Figure 2). For further studies we used the ICAM1-eGFP reporter to screen kinase inhibitors for their effects on TNF-α signalling.


A
Day -2
0
4
8
12
40
mTesR1
Liver Differentiation Medium (LDM)
LDM-AA
LDM-AAGLY
HLC
Activin A
BMP4
FGF1
HGF
Wnt3a
Doxycyline
DMSO
Replating
Day -2
0
3
6
14
21
CMLC
mTesR1
Cardiomyocyte Differentiation Medium (CDM)
Activin A
XAV939
BMP4
CHIR99021
Replating
Day 0
2
3
4
16
17
20
Proximal Tubule Differentiation Medium (CDM)
PTLC
TTNPB
TTNPB
EGF
EGF
FBS
EGF
CHIR99021
FGF10
GW788388
GW788388
B
CMLC
HLC
PTLC
log2 Normalized Counts
KCNH2
MYL2
NKX2-5
TNNT2
ALB
CYP3A4
HNF4A
SERPINA1
SLC10A1
AQP1
CLDN2
LRP2
TJP3
Gene
C
TNF
cell_type
TNFR pathway
NF-κB target
TNFRSF1A
TNFRSF1B
RIPK1
TRADD
TRAF2
TRAF5
RBCK1
SHARPIN
RNF31
TAB2
TAB3
MAP3K7
CHUK
IKBKB
IKBKG
NFKBIA
NFKB1
REL
RELA
BCL3
CCL2
CCL20
CCL5
CD40
CSF2
CXCL1
CXCL2
CXCL3
CXCL5
CXCL6
EBI3
ELF3
GATAD2A
GRAMD1B
HIVEP1
ICAM1
IL1RN
IL23A
IL6
IRAK2
IRF1
JUNB
NFKB2
NFKBIZ
NOD2
PIGR
PTX3
SELE
SOCS3
SOD2
SSH1
TIMP1
TNFAIP3
VCAM1
XPO6
ZC3H12A
Log2 counts
TNFα
No
Yes
Lineage
hiPSC
CMLC
HLC
PTLC
Pathway/target
TNFR pathway
NF-κB target
D
TK
TKL
STE
CMGC
CK1
AGC
CAMK
hiPSC
CMLC
HLC
PTLC

◀ **Figure 1. Characterization of differentiated iPSCs towards hepatocyte, cardiomyocyte and proximal tubular-like cells. A** Overview of differentiation schemes for hepatocyte-like cells (HLCs), cardiomyocyte-like cells (CMLCs) and proximal tubular-like cells (PTLCs) **B** mRNA expression levels of cell type specific markers. Data is log2 counts per million normalized. Asterisks indicate significant (fdr p-adjusted ≤ 0.01) expression compared to towards induced pluripotent stem cells (hiPSC) control. **C** mRNA expression levels of TNF-α signalling pathway related (target) genes. Data is log2 counts per million normalized. **D** Kinome tree showing the expression of various kinases per cell type. Blue indicates undifferentiated iPSCs, orange indicate HLCs, red indicates CMLCs and green indicates PTLCs. Size of the dots indicate the log2 normalized counts of each kinase gene. See supplementary Table 1 for the normalized count data.

Proximal tubular cells are most susceptible towards KI-induced changes of ICAM1-eGFP expression

760 kinase inhibitors were screened for their potential to interfere with TNF-α-induced ICAM1 expression in the three different lineages (Figure 3A). Upon differentiation, cells were treated for eight hours with each individual KI, followed by a TNF-α challenge. Forty-eight hours after KI exposure, eGFP levels were measured. Thresholds for hit identification were then calculated based on point-of-departure approach as used previously[265]. Here, we have used the dose-response curve of TNF-α treated cells and calculated the PoD of the ICAM1-eGFP expression in the various lineages to identify compounds that reduce TNF-target gene levels (Figure 3B, dashed red line). Most of the KIs that blocked ICAM1-eGFP expression overlapped between the three lineages (Figure 3C, Supplemental Table S3). Next, we checked the intended targets of the various inhibitors and their stage in clinical development based on the manufacturer's compound annotations and ChemBL data (Figure 3D, 3E). The top three most frequently identified intended targets for these compounds were related to protein tyrosine kinase signalling, PI3K/AKT/mTOR and angiogenesis pathway signalling, among other pathways (Figure 3D). For these three respective pathways, ten, six and seven inhibitors already entered clinical trials (Figure 3E).

Next, we also assessed enhancers of ICAM1-eGFP expression using the same approach. Again, the threshold for TNF target gene upregulation was calculated based on the point-of-departure approach, now for enhancement compared to control conditions (Figure 4A, dashed red line). Interestingly, here little overlap of KIs that significantly enhanced ICAM1-eGFP expression was found between different cell types (Figure 4B, Supplemental table S3). Targets that enhanced ICAM1-eGFP induction included PI3K/mTOR AKT signalling (e.g. bimiralisib, GDC-0084, pictisilib) and cell cycle inhibitors (e.g. palbociclib isethionate, SU9516) (Figure 4C). Remarkably, half of the identified PI3K/AKT/mTOR (12/24) and cell cycle inhibitors (6/12) has already entered clinical trials (Figure 4D).

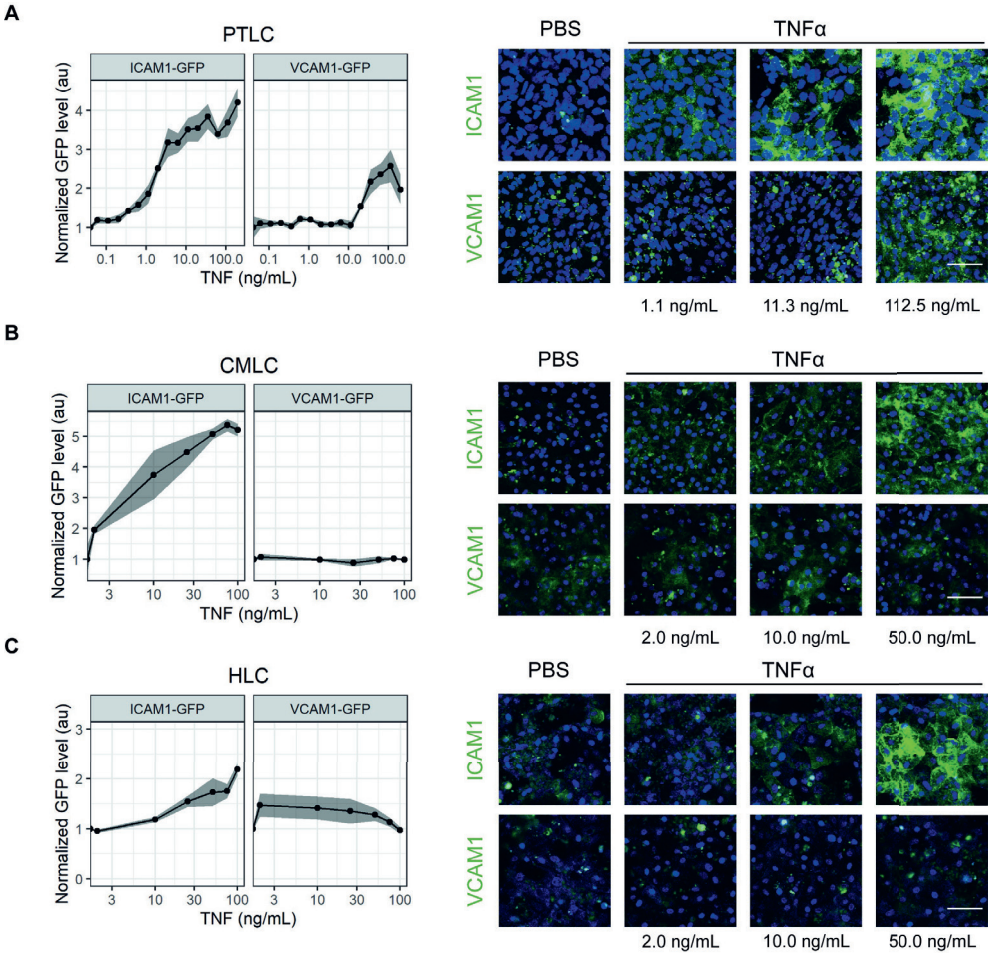


Figure 2. TNF-α-induced response in iPSC ICAM1-eGFP and VCAM1-eGFP reporters. Normalized ICAM1-eGFP and VCAM1-eGFP expression of PTLCs (**A**), CMLCs (**B**) and HLCs (**C**) after TNF-α stimulation for 24 h with indicated concentrations. The average value ± standard deviation (grey area) is shown for 3 independent biological replicates. Scale bar: 50 µm.

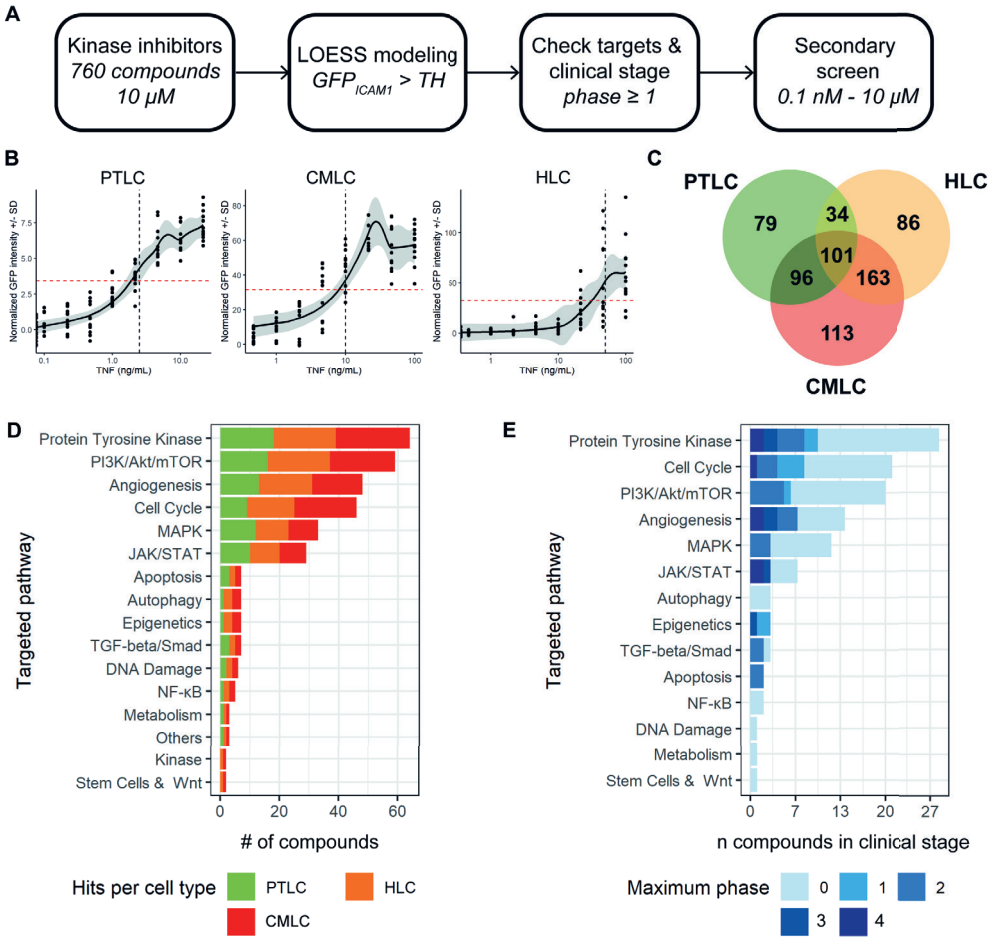
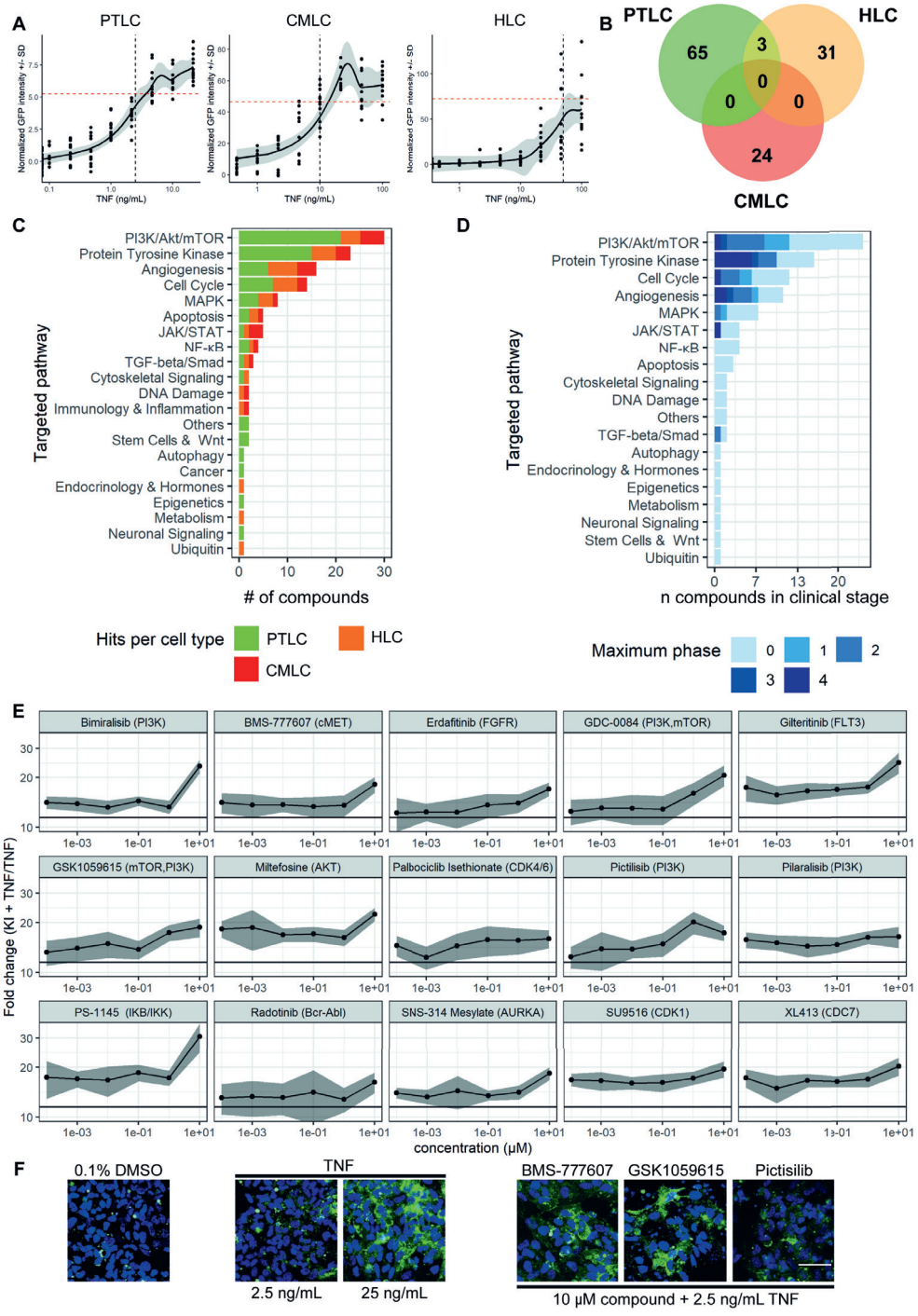


Figure 3. High-throughput screening of kinase inhibitors that repress ICAM1-eGFP expression in HLC, CMLC and PTLC lineages. A Flowchart of the screen. **B** Point-of-departure (PoD) calculations per reporter. Cells were treated with indicated concentrations of TNF-α. Thereafter, a loess curve-fit was performed with estimated standard errors between the lowest and highest TNF-α concentration. The black dashed vertical line indicates the used TNFα concentration per cell type. The PoD (i.e. threshold for reduced ICAM1-eGFP expression) was set at the point where the predicted ICAM1-eGFP expression – standard error was larger than the ICAM1-eGFP + standard error at the used TNF-α concentration. The PoD is indicated by the horizontal red dashed line. **C** Venn diagram showing the identified hits in the primary screen for each iPSC lineage. **D** Pathways that are targeted by compounds identified in the primary screen. **E** Clinical phase of the identified kinase inhibitors in the primary screen


A
PTLC
CMLC
HLC
Normalized GFP intensity +/- SD
TNF (ng/mL)
B
PTLC
HLC
CMLC
65
3
31
0
0
0
24
C
Targeted pathway
PI3K/Akt/mTOR
Protein Tyrosine Kinase
Angiogenesis
Cell Cycle
MAPK
Apoptosis
JAK/STAT
NF-κB
TGF-beta/Smad
Cytoskeletal Signaling
DNA Damage
Immunology & Inflammation
Others
Stem Cells & Wnt
Autophagy
Cancer
Endocrinology & Hormones
Epigenetics
Metabolism
Neuronal Signaling
Ubiquitin
of compounds
D
Targeted pathway
n compounds in clinical stage
Hits per cell type
PTLC
HLC
CMLC
Maximum phase
E
Bimiralisib (PI3K)
BMS-777607 (cMET)
Erdafitinib (FGFR)
GDC-0084 (PI3K,mTOR)
Gilteritinib (FLT3)
GSK1059615 (mTOR,PI3K)
Miltefosine (AKT)
Palbociclib Isethionate (CDK4/6)
Pictilisib (PI3K)
Pilaralisib (PI3K)
PS-1145 (IKB/IKK)
Radotinib (Bcr-Abl)
SNS-314 Mesylate (AURKA)
SU9516 (CDK1)
XL413 (CDC7)
Fold change (KI + TNF/TNF)
concentration (μM)
F
0.1% DMSO
TNF
2.5 ng/mL
25 ng/mL
BMS-777607
GSK1059615
Pictisilib
10 μM compound + 2.5 ng/mL TNF

◀ **Figure 4. High-throughput screening of kinase inhibitors that enhance ICAM1-eGFP expression in HLC, CMLC and PTLC lineages. A** Point-of-departure (PoD) calculations per lineage. Cells were treated with indicated concentrations of TNFα. Thereafter, a loess curve-fit was performed with estimated standard errors between the lowest and highest TNFα concentration. The black dashed vertical line indicates the used TNFα concentration per cell type. The PoD (i.e. threshold for enhanced ICAM1-eGFP expression) was set at the point where the predicted ICAM1-eGFP expression – standard error was larger than the ICAM1-eGFP + standard error at the used TNFα concentration. The PoD is indicated by the horizontal red dashed line. **B** Venn diagram showing the identified hits in the primary screen for each hiPSC lineage. **C** Pathways that are targeted by compounds identified in the primary screen. **D** Clinical phase of the identified kinase inhibitors in the primary screen. **E** Concentration–response curves of validated hits in PTLC-ICAM1-eGFP reporter cells. Data shown indicates fold-change normalized to 0.1% DMSO + 2.5 ng/mL TNF-α, indicated by the horizontal black line. **F** Example images of PTLC samples of control conditions and after KI + TNF exposure (data shown in E). For the compounds, example images are shown for samples treated using 10 µM of the indicated compound and 2.5 ng/mL TNF. Scale bar: 50 µm. Data is shown as mean ± standard deviation (grey area) for three independent biological replicates.

Since PTLCs were most sensitive for identification of the effects of KIs, possibly due to relatively high sensitivity towards TNF-α, we further focused on this cell type and performed a secondary screen using a concentration-response analysis to address the potency of the different KIs. We particular focused on the enhancers of the ICAM1-eGFP induction that have entered clinical trials, since this could impact on stimulation of inflammatory responses[266]. In the secondary screen, a significant enhancement of ICAM1-eGFP expression for 16/68 of the candidate hits was found and these compounds were considered validated hits (Figure 4E, 4F); for most of these KIs enhancement of ICAM1 expression was observed between 1 and 10 µM. For comparison of our screening concentrations to observed human maximum blood plasma concentrations (Cmax), we searched in literature for clinical trial reports. For ten of the validated hits, a Cmax ranging between 0.26 and 78.3 µM was found (Table 1), suggesting that the concentrations used in the secondary screen fall within a physiologically relevant range[267–275]. For the validated compounds, different targets were impacted, including PI3K/mTOR related targets (bimiralisib, GDC-0084, GSK1059615), CDK related targets (palbociclib isethionate, SU9516, XL413) and cMET (BMS-777607).

Validated hits are associated with renal adverse events in the clinic

Increased inflammation can lead to an increase in leukocyte recruitment to the site of injury and thereby contribute to adverse effects in acute kidney injury[266].

Table 1. Overview of maximum blood plasma (Cmax) concentrations of validated hits. Overview of all validated KI that enhance ICAM1-eGFP expression. NA indicates no pharmacokinetic data could be found. For each compound, the maximum tested dose and related Cmax in the referred study was considered.

Name	Target	Molecular weight (g/mol)	Clinical Phase	Maximum dose	Cmax (ng/mL)	Cmax (µM)	Reference
Bimiralisib	PI3K	411.4	2	200 mg	1200	2.92	Janku et al. (2024)
BMS-777607	cMET	512.9	pre-clinical	NA	NA	NA	NA
Edafitinib	FGFR	446.6	4	12 mg	2690	6.02	Markham (2019)
GDC-0084	PI3K	382.4	2	65 mg	99.4	0.26	Wen et al. (2020)
Gilteritinib	FLT3	552.7	4	120 mg	282	0.51	James et al. (2020)
GSK1059615	PI3K	333.4	pre-clinical	NA	NA	NA	NA
Miltefosine	AKT	407.6	4	150 mg	31900	78.3	Del mar Castro et al. (2017)
Palbociblib	CDK4/6	447.5	4	150 mg	91	0.20	Flaherty et al. (2012)
Pictisilib	PI3K	513.6	2	450 mg	1001	1.95	Sarker et al. (2015)
Pilaralisib	PI3K	541.0	2	600 mg	21600	39.9	Wheler et al. (2017)
PS-1145	IKB/IKK	322.8	pre-clinical	NA	NA	NA	NA
Radotinib	BCR-ABL	530.5	3	400 mg	250	0.47	Seo et al. (2017)
SNS-314	AURKA	430.9	1	NA	NA	NA	NA
SU9516	CDK1	241.3	1	NA	NA	NA	NA
XL413	CDC7	326.2	2	100 mg	5993.5	18.4	Clinical trials database, NCT00886782

Therefore, we questioned whether the identified KIs that enhance ICAM1 signalling are associated with renal adverse events in the clinic or clinical trials. For this, the FDA adverse events reporting system (faers, https://open.fda.gov/data/downloads/) and clinical trial transformation initiative database (www.clinicaltrials.gov) were mined for any renal adverse event. Four of the identified hits (palbociclib, miltefosine, gilteritinib and erdafitinib) have FDA approval and are currently on the market (Figure 5A). Both miltefosine and gilteritinib have black box warnings for teratogenicity and carcinogenicity, respectively, but not for renal toxicity. As expected, for these marketed drugs we could find more reports of renal adverse events than for the drugs that are at earlier stages of clinical development (Figure 5B). Although data is limited for the remaining KIs, most of those drugs already showed some (inflammatory-related) renal adverse events during phase 1/2 clinical trials. Of the marketed KIs, both palbociclib and gilteritinib are frequently associated with acute kidney injury and impairment of renal function in the clinic (Figure 5C). Miltefosine is associated with impairment of renal function and tubulointerstitial nephritis. Of the drugs that are currently in early stages of clinical trials, bimiralisib and pictilisib are associated with renal injury and renal failure, respectively. For other KIs, mostly less severe kidney related events were identified (e.g. proteinuria, dysuria, glucose in urine), although the limited sample size for these compounds does not allow strong conclusions. Moreover, more severe kidney disease in future clinical use cannot be ruled out upon observation of these biomarkers. For example, proteinuria can be an early marker for more severe (kidney) pathologies[276,277].

Enhanced ICAM1 expression is indicative for increased chemokine secretion

As upregulation of ICAM1 expression is indicative for increased leukocyte attraction[278], we tested whether TNF-α-stimulated PTLCs induce the transcription and increased protein secretion of chemokines and cytokines, with a focus on those that are available within the BioLegend LegendPlex pro-inflammatory panels (Figure 6A). Despite high *IL23A* mRNA levels upon treatment with TNF-α, transcription of the selected cytokine genes was not significantly induced and *IL-18* expression showed even significant downregulation (fdr p-adj = 0.04). Expression of the chemokine genes *CXCL5, CXCL10, CXCL1, CCL2 and CCL11* was significantly (fdr p-adj ≤ 0.05) upregulated by TNF-α, whereas for most other selected chemokine genes mRNA levels showed an upward but non-significant trend (Figure 6A). In line with these findings, TNF-α exposed PTLCs showed increased chemokine secretion in a concentration-dependent manner (Figure 6B). We then determined whether the KIs that enhanced ICAM1-eGFP induction also increased chemokine secretion. Prior treatment of PTCLs with several KIs, including miltefosine, bimirasilib, and pictisilib, enhanced the TNF-α-induced secretion of CCL20 and CXCL8(Figure 6C). Interestingly, an increase in CCL20 and CXCL8 secretion

could also be observed for compounds that did not strongly affect ICAM1 expression in PTLCs, including AMG319 and CMLC hit KX2-391[279].

Identified kinase inhibitors enhance TNF target gene expression via off target effects

We wondered about the selectivity of the candidate enhancer hits and characterized them by mining the ChEMBL database (https://www.ebi.ac.uk/chembl/) for possible on- and off-targets. pChEMBL values were used to identify candidate KI targets by comparing inhibitory or dissociation constants (Figure 7A) or IC50 values (Figure 7B) for these targets. Out of the 16 KIs that increased TNF-α signalling in PTLCs, three compounds were found in the database: pictilisib, BMS-777607 and GSK1059615. For pictisilib and BMS-777607 it was validated that these compounds had the highest affinity for their intended target (PI3K/AKT and cMET, respectively). Furthermore, many other kinases were also identified as targets of pictisilib and BMS-777607 within the range of our screening concentrations (0.1 – 10 µM; Figure 4F). For GSK1059615 no data was available on the intended target (PI3K/AKT/mTOR), but many off targets (e.g. CLK1, CLK2, TAOK1) were reported within screening concentration range. BMS-777607 (AXL, MET, MST1R, TYRO3 inhibitor) had many off-targets that were closely related to the intended target in the tyrosine kinase domain, shown by the close proximity of the off-targets in the kinome tree (Figure 7C). On the contrary, pictilisib (PI3K/mTOR inhibitor) had many structurally different targets throughout the kinome, suggesting that this compound might be non-specific. Similarly, GSK1059615 (AKT1/mTOR inhibitor) also has quite diverse off-targets with high affinity, although the number of potential off-targets was less compared to pictilisib. We verified whether these potential intended and off targets are also present in PTLCs, CMLCs and HLC. mRNA expression of these KI targets was highly similar and the majority of these genes showed moderate to high expression values (Suppl. Figure S3). The various targets for these three inhibitors clustered together in the kinome map: pictilisib (CMGC kinases), BMS-777607 (tyrosine kinases, TK) and GSK1059615 (AGC kinases; Figure 7C), all identified off-targets were mapped on the kinome map [263]. Next, we used StringDB to evaluate whether the off-targets were associated with the IKK-complex (CHUK, IKBKB, IKBKG), IκBα (NFKBIA) and the genes for canonical NF-κB (RELA, P65) signalling[280]. To minimize the possibility of finding false positive relationships, nodes were only included if (i) there was a high confidence (≥ 0.7) for a relationship between genes and (ii) the relationship has been described in various literature, shown in experiments or in databases. Of relevance, 29/75 candidate off-target kinases showed an (in)direct relationship with the NF-κB signalling pathway components (Figure 7D). The expression of the different kinases was not affected by TNF-α treatment (Supplemental Figure 4).

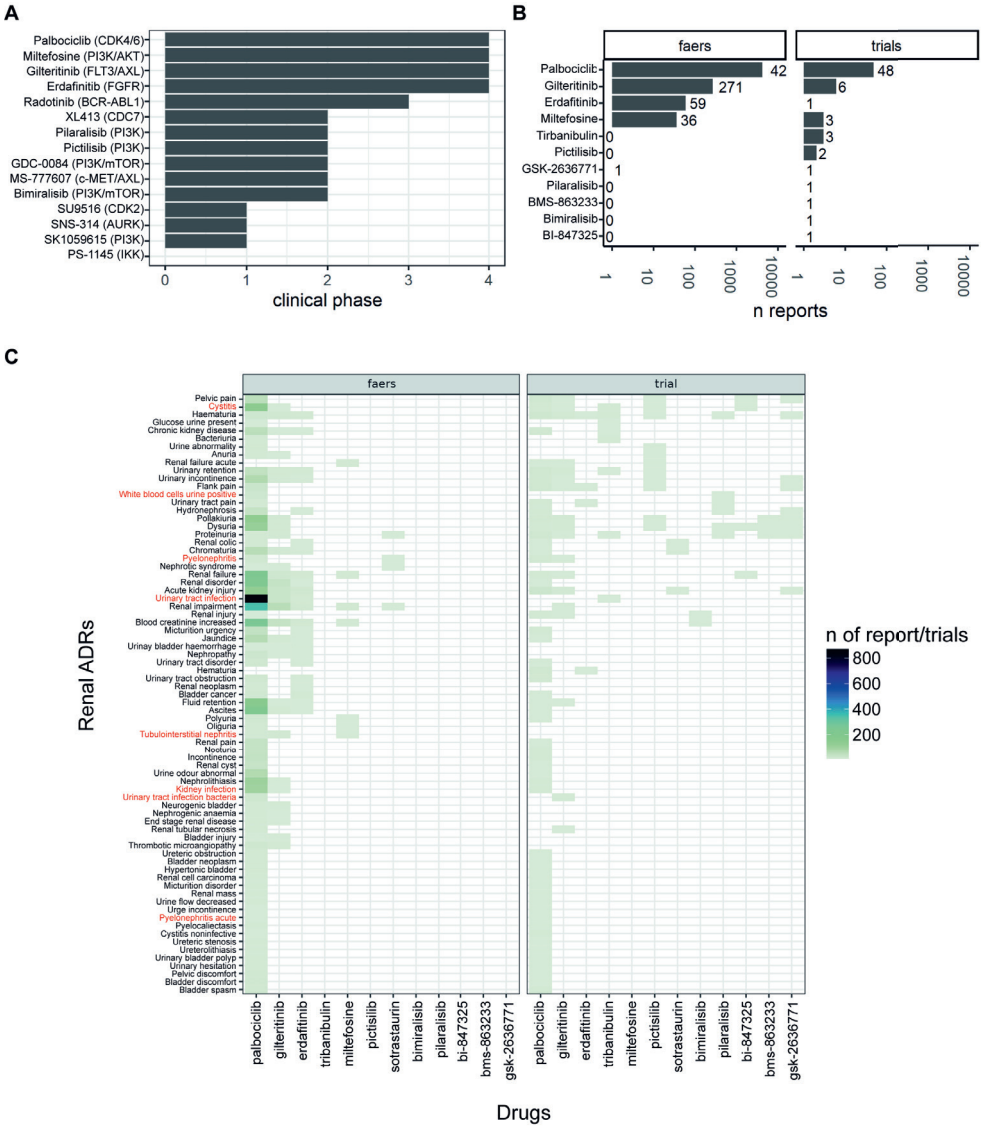


Figure 5. Clinical renal injury associations of ICAM1-eGFP enhancing kinase inhibitors. A Clinical stage of identified kinase inhibitors. Colour indicates whether marketed (phase 4) compounds have a black box warning. **B** Total number of renal injury events identified in faers or from clinical trials (www.clinicaltrials.gov) per kinase inhibitor. **C** Renal injury events identified for each compound in faers or within the clinical trial database. Red marked adverse events are associated with inflammation. A darker colour indicates a higher frequency of the mentioned pathology by the indicated compound

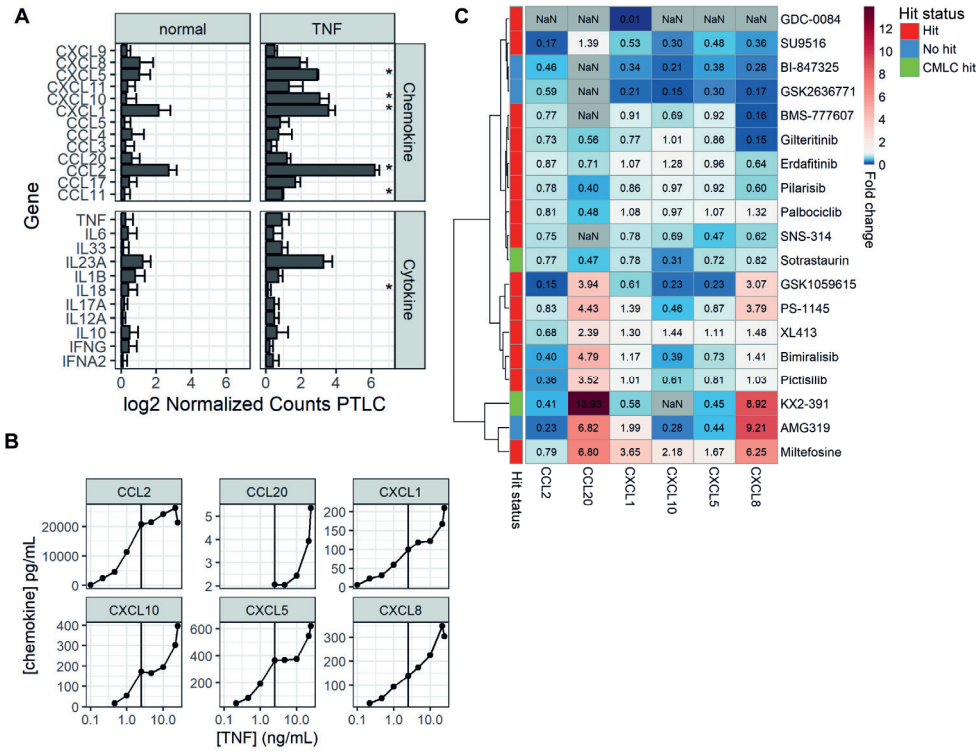


Figure 6. Effect of ICAM1-eGFP enhancing kinase inhibitors on chemokine and cytokine expression in PTLCs. A) mRNA expression of chemokines and cytokines of the Biolegend Legendplex panels in proximal tubular cells in unstimulated and TNF-α-stimulated conditions. Error bar indicates standard deviation based on three independent biological replicates. Asterisks indicate significant (fdr p-adjusted ≤ 0.05) differential expression upon TNF-α treatment compared to unstimulated conditions. **B)** Concentration of various chemokines in PTLC medium upon stimulation with different concentrations of TNF-α. PTLCs were stimulated with indicated concentrations TNF-α for 16 h. Thereafter, medium was harvested and chemokine concentration was measured using the LegendPlex assay. Vertical line indicates a concentration of 2.5 ng/mL TNF-α, which is the concentration that was used for the high-throughput screen in Fig. 3. Data is shown for a single biological replicate. **C)** Concentration in PTLC medium of selected chemokines after treatment of PTLCs with mentioned compounds and TNF-α. PTLCs were treated with compounds for 8 h, followed by stimulation with 2.5 ng/mL TNF-α for 16 h. Then, medium was harvested and chemokine concentration was measured using the LegendPlex assay. Data was fold change normalized towards the 0.1% DMSO + 2.5 ng/mL TNF-α control. Red indicates increased chemokine expression; blue indicates decreased chemokine expression. NaN (grey) indicates that no significant secretion of chemokines was measured. The average value of two independent biological replicates is shown.

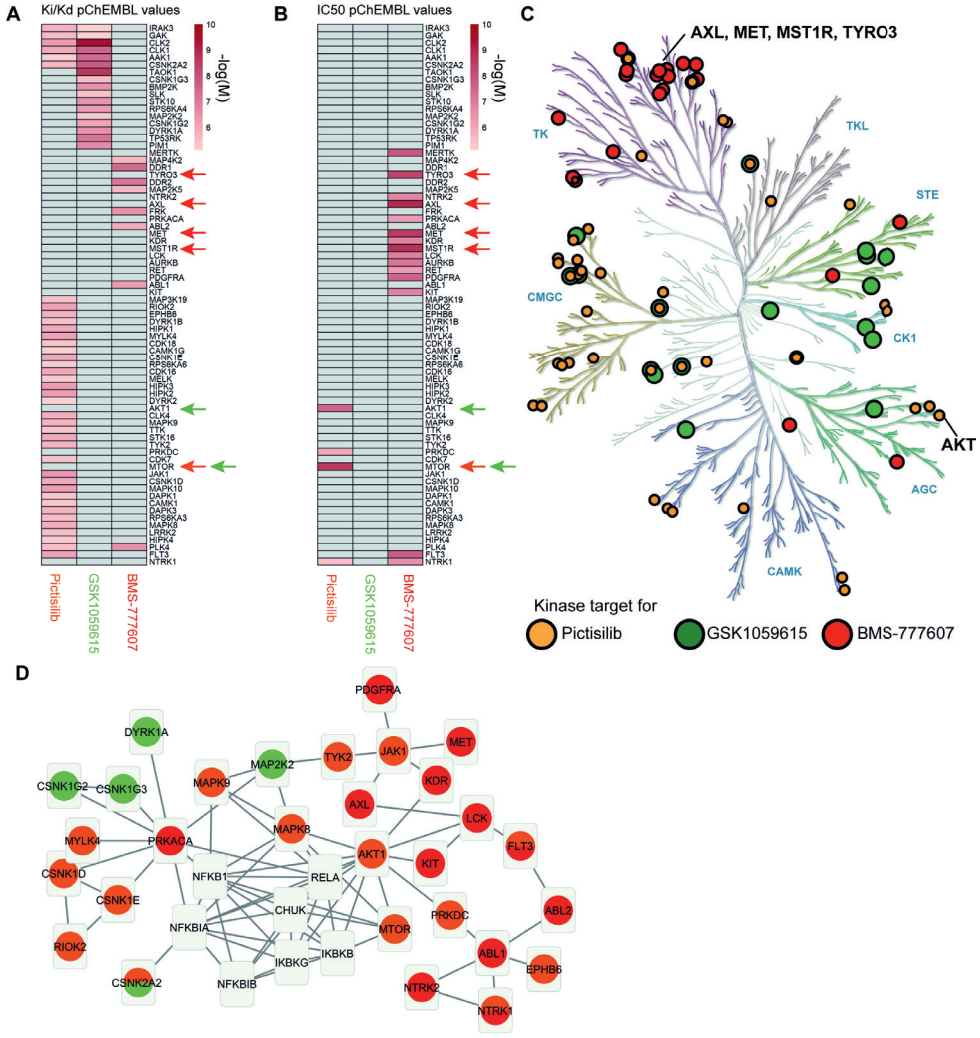


Figure 7. Kinome target interaction of ICAM1-eGFP enhancing kinase inhibitors. A and B) Ki/Kd. A) or IC50 B) values of identified targets for selected compounds picitisilib, GSK1059615 and BMS-77607. Arrows indicate the intended targets of the corresponding compound (indicated by the colour). pChEMBL value is indicated by the colour, with increasing intensity being a higher value. Grey colour indicates that the compound does not target the gene. In the case multiple pChEMBL values were found, the highest value is shown in the heatmap. **C)** Kinome tree representing the kinases targeted by the compounds. Colour of the dots is similar to the presented colours for the kinase inhibitors shown at A, with orange being pictisilib, red being BMS-77607 and green being GSK1059615. Size of the dots is for aesthetic purposes. **D)** StringDB plot shows the connection between potential targets of the compounds and key drives of the TNF-α signalling pathway. Colours correspond to the same compounds as shown in A–C.

Discussion

In this study we assessed the vulnerability of kinase inhibitors to modulate the TNFα signalling pathway and assessed the effect of 760 KIs that cover the majority of the kinome on the expression of ICAM1-eGFP in hiPSC-derived PTLC, CMLC and HLC lineages. We uncovered different KIs that inhibit ICAM1 expression and are common between the three lineages. Most candidates enhanced ICAM1-eGFP expression with little overlap between different cell types and strongest effects were found in PTLCs. Three KIs, including the clinical applied miltefosine, also enhanced TNFα-induced chemokine CCL20 and CXCL8 expression. Three clinical marketed KIs that enhanced ICAM1-eGFP expression in PTLCs have demonstrated increased reporting of adverse renal effects. Additionally, unintended kinase inhibitor activity was associated with three inhibitors that enhanced ICAM1-eGFP expression. Our results indicate the liability of kinase inhibitors to modulate TNFα-mediated signalling and promote inflammatory responses. We propose a pre-clinical testing strategy to select KIs that demonstrate an unintended modulation of TNFα signalling for further evaluation. This could involve different cell lineages derived from hiPSC-ICAM1-eGFP reporters in combination with high throughput imaging and complementary orthogonal assays to measure chemokine secretion.

In our studies we used hiPSC-derived PTLCs, CMLCs and HLCs where ICAM1 was endogenously tagged with eGFP with an isogenic background. Yet, we identified different KIs that affected TNFα-induced ICAM1 expression across the three different lineages. This could relate to slight differences in mRNA expression of the various intended kinase targets between the different hiPSC-derived cell types. Additionally, differential expression of various transporter proteins in the differentiated cell lines could lead to differences in intracellular compound concentrations[281]. Although the induction of TNFα pathway downstream targets was largely similar between the three lineages, we cannot exclude that the regulation of the TNFα-signalling pathway is different between these cell types. Given these differences, this would advocate to assess liability of candidate KIs for TNFα-signalling modulation in different lineages susceptible for KI-related adverse drug reactions, which is well possible using our iPSC-based approach. However, some frequently observed KI toxicities like intestinal toxicity are likely non-specific consequences of their general proliferation-suppressive effects, which should be taken into account when setting up these assays[282].

In the present study we did not identify a specific class of KIs that affect TNFα-induced ICAM1-eGFP expression in PTLCs. This would suggest that unintended kinase inhibition is a risk factor that contributes to the modulation of TNF-α-signalling. For three KIs that enhanced ICAM1-eGFP expression we observed diverse kinase targets in ChEMBL (BMS-777607, GSK1059615 and pictisilib; see figure 7). Moreover, for most KIs

that we identified there is no qualitative and quantitative kinase inhibitor information available, making a generalization difficult. Typically, highly selective kinase inhibitors are preferred for clinical application, although also broad-spectrum kinase inhibition is successfully used in a clinical setting[283]. Further detailed datasets on kinase inhibitor spectrum and potency will be required to better understand the relationship between selectivity and specificity of KIs and adversity liabilities related to modulation of inflammatory signalling.

The presented secondary screen was performed using a physiological relevant concentration range for the identified kinase inhibitors. Among the validated hits, increased ICAM1-eGFP expression was observed at concentrations near the Cmax and up to 50-fold higher, as exemplified by palbociclib. Therefore, we conclude that the KI concentrations that induce TNFα-mediated ICAM1-eGFP expression may have clinical relevance. This may in particular be the case in the context of renal toxicity, since KIs are also often substrates for various drug transporters involved in renal clearance by the proximal tubular cells[284,285]. Additionally, KIs may be used in combination with classical anticancer drugs that cause renal toxicity involving inflammatory signalling, such as observed for cisplatin[286,287]. Additionally, for the liver the first pass effect after oral administration typically results in higher concentration in the liver compared to general plasma Cmax levels[288].

Treatment with several KIs (e.g. PS-1145, miltefosine, GSK1059615) resulted in enhanced ICAM1 expression, as well as increased CXCL8 expression levels (Fig. 6D). Enhanced levels of CXCL8 *in vivo* are associated with neutrophil recruitment via the CXCR8/ICAM1 axis[289]. During this innate immune response, IL-17 is produced by PTLCs which leads to synergistic production of other chemokines, including CCL20[290]. In the current study CCL20 is reported to be enhanced upon treatment with various KIs, including kidney injury-associated drugs pictilisib and bimiralisib (Fig. 5C). In mouse models, upregulation of this chemokine is associated with T cell recruitment, renal tissue injury and loss of kidney function[291].

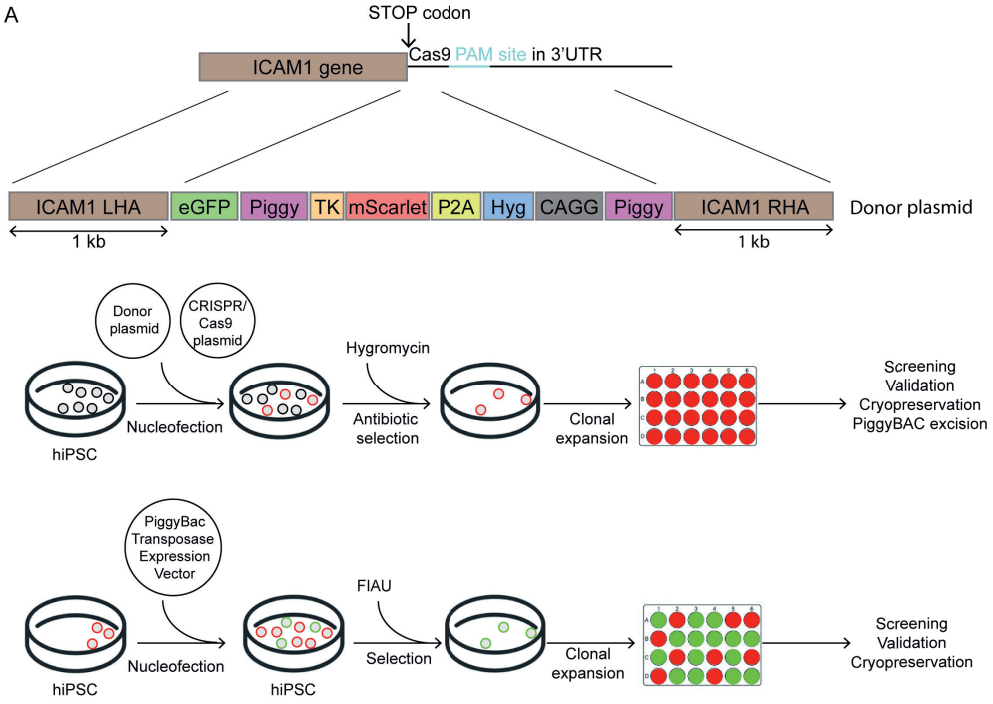
Using the ChEMBL biological activity database, we identified targets for three KIs (pictisilib, GSK1059615, BMS-77607) with an affinity within therapeutic ranges (Fig. 7A, 7B). Moreover, for most of these targets we identified a link with key components of the NF-κB signalling pathway (Fig. 7D). Although this data provides information about possible mechanisms in general, we did not establish whether the inhibition of these kinases is directly driving the enhanced ICAM1-eGFP expression in PTLCs. Given that the (off-)targets of the three selected KIs are dispersed throughout the kinome and show little overlap with TNFα-related genes, it seems unlikely that these compounds intrinsically promote TNFα signalling. Since the PI3K/AKT/mTOR pathway (target of

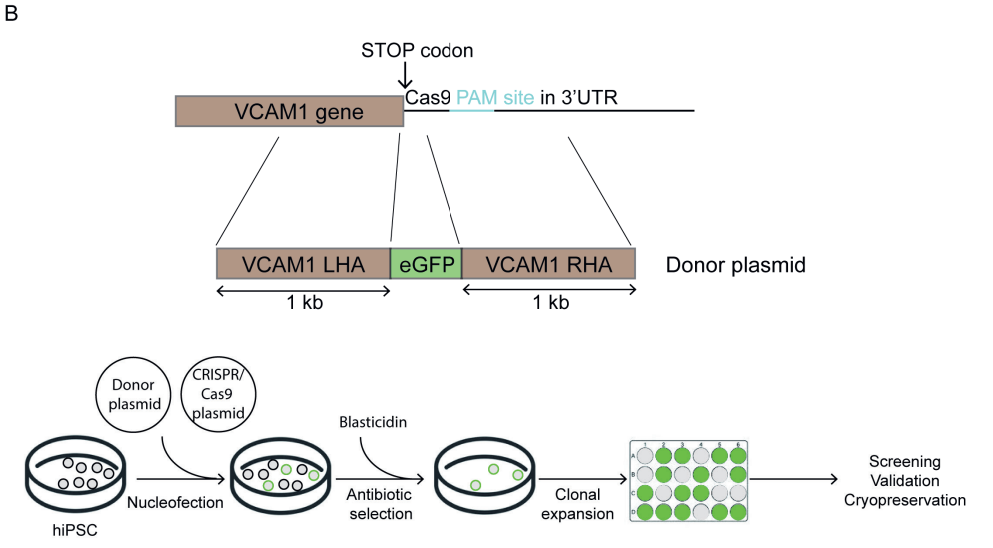
pictilisib and GSK1059615; fig 7A, 7B) and TYRO3, AXL and MER (TAM) receptor kinases (target of BMS-777607; fig 7A, 7B) are known to be able to modulate TNFα signalling outcome[292,293], we anticipate that the differential target gene expression is mediated via these pathways.

The broad-spectrum effects of these inhibitors demonstrate the complexity in uncovering the exact mechanisms underlying the enhanced TNFα-mediated ICAM1-eGFP expression. Here we used a specific ICAM1-eGFP reporter that allows specific assessment of TNFα-signalling modulation in a high throughput live-cell imaging-based strategy. Novel cost-effective high throughput transcriptomics approaches including TempO-Seq or DRUG-seq[294] could facilitate additional orthogonal mechanisms underpinning the effects of the KIs on TNFα signalling, as well as other pathways that we did not cover in the current study.

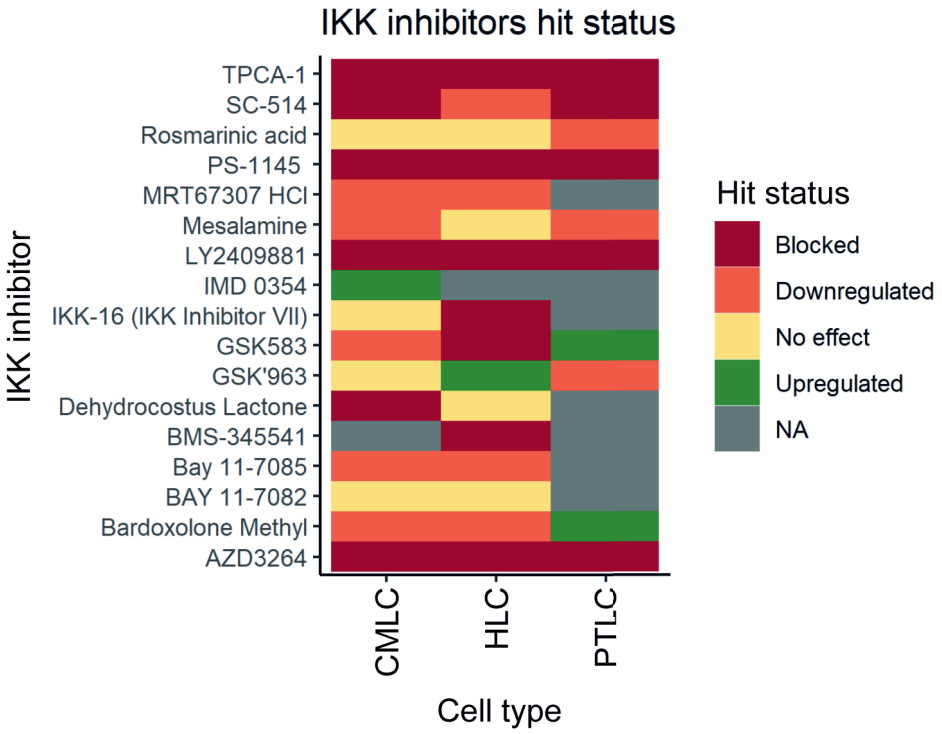
In conclusion, we demonstrate the feasibility and applicability of hiPSC-ICAM1-eGFP differentiated in different cell lineages to assess the effect of KIs on TNFα-signalling. We anticipate that this reporter can be applied to assess the effect of other small molecules or therapeutic modalities on inflammatory signalling. Future perspectives may involve the implementation of these reporters in 3D hiPSC-derived organoids models of kidney, liver and heart models in combination with isogenic hiPSC-derived immune cells to investigate the effect of kinase inhibitors on inflammatory response in human physiological relevant models.

Supplemental Figures

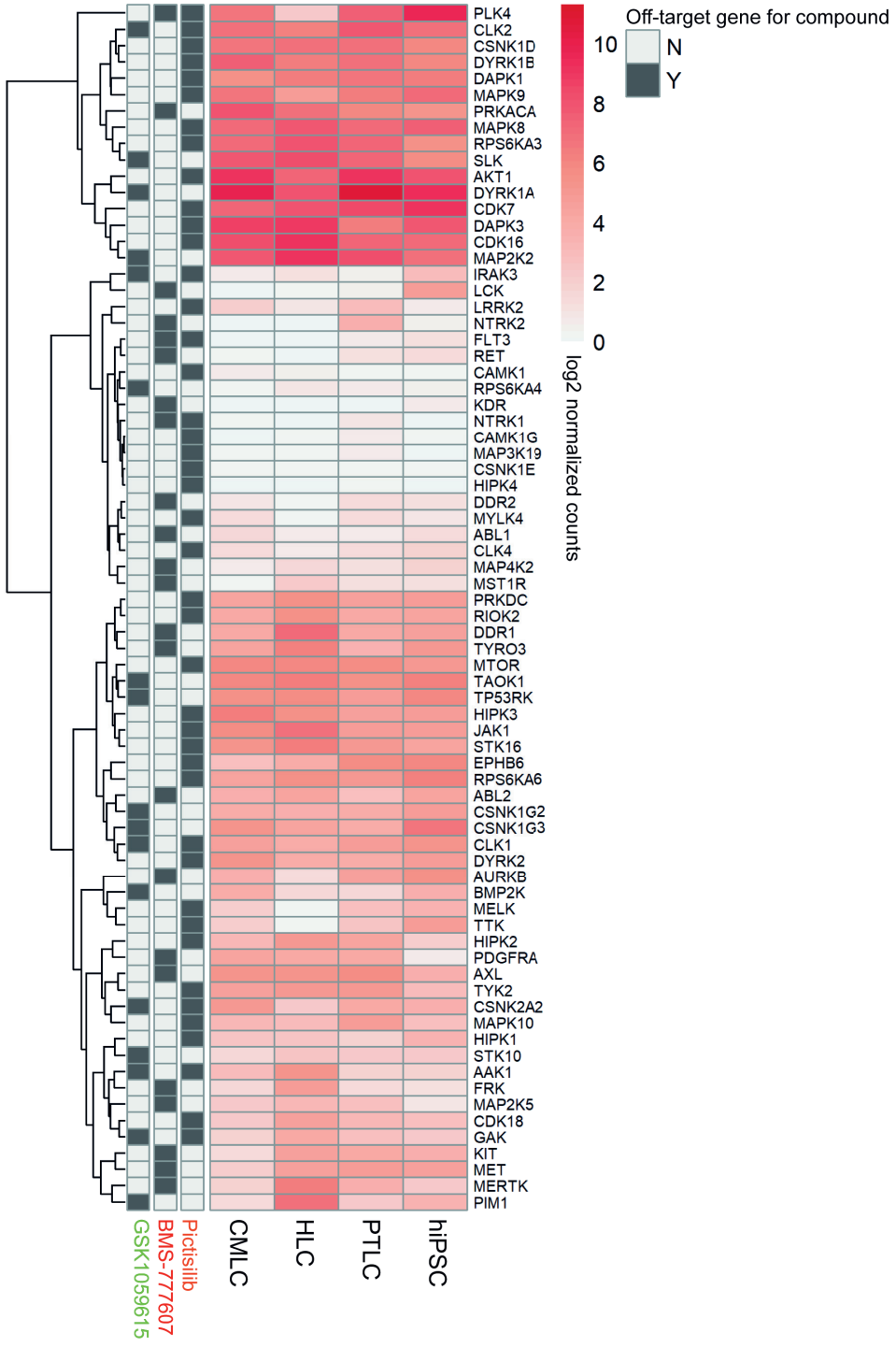




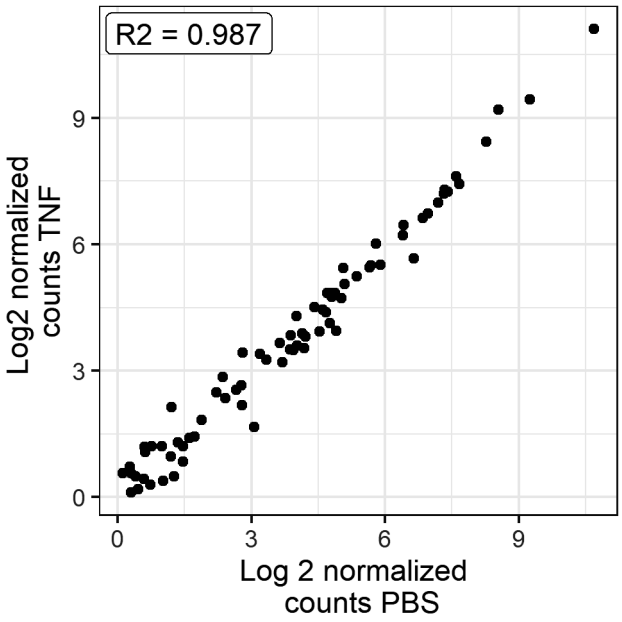
◀ **Supplemental Figure 1. Generation of eGFP fluorescent reporter hiPSC lines. A)** Targeting strategy for endogenous tagging of ICAM1. The eGFP sequence was inserted in frame in the c-terminal end of the ICAM1 gene. A selection cassette containing the hygromycin resistance gene was used to select for targeted clones. Subsequently, the selection cassette was removed using the Excision Only PiggyBac Transposase Expression Vector followed by negative selection of eGFP targeted clones without auxiliary regions using FIAU and further screened for correct integration of eGFP. **B)** VCAM1 was c-terminally tagged with eGFP and selected using transient blasticidin resistance derived from the donor plasmid and further screened for correct eGFP integration using junction PCR and Sanger sequencing.



Supplemental Figure 2. Hit status of IKK inhibitors from the screened kinase inhibitor library. Heatmap showing the hit identification status of various inhibitors of the IKK complex.


Off-target gene for compound
N
Y
10
8
6
4
2
0
log2 normalized counts
PLK4
CLK2
CSNK1D
DYRK1B
DAPK1
MAPK9
PRKACA
MAPK8
RPS6KA3
SLK
AKT1
DYRK1A
CDK7
DAPK3
CDK16
MAP2K2
IRAK3
LCK
LRRK2
NTRK2
FLT3
RET
CAMK1
RPS6KA4
KDR
NTRK1
CAMK1G
MAP3K19
CSNK1E
HIPK4
DDR2
MYLK4
ABL1
CLK4
MAP4K2
MST1R
PRKDC
RIOK2
DDR1
TYRO3
MTOR
TAOK1
TP53RK
HIPK3
JAK1
STK16
EPHB6
RPS6KA6
ABL2
CSNK1G2
CSNK1G3
CLK1
DYRK2
AURKB
BMP2K
MELK
TTK
HIPK2
PDGFRA
AXL
TYK2
CSNK2A2
MAPK10
HIPK1
STK10
AAK1
FRK
MAP2K5
CDK18
GAK
KIT
MET
MERTK
PIM1
GSK1059615
BMS-777607
Pictisiib
CMLC
HLC
PTLC
hiPSC

◀ **Supplemental Figure 3. Expression of potential targets for pictisilib, GSK1059615 and BMS-777607.** Genes were selected on potential targets for the shown compounds in figure 6A and 6B. Presented values are log2 counts per million normalized values for each independent gene.



Supplemental Figure 4. Pearson correlation plot of gene expression data of genes shown in A in normal conditions and after TNF-α stimulation.

Supplemental Tables

Supplemental Table 1. Overview of kinases in the human kinome and the relative log2 counts per million normalized expression values. Log2 normalized expression values for human kinases are given for the various lineages; cardiomyocyte-like cells (CMLCs), hepatocyte-like cells (HLCs), proximal tubular-like cells (PTLCs) and induced-pluripotent stem cells (hiPSCs). Color indicates high (red) or low (blue) expression relative to other kinases.

gene	CMLC	HLC	PTLC	hiPSC
AAK1	14.43	25.76	9.46	9.64
LMR1	6.91	0.85	7.55	4.85
ABL1	7.97	3.07	3.64	6.97
ABL2	18.18	21.91	13.85	21.77
ABR	33.28	25.29	29.25	23.57
ALK2	19.35	30.59	16.87	21.28
ALK4	8.01	6.35	6.44	5.92
ALK7	0.00	4.92	2.27	2.16
ACTR2	13.30	14.93	16.35	16.98
ACTR2B	16.58	13.17	21.80	20.69
ALK1	0.86	0.28	2.98	0.78
ADCK1	23.22	18.36	19.82	23.02
ADCK2	19.63	30.49	16.47	17.32
ADCK5	19.25	24.91	16.78	10.44
AKT1	45.44	36.50	46.21	40.54
AKT2	14.09	6.31	18.02	15.36
AKT3	24.13	23.88	28.87	26.90
ALK	0.90	0.00	5.68	2.01
AlphaK3	8.42	9.25	18.04	3.33
AlphaK2	35.65	23.77	10.42	2.08
AlphaK1	40.92	30.99	17.55	22.59
MISR2	23.16	12.90	19.25	0.78
SgK288	0.61	2.18	5.00	1.58
ARAF	22.88	13.01	22.17	16.41
ATM	26.44	19.88	31.34	27.64
ATR	22.91	18.14	24.08	26.22
AurA	15.66	3.80	17.78	16.96
AurB	17.84	6.33	22.65	27.54
AurC	4.94	12.24	10.22	9.58
AXL	26.28	25.70	28.26	18.25
BAZ1A	10.28	14.58	18.52	14.31
BAZ1B	32.30	32.27	30.56	34.51
BCKDK	18.03	19.33	14.00	13.83
BCR	28.67	35.00	25.83	37.36
BLK	0.00	0.00	0.00	0.00
BLVRA	16.47	15.54	9.93	8.10
BIKE	19.53	8.17	8.08	18.73
BMPR1A	31.71	29.70	23.34	31.41
BMPR1B	5.44	22.91	36.42	17.43

gene	CMLC	HLC	PTLC	hiPSC
JNK1	35.33	38.75	35.97	37.29
JNK2	33.53	23.61	32.06	34.93
MAPKAPK2	46.38	45.16	40.95	32.74
MAPKAPK3	10.65	4.44	8.99	11.64
MAPKAPK5	14.73	9.97	11.48	16.45
MARK1	7.67	4.93	9.45	11.27
MARK2	8.42	14.93	8.57	10.19
MARK3	19.40	29.04	18.92	19.46
MARK4	4.38	0.60	7.31	7.80
MAST1	0.80	0.34	8.89	3.97
MAST2	25.74	26.66	14.29	18.21
MAST3	0.93	2.81	4.31	0.80
MAST4	2.96	10.53	3.21	7.19
MASTL	26.29	24.86	20.42	42.14
CTK	0.00	0.41	2.71	6.83
MELK	10.48	0.97	13.93	16.96
MER	9.20	32.31	18.48	11.02
MET	10.51	22.34	24.52	23.05
MINK	6.11	20.17	11.73	7.20
MNK1	5.70	18.61	3.75	2.81
MNK2	36.29	37.03	38.77	36.13
MLKL	0.59	13.86	1.58	14.61
MOK	7.90	2.56	10.56	1.46
MOS	0.42	0.19	1.36	0.00
RON	1.70	11.83	5.14	5.72
FRAP	29.34	29.95	29.00	25.03
MUSK	0.00	0.13	2.61	0.68
smMLCK	13.88	1.68	5.72	15.30
skMLCK	3.74	0.00	10.61	4.83
caMLCK	43.74	8.60	5.56	4.17
SgK085	6.80	0.81	6.33	4.04
MYO3A	0.79	21.44	11.77	8.01
MYO3B	0.16	7.38	4.06	0.80
NEK1	16.94	13.89	13.56	16.57
NEK10	31.59	12.08	12.36	15.02
NEK11	3.71	12.99	10.36	3.69
NEK2	22.89	1.04	31.24	22.99
NEK3	9.43	4.57	8.20	8.39
NEK4	23.30	29.32	21.56	29.40

BMPR2	47.55	47.90	41.63	37.31
BMX	0.00	1.86	2.56	0.00
BRAF	14.68	23.93	13.86	18.41
BRD2	17.61	15.58	16.21	20.43
BRD3	39.45	38.58	41.65	39.06
BRD4	34.24	40.57	41.70	32.34
BRDT	0.25	0.72	1.90	9.68
BRSK1	18.57	2.97	32.06	23.09
BRSK2	3.03	1.76	16.10	18.59
BTK	1.43	0.61	2.19	0.78
BUB1	26.41	2.22	21.06	35.97
BUBR1	13.64	0.53	14.68	27.05
CaMK1a	3.17	2.61	1.53	0.80
CaMK1d	4.51	3.36	11.31	7.66
CaMK1g	0.24	0.85	2.98	0.78
CaMK2a	5.35	0.00	1.09	0.00
CaMK2b	13.91	0.17	7.34	1.58
CaMK2d	34.53	21.94	24.34	12.74
CaMK2g	16.40	14.97	19.23	19.19
CaMK4	0.00	0.00	0.90	0.00
CaMKK1	1.43	0.00	1.91	4.38
CaMKK2	22.92	27.94	24.11	26.32
VACAMKL	0.00	0.26	14.27	23.95
CASK	23.37	34.34	22.81	28.18
MRCKa	19.51	30.04	22.25	22.38
MRCKb	24.95	25.21	21.81	22.95
DMPK2	14.33	38.24	29.21	22.21
CDC7	13.94	10.53	14.71	24.30
CDC2	36.52	0.57	38.38	43.24
CDK10	32.51	35.32	30.26	33.26
PITSLRE	26.70	25.85	24.44	24.67
CRK7	12.59	17.34	15.22	19.19
CHED	6.17	2.72	10.74	10.05
PFTAIRE1	31.30	20.67	26.14	27.11
PFTAIRE2	0.28	0.19	17.97	0.00
PCTAIRE1	41.22	46.18	36.59	35.18
PCTAIRE2	20.35	12.57	17.61	21.01
PCTAIRE3	11.61	22.42	15.93	13.39
CDK11	26.33	23.89	26.63	20.60
CDK2	15.92	6.76	13.50	12.03
CCRK	12.50	19.30	24.89	3.23
CDK3	1.95	2.84	5.41	1.36
CDK4	46.07	40.40	56.54	46.83
CDK5	15.40	26.37	18.30	11.42
CDK6	37.83	23.95	32.21	37.83
CDK7	36.00	39.53	42.71	46.08
CDK8	21.57	16.41	15.70	25.25
CDK9	13.09	21.79	11.45	13.62

NEK5	5.78	6.35	16.37	8.01
NEK6	28.07	31.41	21.79	19.19
NEK7	38.92	20.82	26.83	24.41
NEK8	0.86	10.12	2.48	5.25
NEK9	11.39	24.58	13.49	6.01
NIM1	0.00	0.00	0.51	0.00
NLK	7.99	4.40	8.03	20.05
ANPa	1.40	22.84	2.35	2.17
ANPb	5.70	9.74	6.64	1.48
NRBP1	29.14	34.84	25.75	28.63
NRBP2	19.56	19.37	17.27	10.60
NRK	0.35	13.00	8.83	8.27
TRKA	0.61	0.00	4.97	0.00
TRKB	0.28	0.00	18.21	2.28
TRKC	0.00	0.00	15.61	5.52
NuaK1	9.13	4.37	6.40	10.30
NuaK2	19.00	22.03	28.83	29.45
Obscn	28.93	14.08	20.44	12.99
OSR1	16.34	6.96	20.89	16.87
PAK1	9.06	29.35	13.74	26.74
PAK2	32.77	36.79	30.07	34.86
PAK3	0.65	3.46	12.76	17.52
PAK4	13.75	13.62	13.57	9.82
PAK5	0.00	0.18	2.38	2.63
PAK6	6.76	20.46	7.80	4.78
PAN3	19.16	13.11	24.74	30.57
PASK	8.20	9.12	17.35	19.13
PBK	28.36	9.19	30.41	20.04
PDGFRa	21.23	20.88	20.13	3.44
PDGFRb	20.24	12.90	14.24	20.49
CLIK1L	9.76	13.45	17.75	7.71
PDHK1	34.20	8.50	22.57	27.45
PDHK2	24.75	10.56	20.06	5.85
PDHK3	28.59	25.97	36.73	32.22
PDHK4	13.56	23.19	13.97	0.00
PDK1	20.61	26.08	17.06	17.25
SgK269	40.31	31.68	37.89	37.71
PHKg1	4.15	1.38	10.02	2.04
PHKg2	17.63	27.38	15.16	20.91
PIK3R4	38.24	26.64	38.11	46.73
PIM1	6.40	34.36	11.11	17.19
PIM2	18.39	28.44	23.17	47.60
PIM3	8.94	21.73	10.24	9.52
PINK1	35.38	39.42	33.55	21.81
SgK493	23.42	23.81	26.75	19.61
MYT1	13.11	1.23	11.09	17.10
PKN1	29.98	36.13	34.13	29.45
PKN2	28.94	25.63	20.37	26.76

CDKL1	6.18	8.86	4.00	10.90
CDKL2	1.99	0.85	3.66	4.49
CDKL3	3.78	0.95	4.14	5.52
CDKL4	0.40	1.27	1.11	1.21
CDKL5	22.10	25.39	20.33	27.11
Col4A3BP	30.10	34.45	27.66	37.15
CHK1	34.56	21.15	38.48	40.76
CHK2	8.92	12.71	15.31	14.83
IKKa	16.63	23.96	12.63	24.03
CRIK	17.40	2.25	32.34	21.10
CLK1	22.67	19.69	23.78	26.64
CLK2	33.79	30.95	38.32	34.26
CLK3	7.15	15.62	8.75	7.18
CLK4	6.79	3.27	7.34	8.76
ADCK3	20.75	19.61	11.55	24.00
ADCK4	29.40	36.09	27.78	20.45
FMS	1.77	29.42	3.06	3.33
CSK	36.06	33.81	33.24	33.55
CK1a	31.91	30.76	23.62	27.77
CK1a2	0.00	0.00	0.54	0.00
CK1d	32.99	33.69	34.24	30.14
CK1e	0.96	0.77	1.52	1.21
CK1g1	28.36	30.65	31.40	30.78
CK1g2	18.97	18.19	19.39	23.95
CK1g3	26.01	21.74	19.35	32.58
CK2a1	19.95	24.82	15.83	26.18
CK2a2	25.30	11.58	20.93	18.61
DAPK1	27.01	32.05	33.22	32.34
DAPK2	3.98	7.95	5.99	9.66
DAPK3	42.86	44.74	31.99	39.17
DCAMKL1	0.00	0.39	5.13	7.28
DCAMKL2	5.21	0.15	3.56	0.00
DCAMKL3	2.80	1.78	2.79	7.62
DDR1	20.56	35.06	20.04	22.55
DDR2	4.40	1.00	7.32	5.72
DMPK1	38.25	21.67	28.11	22.09
SgK496	11.80	8.73	21.27	9.61
DYRK1A	49.28	39.56	53.42	47.18
DYRK1B	37.68	31.78	34.79	29.35
DYRK2	26.42	19.79	19.68	24.13
DYRK3	30.63	12.27	26.07	24.20
DYRK4	0.86	0.00	4.37	0.00
eEF2K	8.24	10.55	10.01	4.96
EGFR	1.51	36.31	10.04	0.68
HRI	23.93	23.73	26.95	25.00
PKR	23.64	11.34	22.19	31.26
PEK	21.08	23.97	17.76	24.61
GCN2	33.14	33.97	27.32	34.41

PKN3	3.00	2.62	4.55	5.35
PLK1	14.03	6.96	19.50	26.63
PLK2	28.28	22.93	41.48	29.80
PLK3	1.84	6.85	4.19	5.18
PLK4	32.64	11.49	37.96	47.72
CaMK1b	4.30	0.00	3.17	1.64
SgK196	15.59	14.97	12.67	14.91
SgK223	3.44	3.90	13.89	14.25
AMPKa1	25.68	35.29	20.00	24.50
AMPKa2	24.52	26.16	13.24	14.23
PKACa	40.25	33.78	29.51	25.73
PKACb	21.79	16.99	18.93	25.64
PKACg	0.15	0.00	1.16	0.00
PKCa	6.61	5.01	4.45	7.20
PKCb	3.62	3.77	10.56	12.76
PKCd	11.08	20.46	15.70	24.10
PKCe	21.10	21.04	23.35	8.83
PKCg	0.00	0.00	10.44	9.69
PKCh	10.73	4.86	5.46	2.51
PKCi	34.94	35.16	36.28	41.18
PKCt	0.90	1.33	0.88	13.35
PKCz	7.72	12.06	7.24	3.69
PKD1	21.28	11.98	23.76	21.90
PKD2	6.36	13.93	10.30	12.30
PKD3	32.27	24.82	32.16	44.33
DNAPK	21.78	27.83	23.03	24.44
PKG1	14.84	2.71	28.33	29.64
PKG2	5.12	6.36	12.74	8.64
PRKX	7.12	6.85	8.16	30.81
PRP4	28.97	30.92	24.24	36.22
PSKH1	8.84	20.83	8.62	8.93
PSKH2	0.00	0.00	1.04	0.78
FAK	12.11	3.83	13.14	18.55
PYK2	3.82	18.93	13.20	0.00
BRK	0.15	1.45	2.57	1.36
CCK4	26.82	23.32	36.90	24.92
Slob	9.91	5.17	4.66	2.79
RAF1	28.00	26.06	21.05	26.41
RET	0.87	0.13	6.03	6.53
RIOK1	34.41	36.41	39.02	39.57
RIOK2	20.77	26.94	21.06	22.07
RIOK3	27.99	34.21	21.82	21.76
RIPK1	21.09	27.53	18.82	24.75
RIPK2	35.86	26.95	40.51	42.40
RIPK3	2.87	18.47	10.34	0.68
ANKRD3	0.00	14.60	16.54	1.99
RNAseL	10.07	29.26	15.26	3.84
ROCK1	35.48	34.00	40.00	34.17

EphA1	1.23	34.35	25.74	42.06
EphA10	0.00	0.00	2.95	10.26
EphA2	10.96	13.10	6.76	16.26
EphA3	20.96	0.18	13.70	7.94
EphA4	13.59	1.03	10.66	7.56
EphA5	1.11	0.40	4.57	0.80
EphA6	3.13	7.97	12.43	13.46
EphA7	17.11	0.00	17.48	12.16
EphA8	2.57	0.86	16.18	28.98
EphB1	0.00	0.34	2.80	2.51
EphB2	17.25	0.96	25.07	22.32
EphB3	29.82	4.90	30.43	3.39
EphB4	36.45	44.36	45.94	47.07
EphB6	13.39	19.89	28.40	29.26
ErbB2	55.42	47.34	49.41	50.88
ErbB3	11.09	22.49	15.18	18.76
ErbB4	35.86	3.92	30.34	6.33
IRE1	2.02	14.47	3.33	1.64
IRE2	0.00	0.41	1.13	1.21
FASTK	23.14	30.86	17.44	17.43
FER	39.90	35.11	45.84	36.71
FES	16.19	29.15	20.80	18.10
FGFR1	14.82	2.29	15.68	27.05
FGFR2	22.47	18.34	38.21	33.89
FGFR3	3.68	18.66	21.99	7.84
FGFR4	0.76	40.76	10.27	23.88
FGR	0.42	0.00	1.79	0.00
FLT1	15.74	2.16	2.42	36.46
FLT3	0.00	0.30	3.13	5.27
FLT4	0.28	0.00	3.49	6.44
FRK	7.95	23.54	6.80	5.25
FYN	35.84	19.79	39.48	33.04
GAK	8.80	20.01	14.04	11.81
RHOK	0.00	0.00	1.56	1.40
BARK1	14.83	22.13	20.53	13.08
BARK2	27.02	45.63	30.73	35.76
GPRK4	2.55	4.21	1.14	0.00
GPRK5	8.02	3.48	6.94	0.00
GPRK6	4.46	5.61	6.09	13.09
GPRK7	1.72	2.26	4.37	0.00
GSK3A	21.85	15.91	24.99	18.93
GSK3B	38.87	25.74	30.25	40.50
GTF2F1	18.92	23.32	19.33	16.72
HSER	0.27	0.61	0.71	2.01
CYGD	0.00	0.15	3.49	1.58
CYGF	0.00	0.00	1.03	0.68
Haspin	4.12	0.62	5.88	17.39
HCK	0.00	0.19	2.72	2.17

ROCK2	41.22	44.27	38.47	41.57
ROR1	23.02	20.84	15.77	35.77
ROR2	25.01	13.11	14.88	12.73
ROS	0.24	0.94	2.76	0.00
RSK1	2.65	4.08	3.77	9.53
RSK3	5.78	8.32	8.03	3.31
RSK2	35.06	39.54	37.02	27.69
MSK2	1.14	4.93	3.81	2.01
MSK1	14.68	21.57	20.34	13.84
RSK4	21.13	27.00	25.48	30.58
p70S6K	10.29	18.28	15.68	13.92
p70S6Kb	18.78	19.89	15.30	12.30
RSKL1	29.24	28.57	25.06	26.87
RSKL2	5.32	11.33	6.65	14.26
SgK494	19.46	19.02	20.75	28.86
RYK	24.03	18.31	22.22	29.61
SBK	13.69	14.58	27.22	34.18
SgK069	0.48	0.00	2.45	0.00
SgK110	0.00	0.00	0.81	0.78
SCYL1	27.55	37.02	19.37	25.53
SCYL2	37.50	31.69	32.60	38.00
SCYL3	20.96	15.75	21.76	16.10
SGK1	16.80	24.33	18.93	15.36
SGK2	1.76	16.19	12.56	1.21
SGK3	2.50	3.44	6.01	3.59
SIK	23.60	39.14	25.51	17.04
QIK	18.86	22.50	19.57	16.08
QSK	26.81	22.44	16.55	28.06
SLK	39.04	40.91	36.64	28.74
SMG1	33.74	28.68	30.54	42.28
SNRK	11.86	12.63	9.71	18.91
SPEG	5.86	0.00	2.79	0.00
SRC	14.97	27.78	15.55	13.44
SRM	0.00	0.00	0.19	1.88
SRPK1	25.58	25.64	25.51	34.78
SRPK2	8.51	3.74	4.71	8.84
MSSK1	27.96	0.00	2.76	0.68
LOK	7.62	12.48	11.76	11.51
LKB1	26.93	23.66	28.46	24.78
MPSK1	26.02	32.10	25.07	21.76
DRAK1	17.82	15.05	8.85	24.30
DRAK2	20.03	25.74	23.63	20.10
G11	2.24	2.58	3.28	3.39
MST3	7.85	13.01	10.09	14.25
YSK1	35.82	34.69	37.71	31.09
MST4	16.63	21.50	9.45	17.09
MST2	30.83	32.47	28.29	30.11
SgK396	3.23	14.20	3.72	3.09

HIPK1	12.35	12.57	8.61	16.95
HIPK2	16.56	25.52	22.10	10.46
HIPK3	32.52	27.80	23.34	23.58
HIPK4	0.00	0.00	1.35	0.00
HUNK	20.44	14.09	27.60	22.04
ICK	26.72	34.99	24.02	33.44
IGF1R	22.15	25.64	28.36	24.00
IKKb	11.74	9.06	12.03	10.80
IKKe	5.15	6.19	3.77	6.15
ILK	51.94	50.98	50.57	37.72
INSR	38.24	48.77	28.51	35.53
IRR	0.95	0.00	2.69	0.00
IRAK1	12.02	16.45	17.68	14.25
IRAK2	1.91	25.36	2.75	1.64
IRAK3	3.94	5.78	2.27	14.78
IRAK4	13.45	13.63	15.59	10.92
ITK	0.27	2.49	1.25	0.68
JAK1	29.09	34.63	24.12	23.95
JAK2	18.37	13.80	9.72	7.47
JAK3	4.54	6.24	20.73	5.01
Trad	3.66	2.10	12.58	2.04
KDR	0.51	0.14	0.55	3.05
KIT	6.48	23.24	20.74	17.77
KSR1	21.01	36.45	25.29	24.68
KSR2	0.00	2.49	2.60	2.79
LATS1	18.62	21.35	20.94	27.33
LATS2	22.71	28.21	16.50	21.52
LCK	0.00	1.25	2.02	24.43
LIMK1	12.62	25.58	18.57	16.97
LIMK2	22.46	30.09	22.03	20.98
LMR2	3.60	13.24	4.59	3.69
LMR3	3.47	21.88	23.91	17.96
LRRK1	0.00	1.15	2.52	1.21
LRRK2	9.80	4.13	15.30	3.60
LTK	0.64	14.70	0.00	0.00
LYN	6.83	10.03	7.31	19.35
MAK	2.39	0.14	14.10	1.64
MAP2K1	35.01	33.79	35.14	36.40
MAP2K2	38.34	45.99	41.38	34.35
MAP2K3	15.71	25.30	11.63	15.15
MAP2K4	34.60	24.68	28.68	36.88
MAP2K5	10.93	15.42	13.29	4.84
MAP2K6	3.49	4.61	8.45	9.37
MAP2K7	32.74	27.91	37.08	36.78
MAP3K1	28.40	33.88	31.02	30.77
MLK2	1.92	5.57	2.25	0.68
MLK3	20.26	27.84	26.59	19.83
DLK	8.21	5.26	8.79	10.55

YANK1	0.59	0.31	6.95	0.78
YANK2	0.96	0.00	5.91	3.86
YANK3	15.03	13.89	20.83	22.21
STK33	36.59	23.63	35.95	35.93
CLIK1	0.99	1.25	5.41	4.57
Fused	28.17	24.46	29.19	27.74
NDR1	17.50	11.72	12.57	12.93
NDR2	23.51	16.93	15.75	28.07
STLK3	49.54	43.99	43.71	33.16
MST1	16.81	24.91	21.22	23.25
SgK495	22.42	29.87	25.19	16.38
SgK071	0.34	0.66	2.69	0.78
STLK5	25.71	30.55	21.46	24.74
STLK6	35.01	30.96	29.67	33.41
SuRTK106	0.48	18.55	4.36	2.44
SYK	0.00	0.54	3.57	0.00
TAF1	28.96	25.01	24.49	32.53
TAF1L	0.00	0.44	2.01	0.00
TAO1	29.24	32.47	26.84	30.76
TAO2	30.93	27.54	34.78	23.66
TAO3	21.76	33.85	21.94	16.95
TBCK	9.35	7.71	8.52	14.79
TBK1	7.00	9.59	8.30	13.76
TEC	4.12	16.47	4.99	9.36
TIE2	20.00	1.21	11.42	32.02
TESK1	16.24	21.59	17.61	15.03
TESK2	3.20	17.10	5.75	16.72
SgK307	4.46	3.88	8.20	10.57
TGFbR1	31.11	51.26	36.00	33.28
TGFbR2	36.95	43.80	35.63	22.98
TIE1	1.29	0.00	6.57	9.05
TLK1	23.10	8.22	21.57	39.97
TLK2	25.71	31.15	21.98	31.98
TNIK	28.65	33.07	30.83	29.69
TNK1	0.00	11.73	3.75	5.61
ACK	16.91	16.49	13.73	17.79
HH498	34.95	0.15	1.09	0.00
PRPK	27.84	28.17	24.41	29.32
Trb1	36.61	25.15	18.00	32.14
Trb2	0.89	1.20	7.00	2.44
Trb3	15.75	29.07	30.95	41.17
TIF1a	45.83	37.68	37.84	45.41
TIF1b	46.29	46.36	49.70	52.91
TIF1g	21.59	15.03	25.10	25.45
TIF1D	1.28	3.09	7.96	0.68
Trio	7.89	17.04	10.70	7.83
ChaK2	0.83	1.40	1.75	8.70
ChaK1	31.66	29.80	30.95	32.87

LZK	19.05	28.77	24.69	8.28
NIK	6.76	15.48	13.52	12.59
MAP3K7	2.65	10.65	4.76	9.85
MAP3K19	0.70	0.97	3.03	0.00
MAP3K2	27.97	23.06	27.68	32.24
ZAK	28.62	9.26	18.39	19.86
MLK4	2.56	20.16	3.96	26.96
MAP3K3	10.64	23.03	8.12	13.49
MAP3K4	17.76	11.93	17.26	20.04
MAP3K5	1.32	0.47	2.13	1.58
MAP3K6	8.37	7.86	3.37	8.11
TAK1	36.59	31.16	37.34	37.12
COT	16.30	24.51	33.73	18.64
MLK1	0.15	7.79	3.34	1.58
HPK1	2.02	7.33	6.05	7.13
GCK	3.60	7.44	5.97	9.35
KHS2	39.06	33.38	35.19	46.18
HGK	27.20	32.11	23.54	24.53
KHS1	43.10	35.98	42.09	42.37
Erk2	20.96	14.49	12.33	19.19
JNK3	15.89	15.24	23.50	14.16
p38b	5.63	9.70	20.99	2.62
p38g	20.01	12.12	17.06	16.10
p38d	11.61	46.89	21.67	17.05
p38a	31.12	30.73	32.17	31.23
Erk7	2.61	1.68	30.41	6.79
Erk1	32.37	39.62	37.52	34.35
Erk4	7.62	11.24	7.35	2.08
Erk3	27.34	29.87	23.56	38.07
Erk5	29.85	31.22	34.59	29.86

TRRAP	27.78	21.71	23.92	33.40
TSSK1	1.08	0.26	1.66	0.00
TSSK2	0.15	0.19	1.83	1.40
TSSK3	5.02	0.90	14.52	3.09
TSSK4	2.21	7.41	9.95	3.97
SSTK	0.88	3.55	3.46	2.28
TTBK1	2.56	1.44	16.85	18.29
TTBK2	2.53	0.36	2.10	1.21
TTK	9.74	0.59	12.06	23.98
TTN	25.77	4.35	0.71	6.06
TXK	0.00	1.23	1.15	0.78
TYK2	23.31	25.06	25.28	14.89
TYRO3	22.12	30.70	16.68	24.81
KIS	28.06	32.75	23.47	30.64
ULK1	23.77	21.81	26.87	19.85
ULK2	26.08	10.45	35.60	14.88
ULK3	32.30	33.74	32.96	26.87
ULK4	20.71	8.61	23.06	34.77
VRK1	30.25	21.05	34.68	40.35
VRK2	23.59	29.25	22.60	21.88
VRK3	15.54	19.47	17.13	7.09
Wee1	43.64	21.57	32.84	44.94
Wee1B	0.00	0.00	1.97	0.00
Wnk1	36.03	39.40	34.29	36.22
Wnk2	15.64	1.61	13.70	7.94
Wnk3	1.07	2.98	2.45	3.69
Wnk4	0.62	3.26	16.99	5.75
YES	20.77	25.22	25.07	38.09
ZAP70	0.40	0.42	3.99	0.80

Supplemental Table 2. gRNA and primer details for targeting ICAM1 and VCAM1.

gRNA sequences

Target	gRNA sequence	PAM	Gene strand	bp between insertion site and PAM site
VCAM1	TAATGCTTGATATGTTCAAC	TGG	+	21
ICAM1	CCCTGAACCTATCCCGGGAC	AGG	+	14

Junction PCR primer sequences

Target	Left/right homology arm (HA)	Fw/Rvs	Sequence
VCAM1	Left	Fw	GTAGCATGCTGGCTGTTCAGTGATGGAC
		Rvs	GTTGTCGACCACTTTTGACTTCTGTGCTTCTAC
	Right	Fw	GATGGATCCCTGATGCTTGATATGTTCAACTGGAGAC
		Rvs	GTAGAGCTCAGTCTGGCACCAAGAAATCTAC

Supplemental Table 3. Effect size of all kinase inhibitor library compounds. Each x_hit_status compound gives the hit status for a compound for that specific cell type (x) for ICAM1-GFP expression. NA means no measurement due to cell death or image artefacts. Data are based on 1 replicate experiments.





CHAPTER 6

GENERAL DISCUSSION AND FUTURE PERSPECTIVES

Immune-related adverse drug reactions (ADRs) remain a major challenge in drug development and safety assessment due to their poor predictability. Preclinical studies for toxicity testing are performed to predict the behaviour of a certain compoun**d.** Identifying potential toxicities at early stages of drug development can reduce costs and length of preclinical studies and help prevent late-stage failures in clinical trials or post–market approval. Therefore, increasing effort has been directed toward the development of new approach methodologies that integrate cell-based assays, computational modelling, and omics technologies to replace, reduce, and refine traditional animal testing in accordance with the principles of the 3Rs. The goal is to enable faster, more predictive, and mechanistically informed assessment of chemical safety hazards[295]. In addition, the FDA Modernization Act 2.0, passed in December 2022, permits the use of alternatives to animal testing for drug safety evaluation in the USA, allowing selection of the most appropriate testing methods from early development onward and thereby improving accuracy and accelerating drug development[296]. Although this new legislation is active in the USA, it did not change European laws, however it is expected that it will accelerate a shift towards non-animal testing globally in the future. In lines with these expectations, this thesis is centred around the development of establishing accurate and predictive *in vitro* cell models to enhance clinical translation related to immune-mediated adverse reactions.

Challenges with hepatocyte models for toxicology research

In the past, animal models were primarily used for safety prediction. However, animal models bring several limitations, including biological differences between species, poor translation of results, poor experimental design, lack of reproducibility, and the inability to model complex human conditions[297,298]**.** Atkins et al. describe the minimal correlation of animal studies and actual human toxicities in phase I clinical trials with a positive predictive value of 0.65 and negative predictive value of only 0.5[299]. In addition, Marshall et al. report on a failure rate of 92% while translating animal testing to actual human toxicity that is the result of unexpected safety that was not predicted using animal models, or due to the lack of efficacy[300]. Examples of drugs for which animal studies were not reliable predictors of human toxicity include TGN1412, developed for autoimmune diseases, and fialuridine, intended for the treatment of hepatitis B. In both cases, clinical trials resulted in critically ill volunteers who suffered life-long complications or even death[301,302].

In the work presented in **chapter 2**, we aimed to improve a preclinical safety testing approach that utilizes HepG2 liver carcinoma cells cultured as 3D spheroids in a Matrigel layer[303]. 3D culturing of those HepG2 cells in a Matrigel basement membrane induced self-organization and differentiation to polarized spheroids that are more mature compared to 2D HepG2 cultures. Our lab has also demonstrated increased

sensitivity of HepG2 spheroids towards the identification of hepatotoxic compounds using high-throughput screening[303,304]**.** Matrigel is a poorly defined animal-based matrix with high lot-to-lot variability, which likely affects reproducibility. Therefore, in **chapter 2**, we developed an alternative synthetic matrix where chemical composition and material properties can be controlled to improve maturation. This supramolecular matrix was co-assembled with arginylglycylaspartic acid (RGD)-functionalized squaramide-based and native monomers as they are known to be crucial for cell differentiation via integrin signalling[305,306].

HepG2 differentiation proved to be enhanced compared to the standard Matrigel matrix as assessed by the increased expression of various phase I, and II metabolic enzymes *(CYP2D6, CYP1A2, CYP3A5, UGT1A1),* drug transporters (*NCTP*), and liver markers (*HNF4A*). We believe that hepatocyte maturation can be even further improved in the future by modification of the terminal azide on squaramide 3 as the current gel is considered a soft hydrogel with a stiffness below 100 Pa, while the liver stiffness in healthy individuals is between 3.5-6 kPa[307]. Furthermore, the applicability of the current gel can also be extended to other cell types, including NIH/3T3 fibroblasts, hiPSCs and hiPSC-derived endothelial cells[308].

***In vitro* liver models to identify the role of inflammation in DILI**

The healthy human liver is usually perceived as an immunologically tolerant organ that actively promotes immune tolerance to harmless substances like gut bacteria and food that are delivered from the intestine to the liver via the portal vein. This is mediated through a subset of specialized liver cells, including liver sinusoidal endothelial cells, dendritic cells and Kupffer cells[309]**.** Nevertheless, during infections, Kupffer cells quickly respond to pathogens by producing various cytokines, including TNF-α, IL-1β and IL-6 as well as chemokines like MIP-1α and RANTES thereby activating and recruiting other subsets of immune cells that help resolve the infection[310,311]**.** Liver inflammation itself can act as a driver of DILI and therefore needs to be considered in drug liability testing. To study this, an immune responsive *in vitro* model is required. Therefore, in **chapter 3**, we assessed the responsiveness of five different *in vitro* models to various pro-inflammatory (TNF-α, IL-1β, IL-6, IL-12 and IL-18) and anti-inflammatory (IL-10) cytokines secreted by Kupffer cells[312]**.** We concluded that unstressed hepatocytes are unresponsive to IL-12, IL-18, and IL-10 as identified by the lack of differential expressed genes (DEGs) upon targeted sequencing and the minimal expression of the cytokine receptors required for downstream signalling. Nevertheless, IL-12 and IL-18 likely contribute indirectly to DILI by acting synergistically to drive a strong type I immune response through activation of NK and T cells, which in turn

exacerbates liver damage[313]. Notably, IL-18 has been reported to aggravate liver injury in a mouse model of acetaminophen-induced acute liver damage[314].

Although all five liver models examined in this study exhibited a response to IL-1β, the liver microtissues demonstrated the highest level of differential gene expression after transcriptomic analysis. This could be attributed to the responsiveness of the multiple liver cell types, hepatocytes, Kupffer cells, and stellate cells, to this cytokine, which collectively contributes to the relatively high number of DEGs[315,316]. Interestingly, target genes of canonical NF-κB transcription factors were not differentially upregulated as assessed by transcriptomic analysis across all five models. This was reflected by similar upregulation of inflammation-associated weighted gene co-expression analysis (WGCNA) modules in all test systems. Therefore, all five models can be utilized to study IL-1β-induced inflammation of the liver and its contribution to DILI reactions.

We further focused on TNF-α, a pleiotropic cytokine well-known for its contribution to idiosyncratic DILI (iDILI). TNF-α-mediated DILI has been identified for several drugs including amiodarone, trovafloxacin, ranitidine, diclofenac, sulindac, and halothane[317–323]. Deeper understanding of how drugs interact with the pathway downstream of the TNF receptor complex is of utmost importance to predict and prevent such drug-cytokine reactions. Although drug/TNF-α synergistic toxicity has been observed in PHH[324,325], it is not the preferred model system to study drug/TNF-α interactions due to the large interindividual variability across PHH donors in response to TNF-α [326]. We observed that our pooled donor primary human hepatocytes (PHH) also exhibit a weaker response to TNF-α than the other test systems. Based on our data, we identified hiPSC-derived HLCs and advanced HepG2 models as the preferred systems for studying TNF-α–induced inflammation and its role in iDILI. This conclusion is supported by their comparable, but stronger, upregulation of TXG-MAPr modules linked to NF-κB and TNF-α signalling compared to PHH, as well as their similar responses to diclofenac and trovafloxacin/TNF-α co-exposures. We ultimately chose hiPSC-derived HLCs for a proof-of-concept screen using NSAIDs, because of their benign origin. HepG2 cancer cells show differences in stress response signalling compared to normal hepatocytes, for instance caused by NF-κB– and MAPK-related mutations[327], that are likely to impact on the results of our assays. Finally, we showcase alterations in inflammatory stress pathway activation using an ICAM1-eGFP hiPSC reporter line upon NSAID/TNF-α incubation and cytotoxicity as predicted with several NSAIDs that are known to induce iDILI[328].

HiPSC models for toxicity assessment

HiPSC-based preclinical models are transforming toxicity testing by offering human-relevant, patient-specific cells for predicting drug toxicities. They allow for differentiation in every cell type of interest, allowing preclinical testing in various lineages, including the heart, kidney, and liver as we have shown in **chapter 5**. While hiPSC models can be used as a NAM, they possess several limitations, including costly and time-consuming differentiation programs, batch-variability and limited cryopreservation possibilities upon differentiation[329]. We propose several strategies to address this. First, quality control must be performed to ensure pluripotency and genetic integrity of the hiPSC lines of interest. Specific hiPSC colony morphology may be examined using light microscopy, and pluripotency should be confirmed by expression of OCT4, SOX2, SSEA4, and TRA-1-60. Genomic stability must be established through both karyotyping and copy-number variation analyses. Differentiation potential is finally assessed through trilineage differentiation into all three germ layers[330]. To confirm successful differentiation, efficiency must be assessed using lineage-specific markers, such as HNF4A and CYP3A4 for hepatocytes, cTnT1 for cardiomyocytes, and megalin for renal proximal tubule cells[150,331,332].

The cryopreservation of fully differentiated cells or intermediate populations may minimize batch variation and facilitate more efficient planning of labor-intensive differentiation workflows and has been described already for hepatocyte-, cardiomyocyte, and promixal tubule-like cells[331,333,334]. Taken together, implementation of all the above-mentioned suggestions would contribute to the generation of large, well-characterized, and standardized batches of hiPSC-derived cells that are essential for drug screening.

***In vitro* models to study inflammation-associated drug-induced hepatotoxicity**

Inflammation-mediated DILI remains challenging to identify using current preclinical models and unfortunately, incidence is too low to capture in clinical trials. Consequently, this ultimately results in post-market drug withdrawal. Therefore, there is an urgent need for preclinical models that can capture immuno-inflammatory hepatotoxicity. One of the mechanisms driving immune-mediated DILI are cytokine-drug reactions. We specifically describe that TNF-α/drug reactions can be identified in hiPSC-derived lineages in **chapters 2 and 5**. However, other cytokines, including IFN-γ have also been shown to synergize with drugs in HepG2 and PHH[335]. Therefore, performing drug/IFN-γ experiments using the hiPSC eGFP reporter for the IFN-γ-induced transcription factor IRF1 that was generated in **chapter 4**, may enhance our understanding of drug/IFN-γ synergism during early drug development in the future. We recognize that the aforementioned cytokines are not the sole drivers of synergistic drug

cytotoxicity and that cell–cell interactions play a significant role. Recently, Seongyea et al. showed that hiPSC-derived hepatic organoids with incorporated hiPSC-derived macrophages were significantly more sensitive to hepatotoxic drugs compared to hepatic organoids itself. Furthermore, hepatic maturity was enhanced in the hepatic organoid-Kupffer cell model compared to the hepatic organoid itself[336]. Therefore, I envision that this model opens doors for hepatotoxicity testing in the future.

Following innate immune cell activation, the adaptive immune response is also thought to play a critical role in the development of iDILI[337]. For example, reactive metabolites or neoantigens can be taken up by antigen-presenting cells and presented to $CD4^+$ helper T cells via the HLA complex. In the presence of costimulatory molecules such as CD80, CD86, and CD40, along with relevant cytokines, this process induces the proliferation of T cells that specifically recognize drug-modified peptides. Ultimately, this can lead to T cell–mediated hepatocyte death[338]. It is likely that susceptibility to iDILI development is dependent on HLA genotype as has been shown for flucloxacillin (HLA-B * 57:01)[339] and vancomycin (HLA-A *32:01)[340] among others. Integrating the adaptive immune system in current preclinical hepatocyte models remains challenging. However, the use of patient-matched hiPSC-derived cells to form 3D multicellular liver models shows potential for iDILI prediction. By using hiPSC-derived cells, we can generate a more personalized and genetically defined system suitable for high-throughput screening, as demonstrated in this thesis. Incorporating patient-derived or genetically modified hiPSCs harbouring SNPs in HLA genes or cytokines[341] will be essential for improving iDILI prediction in the future.

Fluorescent reporters for stress pathway activation

Our lab has shown the potential of fluorescent reporters tagged to proteins involved in stress pathway activation for drug-induced hepatotoxicity prediction. We previously generated fluorescent reporters in HepG2 cells using the BAC recombineering technology[342] and several studies have shown the suitability of this system to identify hepatotoxic drugs in a high-throughput setting[343–345]. Reporter gene integration using the BAC technology is a random process leading to multiple integrations within the genome that potentially affect general cell behaviour and downstream signalling of the transgene. To overcome random integration in the genome, the CRISPR/Cas9 technology is a suitable alternative to introduce a fluorophore scar-free at the gene of interest[346,347]. Roberts et al. were one of the first that showed that this method allows for fluorescent tagging of genes related to cell organization and that the generated fluorescent hiPSC lines retained the capacity to differentiate in all three germ layers[348]. In our lab, we generated and assessed the functionality of a HMOX1-eGFP hiPSC reporter to track oxidative stress response activation in various lineages including cardiomyocytes, neuronal cells, and renal proximal tubular cells[349]. We concluded that

eGFP intensity increased in a dose-dependent manner upon oxidative stress induction, but that the dynamics vary among lineages and stressors. This approach facilitates the evaluation and comparison of sensitivity to certain drugs across organs. In **chapter 4**, we have established a panel of eGFP fluorescent reporters in hiPSC for inflammatory stress induction and show their functionality in different lineages. All fluorescent reporters in this chapter were generated through heterozygous tagging to prevent the fluorophore-fusion product from affecting the functionality of the endogenous protein, although this also affects the sensitivity of the reporter. To increase signal-to-noise ratio, alternative green monomeric fluorescent proteins can be selected for fluorescent reporter generation that are brighter compared to eGFP. Examples of these novel variants are mNeonGreen, StayGold and mBaoJin, which not only exhibit enhanced brightness, but also increased photostability[350–352]. A limitation, however, of using green (488 nm) fluorophores is the autofluorescence of compounds as we experienced in **chapter 5**. To overcome this issue, we propose using fluorescent reporters in the (far) red spectrum, including mScarlet (red), mKate2 and Katushka2S[353,354]. In **chapter 3, 4, and 5** we were dependent on the nuclear staining $Hoechst_{33342}$ for single cell segmentation. Especially hiPSC-derived HLCs have the tendency to pump out $Hoechst_{33342}$ from the nucleus to the cytoplasm due to the high expression of nuclear transporters, resulting in difficulties with single-cell identification. In future studies, we propose to integrate a constitutively active reporter construct (e.g. TagBFP) tagged to histone 2B[355] to mitigate single cell segmentation errors.

Fluorescent reporter gene selection

We believe selecting appropriate reporter genes for stress pathway induction is crucial for drug safety evaluation. Therefore, we identified potential candidate genes for fluorescent tagging in a systematic manner in **chapter 4**. We specifically utilized weighted gene co-expression network analysis (WGCNA) on the TG-GATES dataset from primary human hepatocytes and rat liver exposed to hepatotoxic compounds and inflammatory inducers to identify genes that are most predictive for the identification of drugs that induce hepatotoxicity[356,357]. We systematically selected genes from predictive modules related to inflammation in both test models after TNF-α, IL-1β, and LPS incubation to increase confidence that these genes are truly associated with inflammatory stress induction. This resulted in the selection and CRISPR/Cas9-mediated generation of five hiPSC eGFP fluorescent reporters including A20, VCAM1, IRF1, LCN2 and RND1. A20 is known for its role as a canonical NF-κB downstream target that acts as a negative regulator of the same pathway via RIPK1[358,359]. VCAM1 is an adhesion molecule produced upon NF-κB activation promoting leukocyte adhesion and migration[360]. NF-κB signalling activation induces the expression of LCN2 finally

resulting in bacterial growth inhibition[361]. IRF1 is primarily known for its activation by type I interferons but is also upregulated upon stimulation with TNF-α and IL-1β[362]. Literature regarding the role of RND1 in inflammation appeared to be limited, but one study described its induction by pro-inflammatory cytokines in HEK293 cells[363] and therefore, we decided to take this candidate along in the CRISPR/Cas9 tagging procedure.

One target biomarker that was not systematically selected via WGCNA but was taken along as reporter candidate is ICAM1. We included this marker as it is a well-known adhesion molecule upregulated in the liver during pro-inflammatory conditions[364,365]. Additionally, previously our lab showed that the HepG2-ICAM1-eGFP reporter serves as a reliable predictor of altered inflammatory responses upon exposure to a variety of drugs, including diclofenac and azathioprine with inhibiting and enhancing immune modulatory effects respectively. In **chapter 5**, we explored the use of the established hiPSC-ICAM1-eGFP reporter to identify kinase inhibitors (KIs) with TNF-α-mediated modulatory capabilities in cardiac-, renal-, and liver-like lineages[366]. Several of the clinically relevant KIs that enhance ICAM1-eGFP expression were found to be associated with renal adverse events showcasing the applicability of this imaging-based hiPSC-ICAM1-eGFP reporter to identify KIs with immune modulatory effects. While in this thesis we specifically focused on fluorescent reporters in hiPSC for the inflammatory stress response, we have applied the same methodology to systematically identify predictive genes for drug safety evaluation for the DNA damage pathway, the ER/UPR stress response pathway and the oxidative stress response (van den Berk, and Bob van de Water, unpublished data). In the future, we believe that the generation of dual reporters capturing multiple response pathways in one hiPSC line would further promote our knowledge on drug-specific adverse reactions as various stress response pathways, including the ones mentioned above, can trigger and consequence inflammation[367–369]. In addition, similar approaches for the selection of reporter candidate genes should also be used future for other cell types including cardiomyocytes and proximal tubule cells to ensure utilizing the correct and most predictive biomarkers in those lineages.

For RND1 and LCN2 we were unable to generate functional fluorescent reporters that were activated upon inflammation induction. This can be explained in several ways. Firstly, the accessibility of the target locus within the genome is a primary factor as sites in open, less condensed euchromatin are more accessible to Cas9 compared to densely packed heterochromatin. Another crucial factor that could influence the functionality of a (fluorescent) protein is the location of the insertion of the fluorescent protein. Both N-terminal and C-terminal tagging come with specific challenges, particularly when critical signalling sequences or localization peptides are present in

these regions[370]. In our work, we decided to apply C-terminal tagging to all our gene candidates. For A20 and ICAM1 we were confident that tagging the C-terminus would result in a functional fluorescent protein as reporters for these targets were established and proved functional in previous work of our lab in HepG2 cells[342]. However, we were lacking information regarding C- or N-terminal tagging of the other candidates, and this could also potentially explain the dysfunctionality of the RND1 and LCN2 reporter. Especially, the RND1 C-terminus contains a CAAX motif that is crucial for post translational modification and membrane trafficking and disruption may lead to protein dysfunction[371]. Nevertheless, we were able to generate functional reporters for A20, IRF1, and ICAM1 that could be predictive for inflammatory-related adverse drug reactions in the future.

Sensitivity to TNF-α- induced adverse drug reactions across cell lineages

All cell types within and across an organ use similar stress response mechanisms to cope and manage several different stressors, including xenobiotics. These pathways serve to maintain or reestablish cellular homeostasis in response to perturbations in cellular processes[372]. One could therefore argue whether it is required to test a panel of compounds in different cell types, or that outcome in one cell type can be extrapolated to other lineages as well. The adaptive stress response comprises several phases, including 1) the baseline non-stress state; 2) the reactivity phase, which functions to detect, mitigate, and cope with the challenge; and 3) the recovery phase, which facilitates the return to the non-stress state or cellular homeostasis[373]. However, when stress is excessive or adaptive mechanisms fail, a more severe outcome may occur, leading to the activation of cell death pathways. Various parameters influence adaptation to drug-induced stress, including magnitude and duration of the stimulus, disease status, and cell type. Accordingly, a KI screen was performed in three distinct hiPSC-derived cell types to investigate alterations in TNF-α signalling activation upon KI exposure, as described in **Chapter 5**. Although minor differences were observed in the kinome between the cell lineages, we found little overlap in compounds that could upregulate downstream targets of the TNF-α pathway as assessed using the ICAM1-eGFP reporter. This exemplifies that screening identical compounds across multiple cell types can yield divergent results, highlighting the need for parallel screening in different cell types to achieve broad biological coverage. One possible explanation is that most KIs require biotransformation by P450 enzymes, with the resulting toxic metabolites potentially inducing toxicity[374,375]. If this were the case, more hits would be expected in HLCs compared to the other cell types; however, we observed a greater number of hits enhancing ICAM1 expression in PTLCs. Alternatively, it can also be hypothesized that parent compound itself is responsible for adverse reactions in the various lineages. As KIs are a relatively new drug class, with only 85 FDA-approved KIs

on the market in 2025[376], it remained challenging to extrapolate our results to adverse events found in the clinic. Nonetheless, four hits identified in PTLCs (palbociclib, miltefosine, gilteritinib and erdafitinib) have been linked to renal adverse events in the clinic. Notably, palbociclib and gilteritinib were also associated with inflammation-related renal adverse events and therefore this testing approach can be utilized to identify novel drugs with DILI liability in the future. In addition, this study highlights the importance of screening compounds across multiple cell types typically affected by adverse reactions, as target organ-specific liabilities can occur.

Future perspectives and conclusions

This thesis describes the development of new approach methodologies to improve *in vitro* xenobiotic risk assessment, with a particular focus on hiPSC-based models. Although multiple stress response pathways are associated with drug liabilities, this work specifically focused on drug-induced perturbations of TNF-α signalling, as inflammation-related stress remains difficult to detect during the early stages of drug development. The generation and subsequent use of fluorescent reporters in hiPSC-derived cells was shown to be informative to identify drug-induced liabilities related to TNF-α signalling and is expected to support safety assessment in the future.

The use of *in vitro* models for hepatotoxicity assessment is expected to become increasingly important in the future, supporting the principles of the 3Rs by replacing, reducing and refining the use of animals in research. Primary human hepatocytes are likely to remain the gold standard for toxicology research. However, they will increasingly be complemented by other in vitro models within a tiered testing strategy. The use of cancer-derived cell lines, such as HepG2 cells, is anticipated to decline in favour of benign cell models, including hiPSC-derived hepatocytes. These models offer the additional advantage of enabling toxicological assessments across diverse genetic backgrounds, thereby improving the relevance of toxicity testing and supporting more personalized approaches. Although both our work and that of others have demonstrated the ability to identify drug liabilities using HLC, improvements in differentiation protocols remain necessary to better predict drug-induced adversity[377]. This can be achieved via overexpression of cell type-specific transcription factors or adjusting media recipes to induce (metabolic) maturation[378,379]. Further improved maturity can be generated through culturing cells in 3D structures in extracellular matrices, combined with other relevant cell types[380,381]. To potentially replace current gold standards in drug safety assessment, the drug specificity and sensitivity of newly developed hiPSC-based models must be benchmarked against existing reference models. To achieve this, well-characterized reference compounds with known cardiotoxic, nephrotoxic, or hepatotoxic effects should be employed. For example, a

representative set of hepatotoxic and nephrotoxic compounds can be drawn from the TG-GATEs database[382].

In this thesis, we specifically focused on using fluorescent reporters to identify compounds that modulate TNF-α signalling in high-throughput screens. While this approach provides valuable information, it should be complemented with other mechanistic analyses, such as toxicogenomics and the TXG-MAPr for mechanism-based risk assessment, and to identify shared toxicity mechanisms among compounds [383,384]. Ultimately, combining 2D and 3D models with high-throughput screening of fluorescent reporters for stress response pathway activation, alongside toxicogenomics, will enhance mechanistic understanding of drug-induced organ toxicities and support drug development by reducing both costs and timelines.



APPENDICES

REFERENCES
ABBREVIATIONS
NEDERLANDSE SAMENVATTING
LIST OF PUBLICATIONS
ABOUT THE AUTHOR

References

1. Komagamine J. Prevalence of urgent hospitalizations caused by adverse drug reactions: a cross-sectional study. *Sci Rep*. 2024;14(1):1-7. doi:10.1038/s41598-024-56855-z

2. Rodrigues D, Souza T, Jennen DGJ, Lemmens L, Kleinjans JCS, Kok TM De. Drug-induced gene expression pro fi le changes in relation to intestinal toxicity : State-of-the-art and new approaches. *Cancer Treat Rev*. 2019;77(June):57-66. doi:10.1016/j.ctrv.2019.06.004

3. Gavaghan M, Pashley HS. Home Study Program Cardiac Anatomy and Physiology: A Review. *AORN J*. 1999;67(4):800-822.

4. Tucker NR, Chaffin M, Fleming SJ, et al. Transcriptional and Cellular Diversity of the Human Heart. *Circulation*. 2020;142(5):466-482. doi:10.1161/CIRCULATIONAHA.119.045401

5. Litviňuková M, Talavera-López C, Maatz H, et al. Cells of the adult human heart. *Nature*. 2020;588(7838):466-472. doi:10.1038/s41586-020-2797-4

6. Anto Michel N, Ljubojevic-Holzer S, Bugger H, Zirlik A. Cellular Heterogeneity of the Heart. *Front Cardiovasc Med*. 2022;9(April):1-13. doi:10.3389/fcvm.2022.868466

7. Yerra VG, Advani A. Role of CCR2-Positive Macrophages in Pathological Ventricular Remodelling. *Biomedicines*. 2022;10(3):661. doi:10.3390/biomedicines10030661

8. Mamoshina P, Rodriguez B, Bueno-Orovio A. Toward a broader view of mechanisms of drug cardiotoxicity. *Cell Rep Med*. 2021;2(3):100216. doi:10.1016/j.xcrm.2021.100216

9. Destere A, Merino D, Lavrut T, et al. Drug-induced cardiac toxicity and adverse drug reactions, a narrative review. *Therapies*. 2024;79(2):161-172. doi:10.1016/j.therap.2023.10.008

10. Wang X, Chen L, Wei J, et al. *The Immune System in Cardiovascular Diseases: From Basic Mechanisms to Therapeutic Implications*. Vol 10. Springer US; 2025. doi:10.1038/s41392-025-02220-z

11. Song L, Qiu Q, Ju F, Zheng C. Mechanisms of doxorubicin-induced cardiac inflammation and fibrosis; therapeutic targets and approaches. *Arch Biochem Biophys*. 2024;761(August):110140. doi:10.1016/j.abb.2024.110140

12. Zavaleta-Monestel E, García-Montero J, Anchía-Alfaro A, et al. Myocarditis Induced by Immune Checkpoint Inhibitors: An Exploratory Review. *Cureus*. 2024;16(8). doi:10.7759/cureus.67314

13. Mauro MJ, Hehlmann R, Williams LA, et al. Five-year molecular response and overall survival with first- and second-generation tyrosine kinase inhibitors in patients with chronic myeloid leukemia in the chronic phase: a prospective, observational study – SIMPLICITY. *Leuk Lymphoma*. 2025;66(9):1615-1624. doi:10.1080/10428194.2025.2495369

14. Fenchel K, Dale SP, Dempke WCM. Improved overall survival following tyrosine kinase inhibitor (TKI) treatment in NSCLC—are we making progress? *Transl Lung Cancer Res*. 2016;5(4):373-376. doi:10.21037/tlcr.2016.07.01

15. Sayegh N, Yirerong J, Agarwal N, et al. Cardiovascular Toxicities Associated with Tyrosine Kinase Inhibitors. *Curr Cardiol Rep*. 2023;25(4):269-280. doi:10.1007/s11886-023-01845-2

16. Zhu S, Fu K, Li S, et al. Cardiotoxicity of small-molecule kinase inhibitors in cancer therapy. *Exp Hematol Oncol*. 2025;14(1):1-27. doi:10.1186/s40164-025-00660-5

17. Majeed MN, Venkatesan S, Papadatos-Pastos D, et al. Entrectinib-Induced Myocarditis and Acute Heart Failure Responding to Steroid Treatment: A Case Report. *JTO Clin Res Rep*. 2024;5(12):100746. doi:10.1016/j.jtocrr.2024.100746

18. Wallace MA. Anatomy and Physiology of the Kidney. *AORN J*. 1998;68(5):799-820. doi:10.1016/S0001-2092(06)62377-6

19. Qiu C, Huang S, Park J, et al. Renal compartment–specific genetic variation analyses identify new pathways in chronic kidney disease. *Nat Med*. 2018;24(11):1721-1731. doi:10.1038/s41591-018-0194-4

20. Balzer MS, Rohacs T, Susztak K. How Many Cell Types Are in the Kidney and What Do They Do? *Annu Rev Physiol*. 2022;84(1):507-531. doi:10.1146/annurev-physiol-052521-121841

21. Hinson JS, Ehmann MR, Al Jalbout N, Ortmann MJ, Zschoche J, Klein EY. Risk of Acute Kidney Injury Associated With Medication Administration in the Emergency Department. *J Emerg Med*. 2020;58(3):487-496. doi:10.1016/j.jemermed.2019.11.034

22. Hall AM, Trepiccione F, Unwin RJ. Drug toxicity in the proximal tubule: new models, methods and mechanisms. doi:10.1007/s00467-021-05121-9/Published

23. Perazella MA, Rosner MH. Drug-Induced Acute Kidney Injury. *Clinical Journal of the American Society of Nephrology*. 2022;17(8):1220-1233. doi:10.2215/CJN.11290821

24. Markóth C, File I, Szász R, Bidiga L, Balla J, Mátyus J. Ibrutinib-induced acute kidney injury via interstitial nephritis. *Ren Fail*. 2021;43(1):335-339. doi:10.1080/0886022X.2021.1874985

25. Winn SK, Ellis S, Savage P, Sampson S, Marsh JE. Biopsy-proven acute interstitial nephritis associated with the tyrosine kinase inhibitor sunitinib: a class effect? *Nephrology Dialysis Transplantation*. 2008;24(2):673-675. doi:10.1093/ndt/gfn625

26. Fusco S, Garasto S, Corsonello A, et al. Medication-Induced Nephrotoxicity in Older Patients. *Curr Drug Metab*. 2016;17(6):608-625. doi:10.2174/1389200217666160406115959

27. Xiong X, Kuang H, Liu T, Lin JD. A Single-Cell Perspective of the Mammalian Liver in Health and Disease. *Hepatology*. 2020;71(4):1467-1473. doi:10.1002/hep.31149

28. Schulze RJ, Schott MB, Casey CA, Tuma PL, McNiven MA. The cell biology of the hepatocyte: A membrane trafficking machine. *Journal of Cell Biology*. 2019;218(7):2096-2112. doi:10.1083/jcb.201903090

29. Trefts E, Gannon M, Wasserman DH. The liver. *Current Biology*. 2017;27(21):R1147-R1151. doi:10.1016/j.cub.2017.09.019

30. Hosack T, Damry D, Biswas S. Drug-induced liver injury: a comprehensive review. *Therap Adv Gastroenterol*. *SAGE Publications Ltd*. 2023;16. doi:10.1177/17562848231163410

31. Fung M, Thornton A, Mybeck K, Wu JHH, Hornbuckle K, Muniz E. Evaluation of the Characteristics of Safety Withdrawal of Prescription Drugs from Worldwide Pharmaceutical Markets-1960 to 1999. *Drug Inf J*. 2001;35(1):293-317. doi:10.1177/009286150103500134

32. Chen M, Vijay V, Shi Q, Liu Z, Fang H, Tong W. FDA-approved drug labeling for the study of drug-induced liver injury. *Drug Discov Today*. 2011;16(15-16):697-703. doi:10.1016/j.drudis.2011.05.007

33. Weaver RJ, Blomme EA, Chadwick AE, et al. Managing the challenge of drug-induced liver injury: a roadmap for the development and deployment of preclinical predictive models. *Nat Rev Drug Discov*. 2020;19(2):131-148. doi:10.1038/s41573-019-0048-x

34. Hosohata K. Role of Oxidative Stress in Drug-Induced Kidney Injury. *Int J Mol Sci*. 2016;17(11):1826. doi:10.3390/ijms17111826

35. Cheng C, Yuan Y, Yuan F, Li X. Acute kidney injury: exploring endoplasmic reticulum stress-mediated cell death. *Front Pharmacol*. 2024;15. doi:10.3389/fphar.2024.1308733

36. Yan M, Peng C, Lang X, Li Y, Zhang Y. Mechanisms of sorafenib-induced cardiotoxicity: ER stress induces upregulation of ATF3, leading to downregulation of NDUFS1 expression and mitochondrial dysfunction. *Front Pharmacol*. 2025;16. doi:10.3389/fphar.2025.1593290

37. Jamal A. An Insight to Diagnosis and Management of Drug-induced Hepatotoxicity: An Overview. Published online 2021. doi:10.37591/TDD

38. Mennicke M, Zawodniak A, Keller M, et al. Fulminant liver failure after vancomycin in a sulfasalazine-induced DRESS syndrome: Fatal recurrence after liver transplantation: Case report. *American Journal of Transplantation*. 2009;9(9):2197-2202. doi:10.1111/j.1600-6143.2009.02788.x

39. Adair K, Meng X, Naisbitt DJ. Drug hapten-specific T-cell activation: Current status and unanswered questions. *Proteomics*. 2021;21(17-18). doi:10.1002/pmic.202000267

40. Tailor A, Meng X, Adair K, et al. HLA DRB1*15:01-DQB1*06:02-Restricted Human CD4+ T Cells Are Selectively Activated With Amoxicillin-Peptide Adducts. *Toxicological Sciences*. 2020;178(1):115-126. doi:10.1093/toxsci/kfaa128

41. Monshi MM, Faulkner L, Gibson A, et al. Human Leukocyte Antigen (HLA)-B*57:01-Restricted Activation of Drug-Specific T cells Provides the Immunological Basis for Flucloxacillin-Induced Liver Injury. *Hepatology*. 2013;57(2):727-739. doi:10.1002/hep.26077

42. Asif BA, Koh C, Phillips EJ, et al. Vancomycin-Induced Liver Injury, DRESS, and HLA-A∗32:01. *J Allergy Clin Immunol Pract*. 2024;12(1):168-174.e2. doi:10.1016/j.jaip.2023.09.011

43. Shaw PJ, Beggs KM, Sparkenbaugh EM, Dugan CM, Ganey PE, Roth RA. Trovafloxacin enhances TNF-induced inflammatory stress and cell death signaling and reduces TNF clearance in a murine model of idiosyncratic hepatotoxicity. *Toxicological Sciences*. 2009;111(2):288-301. doi:10.1093/toxsci/kfp163

44. Fredriksson L, Herpers B, Benedetti G, et al. Diclofenac inhibits tumor necrosis factor-α-induced nuclear factor-κB activation causing synergistic hepatocyte apoptosis. *Hepatology*. 2011;53(6):2027-2041. doi:10.1002/hep.24314

45. Deng X, Stachlewitz RF, Liguori MJ, et al. Modest inflammation enhances diclofenac hepatotoxicity in rats: Role of neutrophils and bacterial translocation. *Journal of Pharmacology and Experimental Therapeutics*. 2006;319(3):1191-1199. doi:10.1124/jpet.106.110247

46. Zou W, Beggs KM, Sparkenbaugh EM, et al. Sulindac metabolism and synergy with tumor necrosis factor-α in a drug-inflammation interaction model of idiosyncratic liver injury. *Journal of Pharmacology and Experimental Therapeutics*. 2009;331(1):114-121. doi:10.1124/jpet.109.156331

47. Brenner C, Galluzzi L, Kepp O, Kroemer G. Decoding cell death signals in liver inflammation. *J Hepatol*. 2013;59(3):583-594. doi:10.1016/j.jhep.2013.03.033

48. Andrade RJ, Chalasani N, Björnsson ES, et al. Drug-induced liver injury. *Nat Rev Dis Primers*. 2019;5(1). doi:10.1038/s41572-019-0105-0

49. Brenner D, Blaser H, Mak TW. Regulation of tumour necrosis factor signalling: live or let die. *Nat Rev Immunol*. 2015;15(6):362-374. doi:10.1038/nri3834

50. Webster JD, Vucic D. The Balance of TNF Mediated Pathways Regulates Inflammatory Cell Death Signaling in Healthy and Diseased Tissues. *Front Cell Dev Biol*. *Frontiers Media S.A.* 2020;8. doi:10.3389/fcell.2020.00365

51. Hoffmann A, Cheng G, Baltimore D. NF-κB: master regulator of cellular responses in health and disease. *Immunity & Inflammation*. 2025;1(1):2. doi:10.1007/s44466-025-00014-0

52. Guo Q, Jin Y, Chen X, et al. NF-κB in biology and targeted therapy: new insights and translational implications. *Signal Transduct Target Ther*. *Springer Nature*. 2024;9(1). doi:10.1038/s41392-024-01757-9

53. van Loo G, Bertrand MJM. Death by TNF: a road to inflammation. *Nat Rev Immunol*. 2023;23(5):289-303. doi:10.1038/s41577-022-00792-3

54. Sun H, Xia M, Austin CP, Huang R. Paradigm Shift in Toxicity Testing and Modeling. *AAPS J*. 2012;14(3):473-480. doi:10.1208/s12248-012-9358-1

55. Raschi E, Ceccarini L, De Ponti F, Recanatini M. hERG-related drug toxicity and models for predicting hERG liability and QT prolongation. *Expert Opin Drug Metab Toxicol*. 2009;5(9):1005-1021. doi:10.1517/17425250903055070

56. Bouitbir J, Alshaikhali A, Panajatovic M, Abegg V, Paech F, Krähenbühl S. Mechanisms of Cardiotoxicity Associated with Tyrosine Kinase Inhibitors in H9c2 Cells and Mice. *European Cardiology Review*. 2020;15:e33. doi:10.15420/ecr.2020.15.1.PO10

57. Takahashi K, Tanabe K, Ohnuki M, et al. Induction of Pluripotent Stem Cells from Adult Human Fibroblasts by Defined Factors. *Cell*. 2007;131(5):861-872. doi:10.1016/j.cell.2007.11.019

58. Giacomelli E, Bellin M, Sala L, et al. Three-dimensional cardiac microtissues composed of cardiomyocytes and endothelial cells co-differentiated from human pluripotent stem cells. *Development*. Published online January 1, 2017. doi:10.1242/dev.143438

59. Windt LM, Wiendels M, Dostanić M, et al. Miniaturized engineered heart tissues from hiPSC-derived triple cell type co-cultures to study human cardiac function. *Biochem Biophys Res Commun*. 2023;681:200-211. doi:10.1016/j.bbrc.2023.09.034

60. Perazella MA. Renal Vulnerability to Drug Toxicity. *Clinical Journal of the American Society of Nephrology*. 2009;4(7):1275-1283. doi:10.2215/CJN.02050309

61. Faria J, Ahmed S, Gerritsen KGF, Mihaila SM, Masereeuw R. Kidney-based in vitro models for drug-induced toxicity testing. *Arch Toxicol*. 2019;93(12):3397-3418. doi:10.1007/s00204-019-02598-0

62. Aschauer L, Carta G, Vogelsang N, Schlatter E, Jennings P. Expression of xenobiotic transporters in the human renal proximal tubule cell line RPTEC/TERT1. *Toxicology in Vitro*. 2015;30(1):95-105. doi:10.1016/j.tiv.2014.12.003

63. Meijer T, Naderlinger E, Jennings P, Wilmes A. Differentiation and Subculturing of Renal Proximal Tubular-like Cells Derived from Human iPSC. *Curr Protoc*. 2023;3(8). doi:10.1002/cpz1.850

64. Chandrasekaran V, Carta G, da Costa Pereira D, et al. Generation and characterization of iPSC-derived renal proximal tubule-like cells with extended stability. *Sci Rep*. 2021;11(1):11575. doi:10.1038/s41598-021-89550-4

65. Bahtiri S, Hagens TMS, van de Water B, Niemeijer M. Mechanism-based drug safety testing using innovative in vitro liver models: from DILI prediction to idiosyncratic DILI liability assessment. *Expert Opin Drug Metab Toxicol*. *Taylor and Francis Ltd.* 2025;21(7):769-787. doi:10.1080/17425255.2025.2516051

66. Kim Y, Kim H, Kim Y. Advancing hepatotoxicity assessment: current advances and future directions. *Toxicol Res*. *Springer*. 2025;41(4):303-323. doi:10.1007/s43188-025-00289-w

67. Wink S, Hiemstra SW, Huppelschoten S, Klip JE, van de Water B. Dynamic imaging of adaptive stress response pathway activation for prediction of drug induced liver injury. *Arch Toxicol*. 2018;92(5):1797-1814. doi:10.1007/s00204-018-2178-z

68. Boon R, Kumar M, Tricot T, et al. Amino acid levels determine metabolism and CYP450 function of hepatocytes and hepatoma cell lines. *Nat Commun*. 2020;11(1):1393. doi:10.1038/s41467-020-15058-6

69. Vlasveld M, van den Berk L, Piñero J, et al. A broad kinase inhibitor library live cell imaging screen using liver, kidney and cardiac hiPSC-ICAM1-eGFP reporter lineages identifies liabilities for TNFα pathway modulation. *Arch Toxicol*. Published online November 5, 2025. doi:10.1007/s00204-025-04226-6

70. Niemeijer M, Wieęcek W, Fu S, et al. Mapping Interindividual Variability of Toxicodynamics Using High-Throughput Transcriptomics and Primary Human Hepatocytes from Fifty Donors. *Environ Health Perspect*. 2024;132(3):14-17. doi:10.1289/EHP11891

71. Cosgrove BD, King BM, Hasan MA, et al. Synergistic drug-cytokine induction of hepatocellular death as an in vitro approach for the study of inflammation-associated idiosyncratic drug hepatotoxicity. *Toxicol Appl Pharmacol*. 2009;237(3):317-330. doi:10.1016/j.taap.2009.04.002

72. Beggs KM, Fullerton AM, Miyakawa K, Ganey PE, Roth RA. Molecular mechanisms of hepatocellular apoptosis induced by trovafloxacin-tumor necrosis factor-alpha interaction. *Toxicological Sciences*. 2014;137(1):91-101. doi:10.1093/toxsci/kft226

73. Wink S, Hiemstra S, Herpers B, van de Water B. High-content imaging-based BAC-GFP toxicity pathway reporters to assess chemical adversity liabilities. *Arch Toxicol*. 2017;91(3):1367-1383. doi:10.1007/s00204-016-1781-0

74. Roberts B, Haupt A, Tucker A, et al. Systematic gene tagging using CRISPR/Cas9 in human stem cells to illuminate cell organization. *Mol Biol Cell*. 2017;28(21):2854-2874. doi:10.1091/mbc.E17-03-0209

75. Teschke R, Schulze J, Eickhoff A, Danan G. Drug induced liver injury: Can biomarkers assist RUCAM in causality assessment? *Int J Mol Sci*. *MDPI AG*. 2017;18(4). doi:10.3390/ijms18040803

76. Gu X, Albrecht W, Edlund K, et al. Relevance of the incubation period in cytotoxicity testing with primary human hepatocytes. *Arch Toxicol*. 2018;92(12):3505-3515. doi:10.1007/s00204-018-2302-0

77. Fredriksson L, Herpers B, Benedetti G, et al. Diclofenac inhibits tumor necrosis factor-α-induced nuclear factor-κB activation causing synergistic hepatocyte apoptosis. *Hepatology*. 2011;53(6):2027-2041. doi:10.1002/hep.24314

78. Giustarini G, Huppelschoten S, Barra M, et al. The hepatotoxic fluoroquinolone trovafloxacin disturbs TNF- and LPS-induced p65 nuclear translocation in vivo and in vitro. *Toxicol Appl Pharmacol*. 2020;391(October 2019):114915. doi:10.1016/j.taap.2020.114915

79. Fredriksson L, Wink S, Herpers B, et al. Drug-induced endoplasmic reticulum and oxidative stress responses independently sensitize toward TNFα-mediated hepatotoxicity. *Toxicological Sciences*. 2014;140(1):144-159. doi:10.1093/toxsci/kfu072

80. Herpers B, Wink S, Fredriksson L, et al. Activation of the Nrf2 response by intrinsic hepatotoxic drugs correlates with suppression of NF-κB activation and sensitizes toward TNFα-induced cytotoxicity. *Arch Toxicol*. 2016;90(5):1163-1179. doi:10.1007/s00204-015-1536-3

81. Almazroo OA, Miah MK, Venkataramanan R. Drug Metabolism in the Liver. *Clin Liver Dis*. 2017;21(1):1-20. doi:10.1016/j.cld.2016.08.001

82. Andrade RJ, Aithal GP, Björnsson ES, et al. EASL Clinical Practice Guidelines: Drug-induced liver injury. *J Hepatol*. 2019;70(6):1222-1261. doi:10.1016/j.jhep.2019.02.014

83. Kullak-Ublick GA, Andrade RJ, Merz M, et al. Drug-induced liver injury: recent advances in diagnosis and risk assessment. *Gut*. 2017;66(6):1154-1164. doi:10.1136/gutjnl-2016-313369

84. Rowe C, Gerrard DT, Jenkins R, et al. Proteome-Wide Analyses of Human Hepatocytes During Differentiation and Dedifferentiation. *Hepatology*. 2013;58(2):799-809. doi:10.1002/hep.26414

85. Heslop JA, Rowe C, Walsh J, et al. Mechanistic evaluation of primary human hepatocyte culture using global proteomic analysis reveals a selective dedifferentiation profile. *Arch Toxicol*. 2017;91(1):439-452. doi:10.1007/s00204-016-1694-y

86. Gerets HHJ, Tilmant K, Gerin B, et al. Characterization of primary human hepatocytes, HepG2 cells, and HepaRG cells at the mRNA level and CYP activity in response to inducers and their predictivity for the detection of human hepatotoxins. *Cell Biol Toxicol*. 2012;28(2):69-87. doi:10.1007/s10565-011-9208-4

87. Hughes CS, Postovit LM, Lajoie GA. Matrigel: A complex protein mixture required for optimal growth of cell culture. *Proteomics*. 2010;10(9):1886-1890. doi:10.1002/pmic.200900758

88. Ramaiahgari SC, den Braver MW, Herpers B, et al. A 3D in vitro model of differentiated HepG2 cell spheroids with improved liver-like properties for repeated dose high-throughput toxicity studies. *Arch Toxicol*. Published online March 6, 2014. doi:10.1007/s00204-014-1215-9

89. Hiemstra S, Ramaiahgari SC, Wink S, et al. High-throughput confocal imaging of differentiated 3D liver-like spheroid cellular stress response reporters for identification of drug-induced liver injury liability. *Arch Toxicol*. 2019;93(10):2895-2911. doi:10.1007/s00204-019-02552-0

90. Stevens KR, Miller JS, Blakely BL, Chen CS, Bhatia SN. Degradable hydrogels derived from PEG-diacrylamide for hepatic tissue engineering. *J Biomed Mater Res A*. 2015;103(10):3331-3338. doi:10.1002/jbm.a.35478

91. Malinen MM, Palokangas H, Yliperttula M, Urtti A. Peptide Nanofiber Hydrogel Induces Formation of Bile Canaliculi Structures in Three-Dimensional Hepatic Cell Culture. *Tissue Eng Part A*. 2012;18(23-24):2418-2425. doi:10.1089/ten.tea.2012.0046

92. Jeon H, Kang K, Park SA, et al. Generation of Multilayered 3D Structures of HepG2 Cells Using a Bio-printing Technique. *Gut Liver*. 2017;11(1):121-128. doi:10.5009/gnl16010

93. Bhise NS, Manoharan V, Massa S, et al. A liver-on-a-chip platform with bioprinted hepatic spheroids. *Biofabrication*. 2016;8(1):014101. doi:10.1088/1758-5090/8/1/014101

94. Christoffersson J, Aronsson C, Jury M, Selegård R, Aili D, Mandenius CF. Fabrication of modular hyaluronan-PEG hydrogels to support 3D cultures of hepatocytes in a perfused liver-on-a-chip device. *Biofabrication*. 2018;11(1):015013. doi:10.1088/1758-5090/aaf657

95. Krüger M, Oosterhoff LA, van Wolferen ME, et al. Cellulose Nanofibril Hydrogel Promotes Hepatic Differentiation of Human Liver Organoids. *Adv Healthc Mater*. 2020;9(6). doi:10.1002/adhm.201901658

96. Klotz BJ, Oosterhoff LA, Utomo L, et al. A Versatile Biosynthetic Hydrogel Platform for Engineering of Tissue Analogues. *Adv Healthc Mater*. 2019;8(19). doi:10.1002/adhm.201900979

97. Ye S, Boeter JWB, Mihajlovic M, et al. A Chemically Defined Hydrogel for Human Liver Organoid Culture. *Adv Funct Mater*. 2020;30(48). doi:10.1002/adfm.202000893

98. Sorrentino G, Rezakhani S, Yildiz E, et al. Mechano-modulatory synthetic niches for liver organoid derivation. *Nat Commun*. 2020;11(1):3416. doi:10.1038/s41467-020-17161-0

99. Kumar M, Toprakhisar B, Van Haele M, et al. A fully defined matrix to support a pluripotent stem cell derived multi-cell-liver steatohepatitis and fibrosis model. *Biomaterials*. 2021;276:121006. doi:10.1016/j.biomaterials.2021.121006

100. Webber MJ, Appel EA, Meijer EW, Langer R. Supramolecular biomaterials. *Nat Mater*. 2016;15(1):13-26. doi:10.1038/nmat4474

101. Maikawa CL, Smith AAA, Zou L, et al. A co-formulation of supramolecularly stabilized insulin and pramlintide enhances mealtime glucagon suppression in diabetic pigs. *Nat Biomed Eng*. 2020;4(5):507-517. doi:10.1038/s41551-020-0555-4

102. Straßburger D, Stergiou N, Urschbach M, et al. Mannose-Decorated Multicomponent Supramolecular Polymers Trigger Effective Uptake into Antigen-Presenting Cells. *ChemBioChem*. 2018;19(9):912-916. doi:10.1002/cbic.201800114

103. Spaans S, Fransen PPKH, Schotman MJG, et al. Supramolecular Modification of a Sequence-Controlled Collagen-Mimicking Polymer. *Biomacromolecules*. 2019;20(6):2360-2371. doi:10.1021/acs.biomac.9b00353

104. Wang Y, Dillon KM, Li Z, Winckler EW, Matson JB. Alleviating Cellular Oxidative Stress through Treatment with Superoxide-Triggered Persulfide Prodrugs. *Angewandte Chemie*. 2020;132(38):16841-16847. doi:10.1002/ange.202006656

105. Ramos J, Arufe S, Martin H, et al. Glycosyl squaramides, a new class of supramolecular gelators. *Soft Matter*. 2020;16(34):7916-7926. doi:10.1039/D0SM01075H

106. Marchetti LA, Kumawat LK, Mao N, Stephens JC, Elmes RBP. The Versatility of Squaramides: From Supramolecular Chemistry to Chemical Biology. *Chem*. 2019;5(6):1398-1485. doi:10.1016/j.chempr.2019.02.027

107. López C, Ximenis M, Orvay F, Rotger C, Costa A. Supramolecular Hydrogels Based on Minimalist Amphiphilic Squaramide–Squaramates for Controlled Release of Zwitterionic Biomolecules. *Chemistry – A European Journal*. 2017;23(31):7590-7594. doi:10.1002/chem.201701029

108. Castellanos E, Soberats B, Bujosa S, Rotger C, de la Rica R, Costa A. Development of Plasmonic Chitosan–Squarate Hydrogels via Bioinspired Nanoparticle Growth. *Biomacromolecules*. 2020;21(2):966-973. doi:10.1021/acs.biomac.9b01635

109. Saez Talens V, Englebienne P, Trinh TT, Noteborn WEM, Voets IK, Kieltyka RE. Aromatic Gain in a Supramolecular Polymer. *Angewandte Chemie*. 2015;127(36):10648-10652. doi:10.1002/ange.201503905

110. Saez Talens V, Makurat DMM, Liu T, et al. Shape modulation of squaramide-based supramolecular polymer nanoparticles. *Polym Chem*. 2019;10(23):3146-3153. doi:10.1039/C9PY00310J

111. Tong C, Liu T, Saez Talens V, et al. Squaramide-Based Supramolecular Materials for Three-Dimensional Cell Culture of Human Induced Pluripotent Stem Cells and Their Derivatives. *Biomacromolecules*. 2018;19(4):1091-1099. doi:10.1021/acs.biomac.7b01614

112. Saez Talens V, Arias-Alpizar G, Makurat DMM, et al. Stab2-Mediated Clearance of Supramolecular Polymer Nanoparticles in Zebrafish Embryos. *Biomacromolecules*. 2020;21(3):1060-1068. doi:10.1021/acs.biomac.9b01318

113. Albrecht-Gary A, Blanc S, Biaso F, et al. Iron(<scp>III</scp>) Chelation: Tuning of the pH Dependence by Mixed Ligands. *Eur J Inorg Chem*. 2003;2003(14):2596-2605. doi:10.1002/ejic.200200643

114. Tong C, Liu T, Saez Talens V, et al. Squaramide-Based Supramolecular Materials for Three-Dimensional Cell Culture of Human Induced Pluripotent Stem Cells and Their Derivatives. *Biomacromolecules*. 2018;19(4):1091-1099. doi:10.1021/acs.biomac.7b01614

115. van Hoorn H. *Cellular Forces : Adhering, Shaping, Sensing and Dividing*. Leiden University; 2014.

116. Tong C, Wondergem JAJ, Heinrich D, Kieltyka RE. Photopatternable, Branched Polymer Hydrogels Based on Linear Macromonomers for 3D Cell Culture Applications. *ACS Macro Lett*. 2020;9(6):882-888. doi:10.1021/acsmacrolett.0c00175

117. Peng T, Thorn K, Schroeder T, et al. A BaSiC tool for background and shading correction of optical microscopy images. *Nat Commun*. 2017;8(1):14836. doi:10.1038/ncomms14836

118. Park KD, Liu R, Kohn H. Useful Tools for Biomolecule Isolation, Detection, and Identification: Acylhydrazone-Based Cleavable Linkers. *Chem Biol*. 2009;16(7):763-772. doi:10.1016/j.chembiol.2009.06.005

119. Yu C han, Law JBK, Suryana M, Low HY, Sheetz MP. Early integrin binding to Arg-Gly-Asp peptide activates actin polymerization and contractile movement that stimulates outward translocation. *Proceedings of the National Academy of Sciences*. 2011;108(51):20585-20590. doi:10.1073/pnas.1109485108

120. Caswell PT, Zech T. Actin-Based Cell Protrusion in a 3D Matrix. *Trends Cell Biol*. 2018;28(10):823-834. doi:10.1016/j.tcb.2018.06.003

121. Hakkinen KM, Harunaga JS, Doyle AD, Yamada KM. Direct Comparisons of the Morphology, Migration, Cell Adhesions, and Actin Cytoskeleton of Fibroblasts in Four Different Three-Dimensional Extracellular Matrices. *Tissue Eng Part A*. 2011;17(5-6):713-724. doi:10.1089/ten.tea.2010.0273

122. Liu H, Wu M, Jia Y, Niu L, Huang G, Xu F. Control of fibroblast shape in sequentially formed 3D hybrid hydrogels regulates cellular responses to microenvironmental cues. *NPG Asia Mater*. 2020;12(1):45. doi:10.1038/s41427-020-0226-7

123. Zijl F van, Mikulits W. Hepatospheres: Three dimensional cell cultures resemble physiological conditions of the liver. *World J Hepatol*. 2010;2(1):1. doi:10.4254/wjh.v2.i1.1

124. Kim SE, An SY, Woo DH, et al. Engraftment Potential of Spheroid-Forming Hepatic Endoderm Derived from Human Embryonic Stem Cells. *Stem Cells Dev*. 2013;22(12):1818-1829. doi:10.1089/scd.2012.0401

125. Reynolds DS, Tevis KM, Blessing WA, Colson YL, Zaman MH, Grinstaff MW. Breast Cancer Spheroids Reveal a Differential Cancer Stem Cell Response to Chemotherapeutic Treatment. *Sci Rep*. 2017;7(1):10382. doi:10.1038/s41598-017-10863-4

126. Asthana A, Kisaalita WS. Microtissue size and hypoxia in HTS with 3D cultures. *Drug Discov Today*. 2012;17(15-16):810-817. doi:10.1016/j.drudis.2012.03.004

127. Cui X, Hartanto Y, Zhang H. Advances in multicellular spheroids formation. *J R Soc Interface*. 2017;14(127):20160877. doi:10.1098/rsif.2016.0877

128. Brieva TA, Moghe P V. Exogenous cadherin microdisplay can interfere with endogenous signaling and reprogram gene expression in cultured hepatocytes. *Biotechnol Bioeng*. 2004;85(3):283-292. doi:10.1002/bit.10855

129. Lin RZ, Chou LF, Chien CCM, Chang HY. Dynamic analysis of hepatoma spheroid formation: roles of E-cadherin and β1-integrin. *Cell Tissue Res*. 2006;324(3):411-422. doi:10.1007/s00441-005-0148-2

130. Akasov R, Zaytseva-Zotova D, Burov S, et al. Formation of multicellular tumor spheroids induced by cyclic RGD-peptides and use for anticancer drug testing in vitro. *Int J Pharm*. 2016;506(1-2):148-157. doi:10.1016/j.ijpharm.2016.04.005

131. Miyamoto Y, Ikeuchi M, Noguchi H, Yagi T, Hayashi S. Spheroid Formation and Evaluation of Hepatic Cells in a Three-Dimensional Culture Device. *Cell Med*. 2015;8(1-2):47-56. doi:10.3727/215517915X689056

132. Nishikawa T, Tanaka Y, Nishikawa M, et al. Optimization of Albumin Secretion and Metabolic Activity of Cytochrome P450 1A1 of Human Hepatoblastoma HepG2 Cells in Multicellular Spheroids by Controlling Spheroid Size. *Biol Pharm Bull*. 2017;40(3):334-338. doi:10.1248/bpb.b16-00833

133. Park KD, Liu R, Kohn H. Useful Tools for Biomolecule Isolation, Detection, and Identification: Acylhydrazone-Based Cleavable Linkers. *Chem Biol*. 2009;16(7):763-772. doi:10.1016/j.chembiol.2009.06.005

134. Almazroo OA, Miah MK, Venkataramanan R. Drug Metabolism in the Liver. *Clin Liver Dis*. 2017;21(1):1-20. doi:10.1016/j.cld.2016.08.001

135. Guo K, van den Beucken T. Advances in drug-induced liver injury research: in vitro models, mechanisms, omics and gene modulation techniques. *Cell Biosci*. 2024;14(1):1-20. doi:10.1186/s13578-024-01317-2

136. Hosack T, Damry D, Biswas S. Drug-induced liver injury: a comprehensive review. *Therap Adv Gastroenterol*. 2023;16:1-13. doi:10.1177/17562848231163410

137. Li X, Tang J, Mao Y. Incidence and risk factors of drug-induced liver injury. *Liver International*. 2022;42(9):1999-2014. doi:10.1111/liv.15262

138. Kubes P, Jenne C. Immune Responses in the Liver. *Annu Rev Immunol*. 2018;36:247-277. doi:10.1146/annurev-immunol-051116-052415

139. Robinson MW, Harmon C, O'Farrelly C. Liver immunology and its role in inflammation and homeostasis. *Cell Mol Immunol*. 2016;13(3):267-276. doi:10.1038/cmi.2016.3

140. Krenkel O, Tacke F. Liver macrophages in tissue homeostasis and disease. *Nat Rev Immunol*. 2017;17(5):306-321. doi:10.1038/nri.2017.11

141. Shaw PJ, Beggs KM, Sparkenbaugh EM, Dugan CM, Ganey PE, Roth RA. Trovafloxacin enhances TNF-induced inflammatory stress and cell death signaling and reduces TNF clearance in a murine model of idiosyncratic hepatotoxicity. *Toxicological Sciences*. 2009;111(2):288-301. doi:10.1093/toxsci/kfp163

142. Lu J, Jones AD, Harkema JR, Roth RA, Ganey PE. Amiodarone exposure during modest inflammation induces idiosyncrasy-like liver injury in rats: Role of tumor necrosis factor-alpha. *Toxicological Sciences*. 2012;125(1):126-133. doi:10.1093/toxsci/kfr266

143. Deng X, Stachlewitz RF, Liguori MJ, et al. Modest inflammation enhances diclofenac hepatotoxicity in rats: Role of neutrophils and bacterial translocation. *Journal of Pharmacology and Experimental Therapeutics*. 2006;319(3):1191-1199. doi:10.1124/jpet.106.110247

144. Zou W, Beggs KM, Sparkenbaugh EM, et al. Sulindac metabolism and synergy with tumor necrosis factor-α in a drug-inflammation interaction model of idiosyncratic liver injury. *Journal of Pharmacology and Experimental Therapeutics*. 2009;331(1):114-121. doi:10.1124/jpet.109.156331

145. Tasnim F, Huang X, Lee CZW, Ginhoux F, Yu H. Recent Advances in Models of Immune-Mediated Drug-Induced Liver Injury. *Frontiers in Toxicology*. 2021;3(April):1-14. doi:10.3389/ftox.2021.605392

146. Cosgrove BD, King BM, Hasan MA, et al. Synergistic drug-cytokine induction of hepatocellular death as an in vitro approach for the study of inflammation-associated idiosyncratic drug hepatotoxicity. *Toxicol Appl Pharmacol*. 2009;237(3):317-330. doi:10.1016/j.taap.2009.04.002

147. Giustarini G, Huppelschoten S, Barra M, et al. The hepatotoxic fluoroquinolone trovafloxacin disturbs TNF- and LPS-induced p65 nuclear translocation in vivo and in vitro. *Toxicol Appl Pharmacol*. 2020;391(February):114915. doi:10.1016/j.taap.2020.114915

148. Niemeijer M, Wieęcek W, Fu S, et al. Mapping Interindividual Variability of Toxicodynamics Using High-Throughput Transcriptomics and Primary Human Hepatocytes from Fifty Donors. *Environ Health Perspect*. 2024;132(3):14-17. doi:10.1289/EHP11891

149. Niemeijer M, Wiecek W, Huppelschoten S, et al. Transcriptomic profiling of the inter-individual variability of chemical-induced cellular stress response activation in

primary human hepatocytes. *Toxicol Lett*. 2021;350:S31. doi:10.1016/s0378-4274(21)00312-x

150. Boon R, Kumar M, Tricot T, et al. Amino acid levels determine metabolism and CYP450 function of hepatocytes and hepatoma cell lines. *Nat Commun*. 2020;11(1):1393. doi:10.1038/s41467-020-15058-6

151. Wink S, Hiemstra SW, Huppelschoten S, Klip JE, van de Water B. Dynamic imaging of adaptive stress response pathway activation for prediction of drug induced liver injury. *Arch Toxicol*. 2018;92(5):1797-1814. doi:10.1007/s00204-018-2178-z

152. Hiemstra S, Ramaiahgari SC, Wink S, et al. High-throughput confocal imaging of differentiated 3D liver-like spheroid cellular stress response reporters for identification of drug-induced liver injury liability. *Arch Toxicol*. 2019;93(10):2895-2911. doi:10.1007/S00204-019-02552-0/FIGURES/7

153. Love MI, Huber W, Anders S. Moderated estimation of fold change and dispersion for RNA-seq data with DESeq2. Published online 2014:1-21. doi:10.1186/s13059-014-0550-8

154. Steffen M, Zavattaro G. *Lecture Notes in Computer Science: Preface*. Vol 3535. 2005.

155. López-Terrada D, Cheung SW, Finegold MJ, Knowles BB. Hep G2 is a hepatoblastoma-derived cell line. *Hum Pathol*. 2009;40(10):1512-1515. doi:10.1016/j.humpath.2009.07.003

156. Knoll P, Schlaak J, Uhrig A, Kempf P, zum Büschenfelde KHM, Gerken G. Human Kupffer cells secrete IL-10 in response to lipopolysaccharide (LPS) challenge. *J Hepatol*. 1995;22(2):226-229. doi:10.1016/0168-8278(95)80433-1

157. Bachmann M, Pfeilschifter J, Mühl H. A prominent role of interleukin-18 in acetaminophen-induced liver injury advocates its blockage for therapy of hepatic necroinflammation. *Front Immunol*. 2018;9(FEB):1-7. doi:10.3389/fimmu.2018.00161

158. Steuerwald NM, Foureau DM, Norton HJ, et al. Profiles of serum cytokines in acute drug-induced liver injury and their prognostic significance. *PLoS One*. 2013;8(12):1-15. doi:10.1371/journal.pone.0081974

159. Schmidt-Arras D, Rose-John S. IL-6 pathway in the liver: From physiopathology to therapy. *J Hepatol*. 2016;64(6):1403-1415. doi:10.1016/j.jhep.2016.02.004

160. Garcia-Alonso L, Holland CH, Ibrahim MM, Turei D, Saez-Rodriguez J. Benchmark and integration of resources for the estimation of human transcription factor activities. *Genome Res*. 2019;29(8):1363-1375. doi:10.1101/gr.240663.118

161. Callegaro G, Kunnen SJ, Trairatphisan P, et al. The human hepatocyte TXG-MAPr: gene co-expression network modules to support mechanism-based risk assessment. *Arch Toxicol*. 2021;95(12):3745-3775. doi:10.1007/s00204-021-03141-w

162. Wen Y, Lambrecht J, Ju C, Tacke F. Hepatic macrophages in liver homeostasis and diseases-diversity, plasticity and therapeutic opportunities. *Cell Mol Immunol*. 2021;18(1):45-56. doi:10.1038/s41423-020-00558-8

163. Dong Y, Liu Y, Kou X, et al. The protective or damaging effect of Tumor necrosis factor-aα in acute liver injury is concentration-dependent. *Cell Biosci*. 2016;6(1):4-13. doi:10.1186/s13578-016-0074-x

164. Shaw PJ, Beggs KM, Sparkenbaugh EM, Dugan CM, Ganey PE, Roth RA. Trovafloxacin enhances TNF-induced inflammatory stress and cell death signaling and reduces TNF clearance in a murine model of idiosyncratic hepatotoxicity. *Toxicological Sciences*. 2009;111(2):288-301. doi:10.1093/toxsci/kfp163

165. Fredriksson L, Herpers B, Benedetti G, et al. Diclofenac inhibits tumor necrosis factor-α-induced nuclear factor-κB activation causing synergistic hepatocyte apoptosis. *Hepatology*. 2011;53(6):2027-2041. doi:10.1002/hep.24314

166. Beggs KM, Maiuri AR, Fullerton AM, et al. Trovafloxacin-induced replication stress sensitizes HepG2 cells to tumor necrosis factor-alpha-induced cytotoxicity mediated by extracellular signal-regulated kinase and ataxia telangiectasia and Rad3-related. *Toxicology*. 2015;331:35-46. doi:10.1016/j.tox.2015.03.002

167. Hsiao CJJ, Younis H, Boelsterli UA. Trovafloxacin, a fluoroquinolone antibiotic with hepatotoxic potential, causes mitochondrial peroxynitrite stress in a mouse model of underlying mitochondrial dysfunction. *Chem Biol Interact*. 2010;188(1):204-213. doi:10.1016/j.cbi.2010.07.017

168. Agúndez JAG, Lucena MI, Martínez C, et al. Assessment of nonsteroidal anti-inflammatory drug-induced hepatotoxicity. *Expert Opin Drug Metab Toxicol*. 2011;7(7):817-828. doi:10.1517/17425255.2011.574613

169. O'Connor N, Dargan PI, Jones AL. Hepatocellular damage from non-steroidal anti-inflammatory drugs. *QJM*. 2003;96(11):787-791. doi:10.1093/qjmed/hcg138

170. Krenkel O, Tacke F. Liver macrophages in tissue homeostasis and disease. *Nat Rev Immunol*. 2017;17(5):306-321. doi:10.1038/nri.2017.11

171. Niemeijer M, Wieęcek W, Fu S, et al. Mapping Interindividual Variability of Toxicodynamics Using High-Throughput Transcriptomics and Primary Human Hepatocytes from Fifty Donors. *Environ Health Perspect*. 2024;132(3):14-17. doi:10.1289/EHP11891

172. Arconzo M, Piccinin E, Moschetta A. Increased risk of acute liver failure by pain killer drugs in NAFLD: Focus on nuclear receptors and their coactivators. *Digestive and Liver Disease*. 2021;53(1):26-34. doi:10.1016/j.dld.2020.05.034

173. Lebeaupin C, Vallée D, Hazari Y, Hetz C, Chevet E, Bailly-Maitre B. Endoplasmic reticulum stress signalling and the pathogenesis of non-alcoholic fatty liver disease. *J Hepatol*. 2018;69(4):927-947. doi:10.1016/j.jhep.2018.06.008

174. Duque GA, Descoteaux A. Macrophage cytokines: Involvement in immunity and infectious diseases. *Front Immunol*. 2014;5(OCT):1-12. doi:10.3389/fimmu.2014.00491

175. ter Braak B, Niemeijer M, Boon R, et al. Systematic transcriptome-based comparison of cellular adaptive stress response activation networks in hepatic stem cell-derived progeny and primary human hepatocytes. *Toxicology in Vitro*. 2021;73(October 2020). doi:10.1016/j.tiv.2021.105107

176. Fredriksson L, Wink S, Herpers B, et al. Drug-induced endoplasmic reticulum and oxidative stress responses independently sensitize toward TNFα-mediated hepatotoxicity. *Toxicological Sciences*. 2014;140(1):144-159. doi:10.1093/toxsci/kfu072

177. Beggs KM, Fullerton AM, Miyakawa K, Ganey PE, Roth RA. Molecular mechanisms of hepatocellular apoptosis induced by trovafloxacin-tumor necrosis factor-alpha interaction. *Toxicological Sciences*. 2014;137(1):91-101. doi:10.1093/toxsci/kft226

178. Ghosh S, De Smedt J, Tricot T, et al. Hipsc-derived hepatocyte-like cells can be used as a model for transcriptomics-based study of chemical toxicity. *Toxics*. 2022;10(1):1-18. doi:10.3390/toxics10010001

179. Wink S, Hiemstra SW, Huppelschoten S, Klip JE, van de Water B. Dynamic imaging of adaptive stress response pathway activation for prediction of drug induced liver injury. *Arch Toxicol*. 2018;92(5):1797-1814. doi:10.1007/s00204-018-2178-z

180. Ali S, Pimentel JD, Ma C. Naproxen-induced liver injury. *Hepatobiliary and Pancreatic Diseases International*. 2011;10(5):552-556. doi:10.1016/S1499-3872(11)60093-3

181. Thomson P, Fragkas N, Kafu LM, et al. Patients with naproxen-induced liver injury display T-cell memory responses toward an oxidative (S)-O-desmethyl naproxen metabolite but not the acyl glucuronide. *Allergy: European Journal of Allergy and Clinical Immunology*. 2024;79(1):200-214. doi:10.1111/all.15830

182. Guilbaud E, Galluzzi L. A mitochondrial checkpoint to NF-κB signaling. *Cell Death Dis*. 2024;15(7):3-5. doi:10.1038/s41419-024-06868-3

183. Chen X, Shi C, He M, Xiong S, Xia X. Endoplasmic reticulum stress: molecular mechanism and therapeutic targets. *Signal Transduct Target Ther*. 2023;8(1). doi:10.1038/s41392-023-01570-w

184. Lingappan K. NF-κB in oxidative stress. *Curr Opin Toxicol*. 2018;7:81-86. doi:10.1016/j.cotox.2017.11.002

185. Igarashi Y, Nakatsu N, Yamashita T, et al. Open TG-GATEs: a large-scale toxicogenomics database. *Nucleic Acids Res*. 2015;43(D1):D921-D927. doi:10.1093/nar/gku955

186. Guo K, van den Beucken T. Advances in drug-induced liver injury research: in vitro models, mechanisms, omics and gene modulation techniques. *Cell Biosci*. 2024;14(1):1-20. doi:10.1186/s13578-024-01317-2

187. Weaver RJ, Blomme EA, Chadwick AE, et al. Managing the challenge of drug-induced liver injury: a roadmap for the development and deployment of preclinical predictive models. *Nat Rev Drug Discov*. 2020;19(2):131-148. doi:10.1038/s41573-019-0048-x

188. Ercin CN. New classification of drug induced liver injury (DILI) in AASLD guidance: What is next? *Hepatology Forum*. 2024;5(2):61-62. doi:10.14744/hf.2024.2024.0011

189. Bj ES. European Journal of Internal Medicine Drug-induced liver injury : Pathogenesis , epidemiology , clinical features , and practical management. 2022;97(June 2021):26-31.

190. Björnsson ES. The Epidemiology of Newly Recognized Causes of Drug-Induced Liver Injury: An Update. *Pharmaceuticals*. 2024;17(4):1-11. doi:10.3390/ph17040520

191. Lee TYT, Coles JG, Maynes JT, Perry M. iPSC-cardiomyocytes in the preclinical prediction of candidate pharmaceutical toxicity. 2024;(February):1-15. doi:10.3389/fphar.2024.1308217

192. Tricot T, Verfaillie CM, Kumar M. Current Status and Challenges of Human Induced Pluripotent Stem Cell-Derived Liver Models in Drug Discovery. Published online 2022.

193. Snijders KE, Fehér A, Táncos Z, et al. Fluorescent tagging of endogenous Heme oxygenase-1 in human induced pluripotent stem cells for high content imaging of oxidative stress in various differentiated lineages. *Arch Toxicol*. 2021;95(10):3285-3302. doi:10.1007/s00204-021-03127-8

194. Boon R, Kumar M, Tricot T, et al. Amino acid levels determine metabolism and CYP450 function of hepatocytes and hepatoma cell lines. *Nat Commun*. 2020;11(1):1393. doi:10.1038/s41467-020-15058-6

195. Lu J, Jones AD, Harkema JR, Roth RA, Ganey PE. Amiodarone exposure during modest inflammation induces idiosyncrasy-like liver injury in rats: Role of tumor necrosis factor-alpha. *Toxicological Sciences*. 2012;125(1):126-133. doi:10.1093/toxsci/kfr266

196. Shaw PJ, Beggs KM, Sparkenbaugh EM, Dugan CM, Ganey PE, Roth RA. Trovafloxacin enhances TNF-induced inflammatory stress and cell death signaling and reduces TNF clearance in a murine model of idiosyncratic hepatotoxicity. *Toxicological Sciences*. 2009;111(2):288-301. doi:10.1093/toxsci/kfp163

197. Deng X, Stachlewitz RF, Liguori MJ, et al. Modest inflammation enhances diclofenac hepatotoxicity in rats: Role of neutrophils and bacterial translocation. *Journal of Pharmacology and Experimental Therapeutics*. 2006;319(3):1191-1199. doi:10.1124/jpet.106.110247

198. Fredriksson L, Herpers B, Benedetti G, et al. Diclofenac inhibits tumor necrosis factor-α-induced nuclear factor-κB activation causing synergistic hepatocyte apoptosis. *Hepatology*. 2011;53(6):2027-2041. doi:10.1002/hep.24314

199. Wink S, Hiemstra SW, Huppelschoten S, Klip JE, van de Water B. Dynamic imaging of adaptive stress response pathway activation for prediction of drug induced liver injury. *Arch Toxicol*. 2018;92(5):1797-1814. doi:10.1007/s00204-018-2178-z

200. Callegaro G, Kunnen SJ, Trairatphisan P, et al. The human hepatocyte TXG-MAPr: gene co-expression network modules to support mechanism-based risk assessment. *Arch Toxicol*. 2021;95(12):3745-3775. doi:10.1007/s00204-021-03141-w

201. Igarashi Y, Nakatsu N, Yamashita T, et al. Open TG-GATEs: A large-scale toxicogenomics database. *Nucleic Acids Res*. 2015;43(D1):D921-D927. doi:10.1093/nar/gku955

202. Van Den Berg CW, Elliott DA, Braam SR, Mummery CL, Davis RP. Differentiation of human pluripotent stem cells to cardiomyocytes under defined conditions. *Methods in Molecular Biology*. 2014;1353(1):163-180. doi:10.1007/7651_2014_178

203. Labun K, Montague TG, Krause M, Torres Cleuren YN, Tjeldnes H, Valen E. CHOPCHOP v3: Expanding the CRISPR web toolbox beyond genome editing. *Nucleic Acids Res*. 2019;47(W1):W171-W174. doi:10.1093/nar/gkz365

204. Yan K (Leiden U, Verbeek FJ (Leiden U. Segmentation for high-throughput image analysis: watershed masked clustering. *Lecture Notes in Computer Science*. Published online 2012:25-41.

205. Satoh S, Nussler AK, Liu Z, Departments AWT. Proinflammatory cytokines and endotoxin stimulate ICAM-1 gene expression and secretion by normal human hepatocytes. Published online 1994.

206. Ye L, Chen H, Wah K, et al. Aflatoxin B 1 Induces Inflammatory Liver Injury via Gut Microbiota in Mice. Published online 2023. doi:10.1021/acs.jafc.3c02617

207. Borrelli E, Heyman R, Hsi M, Evans RM. Targeting of an inducible toxic phenotype in animal cells. 1988;85(October):7572-7576.

208. Cardiotoxicity D induced, Ma W, Wei S, Zhang B, Li W, Finlay D. Molecular Mechanisms of Cardiomyocyte Death in. 2020;8(June):1-17. doi:10.3389/fcell.2020.00434

209. Woolbright BL, Jaeschke H, City K, City K. HHS Public Access. 2019;4(5):346-357. doi:10.1007/s40495-018-0147-0.Mechanisms

210. Amina D, Nawaz A, Sher F. Chemico-Biological Interactions Unveiling drug induced nephrotoxicity using novel biomarkers and cutting-edge preventive strategies. 2024;388(September 2023). doi:10.1016/j.cbi.2023.110838

211. Roberts B, Haupt A, Tucker A, et al. Systematic gene tagging using CRISPR / Cas9 in human stem cells to illuminate cell organization. Published online 2016. doi:10.1091/mbc.E17-03-0209

212. Poser I, Sarov M, Hutchins JRA, et al. BAC TransgeneOmics: a high-throughput method for exploration of protein function in mammals. *Nat Methods*. 2008;5(5):409-415. doi:10.1038/nmeth.1199

213. Schep R, Tr M, Verg X, et al. Chromatin context-dependent effects of epigenetic drugs on CRISPR-Cas9 editing. 2024;(July):8815-8832.

214. Chen B. Pluripotent stem cells are insensitive to the cytotoxicity of TNF α and IFN γ. Published online 2015.

215. Kolenc OI, Quinn KP. Evaluating Cell Metabolism Through Autofluorescence. 2019;30(6):875-889. doi:10.1089/ars.2017.7451

216. Kurokawa H, Deguchi R, Endo K, et al. A highly photostable and bright green fluorescent protein. 2022;40(July). doi:10.1038/s41587-022-01278-2

217. Shaner NC, Lambert GG, Chammas A, et al. HHS Public Access. 2013;10(5):407-409. doi:10.1038/nmeth.2413.A

218. Bindels DS, Haarbosch L, Weeren L Van, et al. mScarlet : a bright monomeric red fluorescent protein for cellular imaging. 2017;14(1). doi:10.1038/nmeth.4074

219. Prakash N. Generation of a NES -mScarlet Red Fluorescent Reporter Human iPSC Line for Live Cell Imaging and Flow Cytometric Analysis and Sorting Using CRISPR-Cas9-Mediated Gene Editing. Published online 2022.

220. Koch B, Nijmeijer B, Kueblbeck M, Cai Y, Walther N, Ellenberg J. Generation and validation of homozygous fluorescent knock-in cells using CRISPR–Cas9 genome editing. *Nat Protoc*. 2018;13(6):1465-1487. doi:10.1038/nprot.2018.042

221. Telbisz Á, Hegedüs C, Váradi A, Sarkadi B, Özvegy-laczka C. Special Section on Transporters in Toxicity and Disease Regulation of the Function of the Human ABCG2 Multidrug Transporter by Cholesterol and Bile Acids : Effects of Mutations in Potential Substrate and Steroid Binding Sites s. 2014;(April):575-585.

222. Siramshetty VB, Nickel J, Omieczynski C, Gohlke B oliver, Drwal MN, Preissner R. WITHDRAWN — a resource for withdrawn and discontinued drugs. 2015;(November). doi:10.1093/nar/gkv1192

223. Todo M, Gatate Y, Nakano S, Kaneko G, Hagiwara M, Takahashi T. Early detection of myocarditis caused by immune checkpoint inhibitor therapy with nivolumab and ipilimumab for advanced recurrent renal cell carcinoma. *Cancer Immunology, Immunotherapy*. 2025;74(3):1-11. doi:10.1007/s00262-025-03945-0

224. Vitale R, Marzocco S, Popolo A. Role of Oxidative Stress and Inflammation in Doxorubicin-Induced Cardiotoxicity : A Brief Account. Published online 2024.

225. Mitchell S, Tsui R, Tan ZC, Pack A, Hoffmann A. explore diverse biological contexts. 2023;16(776):1-25. doi:10.1126/scisignal.abo2838.The

226. Bhatt D, Ghosh S. Regulation of the NF- κ B-mediated transcription of inflammatory genes. 2014;5(February):1-9. doi:10.3389/fimmu.2014.00071

227. Cohen P, Cross D, Jänne PA. Kinase drug discovery 20 years after imatinib: progress and future directions. *Nat Rev Drug Discov*. 2021;20(7):551-569. doi:10.1038/s41573-021-00195-4

228. Roskoski R. Properties of FDA-approved small molecule protein kinase inhibitors: A 2023 update. *Pharmacol Res*. 2023;187:106552. doi:10.1016/j.phrs.2022.106552

229. Lee PY, Yeoh Y, Low TY. A recent update on small-molecule kinase inhibitors for targeted cancer therapy and their therapeutic insights from mass spectrometry-based proteomic analysis. *FEBS J*. 2023;290(11):2845-2864. doi:10.1111/febs.16442

230. Shyam Sunder S, Sharma UC, Pokharel S. Adverse effects of tyrosine kinase inhibitors in cancer therapy: pathophysiology, mechanisms and clinical management. *Signal Transduct Target Ther*. 2023;8(1):262. doi:10.1038/s41392-023-01469-6

231. Xiong Y, Wang Q, Liu Y, Wei J, Chen X. Renal adverse reactions of tyrosine kinase inhibitors in the treatment of tumours: A Bayesian network meta-analysis. *Front Pharmacol*. 2022;13. doi:10.3389/fphar.2022.1023660

232. Viganò M, La Milia M, Grassini MV, Pugliese N, De Giorgio M, Fagiuoli S. Hepatotoxicity of Small Molecule Protein Kinase Inhibitors for Cancer. *Cancers (Basel)*. 2023;15(6):1766. doi:10.3390/cancers15061766

233. Grela-Wojewoda A, Pacholczak-Madej R, Adamczyk A, Korman M, Püsküllüoğlu M. Cardiotoxicity Induced by Protein Kinase Inhibitors in Patients with Cancer. *Int J Mol Sci*. 2022;23(5):2815. doi:10.3390/ijms23052815

234. Hutchins E, Yang EH, Stein-Merlob AF. Inflammation in Chemotherapy-Induced Cardiotoxicity. *Curr Cardiol Rep*. 2024;26(12):1329-1340. doi:10.1007/s11886-024-02131-5

235. Woolbright BL, Jaeschke H. Mechanisms of Inflammatory Liver Injury and Drug-Induced Hepatotoxicity. *Curr Pharmacol Rep*. 2018;4(5):346-357. doi:10.1007/s40495-018-0147-0

236. Volarevic V, Djokovic B, Jankovic MG, et al. Molecular mechanisms of cisplatin-induced nephrotoxicity: a balance on the knife edge between renoprotection and tumor toxicity. *J Biomed Sci*. 2019;26(1):25. doi:10.1186/s12929-019-0518-9

237. Webster JD, Vucic D. The Balance of TNF Mediated Pathways Regulates Inflammatory Cell Death Signaling in Healthy and Diseased Tissues. *Front Cell Dev Biol*. 2020;8. doi:10.3389/fcell.2020.00365

238. Brenner D, Blaser H, Mak TW. Regulation of tumour necrosis factor signalling: live or let die. *Nat Rev Immunol*. 2015;15(6):362-374. doi:10.1038/nri3834

239. Dustin ML, Rothlein R, Bhan AK, Dinarello CA, Springer TA. Induction by IL 1 and interferon-gamma: tissue distribution, biochemistry, and function of a natural adherence molecule (ICAM-1). *The Journal of Immunology*. 1986;137(1):245-254. doi:10.4049/jimmunol.137.1.245

240. Singh V, Kaur R, Kumari P, Pasricha C, Singh R. ICAM-1 and VCAM-1: Gatekeepers in various inflammatory and cardiovascular disorders. *Clinica Chimica Acta*. 2023;548:117487. doi:10.1016/j.cca.2023.117487

241. van Loo G, Bertrand MJM. Death by TNF: a road to inflammation. *Nat Rev Immunol*. 2023;23(5):289-303. doi:10.1038/s41577-022-00792-3

242. Yang Y, Jiang G, Zhang P, Fan J. Programmed cell death and its role in inflammation. *Mil Med Res*. 2015;2(1):12. doi:10.1186/s40779-015-0039-0

243. Campana C, Dariolli R, Boutjdir M, Sobie EA. Inflammation as a Risk Factor in Cardiotoxicity: An Important Consideration for Screening During Drug Development. *Front Pharmacol*. 2021;12. doi:10.3389/fphar.2021.598549

244. Miller RP, Tadagavadi RK, Ramesh G, Reeves WB. Mechanisms of Cisplatin Nephrotoxicity. *Toxins (Basel)*. 2010;2(11):2490-2518. doi:10.3390/toxins2112490

245. Giustarini G, Huppelschoten S, Barra M, et al. The hepatotoxic fluoroquinolone trovafloxacin disturbs TNF- and LPS-induced p65 nuclear translocation in vivo and in vitro. *Toxicol Appl Pharmacol*. 2020;391(February):114915. doi:10.1016/j.taap.2020.114915

246. Böhm F, Köhler UA, Speicher T, Werner S. Regulation of liver regeneration by growth factors and cytokines. *EMBO Mol Med*. 2010;2(8):294-305. doi:10.1002/emmm.201000085

247. Wang L, Chen Q, Qi H, et al. Doxorubicin-Induced Systemic Inflammation Is Driven by Upregulation of Toll-Like Receptor TLR4 and Endotoxin Leakage. *Cancer Res*. 2016;76(22):6631-6642. doi:10.1158/0008-5472.CAN-15-3034

248. Benedetti G, Fredriksson L, Herpers B, Meerman J, van de Water B, de Graauw M. TNF-α-mediated NF-κB survival signaling impairment by cisplatin enhances JNK

activation allowing synergistic apoptosis of renal proximal tubular cells. *Biochem Pharmacol*. 2013;85(2):274-286. doi:10.1016/j.bcp.2012.10.012

249. Wang H, Wang Y, Li J, et al. Three tyrosine kinase inhibitors cause cardiotoxicity by inducing endoplasmic reticulum stress and inflammation in cardiomyocytes. *BMC Med*. 2023;21(1):147. doi:10.1186/s12916-023-02838-2

250. Estrada CC, Maldonado A, Mallipattu SK. Therapeutic inhibition of VEGF signaling and associated nephrotoxicities. *Journal of the American Society of Nephrology*. 2019;30(2):187-200. doi:10.1681/ASN.2018080853

251. Markóth C, File I, Szász R, Bidiga L, Balla J, Mátyus J. Ibrutinib-induced acute kidney injury via interstitial nephritis. *Ren Fail*. 2021;43(1):335-339. doi:10.1080/0886022X.2021.1874985

252. Abu Amer N, Avila-Casado C, Kitchlu A. A Case of Acute Interstitial Nephritis Associated with Belvarafenib, a Novel pan-RAF Kinase Inhibitor for Metastatic NRAS Mutant Melanoma. *Journal of the American Society of Nephrology*. 2023;34(11S):482-482. doi:10.1681/asn.20233411s1482b

253. Cuny GD, Degterev A. RIPK protein kinase family: Atypical lives of typical kinases. *Semin Cell Dev Biol*. *Elsevier Ltd*. 2021;109:96-105. doi:10.1016/j.semcdb.2020.06.014

254. Antonia RJ, Hagan RS, Baldwin AS. Expanding the View of IKK: New Substrates and New Biology. *Trends Cell Biol*. *Elsevier Ltd*. 2021;31(3):166-178. doi:10.1016/j.tcb.2020.12.003

255. Canovas B, Nebreda AR. Diversity and versatility of p38 kinase signalling in health and disease. *Nat Rev Mol Cell Biol*. *Nature Research*. 2021;22(5):346-366. doi:10.1038/s41580-020-00322-w

256. Boon R, Kumar M, Tricot T, et al. Amino acid levels determine metabolism and CYP450 function of hepatocytes and hepatoma cell lines. *Nat Commun*. 2020;11(1):1-16. doi:10.1038/s41467-020-15058-6

257. Van Den Berg CW, Elliott DA, Braam SR, Mummery CL, Davis RP. Differentiation of human pluripotent stem cells to cardiomyocytes under defined conditions. *Methods in Molecular Biology*. 2014;1353(1):163-180. doi:10.1007/7651_2014_178

258. Chandrasekaran V, Carta G, da Costa Pereira D, et al. Generation and characterization of iPSC-derived renal proximal tubule-like cells with extended stability. *Sci Rep*. 2021;11(1):1-17. doi:10.1038/s41598-021-89550-4

259. Love MI, Huber W, Anders S. Moderated estimation of fold change and dispersion for RNA-seq data with DESeq2. *Genome Biol*. 2014;15(12):1-21. doi:10.1186/s13059-014-0550-8

260. Yan K, Verbeek FJ. Segmentation for High-Throughput Image Analysis: Watershed Masked Clustering. In: *Lecture Notes in Computer Sciences*. 7610 LNCS. Springer, Berlin, Heidelberg; 2012:25-41. doi:10.1007/978-3-642-34032-1_4

261. Garcia-Alonso L, Holland CH, Ibrahim MM, Turei D, Saez-Rodriguez J. Benchmark and integration of resources for the estimation of human transcription factor activities. *Genome Res*. 2019;29(8):1363-1375. doi:10.1101/gr.240663.118

262. Manning G, Whyte DB, Martinez R, Hunter T, Sudarsanam S. The protein kinase complement of the human genome. *Science (1979)*. 2002;298(5600):1912-1934. doi:10.1126/science.1075762

263. Eid S, Turk S, Volkamer A, Rippmann F, Fulle S. Kinmap: A web-based tool for interactive navigation through human kinome data. *BMC Bioinformatics*. 2017;18(1):1-6. doi:10.1186/s12859-016-1433-7

264. Singh V, Kaur R, Kumari P, Pasricha C, Singh R. ICAM-1 and VCAM-1: Gatekeepers in various inflammatory and cardiovascular disorders. *Clinica Chimica Acta*. 2023;548(May):117487. doi:10.1016/j.cca.2023.117487

265. Vlasveld M, Callegaro G, Fisher C, et al. The integrated stress response- related expression of CHOP due to mitochondrial toxicity is a warning sign for DILI liability. 2024;(December 2023):1-16. doi:10.1111/liv.15822

266. Kellum JA, Romagnani P, Ashuntantang G, Ronco C, Zarbock A, Anders HJ. Acute kidney injury. *Nat Rev Dis Primers*. 2021;7(1). doi:10.1038/s41572-021-00284-z

267. Janku F, Choong GM, Opyrchal M, et al. A Phase I Study of the Oral Dual-Acting Pan-PI3K/mTOR Inhibitor Bimiralisib in Patients with Advanced Solid Tumors. *Cancers (Basel)*. 2024;16(6). doi:10.3390/cancers16061137

268. Markham A. Erdafitinib: First Global Approval. *Drugs*. 2019;79(9):1017-1021. doi:10.1007/s40265-019-01142-9

269. Wen PY, Cloughesy TF, Olivero AG, et al. First-in-human phase i study to evaluate the brain-penetrant PI3K/mTOR inhibitor GDC-0084 in patients with progressive or recurrent high-grade glioma. *Clinical Cancer Research*. 2020;26(8):1820-1828. doi:10.1158/1078-0432.CCR-19-2808

270. James AJ, Smith CC, Litzow M, et al. Pharmacokinetic Profile of Gilteritinib: A Novel FLT-3 Tyrosine Kinase Inhibitor. *Clin Pharmacokinet*. 2020;59(10):1273-1290. doi:10.1007/s40262-020-00888-w

271. Flaherty KT, LoRusso PM, DeMichele A, et al. Phase I, dose-escalation trial of the oral cyclin-dependent kinase 4/6 inhibitor PD 0332991, administered using a 21-day schedule in patients with advanced cancer. *Clinical Cancer Research*. 2012;18(2):568-576. doi:10.1158/1078-0432.CCR-11-0509

272. Sarker D, Ang JE, Baird R, et al. First-in-human phase I study of pictilisib (GDC-0941), a potent pan-class I phosphatidylinositol-3-kinase (PI3K) Inhibitor, in patients with advanced solid tumors. *Clinical Cancer Research*. 2015;21(1):77-86. doi:10.1158/1078-0432.CCR-14-0947

273. Seo HB, Cho S, Yoon YR, Yim DS. Development and validation of analytical method for the determination of radotinib in human plasma using liquid chromatography-tandem mass spectrometry. *Transl Clin Pharmacol*. 2017;25(4):183-189.

274. Wheler J, Mutch D, Lager J, et al. Phase I Dose-Escalation Study of Pilaralisib (SAR245408, XL147) in Combination with Paclitaxel and Carboplatin in Patients with Solid Tumors. *Oncologist*. 2017;22(4):377-e37. doi:10.1634/theoncologist.2016-0257

275. Del Mar Castro M, Gomez MA, Kip AE, et al. Pharmacokinetics of miltefosine in children and adults with Cutaneous leishmaniasis. *Antimicrob Agents Chemother*. 2017;61(3). doi:10.1128/AAC.02198-16

276. Hemmelgarn BR, Manns BJ, Lloyd A, et al. Relation between kidney function, proteinuria, and adverse outcomes. *JAMA*. 2010;303(5):423-429. doi:10.1001/jama.2010.39

277. Kramer AB, Van Timmeren MM, Schuurs TA, et al. Reduction of proteinuria in adriamycin-induced nephropathy is associated with reduction of renal kidney injury molecule (Kim-1) over time. *Am J Physiol Renal Physiol*. 2009;296(5):1136-1145. doi:10.1152/ajprenal.00541.2007

278. Dustin ML, Rothlein R, Bhan AK, Dinarello CA, Springer TA. Induction by IL 1 and interferon-gamma: tissue distribution, biochemistry, and function of a natural adherence molecule (ICAM-1). *The Journal of Immunology*. 1986;137(1):245-254. doi:10.4049/jimmunol.137.1.245

279. Kawai Y, Kaidoh M, Yokoyama Y, Sano K, Ohhashi T. Chemokine CCL2 facilitates ICAM-1-mediated interactions of cancer cells and lymphatic endothelial cells in

sentinel lymph nodes. *Cancer Sci*. 2009;100(3):419-428. doi:10.1111/j.1349-7006.2008.01064.x

280. Szklarczyk D, Kirsch R, Koutrouli M, et al. The STRING database in 2023: protein-protein association networks and functional enrichment analyses for any sequenced genome of interest. *Nucleic Acids Res*. 2023;51(1 D):D638-D646. doi:10.1093/nar/gkac1000

281. Erdei Z, Lorincz R, Szebényi K, et al. Expression pattern of the human ABC transporters in pluripotent embryonic stem cells and in their derivatives. *Cytometry B Clin Cytom*. 2014;86(5):299-310. doi:10.1002/cyto.b.21168

282. Shyam Sunder S, Sharma UC, Pokharel S. Adverse effects of tyrosine kinase inhibitors in cancer therapy: pathophysiology, mechanisms and clinical management. *Signal Transduct Target Ther*. 2023;8(1). doi:10.1038/s41392-023-01469-6

283. Giordano S, Petrelli A. From Single- to Multi-Target Drugs in Cancer Therapy: When Aspecificity Becomes an Advantage. *Curr Med Chem*. 2008;15(5):422-432.

284. Huang KM, Uddin ME, DiGiacomo D, Lustberg MB, Hu S, Sparreboom A. Role of SLC transporters in toxicity induced by anticancer drugs. *Expert Opin Drug Metab Toxicol*. 2020;16(6):493-506. doi:10.1080/17425255.2020.1755253

285. Hulin A, Gelé T, Fenioux C, et al. Pharmacology of Tyrosine Kinase Inhibitors: Implications for Patients with Kidney Diseases. *Clinical Journal of the American Society of Nephrology*. 2024;19(7):927-938. doi:10.2215/CJN.0000000000000395

286. Benedetti G, Fokkelman M, Yan K, Fredriksson L, Herpers B, Meerman J van de, Water B de GM. The nuclear factor κB family member RelB facilitates apoptosis of renal epithelial cells caused by cisplatin/tumor necrosis factor α synergy by suppressing an epithelial to mesenchymal transition-like phenotypic switch. *Mol Pharmacol*. 2013;84(1):128-138.

287. Benedetti G, Fredriksson L, Herpers B, Meerman J, Van De Water B, De Graauw M. TNF-α-mediated NF-κB survival signaling impairment by cisplatin enhances JNK activation allowing synergistic apoptosis of renal proximal tubular cells. *Biochem Pharmacol*. 2013;85(2):274-286. doi:10.1016/j.bcp.2012.10.012

288. Wright DH, Caro L, Cerra M, et al. Liver-to-plasma vaniprevir (MK-7009) concentration ratios in HCV-infected patients. *Antivir Ther*. 2015;20(8):843-848. doi:10.3851/IMP2958.Liver-to-plasma

289. Chung ACK, Lan HY. Chemokines in renal injury. *Journal of the American Society of Nephrology*. 2011;22(5):802-809. doi:10.1681/ASN.2010050510

290. Lee JW, Wang P, Kattah MG, et al. Differential Regulation of Chemokines by IL-17 in Colonic Epithelial Cells. *The Journal of Immunology*. 2008;181(9):6536-6545. doi:10.4049/jimmunol.181.9.6536

291. Turner JE, Paust HJ, Steinmetz OM, et al. CCR6 recruits regulatory T cells and Th17 cells to the kidney in glomerulonephritis. *Journal of the American Society of Nephrology*. 2010;21(6):974-985. doi:10.1681/ASN.2009070741

292. Post SM, Andreeff M, DiNardo C, Khoury JD, Ruvolo PP. TAM kinases as regulators of cell death. *Biochim Biophys Acta Mol Cell Res*. 2021;1868(6):118992. doi:10.1016/j.bbamcr.2021.118992

293. Wang H, Gao L, Zhao C, et al. The role of PI3K/Akt signaling pathway in chronic kidney disease. *Int Urol Nephrol*. 2024;56(8):2623-2633. doi:10.1007/s11255-024-03989-8

294. Ye C, Ho DJ, Neri M, et al. DRUG-seq for miniaturized high-throughput transcriptome profiling in drug discovery. *Nat Commun*. 2018;9(1):1-9. doi:10.1038/s41467-018-06500-x

295. Poh WT, Stanslas J. The new paradigm in animal testing – "3Rs alternatives." *Regulatory Toxicology and Pharmacology*. 2024;153:105705. doi:10.1016/j.yrtph.2024.105705

296. Adashi EY, O'Mahony DP, Cohen IG. The FDA Modernization Act 2.0: Drug Testing in Animals is Rendered Optional. *Am J Med*. 2023;136(9):853-854. doi:10.1016/j.amjmed.2023.03.033

297. Hartung T. The (misleading) role of animal models in drug development. *Frontiers in Drug Discovery*. 2024;4. doi:10.3389/fddsv.2024.1355044

298. Van Norman GA. Limitations of Animal Studies for Predicting Toxicity in Clinical Trials. *JACC Basic Transl Sci*. 2019;4(7):845-854. doi:10.1016/j.jacbts.2019.10.008

299. Atkins JT, George GC, Hess K, et al. Pre-clinical animal models are poor predictors of human toxicities in phase 1 oncology clinical trials. *Br J Cancer*. 2020;123(10):1496-1501. doi:10.1038/s41416-020-01033-x

300. Marshall LJ, Bailey J, Cassotta M, Herrmann K, Pistollato F. Poor Translatability of Biomedical Research Using Animals — A Narrative Review. *Alternatives to Laboratory Animals*. 2023;51(2):102-135. doi:10.1177/02611929231157756

301. McKenzie R, Fried MW, Sallie R, et al. Hepatic Failure and Lactic Acidosis Due to Fialuridine (FIAU), an Investigational Nucleoside Analogue for Chronic Hepatitis B. *New England Journal of Medicine*. 1995;333(17):1099-1105. doi:10.1056/NEJM199510263331702

302. Suntharalingam G, Perry MR, Ward S, et al. Cytokine Storm in a Phase 1 Trial of the Anti-CD28 Monoclonal Antibody TGN1412. *New England Journal of Medicine*. 2006;355(10):1018-1028. doi:10.1056/NEJMoa063842

303. Ramaiahgari SC, den Braver MW, Herpers B, et al. A 3D in vitro model of differentiated HepG2 cell spheroids with improved liver-like properties for repeated dose high-throughput toxicity studies. *Arch Toxicol*. Published online March 6, 2014. doi:10.1007/s00204-014-1215-9

304. Hiemstra S, Ramaiahgari SC, Wink S, et al. High-throughput confocal imaging of differentiated 3D liver-like spheroid cellular stress response reporters for identification of drug-induced liver injury liability. *Arch Toxicol*. 2019;93(10):2895-2911. doi:10.1007/s00204-019-02552-0

305. Gribova V, Gauthier-Rouvière C, Albigès-Rizo C, Auzely-Velty R, Picart C. Effect of RGD functionalization and stiffness modulation of polyelectrolyte multilayer films on muscle cell differentiation. *Acta Biomater*. 2013;9(5):6468-6480. doi:10.1016/j.actbio.2012.12.015

306. Wang X, Ye K, Li Z, Yan C, Ding J. Adhesion, proliferation, and differentiation of mesenchymal stem cells on RGD nanopatterns of varied nanospacings. *Organogenesis*. 2013;9(4):280-286. doi:10.4161/org.26080

307. Roulot D, Czernichow S, Le Clésiau H, Costes JL, Vergnaud AC, Beaugrand M. Liver stiffness values in apparently healthy subjects: Influence of gender and metabolic syndrome. *J Hepatol*. 2008;48(4):606-613. doi:10.1016/j.jhep.2007.11.020

308. Tong C, Liu T, Saez Talens V, et al. Squaramide-Based Supramolecular Materials for Three-Dimensional Cell Culture of Human Induced Pluripotent Stem Cells and Their Derivatives. *Biomacromolecules*. 2018;19(4):1091-1099. doi:10.1021/acs.biomac.7b01614

309. Invernizzi P. Liver auto-immunology: The paradox of autoimmunity in a tolerogenic organ. *J Autoimmun*. 2013;46:1-6. doi:10.1016/j.jaut.2013.08.006

310. Cheng ML, Nakib D, Perciani CT, MacParland SA. The immune niche of the liver. *Clin Sci*. 2021;135(20):2445-2466. doi:10.1042/CS20190654

311. Robinson MW, Harmon C, O'Farrelly C. Liver immunology and its role in inflammation and homeostasis. *Cell Mol Immunol*. 2016;13(3):267-276. doi:10.1038/cmi.2016.3

312. Zhao Y, Zhao S, Liu S, Ye W, Chen W dong. Kupffer cells, the limelight in the liver regeneration. *Int Immunopharmacol*. 2025;146:113808. doi:10.1016/j.intimp.2024.113808

313. Holt MP, Ju C. Mechanisms of drug-induced liver injury. *AAPS J*. 2006;8(1):E48-E54. doi:10.1208/aapsj080106

314. Bachmann M, Pfeilschifter J, Mühl H. A Prominent Role of Interleukin-18 in Acetaminophen-Induced Liver Injury Advocates Its Blockage for Therapy of Hepatic Necroinflammation. *Front Immunol*. 2018;9. doi:10.3389/fimmu.2018.00161

315. Cutolo M, Campitiello R, Gotelli E, Soldano S. The Role of M1/M2 Macrophage Polarization in Rheumatoid Arthritis Synovitis. *Front Immunol*. 2022;13. doi:10.3389/fimmu.2022.867260

316. Reiter FP, Wimmer R, Wottke L, et al. Role of interleukin-1 and its antagonism of hepatic stellate cell proliferation and liver fibrosis in the Abcb4 $^{-/-}$ mouse model. *World J Hepatol*. 2016;8(8):401. doi:10.4254/wjh.v8.i8.401

317. Beggs KM, Fullerton AM, Miyakawa K, Ganey PE, Roth RA. Molecular mechanisms of hepatocellular apoptosis induced by trovafloxacin-tumor necrosis factor-alpha interaction. *Toxicological Sciences*. 2014;137(1):91-101. doi:10.1093/toxsci/kft226

318. Dugan CM, MacDonald AE, Roth RA, Ganey PE. A Mouse Model of Severe Halothane Hepatitis Based on Human Risk Factors. *J Pharmacol Exp Ther*. 2010;333(2):364-372. doi:10.1124/jpet.109.164541

319. Lu J, Jones AD, Harkema JR, Roth RA, Ganey PE. Amiodarone Exposure During Modest Inflammation Induces Idiosyncrasy-like Liver Injury in Rats: Role of Tumor Necrosis Factor-alpha. *Toxicological Sciences*. 2012;125(1):126-133. doi:10.1093/toxsci/kfr266

320. Shaw PJ, Beggs KM, Sparkenbaugh EM, Dugan CM, Ganey PE, Roth RA. Trovafloxacin enhances TNF-induced inflammatory stress and cell death signaling and reduces TNF clearance in a murine model of idiosyncratic hepatotoxicity. *Toxicological Sciences*. 2009;111(2):288-301. doi:10.1093/toxsci/kfp163

321. Zou W, Beggs KM, Sparkenbaugh EM, et al. Sulindac metabolism and synergy with tumor necrosis factor-α in a drug-inflammation interaction model of idiosyncratic

liver injury. *Journal of Pharmacology and Experimental Therapeutics*. 2009;331(1):114-121. doi:10.1124/jpet.109.156331

322. Fredriksson L, Herpers B, Benedetti G, et al. Diclofenac inhibits tumor necrosis factor-α-induced nuclear factor-κB activation causing synergistic hepatocyte apoptosis. *Hepatology*. 2011;53(6):2027-2041. doi:10.1002/hep.24314

323. Tukov FF, Luyendyk JP, Ganey PE, Roth RA. The Role of Tumor Necrosis Factor Alpha in Lipopolysaccharide/Ranitidine-Induced Inflammatory Liver Injury. *Toxicological Sciences*. 2007;100(1):267-280. doi:10.1093/toxsci/kfm209

324. Cosgrove BD, King BM, Hasan MA, et al. Synergistic drug-cytokine induction of hepatocellular death as an in vitro approach for the study of inflammation-associated idiosyncratic drug hepatotoxicity. *Toxicol Appl Pharmacol*. 2009;237(3):317-330. doi:10.1016/j.taap.2009.04.002

325. Cosgrove BD, Alexopoulos LG, Hang T chun, et al. Cytokine-associated drug toxicity in human hepatocytes is associated with signaling network dysregulation. *Mol Biosyst*. 2010;6(7):1195. doi:10.1039/b926287c

326. Niemeijer M, Wieęcek W, Fu S, et al. Mapping Interindividual Variability of Toxicodynamics Using High-Throughput Transcriptomics and Primary Human Hepatocytes from Fifty Donors. *Environ Health Perspect*. 2024;132(3):14-17. doi:10.1289/EHP11891

327. Ghandi M, Huang FW, Jané-Valbuena J, et al. Next-generation characterization of the Cancer Cell Line Encyclopedia. *Nature*. 2019;569(7757):503-508. doi:10.1038/s41586-019-1186-3

328. Maiuri AR, Breier AB, Gora LFJ, Parkins R V., Ganey PE, Roth RA. Cytotoxic Synergy Between Cytokines and NSAIDs Associated With Idiosyncratic Hepatotoxicity Is Driven by Mitogen-Activated Protein Kinases. *Toxicological Sciences*. 2015;146(2):265-280. doi:10.1093/toxsci/kfv091

329. Volpato V, Webber C. Addressing variability in iPSC-derived models of human disease: guidelines to promote reproducibility. *Dis Model Mech*. 2020;13(1). doi:10.1242/dmm.042317

330. Ludwig TE, Andrews PW, Barbaric I, et al. ISSCR standards for the use of human stem cells in basic research. *Stem Cell Reports*. 2023;18(9):1744-1752. doi:10.1016/j.stemcr.2023.08.003

331. Chandrasekaran V, Carta G, da Costa Pereira D, et al. Generation and characterization of iPSC-derived renal proximal tubule-like cells with extended stability. *Sci Rep*. 2021;11(1):11575. doi:10.1038/s41598-021-89550-4

332. Lin Y, Zou J. Differentiation of Cardiomyocytes from Human Pluripotent Stem Cells in Fully Chemically Defined Conditions. *STAR Protoc*. 2020;1(1):100015. doi:10.1016/j.xpro.2020.100015

333. Inui J, Ueyama-Toba Y, Mitani S, Mizuguchi H. Development of a method of passaging and freezing human iPS cell-derived hepatocytes to improve their functions. *PLoS One*. 2023;18(5):e0285783. doi:10.1371/journal.pone.0285783

334. van den Brink L, Brandão KO, Yiangou L, et al. Cryopreservation of human pluripotent stem cell-derived cardiomyocytes is not detrimental to their molecular and functional properties. *Stem Cell Res*. 2020;43:101698. doi:10.1016/j.scr.2019.101698

335. Cosgrove BD, King BM, Hasan MA, et al. Synergistic drug-cytokine induction of hepatocellular death as an in vitro approach for the study of inflammation-associated idiosyncratic drug hepatotoxicity. *Toxicol Appl Pharmacol*. 2009;237(3):317-330. doi:10.1016/j.taap.2009.04.002

336. Jo S, Park SB, Kim H, et al. hiPSC-derived macrophages improve drug sensitivity and selectivity in a macrophage-incorporating organoid culture model. *Biofabrication*. 2024;16(3):035021. doi:10.1088/1758-5090/ad4c0a

337. Teschke R, Uetrecht J. Mechanism of idiosyncratic drug induced liver injury (DILI): unresolved basic issues. *Ann Transl Med*. 2021;9(8):730-730. doi:10.21037/atm-2020-ubih-05

338. Jee A, Sernoskie SC, Uetrecht J. Idiosyncratic Drug-Induced Liver Injury: Mechanistic and Clinical Challenges. *Int J Mol Sci*. 2021;22(6):2954. doi:10.3390/ijms22062954

339. Monshi MM, Faulkner L, Gibson A, et al. Human Leukocyte Antigen (HLA)-B*57:01-Restricted Activation of Drug-Specific T cells Provides the Immunological Basis for Flucloxacillin-Induced Liver Injury. *Hepatology*. 2013;57(2):727-739. doi:10.1002/hep.26077

340. Asif BA, Koh C, Phillips EJ, et al. Vancomycin-Induced Liver Injury, DRESS, and HLA-A∗32:01. *J Allergy Clin Immunol Pract*. 2024;12(1):168-174.e2. doi:10.1016/j.jaip.2023.09.011

341. Guo K, van den Beucken T. Advances in drug-induced liver injury research: in vitro models, mechanisms, omics and gene modulation techniques. *Cell Biosci*. 2024;14(1):1-20. doi:10.1186/s13578-024-01317-2

342. Wink S, Hiemstra S, Huppelschoten S, et al. Quantitative High Content Imaging of Cellular Adaptive Stress Response Pathways in Toxicity for Chemical Safety Assessment. *Chem Res Toxicol*. 2014;27(3):338-355. doi:10.1021/tx4004038

343. Wink S, Hiemstra SW, Huppelschoten S, Klip JE, van de Water B. Dynamic imaging of adaptive stress response pathway activation for prediction of drug induced liver injury. *Arch Toxicol*. 2018;92(5):1797-1814. doi:10.1007/s00204-018-2178-z

344. Vlasveld M, Callegaro G, Fisher C, et al. The integrated stress response-related expression of *CHOP* due to mitochondrial toxicity is a warning sign for <scp>DILI</scp> liability. *Liver International*. 2024;44(3):760-775. doi:10.1111/liv.15822

345. Wijaya LS, Trairatphisan P, Gabor A, et al. Integration of temporal single cell cellular stress response activity with logic-ODE modeling reveals activation of ATF4-CHOP axis as a critical predictor of drug-induced liver injury. *Biochem Pharmacol*. 2021;190:114591. doi:10.1016/j.bcp.2021.114591

346. Ma Y, Zhang L, Huang X. Genome modification by <scp>CRISPR</scp> /Cas9. *FEBS J*. 2014;281(23):5186-5193. doi:10.1111/febs.13110

347. Zhong A, Li M, Zhou T. Protocol for the Generation of Human Pluripotent Reporter Cell Lines Using CRISPR/Cas9. *STAR Protoc*. 2020;1(2):100052. doi:10.1016/j.xpro.2020.100052

348. Roberts B, Haupt A, Tucker A, et al. Systematic gene tagging using CRISPR/Cas9 in human stem cells to illuminate cell organization. *Mol Biol Cell*. 2017;28(21):2854-2874. doi:10.1091/mbc.E17-03-0209

349. Snijders KE, Fehér A, Táncos Z, et al. Fluorescent tagging of endogenous Heme oxygenase-1 in human induced pluripotent stem cells for high content imaging of oxidative stress in various differentiated lineages. *Arch Toxicol*. 2021;95(10):3285-3302. doi:10.1007/s00204-021-03127-8

350. Zhang H, Lesnov GD, Subach OM, et al. Bright and stable monomeric green fluorescent protein derived from StayGold. *Nat Methods*. 2024;21(4):657-665. doi:10.1038/s41592-024-02203-y

351. Ko S, Mizumoto K. Comparison among bright green fluorescent proteins in C. elegans. *MicroPubl Biol*. 2025;2025. doi:10.17912/micropub.biology.001447

352. Shaner NC, Lambert GG, Chammas A, et al. A bright monomeric green fluorescent protein derived from Branchiostoma lanceolatum. *Nat Methods*. 2013;10(5):407-409. doi:10.1038/nmeth.2413

353. Luker KE, Pata P, Shemiakina II, et al. Comparative study reveals better far-red fluorescent protein for whole body imaging. *Sci Rep*. 2015;5(1):10332. doi:10.1038/srep10332

354. Canty L, Hariharan S, Liu Q, Haney SA, Andrews DW. Peak emission wavelength and fluorescence lifetime are coupled in far-red, GFP-like fluorescent proteins. *PLoS One*. 2018;13(11):e0208075. doi:10.1371/journal.pone.0208075

355. Qian Y, Celiker OT, Wang Z, Guner-Ataman B, Boyden ES. Temporally multiplexed imaging of dynamic signaling networks in living cells. *Cell*. 2023;186(25):5656-5672.e21. doi:10.1016/j.cell.2023.11.010

356. Callegaro G, Kunnen SJ, Trairatphisan P, et al. The human hepatocyte TXG-MAPr: gene co-expression network modules to support mechanism-based risk assessment. *Arch Toxicol*. 2021;95(12):3745-3775. doi:10.1007/s00204-021-03141-w

357. Igarashi Y, Nakatsu N, Yamashita T, et al. Open TG-GATEs: A large-scale toxicogenomics database. *Nucleic Acids Res*. 2015;43(D1):D921-D927. doi:10.1093/nar/gku955

358. Pujari R, Hunte R, Khan WN, Shembade N. A20-mediated negative regulation of canonical NF-κB signaling pathway. *Immunol Res*. 2013;57(1-3):166-171. doi:10.1007/s12026-013-8463-2

359. Coornaert B, Carpentier I, Beyaert R. A20: Central Gatekeeper in Inflammation and Immunity. *Journal of Biological Chemistry*. 2009;284(13):8217-8221. doi:10.1074/jbc.R800032200

360. Liu T, Zhang L, Joo D, Sun SC. NF-κB signaling in inflammation. *Signal Transduct Target Ther*. 2017;2(1):17023. doi:10.1038/sigtrans.2017.23

361. Kim S, Shin M, Kim S. Lipocalin 2 activates the NLRP3 inflammasome via LPS-induced NF-κB signaling and plays a role as a pro-inflammatory regulator in murine macrophages. *Mol Med Rep*. 2022;26(6):358. doi:10.3892/mmr.2022.12875

362. Wang L, Zhu Y, Zhang N, et al. The multiple roles of interferon regulatory factor family in health and disease. *Signal Transduct Target Ther*. 2024;9(1):282. doi:10.1038/s41392-024-01980-4

363. Kumar A, Mishra S, Kumar A, et al. Essential role of Rnd1 in innate immunity during viral and bacterial infections. *Cell Death Dis*. 2022;13(6):520. doi:10.1038/s41419-022-04954-y

364. Satoh S, Nüssler AK, Liu ZZ, Thomson AW. Proinflammatory cytokines and endotoxin stimulate ICAM-1 gene expression and secretion by normal human hepatocytes. *Immunology*. 1994;82(4):571-576.

365. Hoque R, Farooq A, Mehal WZ. Sterile inflammation in the liver and pancreas. *J Gastroenterol Hepatol*. 2013;28(S1):61-67. doi:10.1111/jgh.12018

366. Vlasveld M, van den Berk L, Piñero J, et al. A broad kinase inhibitor library live cell imaging screen using liver, kidney and cardiac hiPSC-ICAM1-eGFP reporter lineages identifies liabilities for TNFα pathway modulation. *Arch Toxicol*. Published online November 5, 2025. doi:10.1007/s00204-025-04226-6

367. Mahmoud AM, Wilkinson FL, Sandhu MA, Lightfoot AP. The Interplay of Oxidative Stress and Inflammation: Mechanistic Insights and Therapeutic Potential of Antioxidants. *Oxid Med Cell Longev*. 2021;2021(1). doi:10.1155/2021/9851914

368. Pezone A, Olivieri F, Napoli MV, Procopio A, Avvedimento EV, Gabrielli A. Inflammation and DNA damage: cause, effect or both. *Nat Rev Rheumatol*. 2023;19(4):200-211. doi:10.1038/s41584-022-00905-1

369. Hasnain SZ, Lourie R, Das I, Chen AC, McGuckin MA. The interplay between endoplasmic reticulum stress and inflammation. *Immunol Cell Biol*. 2012;90(3):260-270. doi:10.1038/icb.2011.112

370. Sharma A, Toepfer CN, Ward T, et al. CRISPR/Cas9-Mediated Fluorescent Tagging of Endogenous Proteins in Human Pluripotent Stem Cells. *Curr Protoc Hum Genet*. 2018;96(1). doi:10.1002/cphg.52

371. Oinuma I, Kawada K, Tsukagoshi K, Negishi M. Rnd1 and Rnd3 targeting to lipid raft is required for p190 RhoGAP activation. *Mol Biol Cell*. 2012;23(8):1593-1604. doi:10.1091/mbc.e11-11-0900

372. Jennings P. Stress response pathways, toxicity pathways and adverse outcome pathways. *Arch Toxicol*. 2013;87(1):13-14. doi:10.1007/s00204-012-0974-4

373. Sinha R. Stress and substance use disorders: risk, relapse, and treatment outcomes. *Journal of Clinical Investigation*. 2024;134(16). doi:10.1172/JCI172883

374. Kumar V, Singh P, Gupta SK, Ali V, Verma M. Transport and metabolism of tyrosine kinase inhibitors associated with chronic myeloid leukemia therapy: a review. *Mol Cell Biochem*. 2022;477(4):1261-1279. doi:10.1007/s11010-022-04376-6

375. Duckett DR, Cameron MD. Metabolism considerations for kinase inhibitors in cancer treatment. *Expert Opin Drug Metab Toxicol*. 2010;6(10):1175-1193. doi:10.1517/17425255.2010.506873

376. Roskoski R. Properties of FDA-approved small molecule protein kinase inhibitors: A 2025 update. *Pharmacol Res*. 2025;216:107723. doi:10.1016/j.phrs.2025.107723

377. Ghosh S, De Smedt J, Tricot T, et al. Hipsc-derived hepatocyte-like cells can be used as a model for transcriptomics-based study of chemical toxicity. *Toxics*. 2022;10(1):1-18. doi:10.3390/toxics10010001

378. Boon R, Kumar M, Tricot T, et al. Amino acid levels determine metabolism and CYP450 function of hepatocytes and hepatoma cell lines. *Nat Commun*. 2020;11(1):1393. doi:10.1038/s41467-020-15058-6

379. Feyen DAM, McKeithan WL, Bruyneel AAN, et al. Metabolic Maturation Media Improve Physiological Function of Human iPSC-Derived Cardiomyocytes. *Cell Rep*. 2020;32(3):107925. doi:10.1016/j.celrep.2020.107925

380. Kanebratt KP, Janefeldt A, Vilén L, et al. Primary Human Hepatocyte Spheroid Model as a 3D In Vitro Platform for Metabolism Studies. *J Pharm Sci*. 2021;110(1):422-431. doi:10.1016/j.xphs.2020.10.043

381. Kim H, Im I, Jeon JS, et al. Development of human pluripotent stem cell-derived hepatic organoids as an alternative model for drug safety assessment. *Biomaterials*. 2022;286:121575. doi:10.1016/j.biomaterials.2022.121575

382. Igarashi Y, Nakatsu N, Yamashita T, et al. Open TG-GATEs: A large-scale toxicogenomics database. *Nucleic Acids Res*. 2015;43(D1):D921-D927. doi:10.1093/nar/gku955

383. Callegaro G, Kunnen SJ, Trairatphisan P, et al. The human hepatocyte TXG-MAPr: gene co-expression network modules to support mechanism-based risk assessment. *Arch Toxicol*. 2021;95(12):3745-3775. doi:10.1007/s00204-021-03141-w

384. Vlasveld M, Callegaro G, Fisher C, et al. The integrated stress response-related expression of *CHOP* due to mitochondrial toxicity is a warning sign for <scp>DILI</scp> liability. *Liver International*. 2024;44(3):760-775. doi:10.1111/liv.15822

Abbreviations

ADR	Adverse drug reaction
AIN	Acute interstitial nephritis
AKI	Acute kidney injury
APC	Antigen presenting cell
BAC	Bacterial artificial chromosome
c-IAP	Cellular inhibitors of apoptosis
Cmax	Maximum blood plasma concentration
CMLC	Cardiomyocyte-like cell
DAMP	Danger-associated molecular pattern
DDR	DNA damage response
DEG	Differentially expressed genes
DIKI	Drug-induced kidney injury
DILI	Drug-induced liver injury
eGFP	Enhanced green fluorescent protein
EGS	Eigengenescore
ERK	Extracellular signal-regulated kinase
FADD	Fas-associated death domain
FAERS	FDA Adverse Event Reporting System
HA	Homology arm
HCS	High-content screen
HDR	Homology Directed Repair
hERG	Human Ether-à-go-go
hiPSC	Human induced pluripotent stem cell
HLC	Hepatocyte-like cells
HPLC	High performance liquid chromatography
HTS	High-throughput screening
IAPS	Inhibitors of apoptosis
ICAM1	Intracelular adhesion molecule 1
IFN-γ	Interferon- γ
IκB	Inhibitor of kappa B
IKK	Inhibitor of kappa B kinase
IL	Interleukin
IRF1	Interferon Regulatory Factor 1
JNK	c-JUN NH2-terminal kinase
KI	Kinase inhibitor
LCN2	Lipocalin 2
LPS	Lipopolysaccharide
LSEC	Liver sinusoidal endothelial cell

LUBAC	Linear ubiquitin chain assembly complex
MAPK	Mitogen-activated protein kinase
NAM	New approach methodology
NEMO	NF-κB essential modulator
NF-κB	Nuclear factor kappa-light-chain-enhancer of activated B cells
P-adj	Adjusted P-value
PAM	Protospacer adjacent motif
PAMP	Pathogen-associated molecular pattern
PBMC	Peripheral blood-derived mononuclear cell
PHH	Primary human hepatocyte
PI	Propidium Iodide
PRR	Pattern recognition receptor
PT	Proximal tubule
PTLC	Proximal tubule-like cell
RIPK1	Receptor interacting protein kinase 1
RND1	Rho Family GTPase 1
TNF-α	Tumour necrosis factor-α
TNFAIP3	TNF alpha induced protein 3
TNFR	Tumour necrosis factor receptor
TRADD	TNF receptor associated death domain
WGCNA	Weighted gene co-regulation network analysis
VCAM1	Vascular adhesion molecule 1

Nederlandse samenvatting

Het optreden van ernstige bijwerkingen is een van de belangrijkste oorzaken dat een medicijn de markt niet bereikt of na het goedkeuren wordt teruggetrokken. De lever, de nieren, en het hart worden vaak getroffen door bijwerkingen en de schade die hierbij ontstaat is in veel gevallen onomkeerbaar. De meeste bijwerkingen ontstaan door gebruik van een medicijn in een te hoge dosis en zijn daardoor redelijk voorspelbaar. Bij een zeer klein deel van de patiënten ontstaat de toxiciteit echter ook bij normaal gebruik; dit wordt idiosyncratische toxiciteit genoemd. Er zijn meerdere oorzaken van idiosyncratische toxiciteit, waaronder interacties tussen het medicijn en patiënt-afhankelijke factoren, zoals genetische opmaak van een individu, de aanwezigheid van onderliggende ziekten en ontstekingsreacties. Medicijnen die ernstige idiosyncratische toxiciteit veroorzaken worden minder vaak voorgeschreven en krijgen een extra zware waarschuwing in de bijsluiter. Het is belangrijk om onderzoek te doen naar de mechanismes die leiden tot deze bijwerkingen, om zo in een vroeg stadium te kunnen voorspellen of een patiënt gevoelig is voor deze toxiciteit met als doel om uiteindelijke orgaanschade te voorkomen.

De meeste medicijnen activeren bepaalde processen, zogenaamde adaptieve stress responsen, om organen te beschermen tegen schade. Als de schade binnen de perken blijft, dan kan een cel hiervan herstellen. Echter, wanneer de schade een drempelwaarde heeft bereikt, dan zal deze overschakelen op specifieke celdood programma's. Zowel stress, celdood, als een onderliggende infectie kunnen zorgen dat een bepaald type immuun cellen, genaamd macrofagen, het ontstekingsbevorderende eiwit TNF-α gaan produceren. In een gezonde of minimaal gestreste cel kan TNF-α overleving bevorderen via de activatie van de transcriptie factor NF-κB. In het geval van een door medicijngebruik zeer gestreste cel, kan de aanwezigheid van TNF-α deze balans verstoren en leiden tot celdood.

Om vroeg in de ontwikkeling van een medicijn vast te stellen of een geneesmiddel bepaalde stress veroorzaakt, zijn preklinische experimenten nodig. Er zijn verschillende soorten preklinische weefselkweek modellen beschikbaar om geneesmiddelen op te testen. Echter voor het specifiek bestuderen van TNF-α geïnduceerde stress, is een preklinisch model nodig dat goed reageert op dit ontstekingseiwit om met een zo'n groot mogelijke kans dit type bijwerking op te pikken in het laboratorium.

Een relatief nieuwe categorie modellen voor het bestuderen van orgaanontwikkeling, ziekte en toxiciteit is gecentreerd rond het gebruik van pluripotente stamcellen. Deze stamcellen zijn geherprogrammeerd vanuit een somatische cel bijvoorbeeld uit de huid, urine of het bloed en hebben de capaciteit om vervolgens te differentiëren in elke cel van het lichaam. Door de embryonale ontwikkeling buiten het lichaam na te

bootsen kunnen bijvoorbeeld hepatocyten (lever), cardiomyocyten (hart) en de proximale tubulus (nier) gemaakt worden en vervolgens kunnen deze cellen blootgesteld worden aan geneesmiddelen om de medicijnveiligheid te bestuderen.

In dit proefschrift hebben we verschillende preklinische modellen vergeleken en gebruikt voor het meten van (TNF-α geïnduceerde) stress om zo te bepalen welk model het meest bruikbaar is voor ons in het lab.

In **hoofdstuk 2** hebben we gekeken of een bestaand model dat gebruikt maakt van HepG2 lever carcinoomcellen relevanter gemaakt kan worden. Onder 2D kweekomstandigheden hebben deze kankercellen een lage expressie van eiwitten die essentieel zijn voor het omzetten van geneesmiddelen. Door HepG2 cellen in 3D te kweken in Matrigel wordt de expressie van dit soort eiwitten belangrijk voor metabolisme van een medicijn verhoogd. Matrigel is echter afkomstig uit muizentumoren en is er erg veel variabiliteit tussen verschillende Matrigel batches, waardoor de reproduceerbaarheid niet gegarandeerd kan worden. Door Matrigel te vervangen door een zelf gesynthetiseerde gel met arginylglycylaspartic acid (RGD) peptiden konden we 3D sferoïden genereren met een beter metabolisme dan de sferoïden die in Matrigel werden gemaakt, gebaseerd op de expressie van verschillende enzymen, medicijntransporters en andere essentiële markers die van belang zijn in de lever. Het lijkt erop dat deze nieuwe gel een goed alternatief is om HepG2 sferoïden te maken, maar de toekomst zal moeten blijken of dit nieuwe model ook beter is in het voorspellen van toxiciteit na blootstelling aan geneesmiddelen.

Voor het voorspellen van immuun-gemedieerde toxiciteit is een levermodel nodig dat goed reageert op pro-inflammatoire eiwitten. Daarom hebben we in **hoofdstuk 3** beoordeeld hoe vijf verschillende lever modellen reageren op verschillende immuun-gerelateerde cytokines, zoals TNF-α, IL-1β, IL-6, IL-10, IL-12, en IL-18. De verschillende levermodellen bestonden uit primaire humane hepatocyten, die als de goudstandaard worden gezien binnen het onderzoek naar bijwerkingen van geneesmiddelen in de lever. Daarnaast hebben we HepG2 kankercellen gekweekt in 2 verschillende celkweek media en hebben we pluripotente stamcellen gedifferentieerd naar hepatocyten. Het laatste model bestond uit sferoïden bestaande uit meerdere celtypen (hepatocyten, stellaat cellen en Kupffer cellen) die aanwezig zijn in de lever om zo nog beter de lever na te bootsten. Op basis van TempO-seq analyse, een gerichte RNA sequencing techniek, hadden de meeste cytokines, inclusief IL-6, IL-10, IL-12 en IL-18, een minimaal effect op al deze levermodellen. Het pro-inflammatoire cytokine IL-1β zorgde voor een respons in alle vijf de levermodellen, maar we konden geen verschil opmerken in de mate van reactie. Wanneer we echter het effect van TNF-α bestudeerden, konden we verschillen opmerken in de mate waarop een lever model reageert. Primaire humane hepatocyten reageerden veel minder sterk op TNF-α vergeleken met de andere

modellen en daardoor konden we concluderen dat deze primaire hepatocyten niet het meest geschikte model zijn om de interactie van een medicijn en TNF-α te onderzoeken. Hepatocyten gemaakt van pluripotente stamcellen lieten daarentegen een soortgelijke, maar vele malen sterkere respons zien op TNF-α vergeleken met primaire hepatocyten. Daarom hebben we vervolgens in het stamcelmodel verder onderzocht of niet-steroïde anti-inflammatoire middelen (NSAIDs) en TNF-α met elkaar interacteren en de immuun-gerelateerde stress induceren. Uiteindelijk konden we concluderen dat deze interactie en bijkomende celdood was zoals verwacht met verschillende NSAIDs waarvan al bekend was dat ze immuun-geïnduceerde levertoxiciteit veroorzaken.

Aangezien we in hoofdstuk 3 hebben laten zien dat hepatocyten gemaakt van pluripotente stamcellen goed reageren op immunomodulatoren, besloten we dat dit het beste model was om de interactie van een geneesmiddel en TNF-α verder te onderzoeken op grotere groepen medicijnen. Dit is doorgaans een duur en tijdrovend proces. Idealiter zou de mogelijke toxiciteit van deze kandidaat geneesmiddelen snel en goedkoop bepaald moeten kunnen worden aan de hand van de activatie van stress responses eiwitten, zoals het geval is bij bijvoorbeeld inflammatie. Om te bepalen of er inflammatie optreedt kunnen we pluripotente stamcellen gebruiken waar bepaalde eiwitten gekoppeld zijn aan een fluorescent eiwit, deze vervolgens differentiëren naar hepatocyten en vervolgens blootstellen aan een kandidaat geneesmiddel en TNF-α. Onder de confocale microscoop kleuren deze cellen vervolgens groen op en kunnen we bepalen of er inflammatie is opgetreden. In **hoofdstuk 4** van dit proefschrift beschrijven we een methode om op een systematische manier genen te identificeren die geïnduceerd worden tijdens inflammatie in de lever. A20, LCN2, RND1, IRF1, VCAM1 en ICAM1 werden uiteindelijk geselecteerd als specifieke inflammatoire biomarkers en het fluorescente eiwit eGFP werd gekoppeld aan deze eiwitten om de cel te doen laten oplichten wanneer er inflammatie optreedt. Voor A20, IRF1, VCAM1 en ICAM1 hebben we op een succesvolle manier laten zien dat deze manier van het koppelen van een fluorescent eiwit aan een biomarker werkt in pluripotente stamcellen. Daarnaast kleurden deze cellen ook op wanneer ze werden gedifferentieerd naar hepatocyten. Ten slotte beschreven we dat deze biomarkers niet alleen inflammatie in de lever ontrafelen, maar dat deze fluorescerende pluripotente stamcellen ook gedifferentieerd konden worden naar cardiomyocyten om de activatie van inflammatoire verdedigingsmechanismen aan te tonen.

De bruikbaarheid van deze fluorescerende stamcellen hebben we verder aangetoond in **hoofdstuk 5**. Hier hebben we stamcellen waar het inflammatoire eiwit ICAM1 is gekoppeld aan eGFP gedifferentieerd naar hepatocyten, cardiomyocyten en de proximale tubulus cellen van de nier. Vervolgens hebben we deze cellen behandeld met een relatief nieuwe groep kandidaat geneesmiddelen genaamd kinase remmers

(760 kandidaten) en TNF-α. We hebben als een van de eersten laten zien dat het screenen van zo'n grote set medicijnen mogelijk is met stamcel model. Deze screen heeft aangetoond dat er veel overlap zit tussen geneesmiddelen die de expressie van ICAM1 blokkeren in de verschillende celtypen. Echter, wanneer we kijken naar kandidaten die de expressie van ICAM1, en dus inflammatie, verhogen, dan zien we bijna geen gelijkenis tussen deze kandidaat geneesmiddelen en de verschillende celtypen. Vervolgens hebben we ons verder verdiept in kandidaten die de expressie van ICAM1 verhogen in de proximale tubulus van de nier, aangezien dit wordt geassocieerd met het aantrekken en activeren van immuun cellen die verdere schade aan cellen en organen kunnen veroorzaken. We hebben gevalideerd dat kinase remmers die in klinische trials ook voor verhoogde inflammatie in de nier zorgen, ook geïdentificeerd konden worden in onze screen. Daarnaast hebben we op moleculair niveau laten zien dat dit mogelijk komt door de verhoogde uitscheiding van bepaalde pro-inflammatoire chemokines die verantwoordelijk zijn voor het aantrekken van immuun cellen die op deze manier verdere inflammatie en mogelijke schade stimuleren. Ten slotte beschrijven we dat deze kinase remmers vaak niet specifiek een kinase eiwit remmen, maar dat ze vaak off-target effecten hebben en daardoor mogelijk voor meer bijwerkingen zorgen. Dit benadrukt het belang om in vroege stadia van geneesmiddelontwikkeling al te kunnen voorspellen of een kandidaat wel of niet voor bijwerkingen zorgt.

In dit proefschrift hebben we beschreven hoe we het meest relevante preklinische model om immuun-gerelateerde toxiciteiten in de lever, nieren en het hart kunnen identificeren. Het gebruik van fluorescente reporters voor inflammatie in pluripotente stamcellen en de gedifferentieerde celtypen hiervan dragen hieraan bij. Daarnaast kunnen we met deze preklinische experimenten grote groepen nieuwe geneesmiddelen op een relatief eenvoudige manier testen. Aan de hand van deze uitkomsten kunnen andere vervolg testen worden gedaan die bijdragen aan een breder inzicht van de moleculaire mechanismen achter deze toxiciteiten. Dit draagt bij aan het goedkoop en sneller detecteren van mogelijke bijwerkingen in vroege fases van medicijnontwikkeling en op deze manier zullen nieuwe geneesmiddelen hopelijk in de toekomst sneller op de markt verschijnen.

List of publications

Van den Berk, L.‡, Popović, N.Z.‡, Wijmenga, R.H., Cao, X., Mummery, C.L., Orlova, V.V., Davis, R.P. (2026). Animal component-free differentiation of human pluripotent stem cells into macrophages. *Stem Cell Research*, 93, 103957.
‡ Authors contributed equally

Vlasveld, M.‡, **van den Berk, L.‡**, Piñero, J., Helmke, P. S., Ecker, G. F., van Rossom, R., Schmidt, B. Z., Verfaillie, C., Tassis, K., Callegaro, G., Bouwman, P., & van de Water, B. (2025). A broad kinase inhibitor library live cell imaging screen using liver, kidney and cardiac hiPSC-ICAM1-eGFP reporter lineages identifies liabilities for TNFα pathway modulation. *Archives of Toxicology*, 100(2), 585-601.
‡ Authors contributed equally

Callegaro, G., Schimming, J. P., Piñero González, J., Kunnen, S. J., Wijaya, L., Trairatphisan, P., **van den Berk, L.**, Beetsma, K., Furlong, L. I., Sutherland, J. J., Mollon, J., Stevens, J. L., & van de Water, B. (2023). Identifying multiscale translational safety biomarkers using a network-based systems approach. *IScience*, 26(3), 106094.

Snijders, K. E., Fehér, A., Táncos, Z., Bock, I., Téglási, A., **van den Berk, L.**, Niemeijer, M., Bouwman, P., Le Dévédec, S. E., Moné, M. J., Van Rossom, R., Kumar, M., Wilmes, A., Jennings, P., Verfaillie, C. M., Kobolák, J., ter Braak, B., Dinnyés, A., & van de Water, B. (2021). Fluorescent tagging of endogenous Heme oxygenase-1 in human induced pluripotent stem cells for high content imaging of oxidative stress in various differentiated lineages. *Archives of Toxicology*, 95(10), 3285–3302.

Liu, T.‡, **van den Berk, L.‡**, Wondergem, J. A. J., Tong, C., Kwakernaak, M. C., Braak, B. ter, Heinrich, D., van de Water, B., & Kieltyka, R. E. (2021). Squaramide-Based Supramolecular Materials Drive HepG2 Spheroid Differentiation. *Advanced Healthcare Materials*, 10(11).
‡ Authors contributed equally

Vaes, R. D. W., **van den Berk, L.**, Boonen, B., van Dijk, D. P. J., Olde Damink, S. W. M., & Rensen, S. S. (2018). A novel human cell culture model to study visceral smooth muscle phenotypic modulation in health and disease. *American Journal of Physiology-Cell Physiology*, 315(4), C598–C607.

About the author

Linda van den Berk was born in Rotterdam, The Netherlands, on the 28th of July 1993. She went to the Comenius College in Capelle aan den IJssel, where she obtained her VWO diploma with a major in Nature & Health. In 2011, she started her bachelor's in biology and medical laboratory research at Hogeschool Rotterdam and performed two internships in the laboratory of internal medicine under supervision of Prof. Dr. Hans van Leeuwen and Dr. Marjolein van Driel in the field of bone metastasis in prostate cancer. In 2015, she moved to Maastricht to start her Master Biomedical Sciences with a specialization in developmental biology and oncology at the Transnational University of Limburg, combining an educational programme at Maastricht University and Hasselt University (Belgium). During her first master's thesis, she focussed on the development of a visceral smooth muscle cell culture to study phenotypic modification during pancreatic cancer under supervision of Dr. Sander Rensen and Dr. Rianne Vaes at Maastricht University. During her second master's thesis project, she examined the role of Notch and Wnt signalling during lung development and repair using primary bronchial epithelial cells at Maastricht University in the laboratory of Prof. Dr. Marc Vooijs, under supervision of Dr. Carolien Wansleeben. In 2017, she started her PhD entitled "Advanced models for inflammation-dependent drug-induced organ toxicity" at the division of Cell Signalling and Drug Safety, LACDR, Leiden University under supervision of Prof. Dr. Bob van de Water, Dr. Bas ter Braak and Dr. Peter Bouwman. Currently, Linda is employed at the Leiden University Medical Centre (LUMC) in the lab of Prof. Dr. Christine Mummery and Dr. Richard Davis, focussing on applying pluripotent stem cell models of the immune system and heart to study health and disease.